# Combustion, Performance and Emissions Characteristics of Compression-Ignition Engines Fuelled by Sustainable Fuels

By:
**Ashand Mitra Namasivayam**

A thesis submitted for the degree of
Doctor of Philosophy to the University of London

Supervised by:
**Professor Theodosios Korakianitis**
(a.k.a. Theodosios Alexander)
**Professor Roy J. Crookes**

School of Engineering and Materials Science
Queen Mary University of London

January 2011

# I Abstract

Internal combustion engines are approaching their theoretical maximum efficiency, which could indicate limited future technological improvements in performance and exhaust emissions with standard fuels. In addition, fossil fuel dependence can only be reduced by implementing appropriate renewable fuel sources.

The experimental investigation in this work only concerns the compression-ignition (CI) engine combustion process both in normal operation and "dual-fuel" operation. The dual-fuel mode allows low-cetane number fuel to be used in CI engines, with a "pilot" fuel spray injection of high-cetane number fuel to provide ignition. Initially, rapeseed methyl ester (RME) and two water-in-RME emulsions were compared with normal diesel fuel during normal operation. Neat RME generally performed similarly to diesel fuel, while giving higher specific fuel consumption (SFC) levels. Both water-in-RME emulsions performed fairly similarly to neat RME. This suggests that the cooling effect of water vapourisation was a negligible factor throughout the operating range.

Natural gas dual-fuel operation reduced $NO_x$ at certain conditions and overall $CO_2$ emissions while thermal efficiencies were maintained compared with normal operation. However, significantly higher unburnt hydrocarbons (HC) and CO emissions were recorded at low and intermediate engine loads. For the emulsified pilot fuels, better fuel-air mixing (possibly as a result of "microexplosions") increased $NO_x$ after an equivalence ratio of about 0.6.

Hydrogen dual-fuel operation generally increased $NO_x$ emissions while $CO_2$ emissions were reduced compared with normal operation. Thermal efficiencies remained comparable for all pilot fuels. $NO_x$ emissions in the emulsified fuel cases were generally comparable to the neat RME pilot. Lower volumetric efficiency was also recorded, while power output was limited to maintain engine stability and avoid abnormal combustion caused by excessively high pressure-rise rates (called "hydrogen knock").

Overall, significant optimisation is needed to improve combustion efficiency at low and intermediate engine loads during dual-fuel CI engine operation. As these engines are designed specifically for liquid fuels, substantial engine customisation or even complete redesign (particularly in the fuel supply system) is needed to improve the combustion quality on a scale larger than that seen in this work.

# II Acknowledgements

First and foremost I thank my parents; Ir. Kalyana Lakshmi Raman and Mrs. Shanti Raman for their constant love, support and guidance. I also thank my brother Dr. Satesh Namasivayam for his inspiration.

I thank my supervisors, Professor Theodosios Alexander and Professor Roy Crookes for their instruction and understanding during this project. I also thank Professor Kelvin Bob-Manuel and Dr. John Olsen for their assistance and advice.

I thank the many people in the QMUL support staff; in particular Mr. Mick Etheridge, Mr. Vince Ford, Ms. Jun Ma, and Mr. Chris Straw for their expertise, professionalism and patience.

Finally, I thank all my friends and colleagues I have made over the course of this work for the useful discussions. Special thanks go to Dr. Alvaro Diez for helping immensely in developing the setup of the common-rail system.

# Contents

# List of Figures

# List of Tables

# III Nomenclature

Symbols

| | |
|---|---|
| $(A/F)$ | air-fuel ratio |
| $C_d$ | discharge coefficient |
| $c_\mathrm{v}$ | isochoric specific heat capacity |
| $c_\mathrm{p}$ | isobaric specific heat capacity |
| $E$, $\dot{E}$ | energy, energy rate |
| $(F/A)$ | fuel-air ratio |
| $k$ | power strokes per shaft revolution |
| $L$ | engine load force |
| $m$, $\dot{m}$ | mass, mass flow rate |
| $MF$ | mole fraction |
| $MW$ | molecular weight |
| $n$, $\dot{n}$ | mole, molar flow rate |
| $n'$ | number of revolutions per cycle |
| $N$ | engine speed |
| $P$ | pressure |
| $Q$ | heating |
| $R$ | specific gas constant |
| $t$ | time |
| $T$ | temperature |

| | |
|---|---|
| $U, u$ | internal energy, specific internal energy |
| $V$ | volume |
| $W$, $\dot{W}$ | work, work rate (power) |
| $Y$ | mass fraction |

Greek symbols

| | |
|---|---|
| $\alpha$ | gaseous fuel mole fraction |
| $\beta$ | excess air mole fraction |
| $\gamma$ | water mole fraction, ratio of specific heat capacities |
| $\Delta$ | difference operator |
| $\eta$ | efficiency |
| $\theta$ | angle (crank angle) |
| $\lambda$ | relative air-fuel ratio (inverse of $\phi$) |
| $\rho$ | density |
| $\sigma$ | number of engine cylinders |
| $\phi$ | fuel-air equivalence ratio |

Subscripts

| | |
|---|---|
| a | air |
| b | brake |
| C | cold (temperature) |
| ch | chemical |
| d | displacement |
| f | fuel |
| gf | gaseous fuel |
| H | hot (temperature) |
| intO2 | intake oxygen |
| n | net |
| p | products, pressure |
| pf | pilot fuel |
| r | reactants |
| s | swept |
| st | stoichiometric |
| th | thermal |
| to | to (the system) |
| v | volumetric |

Acronyms

| | |
|---|---|
| ABDC | after bottom dead centre |
| ATC | after top centre |
| ATDC | after top dead centre |
| AGTDC | after gas (exchange) top dead centre |
| BBDC | before bottom dead centre |
| BDC | bottom dead centre |
| BMEP | brake mean effective pressure |
| BTDC | before top dead centre |
| BITDC | before ignition (i.e. combustion) top dead centre |
| BSN | Bosch smoke number |
| CA | crank angle |
| Ch | chemical component |
| CI | compression-ignition |
| CNG | compressed natural gas |
| COV | coefficient-of-variation |
| DoE | design-of-experiments (computations) |
| DME | di-methyl ether |
| ECU | engine control unit |
| EOC | end-of-combustion |
| EGR | exhaust gas recirculation |
| EVC | exhaust valve close |
| EVO | exhaust valve open |
| FFR | fuel flow rate |
| FSD | full scale deflection |
| GISFC | gross indicated specific fuel consumption |
| HC | hydrocarbon |
| HHV | higher heating value |
| HRR | "heat release" rate (energy conversion rate during combustion) |
| IC | internal combustion |
| IHR | integrated "heat release" |
| IVC | inlet valve close |
| IVO | inlet valve open |
| LHV | lower heating value |
| IMEP | indicated mean effective pressure |

| | |
|---|---|
| LNG | liquified natural gas |
| LPG | liquid petroleum gas |
| MBT | maximum brake torque |
| NMHC | non-methane hydrocarbon |
| NG | natural gas |
| NGV | natural gas vehicle |
| OHV | overhead valve |
| PAH | polyaromatic hydrocarbon |
| PCV | pressure control valve |
| PEF | pilot fuel enthalpy fraction |
| PM | particulate matter |
| pps | pictures per second |
| PWM | pulse-width modulation |
| R/P | reserves-to-production ratio |
| Ra | radical component |
| RME | rapeseed methyl ester |
| RON | research octane number |
| rpm or RPM | revolutions per minute, r/min |
| SCR | selective catalytic reduction |
| SI | spark-ignition |
| SFC | specific fuel consumption |
| SOC | start-of-combustion |
| STP | standard temperature and pressure |
| TC | top centre |
| TDC | top dead centre |
| TDCf | firing top dead centre |
| Th | thermal component |
| THC | total hydrocarbons |
| TTW | tank-to-wheels |
| UHC | unburned hydrocarbons |
| VCV | volume control valve |
| VOC | volatile organic compound |
| WOT | wide-open throttle |
| WTT | well-to-tank |
| WTW | well-to-wheels |

# 1 Introduction

The current generation of internal combustion (IC) engines are now under greater scrutiny than ever before. More emphasis has been placed by governments, manufacturers as well as the public on improving the performance of these engines across a wide range of operating conditions. One major reason for this is the current state of the world's fossil fuel supply. Fossil fuel consumption is steadily rising, which can be a result of population growth. This is illustrated in figure 1 and is expected to grow further from current numbers by about 2 billion people in about 30 years time [1]. Total energy consumption has expectedly grown in response (by about 24% over the last 10 years) [2] and is expected to increase further in the future due to the increasing demand. These energy trends can be seen in figure 2. Increased fossil fuel demand requires increased fossil fuel production, which would drain current reserves at a faster rate. According to the BP Statistical World Review [2] there is only about 45 years worth of crude oil supply left at current reserve and production levels. However, this number has remained relatively steady since the 1980s. This is because supplies of crude oil that were previously inaccessible can now be obtained as a result of new technology allowing practical and economical recovery. This is in addition to new reserves being discovered. Despite this, fossil fuel conservation should be maintained and extended as it is a finite resource which will eventually be exhausted.

In addition to increasing demand on current global fossil fuel reserves, about 57% of these reserves are in regions that are in frequent political turmoil [2]. This has resulted in fluctuating oil prices and supply disruptions. For example, it can be seen from figure 3 that oil prices doubled from June 2007 to July 2008, only to halve in May 2009 [3]. Oil prices have been steadily rising since. These fluctuations have resulted in wide public concern over energy security, which in turn led to a greater awareness and practice of energy conservation. The fact that crude oil is a finite resource can only add to this concern. As IC engines are expected to continue to be a major propulsion provider well into the next century, the road transport sector in particular needs more secure and sustainable future fuel sources.

Legislative reduction of certain exhaust gas emissions is another issue facing the current generation of automotive IC engines. The fuels used by these engines (specifically diesel fuel and gasoline) produce significant amounts of pollution as a result of the combustion process, which is released to the atmosphere. This pollution

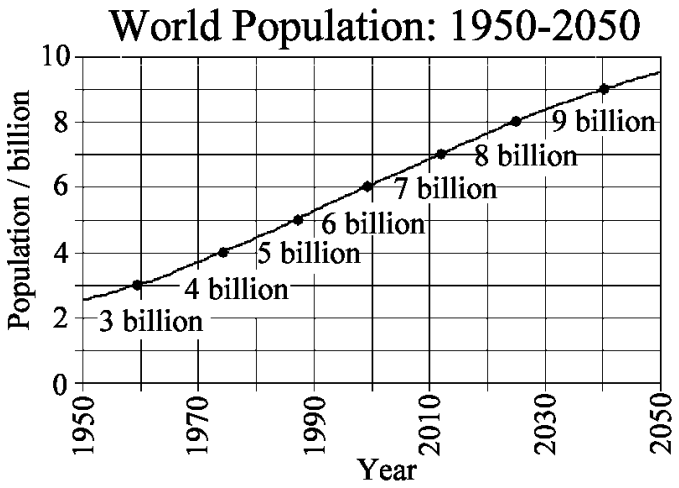


Figure 1: World Population 1950-2050 [1]

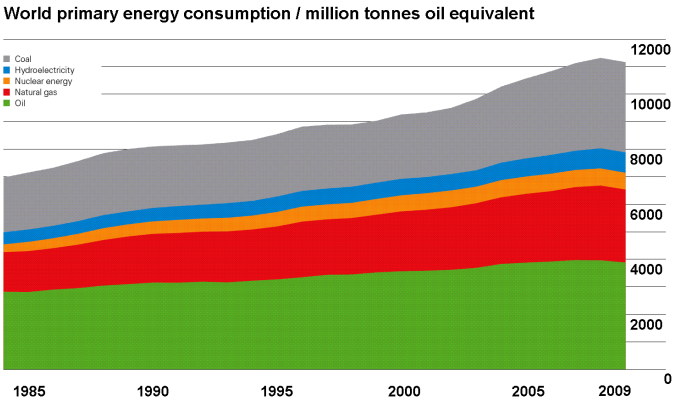


Figure 2: World primary energy consumption from 1984 to 2009, adapted from [2]

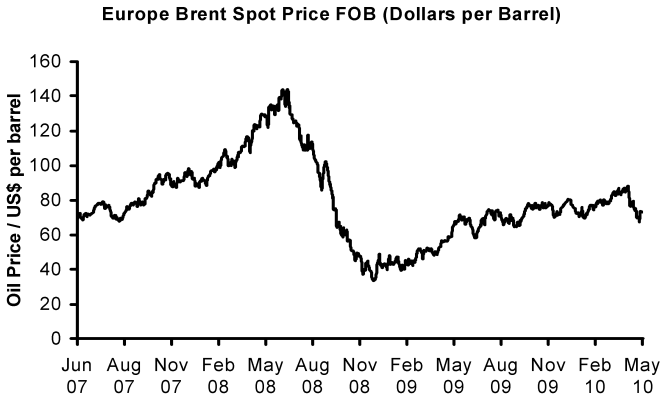


Figure 3: Brent Europe crude oil prices June 2007 to May 2010 [3]

includes controlled emissions such as smoke particulates, nitrogen oxides (which include NO and $NO_2$, collectively known as $NO_x$), unburnt hydrocarbons (HC) in addition to greenhouse gases such as carbon dioxide ($CO_2$). These emissions have

diverse effects on the environment, from causing ground level smog in cities to being suspected of raising the Earth's temperature (as a result of a net addition of greenhouse gas increasing the greenhouse effect). An analysis by the United States Environmental Protection Agency (EPA) [4] on global temperature increases (over the mean average) spanning the last 130 years shows that there is a general steady increase in global temperature rise rates. In 2010, the global temperature rise over the long term average (from 1901-2010) could be about 1 K. This apparently slight increase in global temperature can cause various problems, among them dramatically changing established weather patterns [5]. Automobile exhaust emissions can also cause human respiratory problems due to the presence of toxic gases such as carbon monoxide (CO). Cancer-causing agents (known as carcinogens) such as benzene are also a concern.

In order to curb these emissions governments have introduced laws where vehicular emissions are capped, such as the European emission standard (EURO). This particular standard was introduced in 1992 (EURO 1) and has been getting progressively stricter with new incarnations. These standards apply to all light-duty spark-ignition (SI) and compression-ignition (CI) engined vehicles sold in Europe. For example, the EURO 5 emission regulation came into force in September 2009 [6] and requires both SI as well as CI engined vehicles to reduce their emissions of $NO_x$ (which contributes to smog formation) by about 30% from the previous EURO 4 standard. Table 1 shows the emission levels of CO, total hydrocarbons (THC), non-methane hydrocarbons (NMHC), $NO_x$ and particulate matter (PM) imposed on typical CI and SI engine passenger vehicles (category M). This emission levels have the units of mass (of emission) emitted per unit distance travelled by the test vehicle during the European test cycle.

Table 1: Euro 5 emission limits for a category M vehicle powered by CI and SI engines [6]

| Emission levels / g/km | CI engine limits | SI engine limits |
|---|---|---|
| CO | 0.5 | 1.0 |
| THC | - | 100 |
| NMHC | - | 68 |
| $NO_x$ | 180 | 60 |
| PM | 0.005 | 0.005 |

At the same time, consumers expect parallel increases in performance and reductions in fuel consumption. This is reflected in the literature, where there is a need

to produce more power from smaller powerplants (increasing power output per unit engine mass; otherwise known as specific power) [7–10]. In order to accomplish these goals, a new generation of energy-conversion powerplants would need to be produced. This new generation would have improved thermal efficiency, increased specific power, and reduced harmful exhaust emissions [7, 10]. These trends so far have been accomplished in conventional reciprocating piston engines via innovations such as common rail fuel injection and extensive electronic engine control such as variable valve timing. These systems have worked very well in increasing thermal efficiency and reducing emissions of conventional IC engines. Engine thermal efficiency is increasing with engine size, due to the effect of surface-to-volume ratio and resultant energy rejection as a function of engine size. Currently, the most advanced reciprocating-piston engines (slow speed marine diesel engines, which are the largest reciprocating-piston engines in production) have maximum thermal efficiencies between 50% and 55%. They are approaching their correctly-evaluated Carnot coefficients of 62% to 67% [11], as explained below. This means current engines are far more efficient and approaching perfection than reported in the usual literature in the energy field.

The above claims can be illustrated by a simple Carnot coefficient evaluation example. The Carnot coefficient establishes the maximum efficiency any heat engine running on any fuel can produce when operating between two temperatures ("hot" and "cold"). Assuming a reciprocating piston engine is operating between a cold thermodynamic reservoir and a hot thermodynamic reservoir, the Carnot coefficient ($\eta_{\text{Carnot}}$) is evaluated by:

$$\eta_{\text{Carnot}} = 1 - \frac{T_{\text{C}}}{T_{\text{H}}} \tag{1}$$

where $T_{\text{C}}$ and $T_{\text{H}}$ are the cold reservoir and hot reservoir temperatures of the corresponding Carnot cycle respectively. Care should be taken in selecting appropriate values for $T_{\text{C}}$ and $T_{\text{H}}$ when using this expression.

For instance, it is common to use the maximum (adiabatic) combustion flame temperatures as $T_{\text{H}}$ (about 2500 K), and environmental temperature (about 300 K) as $T_{\text{C}}$. With these values, a maximum Carnot efficiency is about 88%. However, maximum combustion flame temperatures only occur for a small fraction of the time in the overall combustion process and in a small region of the combustion chamber. Therefore, adiabatic or maximum flame temperature is not a suitable representative of a constant temperature during the combustion process. Also with respect to a representative $T_{\text{C}}$, the charge temperature from the beginning to the end of

the exhaust process is much higher than environmental. Therefore, environmental temperature is not a suitable representative of a constant temperature during the energy-rejection process.

A quick estimate of an appropriate value of $T_{\mathrm{H}}$ is the metal temperature of the piston crown, or exhaust valve near the combustion chamber (about 900 K), and for $T_{\mathrm{C}}$ the cooling water temperature (about 340 K), which give a Carnot coefficient of about 62%.

A more elaborate estimate is an evaluation of the average temperature of energy addition and rejection to the working fluid, as evaluated from the temperature-entropy diagram of engines. A simplified example of the average temperatures of energy addition and rejection to an air-standard cycle is shown in figure 4, while the evaluation for the test engine in this thesis is included in appendix F.

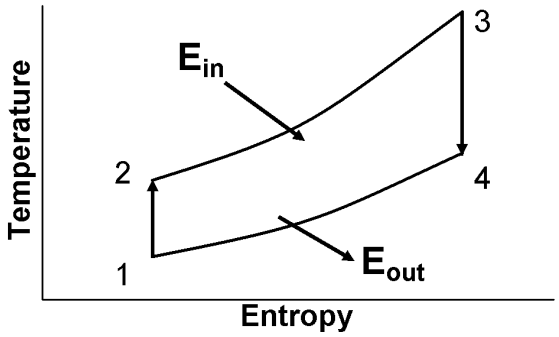


Figure 4: Representation of temperature-entropy diagram for an ideal engine cycle

States 1 to 2 indicate isentropic compression and states 2 to 3 indicate constant-volume (in an Otto-cycle) energy addition ($\mathrm{E_{in}}$). In an ideal Diesel cycle, states 2 to 3 indicate constant-pressure energy addition while an ideal dual cycle indicates partially constant-volume energy addition followed by a constant-pressure energy addition. States 3 to 4 indicate isentropic expansion and states 4 to 1 indicate constant-volume energy rejection ($\mathrm{E_{out}}$). Average values of $T_{\mathrm{H}}$ ($T'_{\mathrm{H}}$) and $T_{\mathrm{C}}$ ($T'_{\mathrm{C}}$) can be found by the following expressions :

$$T'_H = \frac{1}{\Delta S}\left(\int_{E_{in}} T dS\right) \tag{2}$$

$$T'_C = \frac{1}{\Delta S}\left(\int_{E_{out}} T dS\right) \tag{3}$$

where the integral limits for $T'_{\mathrm{H}}$ and $T'_{\mathrm{C}}$ are between states 2-3 and states 4-1 respectively. $\Delta S$ represents the change between initial and final entropy levels of the

respective limits. Using temperature versus specific entropy plots made from experimental data recorded during a representative cycle from the test engine used in this work, the average values of $T'_{\mathrm{H}}$ and $T'_{\mathrm{C}}$ are about 1302 K and 556.7 K respectively (details shown in appendix F). With these values, the Carnot coefficient for the test engine used in this thesis is about 57%, and the maximum brake thermal efficiencies obtained during the tests were of the order of 33%.

While the thermal efficiencies of slow speed marine diesels are approaching their Carnot coefficients, smaller reciprocating piston engines (which represent the majority of piston engines) present significant room for efficiency improvements. One way to collectively tackle the issues discussed previously (specifically minimising fossil fuel consumption, reducing exhaust emissions and improving engine efficiency) is to further investigate alternative fuels used in IC engines. Currently, traditional engine fuels are not infinite energy sources. The level of exhaust emissions permitted as a result of using these fuels in IC engines is being continuously reduced by legislation. Traditional fuels also have specific properties which govern IC engine design, inherently limiting the scope of IC engine operation (i.e. traditional knock limits and $\mathrm{NO_x}$ emissions). Over the course of this work, it was found that there are several alternative fuels, which have been investigated for use in current IC engines. While most of these fuels cannot be made sustainably in the short term via traditional production processes, long-term production possibilities do exist and require more development. The fuels themselves can be used in IC engines with relatively minor modifications, and have properties which can allow for increases in thermal efficiency (i.e. high octane numbers). However, these fuels also produce undesirable effects (in terms of performance and emissions) if engines are not optimised for alternative fuel use.

This work presents an account of three alternative fuels (biodiesel, methane, hydrogen), investigated in the following manner. A complete literature review of each fuel was done, covering current state-of-the-art production process (in addition to sustainable production processes), storage media, and previous work on engine performance and emissions. An experimental assessment of each fuel (used in a common engine under two different operating modes, i.e. normal and dual-fuelling) was then conducted by the author. As a result, all three fuels were investigated as a whole; and in particular with regard to long-term production sustainability and suitability as current vehicular fuels. This provided a complete and unique perspective of these fuels, which (to the author's knowledge) has not been presented in the literature and

is now presented here. In addition, a previously untested method of reducing $NO_x$ emissions during dual-fuel operation (specifically the use of water-in-fuel emulsions as pilot fuel) was investigated. Based on the collective analysis from the presented experiments and the literature review, conclusions of how these fuels currently stand for sustainable engine use are drawn with recommendations for further investigation.

## 1.1 Research Motivation

IC engine research at Queen Mary University previously focused primarily on CI engines powered by various fuels during normal CI engine operation. Dual-fuel CI engine operation with natural gas ignited by a variety of high-cetane number pilot fuels was also investigated prior to the current work. As a result, the following literature review assesses the current state-of-the-art of the above CI engine combustion modes. It was also stipulated at the start of the current work that gaseous hydrogen combustion would be investigated to assess its status as a long-term IC engine fuel. In particular, there are reservations in terms of its suitability for use in current automotive engines as a result of its physical properties. Water addition to the combustion process was also investigated as a control method for high $NO_x$ emissions. With this motivation, the following literature review was conducted.

# 2 Literature Review

## 2.1 Biodiesel as a Diesel Fuel Substitute

Biodiesel in its various forms has been investigated extensively, since the inception of CI engines by Rudolf Diesel. While the term "biodiesel" has been used to describe most alternative diesel fuels, in this work the term applies only to the methyl esters produced via transesterification of triglycerides. These fuels have shown to generally maintain typical CI engine performance when compared with conventional diesel fuel. However, there are also trends of increases in fuel consumption and $NO_x$ emissions, while smoke emissions are reduced. It will be shown in the following section that methyl ester biodiesel is a promising diesel fuel substitute in terms of engine use. However, it cannot be viewed as a long-term substitute as long as the current established feedstocks are used (to produce first-generation fuels). This is primarily because these plant feedstocks compete with food crops and rainforests for land area. Other production methods that employ renewable sources (preferably waste biomass, which is used to produce second-generation biofuel) need to be found to obtain a complete diesel fuel substitute.

### 2.1.1 Overview of Biodiesel Production

Generally, biodiesel (specifically known as methyl ester) is made from triglycerides via a chemically reversible process called transesterification [12–14]. Here triglycerides (usually raw plant oils such as vegetable oil) react together with an alcohol (usually methanol) to produce a methyl ester as well as glycerine as a useful by-product. Catalysts (such as sodium hydroxide) are also used in the process which occurs at elevated pressures and temperatures (of the order of 60 degrees Celsius and 0.2 MPa respectively). In Europe, the feedstock used for this process is usually rapeseed oil while other plant oils have been used in other regions (such as soybean oil in the United States) [12].

Previous work [15, 16] shows results of life cycle analyses of the input energy requirements and $CO_2$ emissions of soybean biodiesel made via transesterification compared with conventional diesel fuel. Here producing 1 MJ of conventional diesel fuel energy requires 1.2 MJ of overall input energy, while producing 1 MJ of soybean biodiesel fuel energy requires a comparable 1.24 MJ of input energy. Other work found very

similar numbers [16]. Reference [15] found that producing 1 MJ of conventional diesel fuel energy generates about 95 g of $CO_2$ while producing 1 MJ of soybean biodiesel energy generates about 41 g of $CO_2$. This significant reduction (of about 60%) is due to the $CO_2$ generated being part of a closed $CO_2$ cycle, where a portion of $CO_2$ emitted during biodiesel production/use is consumed during soybean plant growth (as a result of photosynthesis). Reference [16] shows a greater reduction of about 80%, attributed to the same reason. Figure 5 illustrates this reduction, where the $CO_2$ emissions produced per unit power produced during the test vehicle service is shown. The figure also shows the $CO_2$ reduction when using a biodiesel-diesel fuel blend. However, input energy levels can vary with biodiesels made from different feedstocks. For instance, 1 MJ of biodiesel fuel energy made from jathropa oil can consume between 0.68 MJ and 1.43 MJ of input energy [15]. This variation depends on soil fertility and irrigation levels, which affects the final jathropa seed yield. As a result, the type of plant feedstock in addition to the plant's suitability for local weather and soil conditions has a crucial effect on the viability of the final product.

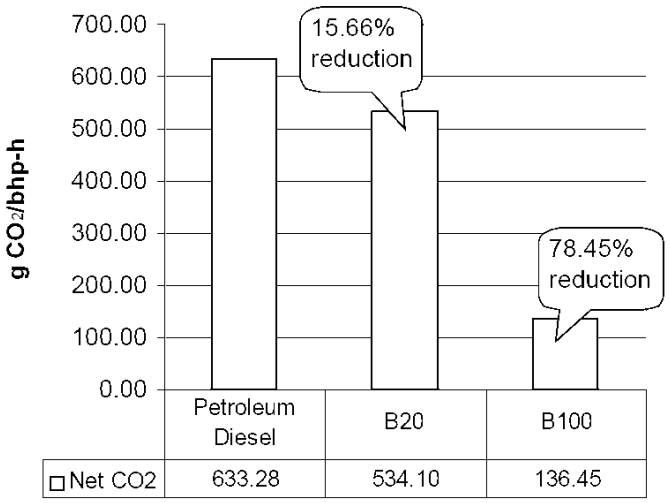


Figure 5: Life cycle $CO_2$ emissions per unit power produced during base vehicle service for diesel fuel, a 20% biodiesel-in-diesel fuel blend (B20) and 100% biodiesel (B100) [16]

Following this, there are also feasibility issues of using so-called "first-generation" biofuels, an umbrella term which includes biodiesel made from seed crops. It has been reported that 72% of Europe's agricultural land is needed for Europe to produce 10% of its total fuel consumption from biofuels [17]. Brazil on the other hand requires 3% of its agricultural land to produce the same amount [17]. This difference is due to a combination of factors, chief among which are differences in available land areas for cultivation and favourable local weather conditions which can allow larger yields [17]. Utilising the available land area for biofuel feedstock also raises

issues regarding competition with established food crops as well as natural rainforests. Increased demand for and use of irrigation as well as cultivation ancillaries (fertiliser, pest control etc) on the scale needed for fossil fuel replacement is also a concern [17]. As a result, these "first-generation" biofuels cannot be viewed as a long-term solution. Renewable fuels produced via other methods which avoids this land issue needs to be considered for long-term biofuel supply. Biomass-to-liquid production processes (such as the Fischer-Tropsch process) can be used to produce a wide range of hydrocarbon fuels using a variety of feedstocks, such as waste plant material. In the Fischer-Tropsch process, the feedstock is gasified at very high temperatures (600 to 900 degrees Celsius) to produce synthesis gas (hydrogen and carbon monoxide) [18]. The synthesis gas is then converted via CO hydrogenation (in the presence of a catalyst) to produce a wide range of hydrocarbons [18]. However, there are issues with cost and process complexity which affect the type and quality of hydrocarbons produced. For example, the non-uniform nature of the feedstock used generates varying quality of the synthesis gas, requiring purification to avoid damaging the catalyst during the hydrogenation process. The catalysts used also have reliability issues over their usage lifetimes [18]. The feedstock used also affects the range of hydrocarbons produced significantly (i.e. some of the hydrocarbons produced might not be suitable for use as fuels). Further end-product processing might be required to narrow the hydrocarbon range produced for a particular purpose (i.e. to produce higher concentrations of hydrocarbons that can be appropriate fuels) [18]. Significant research is needed to refine these processes further in order to allow more robust hydrocarbon fuel production.

Overall, first-generation biodiesel is comparable to diesel fuel in terms of life-cycle energy requirements and can be made fairly easily from fatty oils via transesterification. Life-cycle $CO_2$ emissions are also significantly lower, as the $CO_2$ released during the life-cycle of biodiesel is part of a closed cycle. However, the feedstock for first-generation biodiesel production competes with food crop and rainforests for land use and is not a feasible prospect for replacing conventional diesel fuel in the long term. Biomass-to-liquid processes are promising solutions, however, more research is required in order to make the process more robust and specific in terms of the final product produced.

### 2.1.2 Biodiesel Combustion in Compression-Ignition Engines

Previous work done by Prof. Crookes et.al. [19] found that pure rapeseed methyl ester (RME) biodiesel increases specific fuel consumption (SFC) compared with conventional diesel fuel by about 14%. This follows from the lower specific energy content of biodiesel compared with diesel fuel (38.6 MJ/kg and 42.5 MJ/kg respectively). Extensive review work [12, 13, 20, 21] also report similar trends with other pure biodiesels (such as soybean biodiesel), as shown in figure 6.

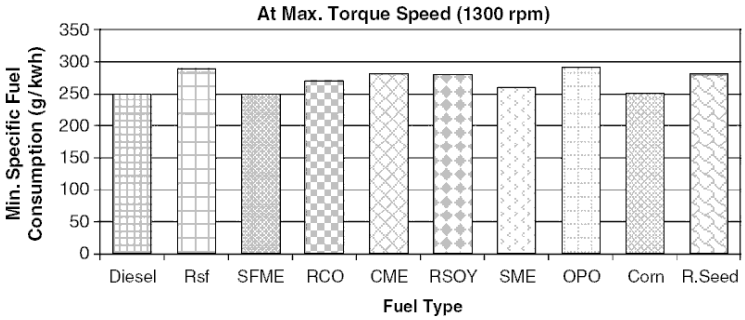


Figure 6: Specific fuel consumption (SFC) levels for various fuels, where Rsf = raw sunflower oil, SFME = sunflower oil methyl ester, RCO = raw cotton seed oil, CME = cottonseed methyl ester, RSOY = raw soybean oil, SME = soybean methyl ester, OPO = opium poppy oil, R.seed = rapeseed oil [20]

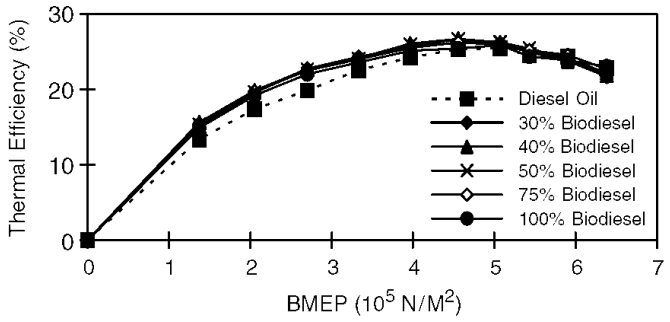


Figure 7: Thermal efficiency comparison with BMEP for pure diesel fuel, linseed oil biodiesel and various linseed oil biodiesel-in-diesel fuel blends [20]

Engine tests with biodiesel-in-diesel fuel blends also show increased SFC levels compared with pure diesel fuel, albeit to a lesser degree. For instance, a 20% rapeseed methyl ester (RME)-in-diesel blend increased SFC levels by about 3% [13,21]. However, there is minimal variation in thermal efficiency between pure biodiesel and pure diesel fuel [19–21]. Figure 7 shows this thermal efficiency trend for pure fuels as well as different biodiesel-in-diesel fuel blends plotted against brake mean effective pressure (BMEP). This is attributed to comparable combustion characteristics

(such as peak cylinder pressure and pressure-rise rates) with conventional diesel fuel [12, 13, 20]. Power output compared with engine operation with conventional diesel fuel is also maintained, with minor power reductions only at full power conditions (of the order of 5%) [21]. This is also attributed to the lower energy content, however, the reduction is minimised by a larger injected fuel mass during engine operation with biodiesel. This is caused by the slightly higher density and viscosity of biodiesel compared with conventional diesel fuel [21]. Slightly shorter ignition delays compared with conventional diesel fuel are also reported, which follows from the generally higher cetane number of biodiesel [20]. However, this trend varies slightly with different biodiesels and their biodiesel-in-diesel fuel blends.

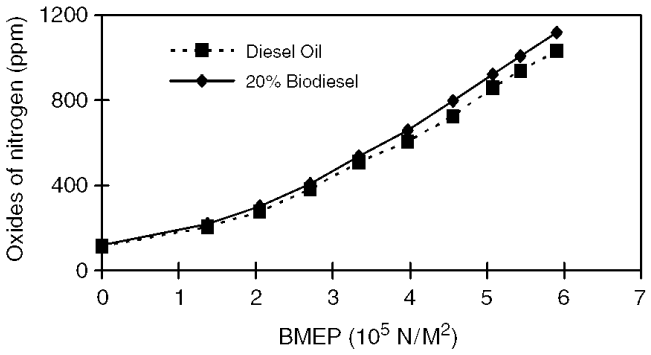


Figure 8: $NO_x$ comparison with BMEP for pure diesel fuel and a 20% linseed oil biodiesel-in-diesel fuel blend [20]

Biodiesels also generally produce similar levels of $NO_x$ emissions compared with conventional diesel fuel however, a significant portion of the literature present slightly higher levels (by about 5-10%) [21]. These cases have been attributed to biodiesels having a higher bulk moduli compared with diesel fuel which results in advanced injection timing, higher premixed combustion rates and higher combustion temperatures [20,21]. Fuels with higher bulk moduli carry a higher speed of sound, which in turn results in faster transferal of the pressure wave from the fuel pump to the injector needle causing earlier injection [22]. This can be seen from the Newton-Laplace equation , shown below:

$$c = \sqrt{\frac{C}{\rho}} \tag{4}$$

where $c$ is the speed of sound, $C$ is the bulk modulus of the medium and $\rho$ is the density of the medium. Biodiesel can have a bulk modulus about 10% higher than diesel fuel [22], which results in a (roughly) 4% increase in the speed of sound. This can result in a 1 crank angle degree advance in injection timing. Previous work [23] has assessed this claim together with other factors (with regards to biodiesel feedstock

and test rig design) when using biodiesel fuel. As a result of different engine configurations and biodiesel types used in the literature, it was concluded that other factors can contribute to higher $NO_x$ emissions in addition to advanced injection timing. The most significant of these are shorter ignition delays, resulting from slightly higher cetane numbers of some biodiesels. This may cause higher post-flame temperatures and hence higher $NO_x$ formation. Shorter combustion durations have also been reported which, when coupled to the shorter ignition delay, may increase the residence time for post-flame $NO_x$ formation to occur [23]. $NO_x$ increases were also noted for biodiesel-in-diesel fuel blends, an example of which can be seen in figure 8 [13, 21]. Smoke emissions during pure biodiesel use are generally reduced compared with conventional diesel levels (of the order of 20-50%), as seen in figure 9 [21].

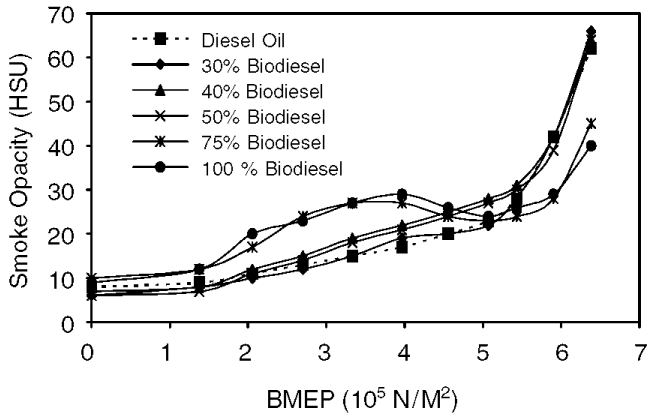


Figure 9: Smoke opacity (Hartridge Smoke Unit, HSU) comparison with BMEP for pure diesel fuel, linseed oil biodiesel and various linseed oil biodiesel-in-diesel fuel blends [20]

Biodiesel-in-diesel fuel blends are more effective in lowering smoke levels compared with pure biodiesel, where a 20% reduction in smoke levels can be obtained with a 20% blend while pure biodiesel reduced smoke levels by about 50% [21]. A combination of factors can cause this smoke reduction; the first being the advanced injection timing caused by the higher bulk modulus of biodiesel. The advanced injection timing allows more air-fuel mixing to occur, preventing fuel-rich regions from forming and reducing soot formation rates during combustion. The added oxygen contained within the chemical structure of biodiesel also contributes to lower smoke levels via enhanced soot oxidation [20, 21]. Fuel molecules are oxidised further during combustion to form CO instead of soot precursors [21]. In addition, biodiesels do not contain polyaromatic hydrocarbons (PAH) which are precursors to soot formation. Lower unburnt hydrocarbon (HC) and carbon monoxide (CO)

levels are also reported (both of the order of 50%) with pure biodiesel use as a result of more complete combustion. This is also a result of the oxygen contained within the chemical structure of biodiesel [20, 21].

Long-term effects of using pure biodiesel and biodiesel-in-diesel fuel blends in conventional CI engines have also been assessed [12, 13, 20]. Biodiesel-in-diesel fuel blends produce about 40% less carbon deposits within the combustion chamber (on the piston and injector nozzle for example) compared with conventional diesel fuel [20]. Other work found [13] that, while no significant difference in engine wear occurs with biodiesel-in-diesel fuel blends, there is soap buildup in the engine lubricating oil. This generates sludge deposits on the rocker assemblies which were not seen with diesel fuel use. Biodiesel is also more susceptible to freezing in cold weather conditions than diesel fuel, in addition to biological degradation over long storage periods.

Overall, methyl ester biodiesel is a suitable substitute for diesel fuel when used in engines. While performance and emissions of different biodiesels can vary compared with diesel fuel, there is a general trend of maintained engine performance. However, an increase in fuel consumption is noted, while there is also an increase in $NO_x$ emissions (the severity of which varies with different methyl esters and test engines). Smoke levels are also reduced. It is likely that with modern common-rail injection systems these differences would be minimised. As modern CI engines are designed to employ low-sulfur diesel fuel, pure biodiesel can be used without any engine modifications. While the effects of long-term use have been investigated with biodiesel-in-diesel blends, there is a lack of results employing pure biodiesel.

## 2.2 Natural Gas as an Automotive Fuel

Natural gas (NG) is a gaseous fossil fuel that has been investigated extensively as a SI and CI engine fuel. It is primarily made up of methane as well as various other gas species, and a detailed typical composition is shown in table 2.

Table 2: Typical natural gas composition by volume [24]

| Species | Content |
|---|---|
| Methane | 92.00% |
| Ethane | 3.00% |
| Propane | 0.70 % |
| Butane | 0.02% |
| Pentane | 0.10% |
| Carbon Dioxide | 0.60% |
| Nitrogen | 3.58% |

Compared with conventional gasoline-powered SI engines, natural gas SI engines can run at higher compression ratios, producing higher thermal efficiencies and increased $NO_x$ emissions. In addition, these engines produce relatively lower power output mainly due to issues with inducting sufficient air for combustion. As for CI engines, the "dual-fuel" mode is required for acceptable engine operation. Here a high-cetane number "pilot" fuel is injected directly into the cylinder providing an ignition source for the premixed natural-gas air charge. Thermal efficiency levels are generally maintained compared with conventional CI engine operation with diesel fuel, while smoke levels are reduced. However, incomplete combustion at low and intermediate engine loads are encountered, resulting in low thermal efficiency and high unburnt HC emissions. Power output is also lower at certain conditions compared with conventional CI engines, for reasons similar to those affecting power output of SI natural gas engines. In both engine types, power output can be maintained with direct in-cylinder natural gas injection. As a result, further development (in particular fuel and air induction) is needed. The current state-of-the-art as well as further refinements/ optimisations are discussed in the following sections.

### 2.2.1 Overview of Natural Gas Production and Supply

Crude oil supplies are limited and new sources of IC engine fuel need to be found. These new fuel sources have to last as long as IC engines remain the dominant automotive powerplant. One of the reasons why natural gas is being investigated as an alternative fuel is its significantly larger proven reserves compared with crude oil. Figure 10 shows the current known reserves-to-production (R/P) ratio for crude oil and natural gas, which are about 45 and 63 years respectively [2]. The figure also shows that these R/P ratios have remained fairly steady just over the last two decades. This is because new reserves being discovered in addition to known but previously inaccessible supplies of natural gas recently becoming accessible as a result of new technology allowing practical and economical recovery.

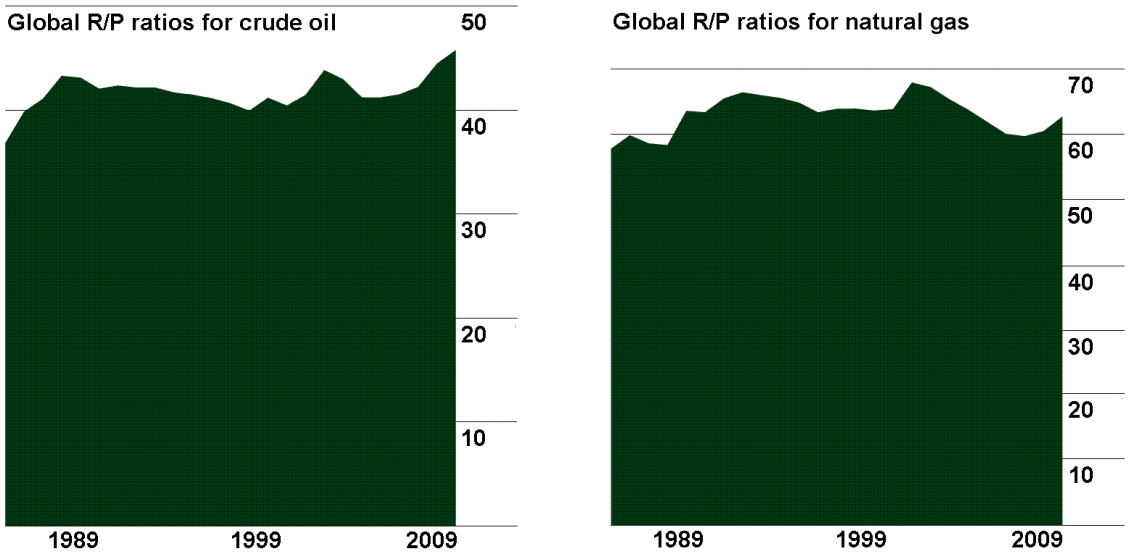


Figure 10: Reserves-to-production (R/P) ratios for crude oil and natural gas from 1985 to 2009, adapted from [2]

There already exists a fairly extensive and developed general supply infrastructure for natural gas as a result of its use in electrical power generation. For example in the UK, natural gas is the largest singular fuel source for electricity generation (providing about 46% of total electrical energy in 2008 [25]). This is a result of a gradual substitution of coal-fired powerplants, mainly in an effort to reduce $CO_2$ emissions. However, there is a lack of a dedicated automotive natural gas refuelling infrastructure. Therefore, natural gas cannot be considered as a complete replacement of conventional fuels for the near term. However, extensive automotive refuelling infrastructures do exist in certain countries such as Brazil. There are nearly two

thousand refuelling stations in place for the over one million natural gas vehicles (NGVs) that are in use [26]. Brazil went down the natural gas route in an effort to reduce their dependence on crude oil [26]. Natural gas is also cheaper to buy compared with conventional fuels. As of 2009, natural gas costs about 0.5 US dollars per 100 MJ of fuel energy (UK Heren NBP Index) while crude oil costs about 1.0 US dollars per 100 MJ (OECD countries cif) [2]. Therefore, while an initial investment would be required to convert a conventional vehicle to a NGV, the lower price of natural gas will return the initial expense over time [27].

As natural gas is a fossil fuel it is not renewable. However, methane (which is the main constituent of natural gas) can be produced in a renewable manner using biological decomposition [28, 29]. Commonly known as biogas or landfill gas, this gas is a by-product of anaerobic biological decomposition. It is usually composed of at least 50% methane and up to 50% $CO_2$, with trace amounts of hydrogen, nitrogen and hydrogen sulfide [24]. As a result, biogas has to be purified prior to use which increases production complexity and cost. Well-to-wheels (WTW) life cycle analyses have been performed [30–32], concluding that fossil natural gas consumes similar amounts of energy per unit mass and produces similar amounts of $CO_2$ to conventional fuels over its life cycle (of the order of 2 MJ/km and 150 g/km respectively). Methane produced from renewable sources such as biomass and landfill gas has significantly lower WTW $CO_2$ than natural gas (about -250 g/km). This means a net reduction of atmospheric $CO_2$ can occur. However, as a result of the added processing and purification required, the energy requirements rise to about 3.5 MJ/km [31]. These numbers correlate to the energy needs/ $CO_2$ emissions of a state-of-the-art European mid-size vehicle travelling a distance of 1 km.

Overall, natural gas is produced in a generally similar manner to crude oil with similar life-cycle energy and emission levels. While natural gas is not renewable, methane (which is the primary constituent of natural gas) can be made renewably via biological decomposition. Use of biogas also allows a net reduction in atmospheric $CO_2$ emissions. Additional processing and purification will be required resulting in increased energy input requirements. There is also a significant natural gas supply and distribution infrastructure already in place (for applications such as electricity production) which can be extended to cover automotive fleet use.

### 2.2.2 Natural Gas Combustion in Spark-Ignition Engines

Previous work [24,33,34] found that engines fuelled by natural gas produces thermal efficiency levels about 5% higher than typical SI engines running gasoline. This can be due to several factors. The first is the high octane number of natural gas, which allows comparatively higher compression ratios to be used. Previous work [24] found that the compression ratio of a typical gasoline SI engine can be increased from 8:1 to 13:1 with natural gas. As a result, thermal efficiency can also be increased [35].

Table 3: Fuel chemical properties and physical characteristics [36]

| Fuels | Gasoline | Diesel | RME | NG | Hydrogen |
|---|---|---|---|---|---|
| Chemical formula | $C_nH_{1.87n}$ | $C_nH_{1.8n}$ | $C_{21}H_{38}O_2$ | $CH_4$ | $H_2$ |
| Density* / kg/m$^3$ | 720-780 | 827-840 | 880 | 0.73* | 0.09* |
| $LHV_f$ / MJ/kg | 44.0 | 42.5 | 36.7-40.5 | 45.0 | 120.0 |
| Cetane number | - | 52.0 | 54.4 | - | - |
| Octane number | 92-98 | - | - | 120 | 120 |
| $A/F_{st}$ | 14.6 | 14.5 | 12.6 | 17.3 | 34.4 |

*0° Celsius, 1 atm

The larger lower heating value ($LHV_f$) of natural gas compared with gasoline erroneously indicates natural gas may produce more power than gasoline during combustion. However, the stoichiometric fuel-air ratio ($F/A_{st}$, inverse of the stoichiometric air-fuel ratio $A/F_{st}$) of methane is lower than that of gasoline (as seen in table 3). As seen from equation 5, fuel parameters can affect power output via the product of $\phi\,(F/A)_{st}\,LHV_f$ that affects engine power significantly.

$$\dot{W}_b \;=\; k\,\eta_{th}\,\eta_v\,\rho_a\,V_d\,N\,\phi\,\left(\frac{F}{A}\right)_{st}\,LHV_f \tag{5}$$

Here power output ($\dot{W}_b$) is related to the number of power strokes per engine revolution ($k$), thermal efficiency ($\eta_{th}$), volumetric efficiency ($\eta_v$), intake air density ($\rho_a$), the engine displacement ($V_d$), engine speed ($N$), equivalence ratio ($\phi$), stoichiometric fuel-air ratio ($F/A_{st}$) and the lower heating value of the fuel($LHV_f$). Despite the positive effects of using natural gas fuel, natural gas SI engines produce lower power levels across the operating range compared with gasoline engines [37]. This is primarily because of the lower density of natural gas, which requires the induction of a large volume of natural gas in order to produce similar power levels as gasoline engines. This volume of gaseous fuel displaces a similar volume of air from entering the engine, therefore reducing volumetric efficiency by up to 10-15% depending

on engine configuration [33]. This results in a corresponding reduction in power. Airflow into the engine can also be further restricted by flow mixers and venturis installed for natural gas induction in retrofitted natural gas engines [37].

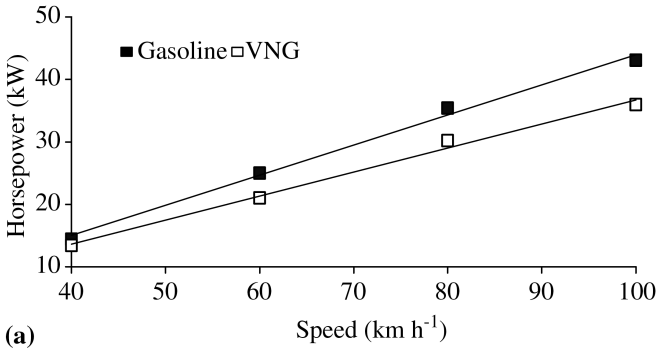


Figure 11: Power comparison for a typical bi-fuel natural gas (vehicular natural gas, VNG)/ gasoline vehicle [36, 37]

Figure 11 shows that engine power can reduce by about 15% when using natural gas as fuel. These tests were taken on a rolling-road dynamometer, with the vehicles accelerating from first to top gear (figure 11 shows data taken when in top gear only). A minor factor that contributes to this is the advanced spark timing these natural gas engines employ. The spark timing (advanced relative to combustion TDC) is required to maintain maximum brake torque (MBT) operation due to the slower flame speed of natural gas. Previous work [38] established that, the spark advance can be up to 10 degrees crank angle earlier compared with conventional gasoline operation depending on engine speed. As ignition is occurring earlier in the cycle, increases in charge pressure from natural gas combustion is working against the piston during the compression stroke, increasing the work transfer from the piston to the charge and reducing the net work the engine is able to produce during the full cycle. A 10 degree advance or retard beyond MBT spark timing (for a gasoline engine at wide open throttle) can reduce torque output by about 2% [35]. As a result, steps should be taken to modify standard gasoline engines converted to run on natural gas in order to compensate for these sources of power loss.

The power loss in conventional gasoline engines converted to run on natural gas (in particular those that are naturally-aspirated) can be minimised by increasing the compression ratio [24], or by forced induction [39, 40]. High compression ratios allow higher pressures and temperatures to be generated in the combustion chamber which increases efficiency and increased power output as a result. Forced induction increases inducted air density compared with typical levels seen in naturally

aspirated engines, directly increasing power output. In reference [39] a 1.0 liter SI engine was operated on both gasoline and natural gas, with and without supercharging. The results showed that natural gas (with natural aspiration) produced 10-15% lower torque output than gasoline. In addition, increasing the compression ratio combined with supercharging (at 0.6 bar boost pressure) increased torque by about 50% from the baseline naturally-aspirated gasoline-fuelled configuration.

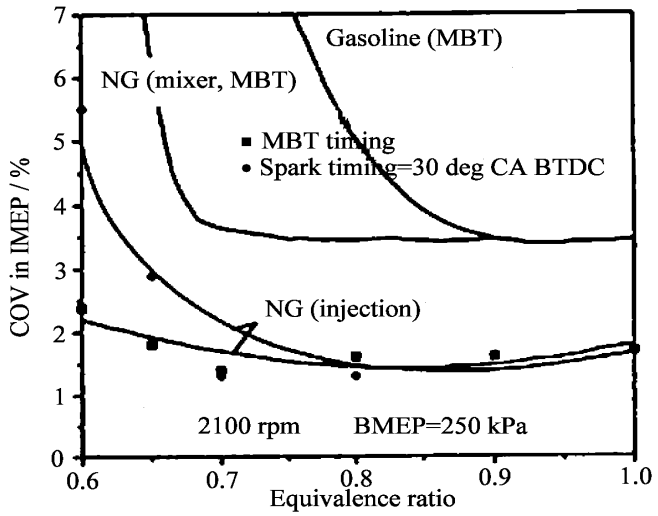


Figure 12: Coefficient of variation in IMEP versus equivalence ratio [33, 36]

Natural gas engines can also run with leaner air-fuel mixtures than typical gasoline engines (which run stoichiometric air-fuel mixtures) as a result of a comparatively wider flammability range [33]. In addition, cycle-to-cycle variations remain of the same order as gasoline engines (4% coefficient of variation in indicated mean effective pressure, COV of IMEP) [33]. This can be seen in figure 12. The figure also shows that the lean operating limit of natural gas (inducted into the engine's intake manifold using a mixer) is extended by about 28% compared with gasoline. However, significantly lower cycle-to-cycle variations of IMEP (about 1.5% COV of IMEP) are produced when natural gas was injected into the intake manifold [33]. Further extension of the lean operating limit was obtained with port fuel-injection. This is because of more precise control and distribution of the air-fuel ratio, which helps maintain a relatively constant air-fuel mixture from cycle-to-cycle. It is desirable to decrease this lean operation limit further, in the hope of obtaining decreased fuel consumption and lower emissions of regulated pollutants. However, under these lean conditions ($\phi \leq 0.6$), cycle-to-cycle variations increase significantly [33]. The slow burning velocity of natural gas, combined with excessive air (which make some local charge regions too fuel-lean) produce excessively low combustion temperatures. This

results in low thermal efficiencies. Misfire can also occur (as a result of some cycles failing to ignite at all), and significant engine damage is a possibility in extreme cases.

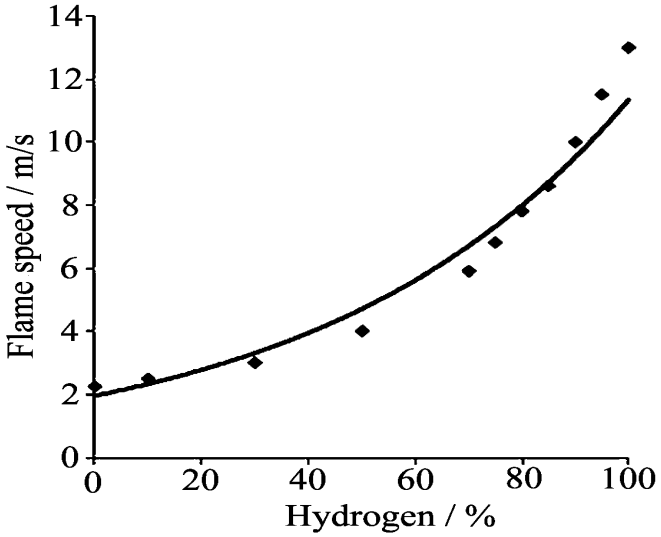


Figure 13: Laminar flame speed variation of a stoichiometric natural gas-air mixture with hydrogen addition by volume [36, 41]

One way to overcome these high cycle-to-cycle variations at very lean operating conditions is to add another fuel with a higher flame speed to the existing natural gas-air mixture. In this regard, adding hydrogen gas to the natural gas-air mixture in the inlet tract has promising results [31, 41–46]. The higher flame speed of hydrogen speeds up combustion, resulting in more fuel being burnt in the time available. The laminar flame speed of the overall stoichiometric air-fuel mixture increases exponentially with hydrogen concentration [41], as shown in figure 13. Previous work [45, 47] found that hydrogen addition has a greater effect on the beginning stages of combustion than in later stages of combustion. This is because hydrogen burns faster than natural gas in the early stages of combustion. This is because the flame development stage (which occurs just after ignition) is less turbulent than the middle and latter stages of flame propagation. Here, the laminar flame speed of hydrogen is about 6 times higher than the laminar flame speed of natural gas (290 cm/s compared with 48 cm/s respectively at 360 K and 1 atm [48]), and is of comparable value to its own turbulent flame speed. However, the turbulent flame speed of natural gas is about 10 times higher than its laminar flame speed [45], so that the turbulent flame speed of natural gas is higher than that of hydrogen. As a result hydrogen addition has a comparatively minor effect on the latter combustion stages. Hydrogen gas addition also introduces hydrogen and hydroxyl (OH) radicals, both of which are

secondary effects which increase combustion reactivity during the flame development period [47].

As a result of the shortened combustion duration, spark timing can be set closer to combustion TDC, starting combustion later in the cycle and reducing the work done on the charge by the piston during compression. As hydrogen has a wide flammability range ($0.1 \leq \phi \leq 7.1$ compared with $0.7 \leq \phi \leq 4$ for gasoline [49]), a relatively small amount of hydrogen can be used. Higher peak combustion chamber pressures are reached with increasing hydrogen gas addition (up to 1 MPa higher) [41]. Efficiency is increased, going up to 21% for a 30% hydrogen substitution by volume, compared with 12% for operation with pure natural gas [41]. Figure 14 indicates that increasing the percentage of hydrogen gas addition by volume in natural gas significantly reduces the COV of IMEP, as a result of the more volatile fuel mixture.

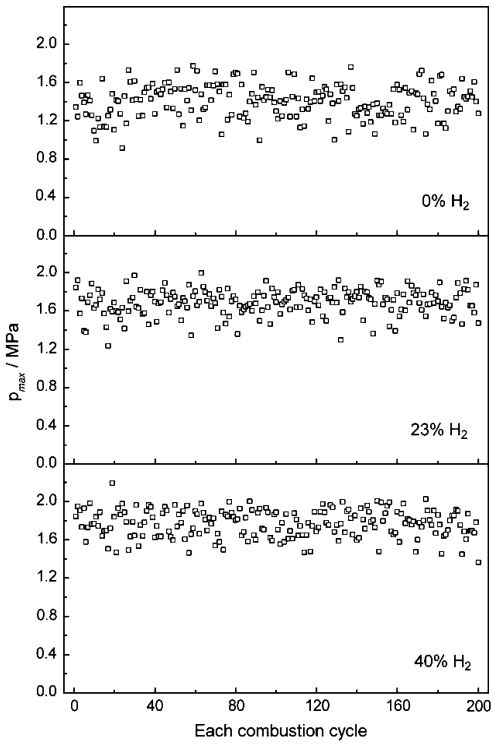


Figure 14: COV of IMEP with increasing hydrogen addition by volume in natural gas [36, 46]

Hydrogen addition in natural gas engines also increases the tolerance of inducted exhaust gas recirculation (EGR) levels [31, 44, 45]. Previous work done with natural gas engines running with EGR has shown that EGR has a detrimental effect on combustion progress at all EGR volume substitutions [31]. This is because, as pure natural gas combustion is relatively slow to begin with, EGR lowers the concentration of oxygen in the inducted charge which further slows flame propagation. This

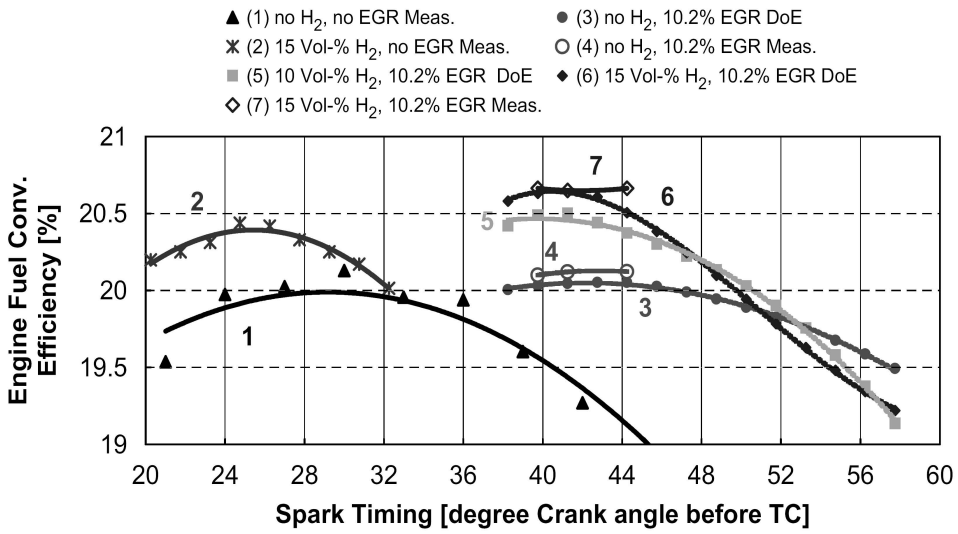


Figure 15: Fuel conversion efficiency comparison with spark timing for various natural gas - hydrogen mixtures and EGR rates [36, 44]

produces comparatively lower combustion temperatures. The higher specific heat capacity of the total inducted charge (as a result of inducting EGR) compared with pure natural gas induction also contributes to this effect [35, 50]. This is evidenced in figure 15, which indicates that peak thermal efficiency occurs at a comparatively advanced spark timing with regards to combustion TDC. Here, peak efficiency occurs at a spark timing of 29 degrees before TDC when fuelled with pure natural gas, while a similar peak thermal efficiency with 10% EGR occurs at a spark timing of 44 degrees before TDC when EGR is used [44]. This advanced timing results in combustion occurring significantly earlier, increasing the work done on the charge by the piston during compression, in addition to increased energy (i.e. "heat") transfer to the cylinder walls.

When a 10% volume substitution of hydrogen was introduced for a maintained EGR level (10% by volume) and spark timing (44 degrees BTDC), thermal efficiency increased about 0.5% [44]. For an EGR substitution of 20% used with hydrogen and natural gas, there was a 20 degrees retard (relative to combustion TDC) in the optimal spark timing compared with the same condition without hydrogen addition [45]. In addition, figure 15 shows that increasing hydrogen addition levels in tandem with increasing EGR levels maintain thermal efficiency levels recorded with the case employing natural gas-hydrogen fuel mixture without EGR, albeit at a retarded spark timing. Other work [31] reported that thermal efficiency and peak combustion pressures values seen with pure natural gas operation are maintained when hydrogen and EGR levels are increased together. However, EGR substitutions of more than

20% by volume produce significantly low peak combustion pressure values compared with pure natural gas operation, in addition to significantly low rates of combustion regardless of the amount of hydrogen substitution for the conditions of the tests in [44].

In terms of exhaust emissions, natural gas SI engines generally produce lower emissions of CO and unburnt non-methane hydrocarbons (HC) compared with conventional gasoline engines [27, 37]. $CO_2$ emissions are slightly reduced [27, 37, 51] due to basic stoichiometry (where 1 g methane produces 2.8 g $CO_2$ while 1 g of gasoline produces 3 g of $CO_2$). The lower equivalence ratio in natural gas engines also results in CO emission reductions of the order of 50% to 90% compared with gasoline engines. Unburned HC emissions are reduced by up to 55% at the same time [37]. However, CO and HC emissions increase significantly at extremely low equivalence ratios as a result of deteriorating combustion quality [27,35,37]. Other work reports the opposite trend however, where total unburned HC emissions (unburnt methane + unburnt non-methane hydrocarbons) increased by about 160% [27]. However, 90% of these HC emissions were unburned methane, and non-methane HC emissions were lowered by about 70% [27]. This is a concern as methane is a powerful greenhouse gas which possesses a global warming potential 30 times more than $CO_2$ (over a period of 100 years) [30]. At the same time, the contribution of methane to smog formation is negligible (unlike non-methane hydrocarbons). The increase of methane emissions is typical of converted gasoline engines to run on natural gas when the engines are not optimally modified [37]. These cases are often end-user conversions, where the engine tuning (such as spark timing, injection timing etc) for the use of natural gas is not optimised in the conversion. In these engines a significant amount of natural gas can escape combustion through flame quenching, adsorption in crevice volumes, and adsorption in the lubrication oil film on the cylinder walls.

NGVs with aftermarket natural gas engine conversions (conversions not explicitly endorsed by the vehicle manufacturer) produce up to 170% higher levels of $NO_x$ emissions compared with typical gasoline levels [27]. The higher $NO_x$ levels result from higher combustion chamber pressures and temperatures, following the advanced spark timing and higher compression ratios. This causes $NO_x$ formation rates to accelerate (compared with normal gasoline operation) during combustion as the compression stroke progresses, because of increasing combustion temperatures. It is likely that, when compression ratios between two engines (one running gasoline

and the other running natural gas) are the same, lean fuel-air mixtures in both natural gas engines and gasoline engines will produce lower $NO_x$ emissions as a result of lower combustion temperatures compared with stoichiometric operation.

Exhaust gas catalysts have been used to reduce these high $NO_x$ emissions, sometimes by more than 90% [52]. Three way catalysts (catalysts that reduce CO, HC and $NO_x$ emissions simultaneously) are common in conventional gasoline engines however, they operate best with a stoichiometric mixture ratio. As natural gas engines can run with relatively fuel-lean mixtures compared with gasoline engines, only selective reduction catalysts can be used under these conditions. However, these catalysts are complex by design, expensive, and difficult to maintain [47] and it is preferable to reduce the emissions in the combustion process itself as a result. One method to achieve this is to introduce a diluent in the natural gas-air charge. This diluent can be a variety of gases, EGR for example. This reduces the oxygen concentration in the charge in addition increasing the specific heat capacity of the charge and reducing flame speeds. These factors combine to reduce peak combustion temperatures, thus suppressing $NO_x$ formation [35, 44, 50]. An example of the level of reduction in $NO_x$ emissions is shown in figure 16, which shows the effect of volumetric substitution of hydrogen (an effect to be discussed later) and mass substitution of EGR in the intake charge on $NO_x$ emissions.

Other gases which are inert can be used as an alternative to EGR [24, 53], such as $CO_2$ and nitrogen ($N_2$). As different gas species have different specific heat capacities ($CO_2$ has a higher specific heat capacity than $N_2$ for instance), and therefore will alter the specific heat capacity of the charge mixture. However, any inert diluent introduced into the intake charge can have detrimental effects on combustion progress, especially with the inherently slow combustion of natural gas. This is shown by the increased emissions of unburned HC, as seen in figure 17.

Previous work has shown that adding gases with higher flame velocities, such as hydrogen gas, to the natural gas-air mixture can increase combustion efficiency [31, 41–46]. Hydrogen addition to natural gas engines without EGR reduces emissions of unburned HC and CO, while at the same time increasing $NO_x$ emissions. These trends can be seen in figures 16 and 17, where results for increasing hydrogen fractions are plotted with increased EGR rates. These emission trends result from the hydrogen shortening the combustion duration and increasing combustion temperatures compared with a particular natural gas-EGR mixture. It has also been

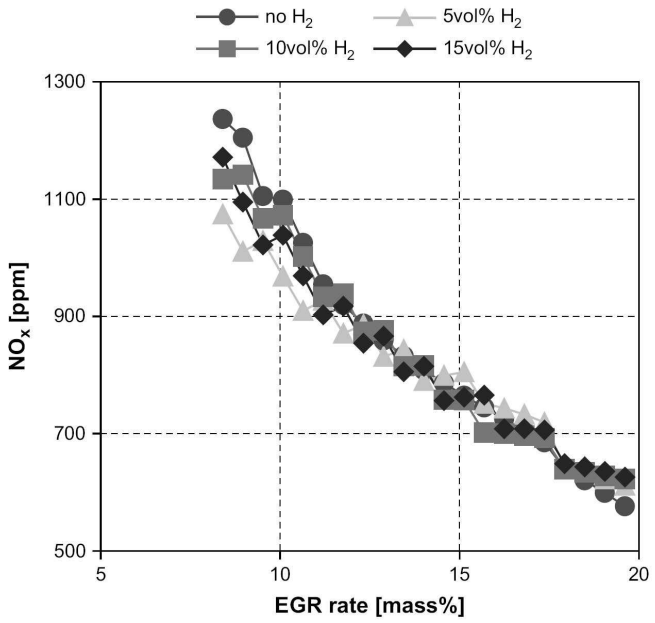


Figure 16: Reduction of $NO_x$ in a natural gas engine with varying hydrogen and EGR levels for a fixed spark timing [31, 36]

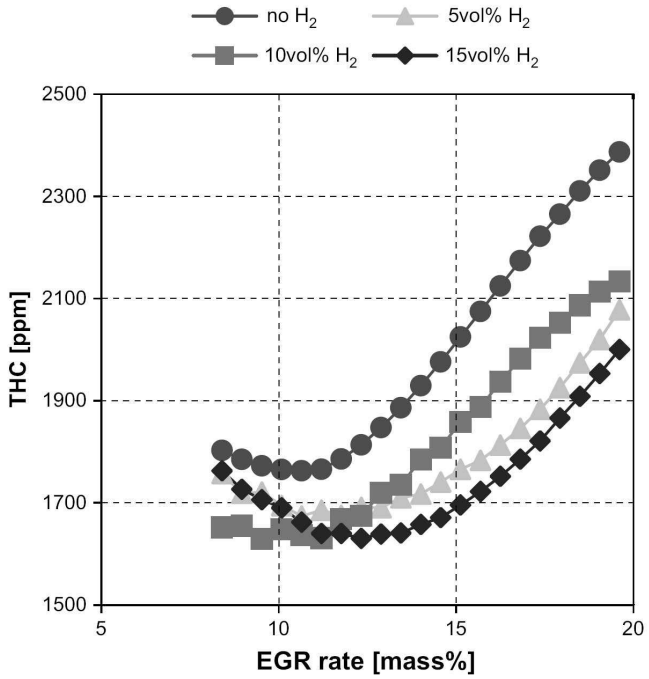


Figure 17: Increase of unburnt HC in a natural gas engine with varying hydrogen and EGR levels [31, 36]

suggested that simultaneous addition of hydrogen and excess air can lead to a decrease in all recorded emissions [43]. However, this only occurs at certain operating conditions [43]. Previous work [31] indicates that, for an engine running with a 10% hydrogen-90% natural gas fuel mixture by volume, $NO_x$ emissions decrease with

increasing EGR mass substitutions. Corresponding decreases in unburned HC emissions were also recorded, albeit up to about EGR levels of about 12%. This can be attributed to more complete combustion as a result hydrogen accelerating combustion, which overcomes the effects of flame speed reduction with lower EGR rates. EGR substitutions of more than 15% have a greater effect on combustion (in terms of flame speed) than a corresponding amount of hydrogen addition to natural gas combustion. In addition, for any EGR substitution level, increasing substitutions of hydrogen in the intake charge produce lower unburned HC levels than the pure natural gas case [31].

The majority of NGVs use port fuel-injected natural gas engines, and the literature presented above considered only engines of this type. However, as natural gas displaces some of the air in the intake manifold upon injection, a reduction in volumetric efficiency occurs, which in turn leads to proportional reduction in power. One way to avoid this problem altogether is to inject fuel directly into the combustion chamber [54]. In addition, direct natural gas injection has been shown to extend the fuel-lean operating limit of normal engine operation compared with port fuel injection [33, 34, 54]. For example, a port injected natural gas engine running very fuel-lean mixtures ($\phi \approx 0.6$) had a COV of IMEP of more than 10%, while the same engine using an in-cylinder injector built into the spark plug was operating at the same equivalence ratio with a COV of IMEP of less than 5% [33]. This is a result of increased mixture turbulence in the cylinder, in addition to locally fuel-rich mixtures that become available close to the spark plug. Flame propagation is also accelerated, resulting in higher rates of energy conversion and higher thermal efficiencies. However, higher levels of $NO_x$ were recorded as a result, caused by high combustion chamber temperatures [33]. Contrary to this, reference [54] reports that $NO_x$ is lower for direct injection engines because of increased charge stratification. It is likely that differing engine parameters play a significant role in these tests, as references [33] and [55] state that there are optimum settings for spark timing (relative to combustion TDC) as well as compression ratio which give an acceptable compromise between performance and emissions for direct injection natural gas SI engines.

Another parameter to consider is fuel injection timing. When fuel injection timing is varied care must be taken not to start injecting the fuel into the cylinder too late. The experiments reported in reference [34] indicate early injection timing (during the intake stroke) increases the combustion chamber pressure and energy conversion rate

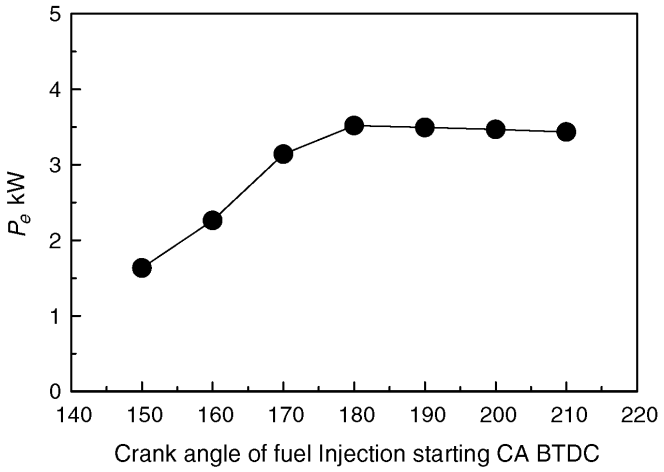


Figure 18: Power output ($P_e$) variation with beginning of injection timing in crank angle degrees BTDC [34, 36]

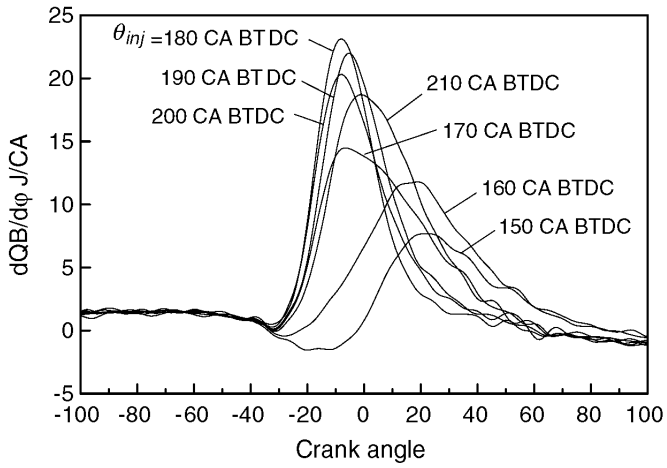


Figure 19: Energy conversion rate during combustion ("heat-release" rate, dQB/d$\varphi$) variation with injection timing advance with regards to combustion TDC [34, 36]

("heat-release" rate), resulting in favorable power output. These trends are shown in figure 18, where 150 degrees BTDC to 180 degrees BTDC (TDC here relates to combustion TDC) are the start-of-injection timings during the compression stroke and 180 degrees BTDC to 210 degrees BTDC are the start-of-injection timings during the intake stroke. The optimum injection timing in this work is shown to be at 180 degrees before combustion TDC. Retarded injection timing during the compression stroke does not allow sufficient time for the fuel to mix and oxidize, resulting in poor flame propagation as well as reduced and delayed peak energy conversion rates ("heat-release" rates). This can be seen in figure 19. Exhaust emissions follow a similar trend to that of engine power output [34]. For example, in figure 20 $NO_x$ emissions increase significantly with injection timing earlier in the

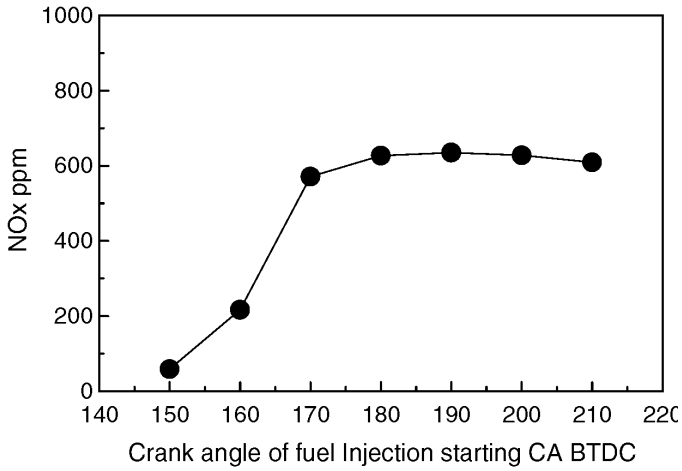


Figure 20: $NO_x$ variation with beginning of injection timing in crank angle degrees BTDC [34, 36]

compression stroke, while there is little effect with further injection timing advance into the intake stroke. HC emissions follow the opposite trend to $NO_x$ emissions while CO emissions did not change significantly with fuel injection timing [34].

Overall, without suitable optimisation (in terms of parameters such as spark timing and compression ratio) natural gas engines produce lower power levels and increased emissions of regulated exhaust gas species compared with conventional gasoline engines. This is due to various factors, such as a higher air-fuel ratio, lower density and slow flame propagation speed. However, it has been shown that natural gas engines can generate higher thermal efficiencies, maintain power levels and reduce regulated exhaust emissions compared with conventional gasoline operation when appropriate engine modifications are carried out [39]. As a result, natural gas engines require significant optimisation in order to obtain a suitable compromise between performance and emissions and be competitive with gasoline-fuelled engines.

### 2.2.3 Natural Gas Combustion in Compression-Ignition Engines

While SI engines are the dominant automotive powerplants (at least in the UK [56]), there is still a significant percentage of passenger vehicles that are powered by compression ignition (CI) engines (about 34% of the current fleet in the UK [56]). In addition, almost 100% of goods vehicles as well as buses use CI engines [56]. As a result, it is pertinent to know how natural gas use in these engines will affect performance and emissions. Natural gas normally does not spontaneously auto-ignite under compression with typical CI engine compression ratios without an ignition source. As a result, a special mode of operation known as dual-fuelling is required for combustion of high-octane number fuels in CI engines. Here, an initial "pilot" injection of high-cetane number fuel is injected directly into the combustion chamber, where the pilot spray mixes with a premixed natural gas-air charge. After an initial ignition delay period, the pilot fuel ignites and begins to burn. Depending on the level of mixing between the natural gas and air, a second delay period occurs after which the natural gas ignites. To illustrate how natural gas dual-fuel combustion progresses, figure 21 is presented [57, 58]. The figure shows a net energy conversion rate during combustion ("heat-release" rate) comparison of dual-fuel operation (with natural gas inducted in the intake manifold) and normal CI engine operation.

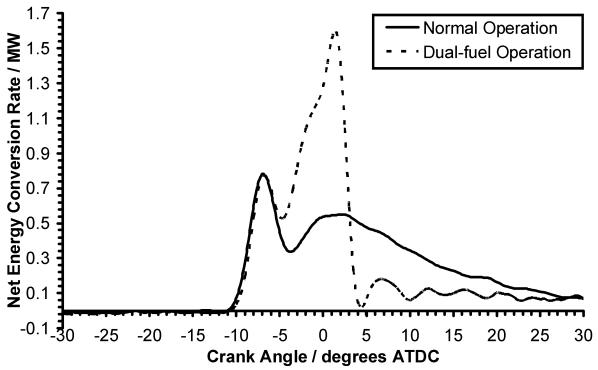


Figure 21: Net energy conversion rate during combustion ("heat-release" rate) comparison for dual-fuel and normal operation at 1000 r/min and 0.6 MPa BMEP, raw data obtained from [57,58]

The initial peaks for both operating modes are very similar in slope and peak values. This is because they both show the premixed combustion phase typical of conventional direct-injection CI engines. Here the liquid fuel (pilot fuel in the dual-fuel case) is injected into the cylinder, which ignites after an initial ignition delay. This ignition delay for natural gas dual-fuel operation is almost the same as normal CI

engine operation. This implies that the effect of species derived from natural gas on the pilot combustion initiation process is negligible. In the natural gas dual-fuel mode, the pilot fuel combustion ignites the natural gas-air mixture, which gives the significantly larger second peak in the natural gas dual-fuel trace. The combustion duration during natural gas dual-fuel operation is also significantly shorter (by about 40 degrees crank angle) compared with normal-fuelling. This faster burn rate is primarily due to the premixed nature of the natural gas-air mixture (as natural gas is inducted via the intake manifold), while the diffusion combustion phase is longer as fuel-air mixture becomes available.

The purpose of this mode is to reduce $NO_x$ and smoke emissions typical of conventional CI engines. Previous work found that dual-fuel engines are fairly effective in doing so, while at the same time maintaining acceptable thermal efficiency levels over the operating range compared with normal CI engine operation [58–67]. While the reduced flame speed during natural gas operation is an issue in SI engines, it is not as significant an obstacle in CI engines. This is because of a number of factors. With typical SI engines only one source of ignition can be produced (the spark plug). When the spark plug ignites, the flame propagates from this single point outward through the charge, generating increasingly high temperatures. In conventional CI engine operation the fuel penetrates into the cylinder during injection and mixes into the charge. When charge conditions allow (pressure, temperature, fuel-air mixing levels etc) these dispersed droplets of fuel spontaneously ignite. This produces multiple ignition points throughout the chamber, resulting in multiple flame fronts and a comparatively faster burn rate. In dual-fuel engines (where the pilot fuel is injected directly into the cylinder), this large spread of points compensates for the slow flame speed of natural gas and allows faster combustion.

As CI engines lack intake throttle valves along the inlet tract, volumetric efficiency is generally higher than typical throttled SI engines. Previous work [68, 69] found that dual-fuel CI engines have slightly reduced volumetric efficiencies compared with normal CI engines, of the order of 1-4%. This minimised effect is due to the apparatus design, where the natural gas enters the intake manifold via a steel tube placed close to the intake valve. This tube, which is permanently installed in the engine, takes up a fixed space in the intake manifold at all times, and therefore affects the flow of air inducted into the engine even during normal CI engine operation. This lowers volumetric efficiency during normal-fuelling and marginally so during dual-fuelling (as a result of further air displacement by the natural gas). This apparatus

also limits the maximum flow rate of natural gas in these dual-fuel studies, which affects power output at high engine speeds. While power output during dual-fuel operation is matched with normal CI engine operation at lower CI engine speeds ($\leq$1000 r/min for example), with this particular induction method dual-fuel CI engines produce significantly lower power levels at high speeds (>1000 r/min). This is because more intake cycles occur per second at high speeds. For a certain natural gas flow rate into the engine, this results in relative fuel starvation with regards to the natural gas supply compared with lower speeds. Other work [61, 64] found that this effect does not occur when a mixing chamber was used to mix the natural gas and air mixture prior to entering the intake manifold. With a mixing chamber, the engine will simply induct more fuel-air mixture at higher speeds at the expense of possibly further reducing volumetric efficiency. Thus the method of natural gas induction into the engine has significant effects on engine operation at different conditions.

Cycle-to-cycle variations of dual-fuel CI engines are comparable to normal CI engines (both produce COV of IMEP levels of about 1%) [70]. Any slight differences can result from a number of factors, most of them are commonly encountered in SI as well as CI engines. For example, there are variations in the amount of natural gas present in the intake charge per cycle, varying degrees of mixing between fresh charge and residual cylinder gases, as well as mixture motion variations in the cylinder per cycle [35, 70].

As in conventional CI engines, there is an ignition delay time present between the start of pilot injection and pilot fuel ignition. In references [68, 71] the pilot fuel ignition delay was extended very slightly during natural gas dual-fuel operation (by about 0.08 ms) which could result from the slightly higher specific heat capacity of the natural gas-air mixture. Dual-fuel CI engines are noisier than normal CI engines throughout the normal operating range [68, 70, 71], and knock-like combustion is encountered at very high loads [72]. The sound heard under these conditions is comparable to the sound heard when low-cetane number fuels are used in conventional CI engines (often called "diesel knock" [35], a result of extended ignition delay). Therefore, this sound is not likely to be knock in the traditional sense (i.e. autoignition of the end-gas ahead of the combustion flame) but instead can be caused by the significantly rapid progress of natural gas-air combustion (after pilot fuel ignition) compared with the mixing-controlled combustion phase in conventional CI engines [68, 71]. This can be seen in figure 21 where the rate of energy conversion

during combustion (i.e. "heat-release") during dual-fuel operation reduces to zero at about 5 degrees ATDC while the rate of energy conversion during normal engine operation reduces to zero after 30 degrees ATDC. During normal CI engine operation, diesel fuel that has mixed with air to about stoichiometric levels during the ignition delay period burns first (shown by the peak occurring at about -7.5 degrees ATDC). This is followed by a longer, lower peak (occurring at about 2.5 degrees ATDC) which results from combustion of fuel-air mixture that is just becoming available, otherwise known as mixing-controlled combustion). For dual-fuel operation, the same figure shows a similar first peak being produced, which is a result of pilot fuel mixing with air during the ignition delay period. Following this there is a second increase in the rate of energy conversion during combustion, which signifies the start of natural gas combustion. This second combustion phase occurs on a much faster rate as the natural gas-air mixture enters the combustion chamber already premixed to a degree similar to conventional port-injected SI engines.

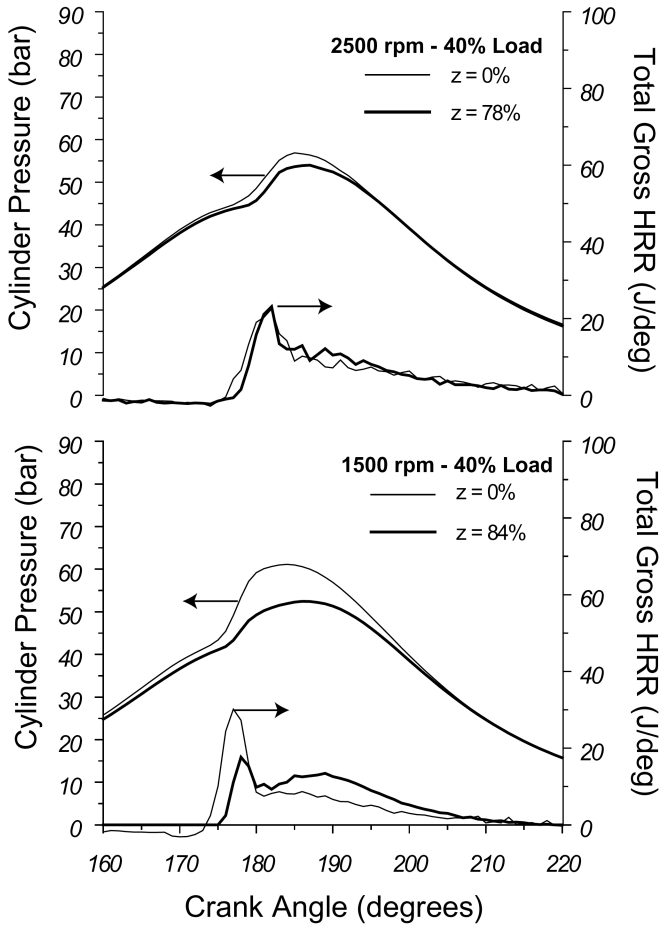


Figure 22: Pressure and rate of energy conversion during combustion ("heat-release" rate, HRR) comparison of dual-fuelling and normal fuelling operation [36, 61]

However, the shorter combustion duration seen in figure 21 is not maintained for all conditions in other literature [61]. This difference can be because of the different natural gas mass fractions employed to hold a particular load in a particular engine. The natural gas mass fraction can be as much as 86% in reference [61] or no more than 70% in reference [68, 71]. This difference in natural gas levels is due to differences in the design of natural gas induction in the two sets of experiments (intake tube versus mixing chamber, as explained before). Figure 22 shows this discrepancy, where the dual-fuel rate of energy conversion peaks are lower compared with normal fuelling, while the reverse is true in figure 21. The "Z" term in figure 22 indicates the level of natural gas enthalpy substitution.

Previous work [68, 71] found that thermal efficiency levels during natural gas dual-fuel operation are similar to normal CI engine levels only at maximum BMEP, while other work [61] indicate significantly lower thermal efficiencies during dual-fuel operation at all conditions. These discrepancies can be due to the fact that stable dual-fuel engine operation depends on the particular engine and natural gas induction system used, as the original engine design parameters affect dual-fuel combustion significantly. At high loads dual-fuel engine performance is similar to normal engine operation, while at low and intermediate loads lower thermal efficiencies compared with normal CI engine operation are recorded [68, 71]. At these low load conditions the pilot fuel fails to ignite most of the main natural gas-air mixture. This is is the result of a comparatively lower charge temperature (and pressure) because of the higher air-fuel ratio [60, 73–75]. To improve part load performance, uncooled EGR can be used to improve combustion quality at these conditions.

Figure 23 shows the increased peak computed rate of energy conversion during combustion (i.e. "heat-release" rate) in addition to a shorter combustion duration with a 2% mass EGR substitution compared with conventional dual-fuel operation [73]. The figure also shows the thermal (Th), chemical (Ch) and radical (Ra) effects of EGR on the energy conversion rate. The thermal effect represents the effect of charge temperature, the chemical effect represents the effect of charge composition, and the radical effects represents the effect of active radicals (i.e. partially oxidised products) present in EGR on the combustion reactions. Compared with the radical effect (which can increase pre-ignition reaction rates) and the chemical effect (which can improve mixture strength), it is the thermal effect of EGR (which increases charge temperature) that is the main factor. This is because the dilution of the charge by the EGR overcomes the potential improvement brought on by the

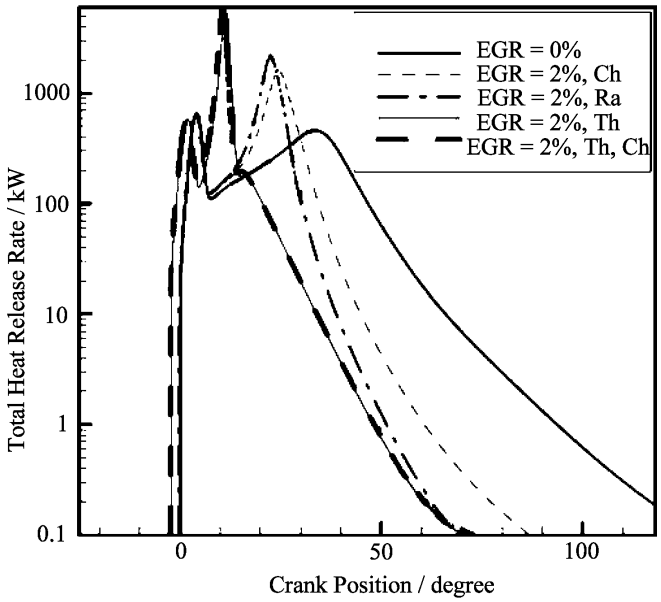


Figure 23: Comparison of computed rate of energy conversion plots ("heat-release" rates) for different EGR components during dual-fuel operation [36, 73]

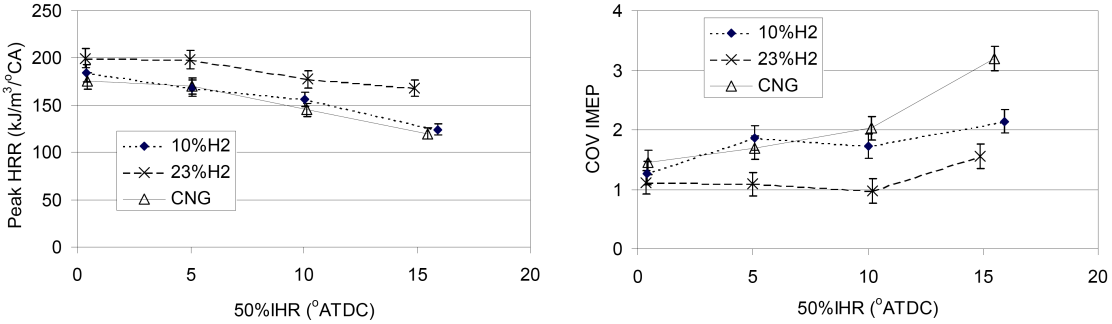


Figure 24: Peak rate of energy conversion during combustion ("heat-release" rate, HRR) and COV variations with combustion injection timing for dual-fuel operation with 40% EGR [36, 76]

chemical and radical components of EGR. Other work [74] found that relatively low EGR levels (of the order of 5% by mass substitution) results in increased pressure-rise rates (which reflects higher combustion rates) at low loads. This is because uncooled EGR increases the temperature of the intake charge and accelerates combustion though it also lowers volumetric efficiency. At high loads, EGR alleviates the "diesel knock"-like combustion (caused by high pressure-rise rates) as it dilutes the intake mixture, reducing the oxygen concentration and slowing combustion. This reverse trend is because the effect of EGR diluting the charge is significantly greater than its heating at high loads, while the reverse occurs at low loads [73, 74].

As per SI engines, excessively high levels of EGR hinders combustion progress significantly. Hydrogen gas addition increases combustion stability and reduces ignition

delay during natural gas dual-fuel engine operation with EGR [76]. Here the COV of IMEP of a natural gas dual-fuel engine with 23% hydrogen substitution by volume (of intake air) as well as an EGR volume substitution of 40% was reduced by about 1%. Figure 24 shows the increase of energy conversion rate ("heat-release" rate, in this case plotted against combustion timing) with increasing hydrogen addition. Here, 50% "IHR" is used to define the combustion timing. By integrating the energy conversion rate during combustion ("heat-release" rate) curve up to a crank-angle where it has reached its maximum value then normalizing by the total combustion energy over the full cycle, the fraction of the energy released in the cycle is determined. The midpoint of this curve (50% of the integrated "heat-release" rate or energy conversion rate curve, defined as the 50% IHR, is plotted against crank angle and is used to define the combustion timing in crank angle [76]. The same figure also shows the lower COV of IMEP with advancing (with respect to combustion TDC) gaseous $H_2$ fuel injection timing. In this case the high flame speed of hydrogen maintains combustion stability despite the high EGR rate. Ignition delay for the gaseous fuel combustion is reduced significantly (by about 20%) and the energy conversion rate during combustion is also increased [76].

In terms of exhaust emissions, natural gas dual-fuel CI engines reduces $NO_x$ emissions significantly compared with normal CI engine operation [58–67]. Here, the reduction can reach about 50% depending on engine type and conditions. Figure 25 shows the typical trend of $NO_x$ emissions from a dual-fuel engine with diesel pilot fuel at two different speeds with varying load levels (in terms of BMEP). The $NO_x$ reduction is due to lower combustion temperatures, resulting from the slower flame speed of natural gas [61]. However, other work [59] reports that $NO_x$ formed during the combustion of the pilot fuel constitutes most of the total $NO_x$ emissions of dual-fuel combustion. Therefore, it is the type and quantity of pilot fuel that significantly affects final exhaust $NO_x$ emissions during dual-fuel operation. Like normal CI engine combustion, there is a critical time period between the start of pilot fuel combustion and the time when peak combustion chamber pressure is reached. In conventional CI engines, this critical time period is usually the first 20 crank angle degrees after pilot fuel ignition [35]. This is because peak combustion chamber temperatures occur during that period. During dual-fuel operation, the premixed pilot fuel-air mixture is compressed to a high temperature during the pilot ignition delay period just prior to combustion, which accelerates the $NO_x$ formation rate during combustion. Combustion of the natural gas-air mixture usually begins when the cycle is already well in the expansion stroke (where the charge is being cooled as

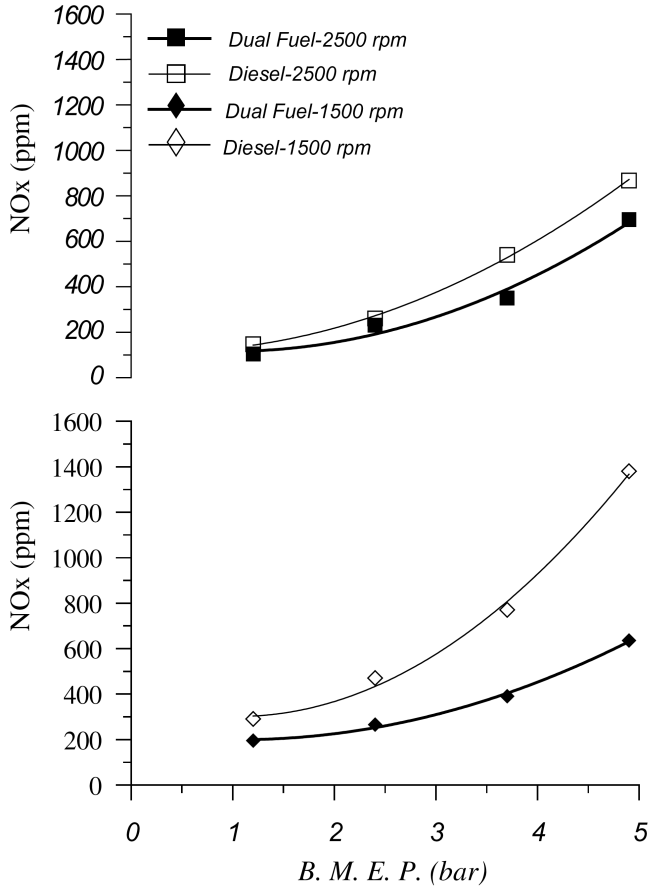


Figure 25: Comparison of $NO_x$ emissions for natural gas dual-fuel operation as function of BMEP [36, 61]

the pressure drops) and $NO_x$ formation rates are lower. This charge cooling, as a result of expansion in addition to mixing between hot and cold gases, freezes $NO_x$ chemistry, preventing decomposition. Attempts have been made to reduce $NO_x$ emissions further, by significantly advancing pilot fuel injection timing [77]. Here, the pilot fuel was allowed time to mix with the natural gas-air mixture in order to avoid locally rich mixtures, which cause high $NO_x$ formation rates.

Smoke and particulate emissions in natural gas dual-fuel engines are very low and in some cases undetectable [58, 60–67]. Natural gas combustion inherently produces little smoke, as natural gas has a lower number of carbon atoms than diesel fuel. Natural gas also has lower quantities of carbon-carbon bonds in addition to a high hydrogen-to-carbon ratio, which combines to lower sooting tendencies [78]. Finally, the natural gas-air mixture usually very well mixed just prior to combustion. This results from the high residence time of the two gases in travelling and mixing from the intake manifold to the combustion chamber. As a result, any particulates recorded

are produced during the pyrolysis of the pilot fuel in the very rich mixture of the pilot fuel spray core [35]. Some of the particulates formed will also be burned during combustion of the natural gas-air mixture, further reducing particulate levels.

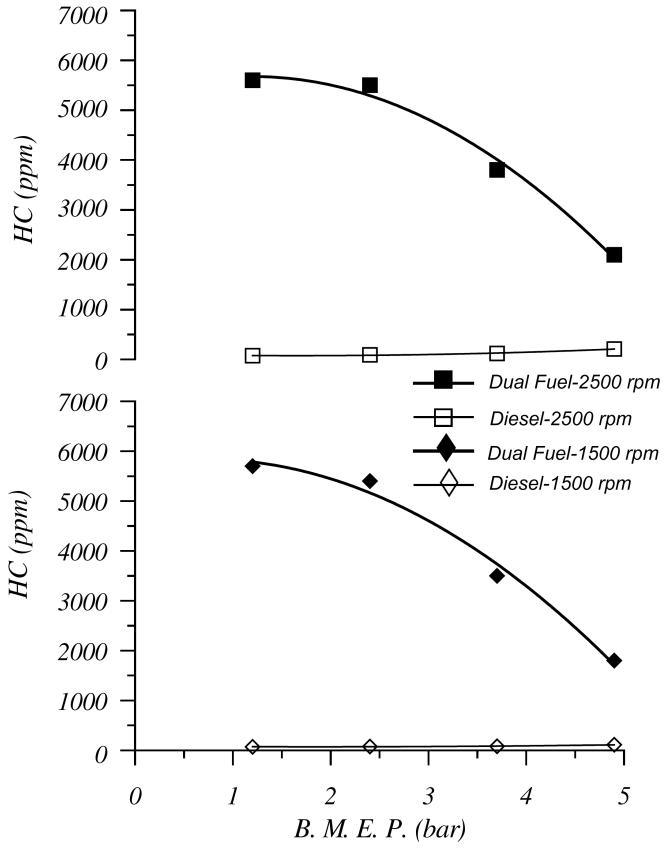


Figure 26: Comparison of HC emissions for dual-fuel operation as function of BMEP [36, 61]

Part-load unburned HC emissions of natural gas dual-fuel CI engines are significantly higher than in normal CI engines, especially at low to intermediate loads [58, 60–62, 64, 65, 67]. Figure 26 indicates HC concentrations of the order of 6000 ppm are recorded during dual-fuel operation, compared with 100 ppm recorded during conventional CI engine operation with diesel fuel [61]. This significant increase is due to unburned natural gas (i.e. methane) surviving to the exhaust. This is a result of the stratified nature of the pilot fuel. It is suggested that the flame (initiated by the pilot fuel) does not propagate throughout the entire charge due to local natural gas-air mixture regions being too fuel-lean to sustain combustion [68,71,74]. There also appears to be an equivalence ratio threshold ($\phi = 0.4$) for natural gas dual-fuel CI engines, below which unburned HC emissions increase with increasing overall equivalence ratio (from $\phi = 0.2$ to $\phi = 0.4$) [63,68,71,79]. Above this threshold unburned HC levels approach those of conventional CI engine operation as the comparatively richer mixtures (though still sub-stoichiometric) result in sufficiently

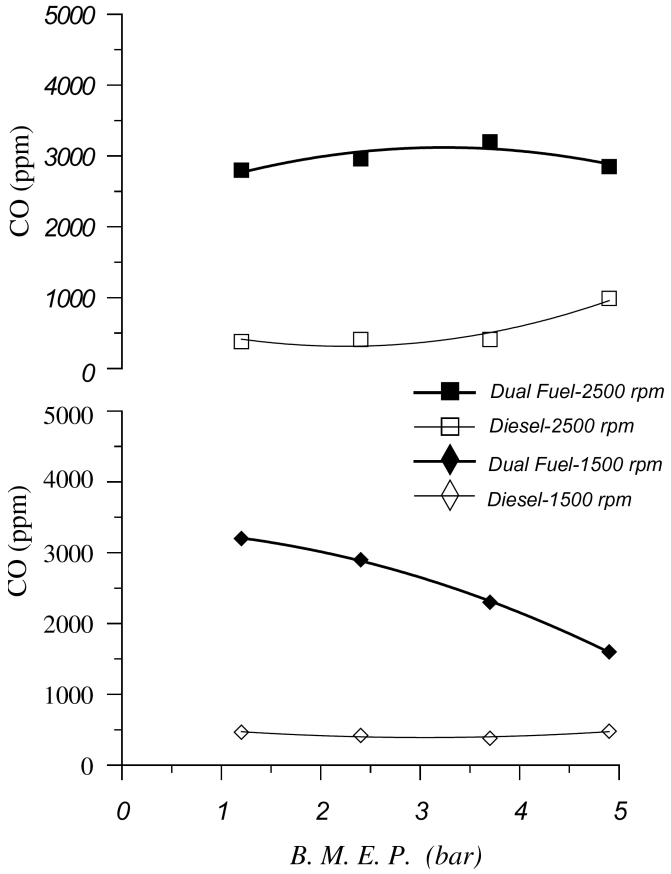


Figure 27: Comparison of CO emissions for dual-fuel operation as function of BMEP [36, 61]

higher combustion temperatures to oxidise most of the fuel. It is also likely that this increase is caused by a significant amount of natural gas entering the crevice volumes of the combustion chamber and escaping combustion. Flame quenching as combustion of the natural gas-air mixture proceeds into the expansion stroke may be a contributing factor [80].

Figure 27 shows the variation of CO emissions with BMEP during natural gas dual-fuel CI operation [61]. CO emissions are significantly higher than normal CI engine operation at all conditions. Some of the literature confirm these trends to some degree, with significant CO emissions at part load [68, 71]. However, in references [68, 71] CO levels progressively approach normal CI engine levels with increasing equivalence ratio, as a result of higher combustion temperatures at high loads.

A number of methods have been designed to improve low-load emission trends of natural gas dual-fuel CI engines. One is the injection of a larger proportion of the pilot fuel contributing to the total combustion energy, which would provide more

ignition points, so that combustion of the natural gas-air mixture would be more complete [77, 81]. While this approach is successful to some extent, it defeats the objective of reducing diesel fuel demand in CI engines.

Another method to improve low-load emission levels is to induct low amounts ($\leq$ 5% by volume) of uncooled EGR. The hotter exhaust gas helps increase combustion temperatures, resulting in lower unburned HC and CO emissions [60, 73–75]. This follows from the increased equivalence ratio (as a result of air substitution with EGR). There is a further chemical effect of this EGR, in the addition of active radicals (partially oxidized combustion products) present in exhaust gas which help to drive the chemical reactions during combustion (as explained earlier) [75].

The diluting effect of EGR also reduces the oxygen concentration in the charge, reducing $NO_x$ emissions (figure 28) as well as HC emissions (figure 29). The increases charge temperature as a result of EGR addition offsets the dilution effect of EGR at low engine loads, while the opposite effect is seen at high loads [75]. EGR volume substitution rates of more than 5% of the intake air during natural gas dual-fuel combustion result in excessively high unburned HC and CO coupled with low $NO_x$ emissions [74]. This is due to the dilution of the intake charge overcoming the positive effects of the hot EGR gases. An attempt to extend the upper limit of EGR rates by adding hydrogen to the charge has been reported in [76]. Hydrogen addition of 23% by volume coupled with an EGR rate of 40% (also by volume) increased $NO_x$ emissions only slightly, while unburned HC and CO emissions were reduced by about 60% and 40% respectively [76]. These trends are caused by the high flame speed of hydrogen, which helps shorten the combustion duration despite the high EGR substitution. Natural gas dual-fuel CI engines also produce lower levels of $CO_2$ than conventional CI engines fuelled with diesel fuel (about 30%) [68, 71]. This is caused by the stoichiometry, where 1 g of methane produces about 2.8 g of $CO_2$, while 1 g of diesel produces about 3.2 g of $CO_2$ during complete combustion in air.

Special consideration has to be given to the type of fuel used to provide ignition, as the pilot fuel is of great importance to the quality of dual-fuel combustion. While conventional diesel fuel has been shown to be an adequate pilot fuel for natural gas dual-fuel CI engines, many other alternative and sustainable fuels have also been tested [19, 58, 68, 71, 82–85]. Among them are select varieties of biodiesel, i.e. the transesterified ester made from vegetable/ organic oils (such as rapeseed oil) and methanol. The biodiesel fuels are fairly similar to diesel fuel in conventional

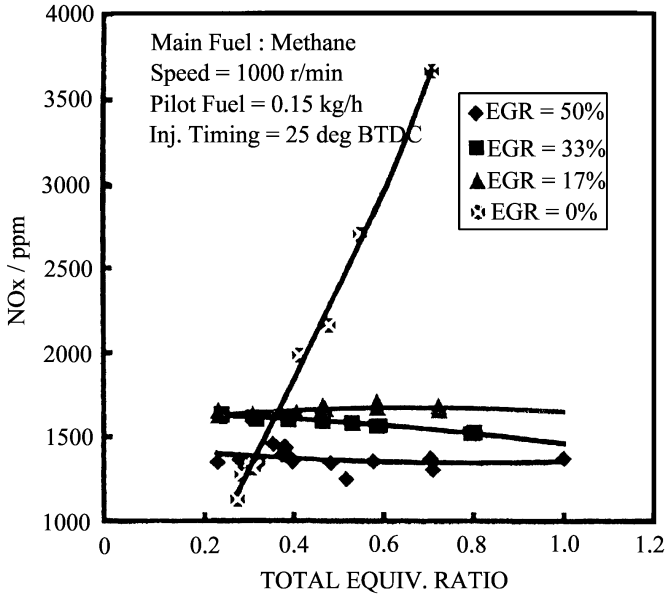


Figure 28: $NO_x$ emission variation with equivalence ratio for different EGR rates during dual-fuel operation [36, 75]

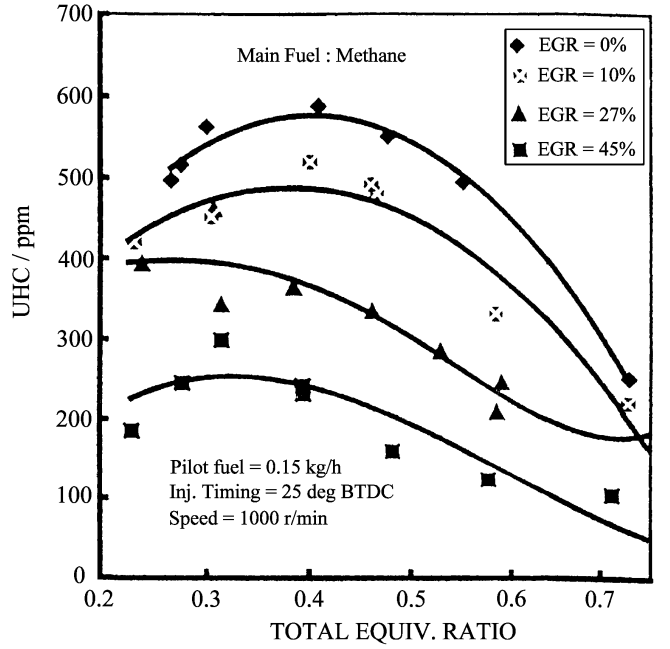


Figure 29: HC emission variation with equivalence ratio for different EGR rates during dual-fuel operation [36, 75]

single-fuel operation in terms of their performance and exhaust emissions [58, 68]. This similarity to diesel fuel is extended to the pilot fuel role. Rapeseed methyl ester (RME) performs very closely to diesel fuel as a pilot fuel in terms of thermal efficiency [58, 68]. The RME pilot fuel ignition delay and peak combustion chamber pressure are also very similar to those of diesel fuel at relatively high load [68, 71].

RME contains oxygen molecules in its chemical composition, which allows a higher degree of fuel oxidation and compensates for the smaller lower heating value. Similar overall trends in exhaust emissions [19,58,68,71,83] are also recorded, where in these works the natural gas contributes from 0% to 68% of the fuel energy with increasing equivalence ratio and BMEP. A slight increase in $NO_x$ and coinciding reduction in HC at high equivalence ratios is caused by the oxygen present in the in RME pilot oxidizing on a larger scale, producing higher combustion temperatures.

With other less well known esters, such as honge oil methyl ester, and jojoba oil methyl ester [82,84,85], differences between their respective performance with diesel fuel as well as between the esters themselves are more apparent. Dual-fuel operation with jojoba-seed methyl ester pilot fuel results in similar efficiencies to the diesel pilot fuel, while dual-fuel operation with the honge oil methyl ester result in lower efficiencies throughout the load range. This is caused by the smaller lower heating value of the honge oil methyl ester [82,84]. Use of the jojoba seed methyl ester pilot fuel [85], with a significantly higher cetane number of 63 , results in lower rates of combustion pressure-rise, reducing noise and "diesel knock" (i.e. metallic sound caused by rapid fuel burning rates) tendency. These methyl ester pilot fuels generally produce higher levels of CO, smoke and HC levels compared with diesel [84]. The differences primarily result from the higher viscosities of the different methyl esters than diesel fuel (up to 19.2 $mm^2/s$, compared with about 5 $mm^2/s$ for diesel fuel) [19, 82, 84, 85]. The viscosity of the pilot fuel affects the spray characteristics and the distribution of flame front and combustion progress across the cylinder.

Gaseous fuels have also been tested in a pilot fuel role [19,68,71,80]. A high-cetane number gaseous pilot fuel allows more homogeneous mixing with the natural gas-air charge during the ignition delay, which improves combustion efficiency at low loads. Dimethyl-ether or DME (a high-cetane number gaseous fuel) used as a pilot fuel produces lower specific $NO_x$ emissions, in addition to higher HC and CO specific emissions during dual-fuel combustion [19, 80]. DME vaporises very quickly upon injection, cooling the charge and lowering combustion temperatures, resulting in the recorded emission levels. DME as injected pilot fuel results in lower thermal efficiency than diesel or biodiesel pilot fuels at the same operating conditions. This is caused by the combined effect of 30% higher mass flow rate and 9% lower $LHV_f$ of DME in order to keep the same pilot energy input to the cylinder.

All the dual-fuel engine studies discussed above were conducted in conventional CI

engines modified to induct natural gas into the combustion chamber via the intake manifold, while maintaining the original in-cylinder injector for pilot fuel injection. Like port-injected SI engines, inducting natural gas via the intake manifold reduces volumetric efficiency, and therefore potential power output. In some studies both the pilot fuel as well as natural gas are injected directly into the cylinder via a common fuel injector [76, 86]. Natural gas dual-fuel engines with direct natural gas injection maintained power output and thermal efficiency levels compared with normal CI engines while comparatively lower emissions of $NO_x$ and particulate matter were also recorded (for similar reasons as the port-inducted tests discussed earlier) [76].

Further improvement in direct natural gas injection dual-fuelled CI engines can be obtained by varying the injection pressure of the natural gas and the diesel pilot fuel jet. During normal CI engine operation (i.e. non-dual-fuel), increasing the fuel injection pressure improves fuel atomisation upon injection as well as fuel-air mixing rates [86, 87]. A similar effect occurs in direct natural gas injection dual-fuel CI engines [86]. Increasing the injection pressure of both the diesel pilot fuel and the natural gas injection (from 21 MPa to 30 MPa) results in a shortened ignition delay of the pilot fuel because of faster mixing between the pilot fuel and air during the ignition delay period [86]. Higher combustion rates are also recorded, resulting in a shorter overall combustion duration [86]. $NO_x$ emissions are increased slightly compared with lower injection pressure conditions, in addition to lower HC, CO and significantly lower smoke emissions. These emission trends are caused by better levels of mixing between the pilot fuel and the natural gas-air mixture, in addition to the faster combustion rates. Thermal efficiency levels were not significantly affected by varying injection pressure [86].

These emission trends are shown in figure 30 (which are plotted in specific terms of mass per unit gross indicated kilowatt hour, GikWhr, where GikWhr is the energy derived from the indicated rather than the brake power). The data was obtained at a particular intake oxygen mass fraction ($Y_{\mathrm{intO2}}$) of 0.19 in the total intake charge, and combustion timing (50% IHR=17.5 degrees ATDC). The figure also shows the gross indicated specific fuel consumption (GISFC), which is proportional to the inverse of thermal efficiency.

These trends vary significantly with the operating conditions, especially with engine speed [86]. At low speeds, the higher injection pressure (30 MPa) have more influence on combustion quality than at high speeds. This is because the higher injection

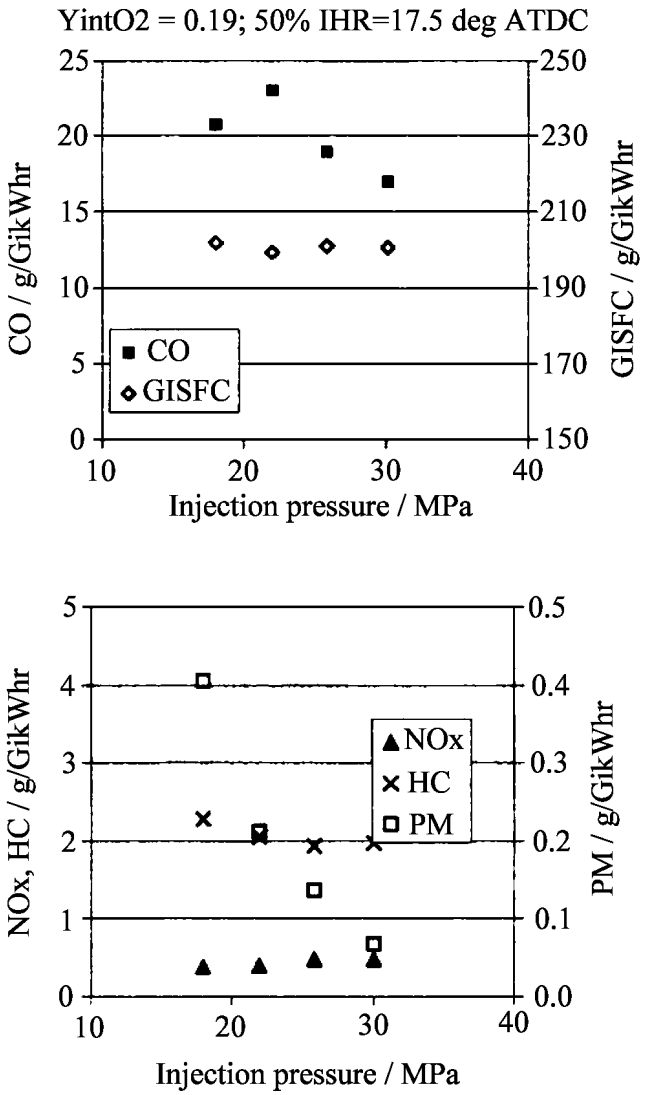


Figure 30: Specific emissions and fuel consumption trends with injection pressure at 1200 r/min [36, 86]

pressures increase turbulence in the cylinder at low speeds, while at high speeds cylinder turbulence is inherently high because of the piston motion. In addition, at a particular engine speed, increased turbulence brought on by the higher injection pressures is more significant at higher loads [86]. This can result from a larger pressure difference between the higher fuel injection pressure and chamber pressure, compared with the lower injection pressures (21 MPa) which are comparatively more effective at low loads. These parameters influence the level and rate of mixing in the cylinder, which in turn influence emission levels. For example, particulate emissions are lowered to a larger extent at higher loads than at lower loads [86].

Overall, natural gas use in CI engines require the dual-fuel mode. Here, the natural

gas-air mixture is ignited by a high-cetane number pilot fuel that is injected directly into the cylinder. There is no significant loss in power in natural gas dual-fuel CI operation compared with conventional CI engine operation provided a sufficient amount of natural gas-air mixture can be admitted in the combustion chamber. Failure of the pilot fuel to ignite the entire natural gas-air charge at the low and intermediate loads (as a result of low charge temperatures) causes lower thermal efficiencies. Low engine operating temperatures at these loads (caused by pockets of local fuel-air mixtures that are too lean to support combustion as the flame propagates along the chamber) also result in lower $NO_x$ emissions compared with normal CI engine operation. Conversely, HC and CO emissions are significantly increased, while at high loads $NO_x$, HC and CO emissions are comparable to normal CI engine levels. However, like SI engines, dual-fuel CI engines require a degree of optimisation, especially during engine operation at low loads. Here, natural gas can be used in smaller proportions compared with the pilot fuel at lower loads to reduce emissions of HC and CO (i.e. the pilot fuel would provide more than 50% of the total fuel energy input). High pressure pilot fuel injection (of the order of 100 MPa) can provide more ignition points distributed more extensively throughout the natural gas air charge. An increased number of smaller-than-standard diesel injector holes allow better atomisation and mixing of the pilot fuel with the natural gas [88, 89]. Uncooled EGR at low to intermediate loads can be used to improve combustion efficiency, and reduce unburned HC as well as CO emissions.

## 2.3 Water Induction in Internal Combustion Engines

In this section, the effects of water addition to the internal combustion process (focusing primarily on CI engines) are presented. There are two methods of adding water to the combustion process; liquid water injection (either in the intake manifold or direct in-cylinder) as well as mixing the inducted liquid fuel with water to form an emulsion (which is inducted via the standard engine fuel induction system). This research is motivated by the potential increase in thermal efficiencies and simultaneous reduction in $NO_x$ as well as smoke emissions. These trends are due to the cooling effect of water droplets vapourising during combustion, lowering combustion temperatures and reducing combustion energy losses (such as to the cylinder walls/ cooling water). In addition, water-in-fuel emulsions cause the "microexplosion" phenomenon which acts as a secondary atomisation process after injection. This allows more homogeneous fuel-air mixtures to be formed, increasing thermal efficiency and reducing smoke emissions. However, the quality of the emulsions depends heavily on how they are prepared and varies significantly in the literature. In this work, only CI engines employing water-in-fuel emulsions are discussed. Both methods have their unique traits, which are discussed in their respective subsections in detail.

### 2.3.1 Water Injection Systems in Spark-Ignition and Compression-Ignition Engines

As the need for higher engine thermal efficiencies and lower fuel consumption grows, engine technology is pushed further forward. This is a positive trend, which results in technologies such as common-rail direct fuel injection systems for CI engines and downsized engines that employ forced induction. These technologies improve the combustion process, producing more work from a lower amount of fuel input energy. However, improved combustion quality usually results in high combustion temperatures which produce high $NO_x$ emissions. In addition, depending on the type of engine and its operating conditions, engine damage can result if the combustion rates (which produce high combustion pressures and temperatures) are excessively high. This can produce abnormal combustion phenomenon such as excessive "diesel knock" in CI engines. While lowering the combustion pressure (usually by lowering the compression ratio) will lower combustion temperatures, this results in lower indicated power output and lower thermal efficiency. Injecting liquid water either via the intake manifold or directly into the cylinder can help balance the conflicting

trend between $NO_x$ emissions and power output, where combustion temperatures are lowered while still maintaining reasonable levels of performance and efficiency [90–93].

The reduction in combustion temperature is due to the water droplets vapourising during the combustion process, absorbing some of the energy produced by combustion. This is in addition to water vapour increasing the overall specific heat capacity of the inducted charge [90]. These effects reduce energy (i.e. "heat") transfer out of the chamber during combustion (such as to the cylinder walls and in exhaust gases) therefore increasing work output and thermal efficiency. Previous work on CI engines [90,91] using direct in-cylinder water injection via a combined fuel/water injector show reductions of $NO_x$ at almost all operating conditions (with a maximum reduction of about 50%) when compared with normal CI engine operation with neat fuel (i.e. no water) injection. Here, up to 65% of the total injected volume is water. The $NO_x$ reduction is due to significantly lower combustion temperatures, where temperature reductions of about 100 K compared with neat fuel operation are recorded [90,91]. With lower water volume substitution of the fuel (between 30% to 45% for example), corresponding reductions in $NO_x$ emissions of the order of 35% are recorded [90]. Unburnt HC and CO emissions are not significantly affected with water injection [91]. As for smoke and particulate emissions, water injection produced varying results in the literature. Reference [90] reported that water injection reduced smoke emissions at low loads. This is due to lower combustion temperatures reducing particulate formation rates during early stages of combustion. At high engine loads however, a longer injection duration (which results in more injected fuel mass) offsets the effect of lower combustion temperatures seen at lower loads. Aside from slowed particulate formation rates, no affect on particulate oxidation was noted with water injection in this work [90]. Reference [91] reported a contradictory trend, where water injection increased smoke emissions at all conditions compared with neat fuel operation. This is due to the water droplets slowing particulate oxidation rates in addition to the formation rates. This could be due to a higher water volume fraction used in reference [91] (a maximum of 65%) compared with reference [90] (a maximum of 45%). Water injection also increases specific fuel consumption (SFC), as a result of more injected mass required to produce a certain power level compared with neat fuel operation [90, 91]. This translates to lower thermal efficiencies. This is due to an extended ignition delay which results in peak pressure occurring too late in the cycle compared with neat fuel operation, producing a comparatively lower work output per cycle [90]. This extension is due to

the lower combustion temperatures, in addition to a longer injection duration compared with net fuel operation. Reference [90] suggests this could be avoided with advanced injection timing to compensate for the longer injection duration. Here, simulated results show that advancing the injection timing by about 7 crank angle degrees (compared with the injection timing with neat fuel operation) can reduce $NO_x$ emissions by about 60% while maintaining specific fuel consumption levels.

Water injection has also been investigated with SI engines burning various gaseous fuels [92, 93]. In a SI engine fuelled with liquid petroleum gas (LPG) with liquid water injected into the intake port [92], water injection increases thermal efficiency compared with normal SI engine operation without water injection. This is due to the cooling effect of water, where vapourisation reduces losses to the cylinder walls as well as the exhaust gas. In addition, the injected water spray cools the intake air in the manifold, increasing its density and giving a mild forced induction effect [93].

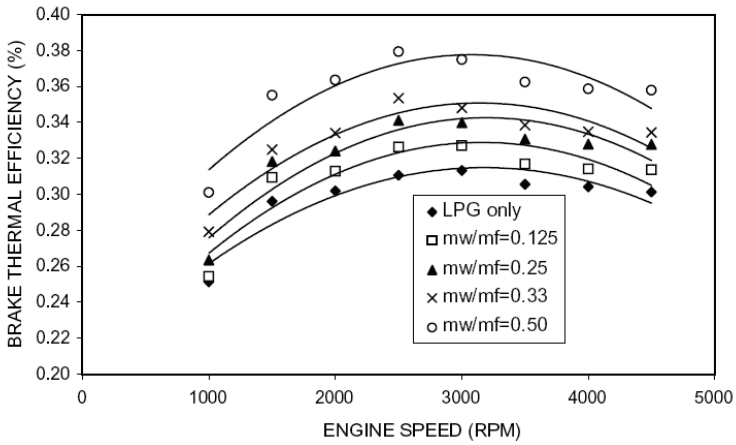


Figure 31: Comparison of brake thermal efficiency against speed for different water/fuel mass flow rate ratios (mw/mf) in a SI engine fuelled with LPG [92]

As seen from figure 31, there is a 6% increase in thermal efficiency for the maximum water mass substitution of fuel. Unfortunately, no emission results are presented in this particular reference. Water injection is also used as a method of preventing backfire and preignition in SI engines powered by volatile fuels, such as hydrogen gas [93]. Here water injection in the intake manifold allows more stable engine operation with hydrogen fuel, especially at high loads. Under these conditions, burning hydrogen fuel (without water injection) produces very high pressure-rise rates causing comparatively violent combustion (termed "hydrogen knock"). This is due to fast-burning rates of hydrogen-air mixtures (compared with normal gasoline for example) in addition to a wider flammability range [93]. The term "hydrogen knock"

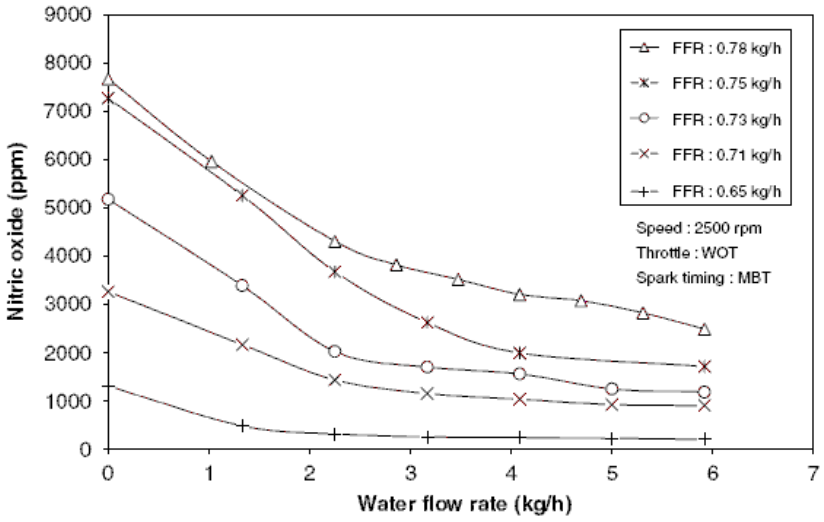


Figure 32: Nitric oxide variation with increasing injected war flow rate for varying fuel flow rates (FFR) in a SI engine fuelled with hydrogen gas [93]

should not be confused with traditional knock (i.e. autoignition of the end-gas ahead of the combustion flame) as it will be used throughout this work to describe the sound caused by unusually high pressure-rise rates in hydrogen engines. Here water acts in a similar manner to a charge diluent (such as recirculated exhaust gas), cooling the charge and reducing the pressure-rise rate. As a result, spark timing is advanced in order to compensate for this effect during conditions employing water injection. In addition, volumetric efficiency is slightly reduced when employing water injection in the intake manifold (of the order of $\leq$5%). There is also no significant variation in the indicated mean effective pressure (IMEP). While hydrogen combustion produces high levels of $NO_x$ (which includes nitric oxide), water injection reduces these levels by up to 70% [93], as shown in figure 32. This reduction is much more than what could be attained with simply retarding the spark timing, a common modification to reduce combustion chamber temperatures.

Overall, water injection has shown to be fairly effective at reducing $NO_x$ emissions, in addition to improving combustion quality. However, should water injection systems be considered for installation on standard vehicles, separate storage and injection systems will be required. In addition, adverse long term effects as a result of corrosion need to be explored in more detail, as this aspect was not discussed in the reviewed literature.

### 2.3.2 Water-in-Fuel Emulsions

Another method of introducing liquid water into the combustion chamber is to emulsify the fuel supply with water. A water-in-fuel emulsion is essentially fuel intimately mixed with water (either via physical or chemical mechanisms), resulting in water droplets suspended within the larger fuel droplet. Emulsions can be either water droplets dispersed in the fuel (water-in-fuel emulsions, which are discussed in this work) or fuel droplets dispersed in water (fuel-in-water emulsions). These emulsions are usually inducted into the engine via the standard fuel system. As a result, water-in-fuel emulsions do not need separate water storage/ delivery systems (as per water injection systems). In addition, there can be no reduction in volumetric efficiency (recorded with port water injection) when using water-in-fuel emulsions. However, the use of water-in-fuel emulsions requires relatively minor modifications to the standard engine components. Like other alternative fuels (such as ethanol and biodiesel), these modifications primarily involve the fuel delivery system, where components such as rubber seals and hoses would need to be replaced with units that can withstand the lower lubricating and increased corrosive properties of water. As the current fleet of diesel-fuelled vehicles is designed to burn low sulfur diesel fuel (which produce comparable wear and tear to renewable biodiesel fuel [94]) these emulsions can be put to use fairly easily.

Previous work [95–101] presents results on emulsified fuel performance and emissions during normal CI engine operation. The water-in-fuel emulsions used in references [95–97] were mixed with an electric mechanical emulsifier (similar to a food blender) and no surfactant or mixing agent was used. Here emulsified diesel fuel with a maximum water volume substitution of 15% lowers $NO_x$ levels by a maximum of about 15%, in addition to lowering smoke emissions (by about 50% during use with raw vegetable oils) compared with neat fuel levels. CO levels are more or less maintained. Like water injection, the water droplets suspended within the fuel droplet vapourise to reduce combustion temperatures. This vapourisation also causes a phenomenon called "microexplosions", which is exclusive to water-in-fuel emulsions. Here, water vapourising within the emulsion droplet results in the violent disintegration of the emulsion droplet, giving a secondary atomisation effect after injection. As an explosion can be defined as a violent and rapid bursting or expansion, the term "microexplosion" as used in the literature will continue to be used throughout this work to define only this phenomenon. "Microexplosions" give a larger distribution of fuel across the combustion chamber, producing a more homo-

geneous fuel-air mixture. This reduces smoke levels and helps maintain thermal efficiency as well as specific fuel consumption levels compared with neat fuel operation. It is noted that emulsified vegetable oil (with similar water volume substitution levels) has a more significant effect on emission trends compared with emulsified diesel fuel with regards to their neat counterparts. This is due to the "microexplosions" having a greater effect on the high density and viscosity of vegetable oil. However, the specific fuel consumption for neat vegetable oil and its emulsions are higher than values seen for neat diesel fuel and diesel fuel emulsions due to the smaller lower heating value of vegetable oil. Emulsified fuels in general also extend ignition delay periods slightly (of the order of 0.1 ms more than neat fuels).

References [98–101] reports generally similar results with water-in-diesel fuel emulsions (with 13%-15% water substitution by volume) made with surfactants. Surfactants are chemicals which lower liquid surface tension, resulting in greater miscibility between two liquids. Here up to 30% lower $NO_x$ emissions are recorded compared with neat fuel operation, while unburnt HC emissions are also lowered by between 60%-90% [98]. Up to 30% lower CO emissions are also recorded [99] while smoke emission trends generally follow references [95–97]. In addition to the better fuel-air mixing caused by the "microexplosions", smoke particulate formation is limited as a result of water vapour diluting the smoke gas species. An increased concentration of hydroxyl (OH) radicals is also present with water addition, which would aid particulate burnout. Similar trends are recorded in reference [101], and are shown in figure 33. In addition, emulsions containing high amounts of water (between 15%-45% by volume) reduces $NO_x$ and smoke emissions significantly. However, this comes at the expense of significantly increased CO and unburnt HC emissions. Emulsion stability is also an issue when dealing with such high water volume substitutions [100].

Thermal efficiency and specific fuel consumption (SFC) trends seem to vary in the literature. For example, SFC is increased significantly (by about 20% compared with neat fuel operation) when water-in-fuel emulsions are used [98]. Other work [99] agrees, as can be seen from figure 34. This increase in SFC with increasing water percentage is due to the reduction in effective fuel percentage contained in the emulsion. However, other work [100] recorded lower SFC levels as well as increased thermal efficiencies with water-in-fuel emulsion use. This is attributed to a more significant effect of "microexplosions" (the exact operating conditions when this occurs is not stated in the reference) in addition to finer atomisation during injection resulting

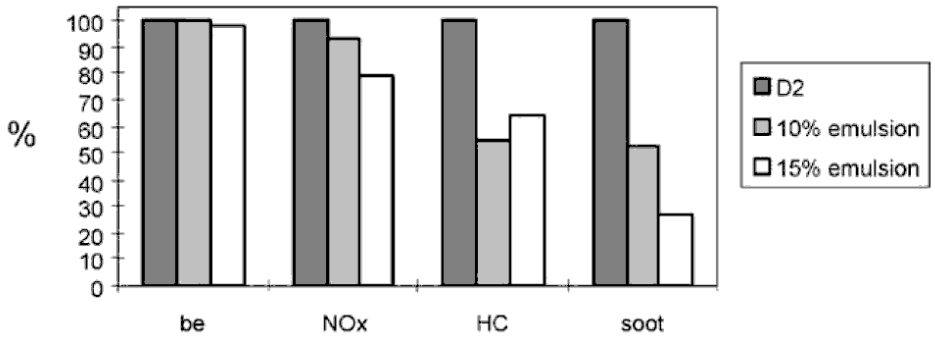


Figure 33: Percentage reduction in specific fuel consumption (be), $NO_x$, unburnt HC and soot during neat diesel fuel operation (D2), a 10% water-in-fuel emulsion and a 15% water-in-fuel emulsion [101]

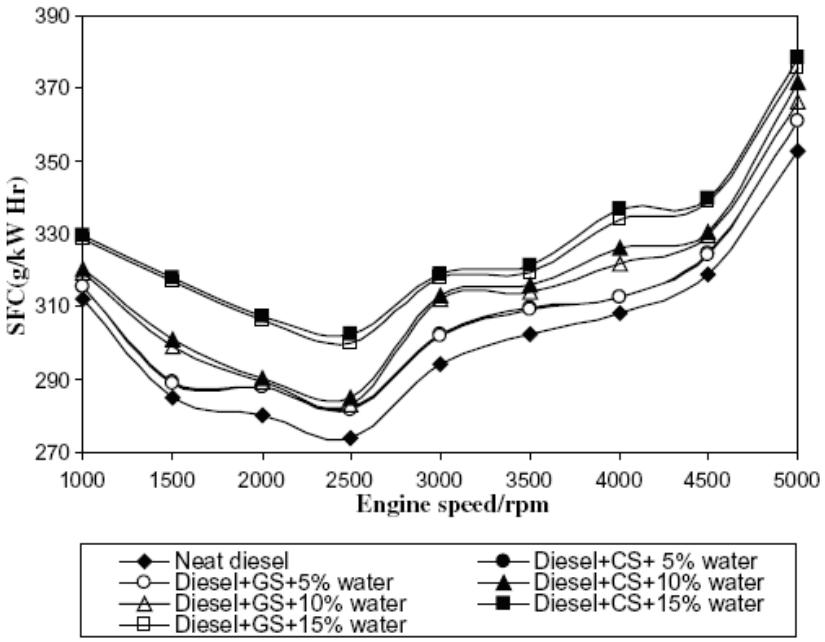


Figure 34: Specific fuel consumption (SFC) variation with engine speed during neat diesel operation and a variety of water-in-diesel fuel emulsions prepared with two different surfactants (conventional surfactant, CS and Gemini surfactant, GS) [99]

from lower fuel-water interfacial tension (compared with neat fuel injection). In addition to these conflicting trends, other work [95–97,101] report generally indifferent SFC trends when running on emulsions (as seen in figure 33). These variations in the published results could be due to experiments conducted with different fuels and different emulsifying methods, resulting in different physical and chemical properties of the emulsions produced. For example, water-in-diesel fuel emulsion viscosities are comparable to neat diesel fuel in some of the literature [102] while other work [103] found that emulsions have over twice the viscosity of diesel. Therefore, the effects

on engine performance and emissions can vary significantly with the different emulsions used. These effects also vary with the operating condition, where different emulsions (with different water volume substitutions) performed best at different engine speeds and loads [95].

Overall, water-in-fuel emulsions are an effective way of reducing $NO_x$ emissions and maintaining efficiencies without having to resort to lowering compression ratios or employing water injection systems. However, the physical and chemical properties of emulsions depend heavily on how they are emulsified and affects their performance during use. In addition, the renewability of emulsions depends on the fuel used in the emulsion (i.e. diesel fuel versus biodiesel fuel).

## 2.4 Hydrogen Gas as an Automotive Fuel

Significant attention is placed on hydrogen gas in recent years as a possible replacement automotive IC engine fuel. This is because, in addition to the limited crude oil supply, hydrogen can be made from a variety of sources. For example, hydrocarbon reforming with steam as well as via water electrolysis using electricity. While life cycle greenhouse gas emissions vary significantly when comparing the different hydrogen production methods, all of them produce lower levels than conventional fuel production. Energy consumption levels are also comparable to conventional fuel production levels. As a result, the status of hydrogen as a zero emission fuel depends on how it is produced. With regards to its use in IC engines, hydrogen combustion produces no products other than water, nitrogen gas and $NO_x$. In addition, it has physical properties which allow potential increases in IC engine thermal efficiency. However, there are issues which need to be addressed; such as high $NO_x$ emissions as well as abnormal combustion (i.e. preignition and "hydrogen knock"). "Hydrogen knock" is due to the higher pressure-rise rates (resulting in high combustion temperatures) during hydrogen engine operation compared with normal engine operation with conventional fuels. In addition, lower power densities are also recorded. This is due to a combination of low volumetric efficiency, high stoichiometric hydrogen-air ratios and low hydrogen energy density by mass. These trends are explained for both SI and CI engines in more detail in their respective subsections.

### 2.4.1 Overview of Hydrogen Gas Production

Unlike crude oil, hydrogen does not exist as free matter on Earth and is instead found in chemical compounds such as water and hydrocarbons [104]. While most hydrogen gas is made from methane using steam methane reforming [105], it can also be produced from liquid water via electrolysis using electricity (either from the grid or renewably). Steam methane reforming is an endothermic catalytic reaction, where methane is heated with steam to produce CO and hydrogen gas. Then a water-gas shift reaction (combining CO with water vapour) is used to oxidise the CO to $CO_2$ as well as produce more hydrogen gas. As a result this process produces $CO_2$ as a by-product [31, 106], which is taken into account in any life cycle emission analyses. As for hydrogen production via water electrolysis, the amount of $CO_2$ produced can vary depending on the electricity source, such as fossil fuel power plants (which has significant greenhouse gas emissions) or nuclear power (which has

minimal greenhouse gas emissions).

Previous work [31, 106] found that the well-to-wheels (WTW) life cycle $CO_2$ emission levels of hydrogen produced via steam methane reforming are generally lower compared with conventional fuel levels (i.e. gasoline, with a maximum reduction of about 55%). As for hydrogen produced by water electrolysis using fossil fuel electricity (i.e. from the grid), overall life cycle $CO_2$ levels are lower than conventional fuels [31]. However, other work found that emissions are increased by about 30% [106]. These differences can be due to the fossil fuel used in the electricity generating power plants, where coal-fired plants [106] produce significantly more $CO_2$ than natural gas fired power plants [31].

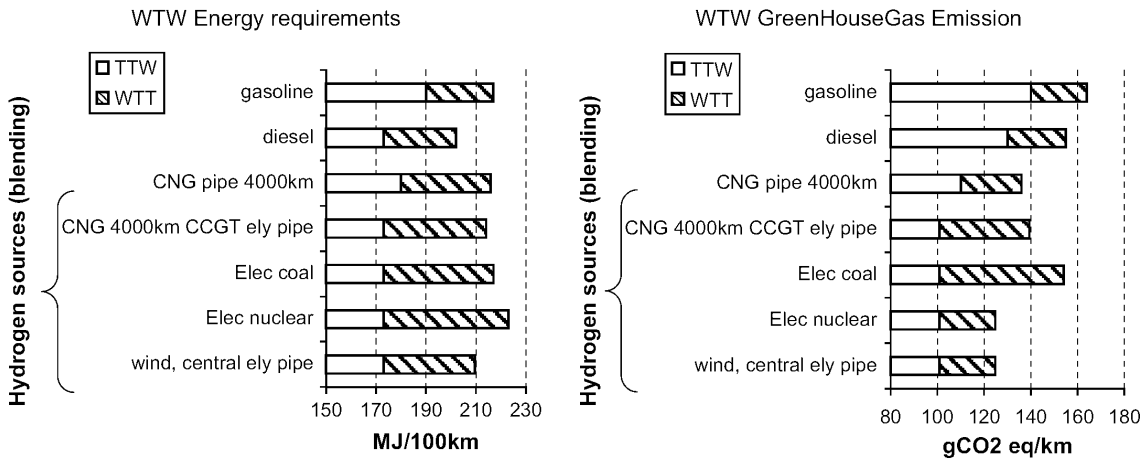


Figure 35: Well-to-wheels energy (consisting of well-to-tank, WTT and tank-to-wheel, TTW components) and $CO_2$ levels of hydrogen production (via electrolysis with electricity from various sources); compared with values for gasoline and diesel fuel [31]

Figure 35 illustrates this, where the data is presented in terms of mass of $CO_2$ produced per unit distance travelled by a hydrogen vehicle. In addition to greenhouse gas emissions, WTW energy consumption levels also vary in the literature. For instance, in reference [31] the WTW energy quantities needed for hydrogen production via steam methane reforming are very similar to conventional fuels, regardless of the methane source [31]. In reference [106] WTW energy levels for conventional fuels are about 50% higher than hydrogen produced via steam methane reforming, and about 16% lower than hydrogen produced via electrolysis using coal-fired power plant electricity. This discrepancy can be due to the life cycle analyses being conducted in different ways. For example, reference [31] compiled their data from literature alone while reference [106] calculated their results from literature as well as models, in this case the GREET (Greenhouse gases, Regulated Emissions, and

Energy use in Transportation) model. In addition, reference [31] based their numbers on the energy requirements and greenhouse gas emissions of manufacturing a state-of-the-art European mid-size vehicle, while reference [106] used average values (i.e. the average calculated between vehicles with maximum manufacturing energy requirements/ greenhouse gas emissions and vehicles with minimum manufacturing energy requirements/ greenhouse gas emissions).

Overall, hydrogen can be made via two different chemical processes, which in turn can use various input energy sources. Hydrogen gas cannot be considered a zero emission fuel if it is made from fossil fuel (i.e. steam methane reforming) or electricity from fossil fuel power plants (i.e. mains electricity) via water electrolysis. In addition, hydrogen produced via water electrolysis with renewable sources of electricity (wind, nuclear etc) possess comparable life cycle energy requirements as well as low emissions of $CO_2$ when compared with levels seen for conventional fuels.

### 2.4.2 Hydrogen Gas Combustion in Spark-Ignition Engines

Where SI combustion processes are concerned, hydrogen gas is very promising as an automotive fuel. Hydrogen gas combustion in air produces no other products than water vapour, nitrogen gas and $NO_x$ [49, 104, 105]. This means hydrogen combustion does not produce the emissions of $CO_2$, CO and unburnt HC normally found in SI engine exhaust gas. In practice however, some soot and unburnt HC is present due to combustion of lubricating oil. Hydrogen gas also has a range of fairly high octane numbers assigned to it (values between 88-130 RON have been quoted, compared with about 92-98 RON for gasoline) [48, 104]. This indicates hydrogen gas resists traditional knock (i.e. autoignition of the end-gas ahead of the combustion flame) to a larger degree than gasoline, and can be used under comparatively higher compression ratios. This allows greater combustion pressures, which increases the work extracted out of the combustion process. Hydrogen also has a wider flammability range in terms of fuel-to-air equivalence ratio ($0.1 \leq \phi \leq 7.1$) compared with gasoline ($0.7 \leq \phi \leq 4$) [49]. This allows ultra-lean fuel mixtures to be used (usually of the order of $\phi \leq 0.5$) [49,104,105]. As a result, engine power output can be controlled via the injected fuel amount (similar to a CI engine) and not via a throttle valve, reducing the pumping losses usually seen in typical throttled SI engines [105]. Hydrogen-air mixtures also generally burn much quicker than conventional fuel-air mixtures (laminar flame speeds are about 6 times faster than gasoline-air mixtures at stoichiometric

levels [48]), which shortens the combustion duration and can significantly influence thermal efficiency [105,107]. For example, the maximum brake torque (MBT) spark timing during hydrogen operation is retarded by about 10 degrees of crank-angle compared with gasoline operation [107]. As a result, combustion occurs in a nearly constant volume [105]. These factors combine to produce higher thermal efficiencies compared with typical gasoline fuelled engines, of the order of 2%-5% [48,107].

As a result of the high pressure-rise rates stemming the high flame speeds, peak combustion pressure recorded during engine operation with hydrogen is higher than typical gasoline levels (of the order of 1-2 MPa) [48]. This generates higher combustion temperatures in the combustion chamber, producing comparatively higher $NO_x$ emissions than gasoline operation. There appears to be a $NO_x$ formation limit with hydrogen engines in general (at equivalence ratios of about 0.5), below which $NO_x$ emissions are comparatively low [105]. These low emissions are due to the lean mixture condition, where the large amount of air brings down the combustion temperatures [107].

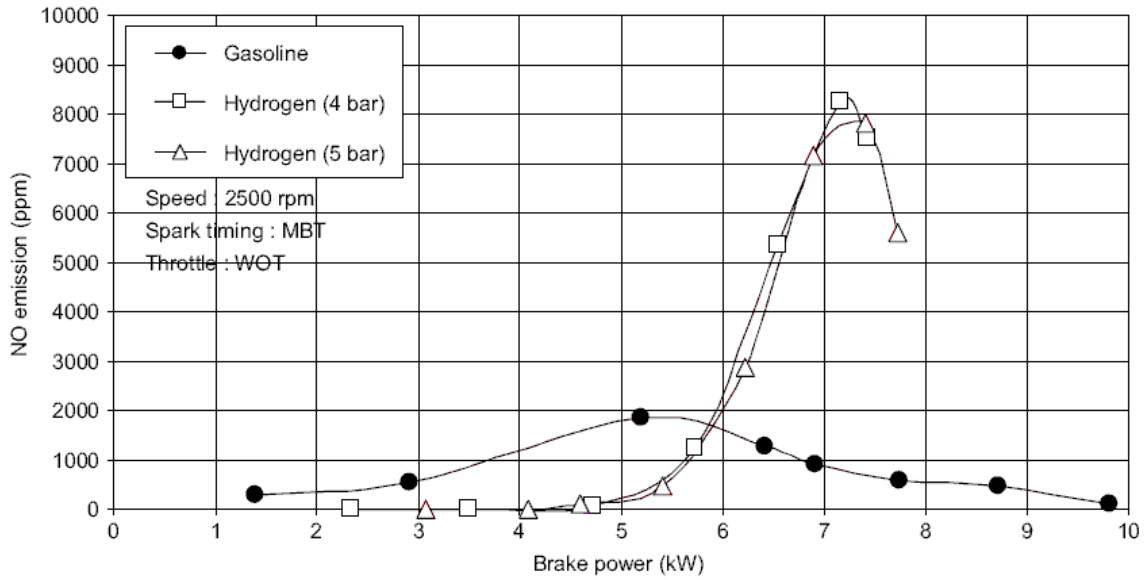


Figure 36: SI engine NO emissions comparison between gasoline operation and hydrogen operation at different supply pressures [107]

Other literature report similar trends, illustrated in figure 36, where $NO_x$ emissions increase significantly after a certain power output threshold compared with gasoline levels (by a maximum of 300%). As a result, at high engine loads some sort of $NO_x$ emissions control is needed. Previous work [108–110] found that adding diluents such as EGR to hydrogen combustion in order to control this increased $NO_x$ emission worked very well. Here EGR dilutes the hydrogen-air charge, reducing the

combustion temperature. In fact, uncooled EGR used in tandem with a three-way exhaust gas catalyst can reduce $NO_x$ emissions during hydrogen combustion to <1 ppm of total tailpipe emissions (while typical gasoline levels are of the order of 1000 ppm) [108, 109]. However, as EGR levels increased thermal efficiency decreased. This is because the hot EGR displaces a significant portion of the intake air (in addition to raising its temperature), reducing available oxygen for combustion. The same work [108,109] also conducted tests on hydrogen combustion with a lean burn strategy (i.e. excess air). While running at the common operating condition which produces the lowest $NO_x$ emissions (about <10ppm), hydrogen engine operation with EGR produced lower thermal efficiency levels (about 4%) than the lean-burn mode. At the same time, the lean burn strategy produced $NO_x$ emissions of about 7000 ppm after a particular equivalence ratio threshold (about 0.45), which is much higher than the maximum $NO_x$ emissions during the EGR mode (of the order of 1 ppm). As a result, while more torque can be produced with the lean burn strategy, this comes at the expense of very high $NO_x$ emissions. If $NO_x$ emissions were maintained at comparable levels to the EGR mode, the torque produced would be lower than the EGR mode [108, 109]. This is because the lean-burn strategy is operating at very low equivalence ratios while the engine is running at stoichiometric during the EGR mode. However, both the lean-burn strategy and operation with EGR produced less torque compared with undiluted hydrogen engine operation [108,109]. Water injection can also be used to curb $NO_x$ emissions [93], with comparable effects to adding diluents. Here, water injection reduced $NO_x$ emissions (by about 70-80%) compared with gasoline engine operation through mechanisms discussed in an earlier section, without any reduction in thermal efficiency.

While hydrogen gas can be used in SI engines fairly easily, there are significant practical issues. While the lower heating value of hydrogen is high compared with gasoline (120 MJ/kg and 44 MJ/kg respectively), it has an extremely low energy content by volume compared with gasoline (10.8 $MJ/m^3$ and 33440 $MJ/m^3$ respectively, assuming densities at standard state conditions). This poses problems in terms of power output, as significantly lower fuel energy would be inducted into the engine when hydrogen gas (at standard state conditions) is used with standard SI engine settings (injection timing, spark timing etc). However, as hydrogen is stored either as a compressed gas or a cryogenic liquid (these systems are discussed in more detail in a later section), this reduction in inducted fuel energy is not as drastic as initially implied. This is because the hydrogen gas delivered to the engine under these conditions has a higher density than at standard state conditions. Previous work [48]

established that for stoichiometric mixtures, hydrogen-air mixtures produce more energy (per unit mass of mixture) than other hydrocarbon fuel-air mixtures. However, hydrogen gas powered engines usually produce about 80% of peak power output recorded during engine operation with hydrocarbon fuels [49, 107]. This is due to limits within the engine design on the amount of hydrogen gas as well as air that can be inducted. Several factors contribute to this. The first is that hydrogen has a stoichiometric air-fuel ratio of 34.2, while gasoline has a typical value of about 14.6. In addition, hydrogen engines inducted into the intake manifold (either via injection or carburetion) have significantly lower volumetric efficiencies compared with port-injected gasoline engines (of the order of 20%-30%) [104, 107, 111]. This is because the injected volume of hydrogen gas displaces a comparable volume of air going into the engine during injection. This reduces the amount of air inducted for combustion, in so doing restricting the amount of fuel that can burn sufficiently and hence power output.

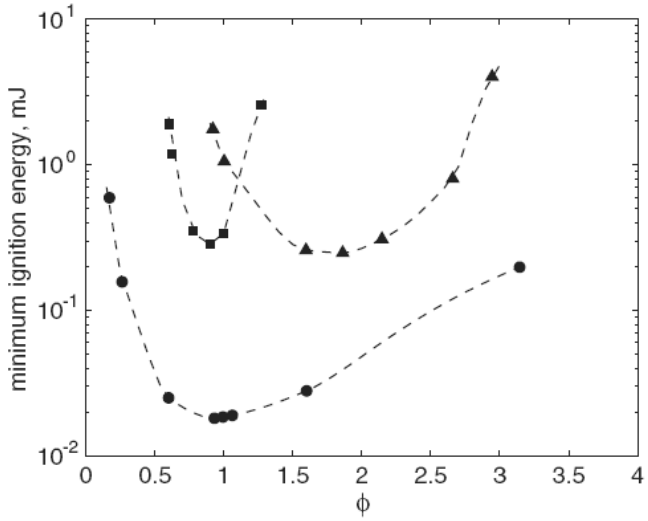


Figure 37: Ignition energy of hydrogen-air (circles), heptane-air (triangles) and methane-air (squares) mixtures plotted against equivalence ratio ($\phi$) [49]

Power output during hydrogen fuelling is also limited by its volatility. In addition to having a wide flammability range, hydrogen-air mixtures have very low ignition energies compared with gasoline-air mixtures, as can be seen in figure 37. As a result, hydrogen-air mixtures can be ignited along the inlet tract in a phenomenon known as backfire [105, 111]. Here, the hydrogen-air mixture can be ignited by a variety of sources (hotspots, hot carbon deposits), the most predominant being hot residual charge gases. Hydrogen is also prone to knocking at high engine load conditions [104]. Figure 38 shows where this knocking region occurs as a function

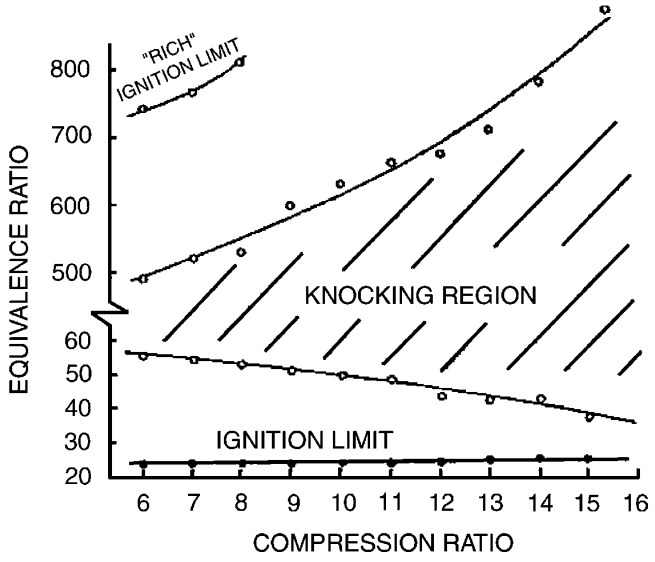


Figure 38: Typical location of knocking region during conventional engine operation with hydrogen fuel, varying with compression ratio and percentile of equivalence ratio [104]

of equivalence ratio and compression ratio. The knocking region becomes wider with compression ratio (increasingly so after a value of about 11). This also limits the operating range of the engine in terms of equivalence ratio (from the figure which shows equivalence ratio in percentage, the equivalence ratio limit is 0.6). This is unexpected as octane numbers of about 130 RON maximum have been reported. It is possible, though not stated explicitly, that the term "knock" used in reference [104] can relate to "hydrogen knock" (unusually high pressure-rise rates resulting from rapid fuel-burning rates) and not the autoignition of the end-gas ahead of the combustion flame. Previous work [48] concludes that a reliable octane number value for hydrogen remains unconfirmed in the literature, as most methods to determine fuel octane numbers (such as the Cooperative Fuel Research, CFR engine) are only applicable to liquid SI engine fuels. This is because the flame speeds of hydrogen-air mixtures are extremely high in the stoichiometric region and depend heavily on air-fuel ratio, voiding the application of these methods [48]. Another rating of traditional knock for gaseous fuels has been developed, and uses methane as the baseline [48]. This is known as the methane number, where a value of 100 indicates high knocking resistance and lower values indicate low knocking resistance. The methane number for hydrogen is stated to be 0, which implies very low knocking resistance. As this is counterintuitive to the previously stated octane numbers, a clearer measure of traditional combustion knock resistance (i.e. the autoignition of the end-gas) for gaseous fuels is needed.

In addition to the work discussed previously which employed port hydrogen induction methods, direct hydrogen gas injection into the combustion chamber has also been investigated [48, 49, 112, 113]. This is an effort to improve volumetric efficiency and avoid the backfire problem found in port-inducted engines. As the hydrogen gas is injected into the combustion chamber, there is no premixed charge in the inlet tract which prevents backfire from occurring in the intake manifold. However, as the mixing time between then hydrogen gas and air (from the start of injection to the spark timing) is reduced compared with port injection, the injection timing is crucial for determining mixture quality [49]. As a result, $NO_x$ emissions also depend heavily on injection timing; where levels generally rise significantly with advance of injection timing relative to combustion TDC (of the order of 5 to 10 times) [49] This is because there is more time for a homogeneous mixture to form when injection timing is advanced, which in turn result in high pressure-rise rates and high peak pressures after ignition [112]. Reported $NO_x$ emission trends are contradictory in the literature however, with some work stating that $NO_x$ increases with advanced injection timing (relative to combustion TDC) and others stating otherwise [49]. This discrepancy is due to different work employing equivalence ratios, which are either greater or less than the $NO_x$ formation limit. For conditions employing equivalence ratios below this limit, the injection timing advance reduces the number of local fuel-rich regions (a source of high $NO_x$ emissions during combustion) [49]. For conditions employing equivalence ratios above this limit, the injection timing advance increases the overall reaction rate which increases $NO_x$ emissions. This is because, at equivalence ratios higher than the $NO_x$ formation limit, the injection timing advance dilutes local rich fuel-air mixtures which normally possess slower overall reaction rates [49]. The local rich regions at these conditions are significantly richer than the local regions discussed for conditions below the $NO_x$ operating limit). Other work [112] also present this trend. Similar trends in thermal efficiency are also reported [49], while other work show a general indifference in thermal efficiency with regards to injection timing [112]. Volumetric efficiency is also consistently higher than engines burning port injected hydrogen, of the order of 10% maximum at high equivalence ratios [113]. As a result, up to 50% higher BMEP levels can be achieved [113]. However, technical issues with direct gaseous fuel injectors are present. For example, high injection pressures (of the order of 10 MPa) in order to overcome compression pressures as well as high flow rates (of the order of 10 g/s) in order to inject enough fuel within the short period between the intake valve closing and spark timing [49]. Current state-of-the-art gaseous direct injectors are not durable enough for automotive ap-

plications, where typical lifespans are around 200 hours when about 20000 hours are expected [48]. It is likely that these issues relate to durability (a common issue with port gaseous injectors), as hydrogen cannot lubricate injector components that are moving or in contact with each other [114].

Overall, SI engine operation with hydrogen fuel produces higher thermal efficiencies than gasoline. However, significantly higher $NO_x$ emissions compared with typical gasoline levels are recorded above a certain equivalence ratio, termed the $NO_x$ formation limit. Below this limit, $NO_x$ emissions are lower than typical gasoline engine levels. Power levels during hydrogen operation are also severely reduced compared with engine operation with gasoline, due to reduced volumetric efficiency combined with a high stoichiometric fuel-air ratio. Abnormal combustion such as backfire and "hydrogen knock" can also occur at lower thresholds compared with normal SI engines, further limiting the engine operating range. Direct hydrogen injection into the combustion chamber can prevent backfire and maintain volumetric efficiency, in addition to increasing power output. However, issues with injector reliability (for both port and direct injection as a result of the lack of lubrication) are present.

### 2.4.3 Hydrogen Gas Combustion in Compression-Ignition Engines

While SI engines are the dominant automotive powerplants (at least in the UK [56]), there is still a significant percentage of passenger vehicles that are powered by compression ignition (CI) engines (about 34% of the current UK fleet). In addition, almost 100% of goods vehicles as well as buses use CI engines [56]. As a result, it is pertinent to know how combustion of hydrogen fuel in these engines will affect performance and emissions. However, igniting hydrogen gas under compression is extremely difficult. There are issues in achieving the correct conditions under which hydrogen can spontaneously ignite, mainly due to its expectedly low cetane number. Previous work [115] found that hydrogen might not ignite spontaneously even with compression ratios ranging up to 29:1. Under simulated CI engine conditions at TDC in a constant volume bomb, direct-injected hydrogen gas ignites at ambient gas temperatures of more than 1100 K, while diesel fuel ignites at about 1000 K at ambient pressure levels of about 6 MPa [116]. In addition, spontaneous hydrogen ignition is heavily dependent on ambient temperature, such that ignition delays (defined as the time between the start of injection and ignition) are reduced by about 80% when the ambient gas temperature inside the bomb is increased by 10% [116].

This temperature dependence raises concerns over the operational stability of spontaneous hydrogen combustion. Previous tests [117] done with hydrogen fuel in a homogeneous charge compression ignition (HCCI) engine found that preignition is prevalent, and ignition can occur anytime over a 10 crank angle degree range. This is due to combustion being initiated by hotspots on the combustion chamber surface, and not spontaneous ignition of the hydrogen-air mixture itself [117]. As a result, an ignition source is required for practical and controlled hydrogen combustion in CI engines.

A common issue was encountered when attempts were made to burn other high-octane number fuels in CI engines. In what is called the "dual-fuel" mode for CI engines, a gaseous high-octane number fuel is usually inducted into a CI engine with incoming air in the intake manifold (giving a largely premixed fuel-air mixture), and then ignited by a "pilot" injection of high-cetane number fuel (usually injected via the standard injection system into the cylinder). The dual-fuel term is separate from the "bi-fuel" term, where two fuels are burned in an engine at different times. Research into dual-fuel applications using hydrogen gas instead of natural gas has been conducted previously, with some work dating back to the 1980s [48, 118–127]. In almost every report (most of which inducted hydrogen via the intake manifold), general increases in thermal efficiency are reported compared with normal CI engine operation. This is due to higher combustion rates (the diffusion phase mainly, compared with normal CI engine operation with diesel fuel) brought on by a more homogeneous hydrogen-air mixture in addition to comparatively faster flame speeds of the hydrogen-air mixture [120, 124, 126, 127]. The high combustion rates are reflected in generally higher pressure-rise rates and peak pressures recorded during dual-fuel combustion [118–120, 123]. In addition, ignition delay times can also be extended during hydrogen dual-fuel operation (by about 0.6 ms) [119]. This is primarily due to the reduced oxygen concentration in the intake charge, as well as an increased specific heat capacity compared with normal CI engine operation.

Figure 39 shows a computed combustion chamber pressure plotted against crank angle for increasing hydrogen-air equivalence ratios during hydrogen dual-fuel operation with a fixed quantity of pilot fuel. Combustion pressures increase significantly from an equivalence ratio of 0.2 to 0.3, while there is an almost vertical slope of the pressure curve after the initial inflection as a result of pilot fuel combustion. This very fast combustion rate is due to the extended ignition delay in addition to the high flame speed of hydrogen, which accelerates combustion further with increasing

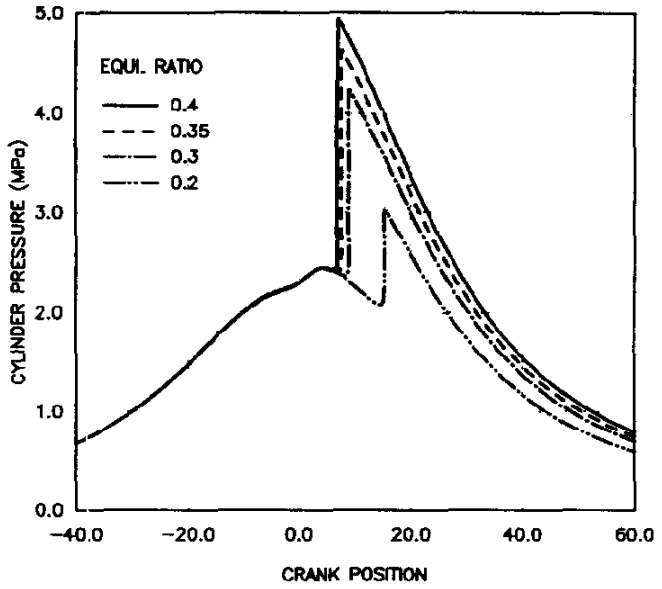


Figure 39: Predicted (i.e. computed) combustion chamber pressure (for different hydrogen-air equivalence ratios) plotted against crank-angle for hydrogen dual-fuel operation (adapted from [123])

hydrogen concentration in the intake charge [123]. When the increase in pressure-rise rates become too significant (at high equivalence ratios), "hydrogen knock" will be an issue (as discussed in the previous section) [123].

Figure 40 shows hydrogen dual-fuel operation increases thermal efficiency throughout the load range and at every hydrogen port injection timing (with regards to gas-exchange top dead centre, GTDC) compared with normal CI engine operation with diesel fuel. Varying the hydrogen port injection timing affects thermal efficiency levels significantly only at the high loads, where significantly retarded injection timing with regards to combustion TDC reduces thermal efficiency to normal CI engine levels. This is due to hydrogen gas being injected too late in the intake stroke, reducing the homogeneity of the hydrogen-air mixture compared with earlier hydrogen injection timings. In addition, the authors of this work [121] lowered the hydrogen energy fraction while at the same time increasing the diesel fuel energy fraction when increasing engine load. As a result, the hydrogen energy fraction goes from 18% at zero load condition to 6% at full load. It is likely, though not explicitly stated in the work, that this was done to avoid unusually high pressure-rise rates (i.e. "hydrogen knock") at high engine loads. As a result, the influence of hydrogen gas on combustion diminishes at high load in this work.

Figure 41 shows hydrogen dual-fuel operation increases $NO_x$ emissions significantly

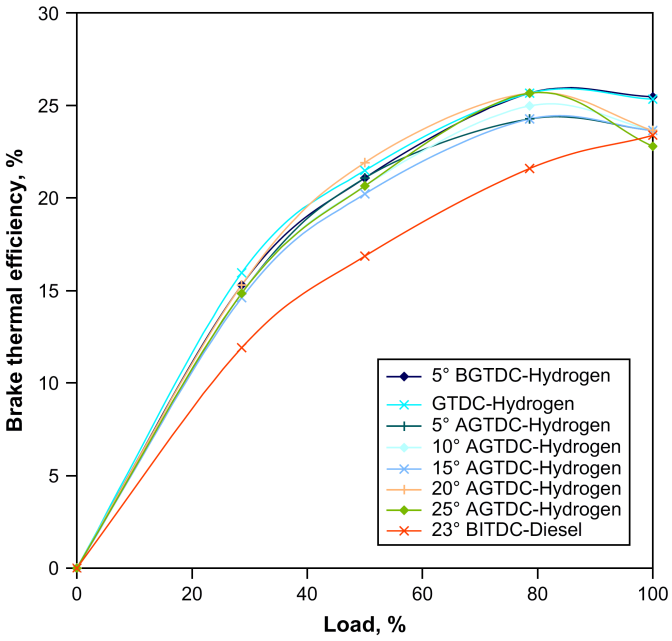


Figure 40: Efficiency and engine load comparison between normal CI engine operation with diesel fuel (diesel fuel injection timing set at 23 degrees before ignition TDC, BITDC) and hydrogen dual-fuel operation with diesel pilot fuel at varying hydrogen port injection timings with regards to gas-exchange top dead centre (GTDC) [121]

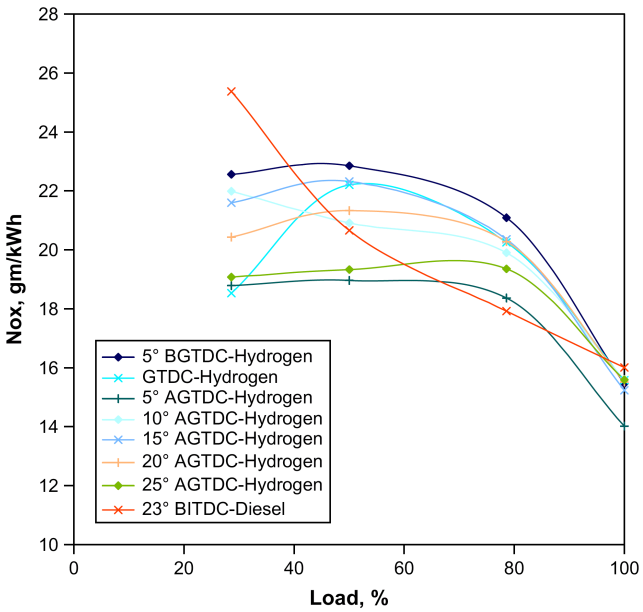


Figure 41: $NO_x$ and engine load comparison between normal CI engine operation with diesel fuel (diesel fuel injection timing set at 23 degrees before ignition TDC, BITDC) and hydrogen dual-fuel operation with diesel pilot fuel at varying hydrogen port injection timings with regards to gas-exchange top dead centre (GTDC) [121]

compared with normal CI engine operation for most of the load range. This is due to the high rates of combustion during hydrogen dual-fuel operation increasing $NO_x$

formation rates. At high loads, $NO_x$ levels drop below normal CI engine operation levels. This is due to the lower energy fraction of hydrogen at this condition compared with hydrogen energy levels at lower loads. A universal increase in $NO_x$ emissions is seen with fixed or increasing hydrogen energy fraction in other work by the same authors [127, 128]. Hydrogen injection timing also has a significant effect on $NO_x$ emissions, primarily at low and intermediate loads. Here, the $NO_x$ emission trend is affected by the hydrogen-air mixture quality, which is dependant on its residence time in the inlet tract prior to ignition.

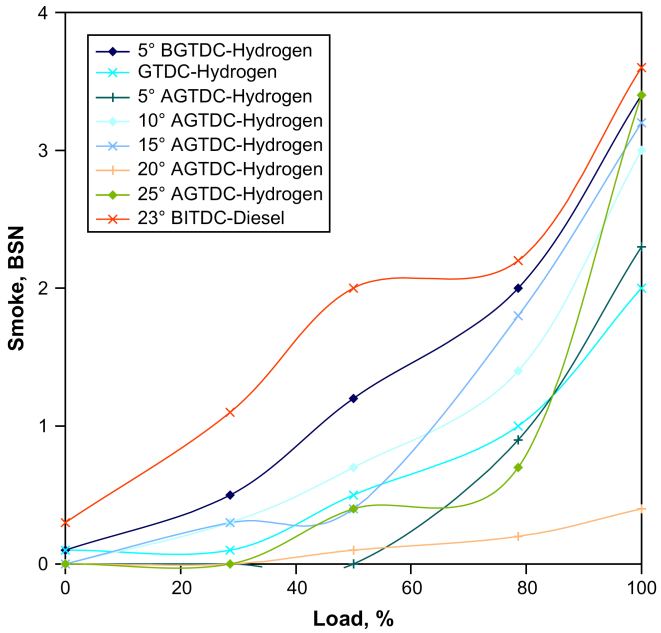


Figure 42: Smoke and engine load comparison between normal CI engine operation with diesel fuel (diesel fuel injection timing set at 23 degrees before ignition TDC, BITDC) and hydrogen dual-fuel operation with diesel pilot fuel at varying hydrogen port injection timings with regards to gas-exchange top dead centre (GTDC) [121]

Smoke and PM levels (shown in figure 42) are lower compared with normal CI engine operation due to several factors. Firstly, there is a reduction in the amount of carbon in the inducted fuel (due to hydrogen replacing a portion of the fuel energy). Secondly, the higher combustion rates and chamber temperatures help burn off particulate matter which would normally remain during normal CI engine combustion. Like $NO_x$ emissions, smoke levels are affected by the hydrogen injection timing and is generally governed by the fuel-air mixture quality. CO emissions are also generally maintained at low and intermediate loads, while increased levels are found at high loads [127, 128]. This increase is due to a comparatively lower oxygen concentration at high hydrogen energy substitutions.

The increased $NO_x$ emissions and "hydrogen knock" tendencies during hydrogen dual-fuel operation compared with normal CI engine operation need to be reduced as they are major constraints on engine power output. Previous work [122, 124, 128] showed that, hydrogen dual-fuelling with EGR produces lower thermal efficiencies than hydrogen dual-fuelling without EGR. For example, a 25% EGR substitution of total intake charge volume reduced efficiency by about 3% [122]. This is primarily due to the dilution effect of EGR, where the oxygen concentration of the intake charge is reduced. However, thermal efficiencies for both dual-fuel cases remain higher than normal CI engine operation throughout the load range. In addition, decreasing volumetric efficiency with increasing EGR rates are significant. For example, a 10% EGR volume substitution of the intake charge reduces volumetric efficiency by about 15% compared with hydrogen dual-fuel operation without EGR [124]. Hydrogen dual-fuelling with EGR also reduces $NO_x$ emissions significantly (by about 14% at a 25% EGR substitution of intake volume) [122]. Other work [124] shows that $NO_x$ emissions can be reduced to normal CI engine levels with at least a 10% EGR volume substitution. This reduction is due to lower combustion temperatures, brought on by reduced combustion rates. Reduced combustion rates (which correspond to reduced pressure-rise rates) also can mean reduced "hydrogen knock" tendencies. This is further illustrated by lower exhaust gas temperatures [124]. At the same time, EGR addition to hydrogen dual-fuel operation can increase particulate emissions compared with hydrogen dual-fuel operation without EGR [124, 128]. This is due to reduced soot oxidation (as a result of the lower combustion temperatures), in addition to the dilution of the intake air. As a result, hydrogen dual-fuel operation with EGR produces smoke levels similar to normal CI engine operation [122, 124, 128]. In addition, increases in unburnt HC, CO and $CO_2$ emissions with EGR addition are also recorded.

In almost all of the hydrogen dual-fuel literature discussed above, diesel fuel is the sole pilot fuel employed. However, there have been limited studies with alternative pilot fuels (i.e. biodiesel) [48, 129, 130]. Generally, biodiesel (in the form of methyl esters) is a renewable high-cetane number fuel produce from raw organic oils (such as vegetable oil) via transesterification with methanol. These fuels are fairly similar to diesel fuel in conventional CI engine operation in terms of their performance and exhaust emissions [12, 13, 58, 68]. This similarity to diesel fuel is expected to be extended to the pilot fuel role. When used as pilot fuels, thermal efficiency and $NO_x$ emissions are lower with rubber seed oil methyl ester pilot fuel (with hydrogen gas providing an energy share of about 10% during dual-fuel com-

bustion) when compared with tests with a diesel fuel pilot [129]. Emissions are also affected, where unburnt HC, CO and smoke emissions for the methyl ester pilot are higher [129]. Similar trends are reported for CI engine tests running Jathropa oil pilot fuel and an optimum hydrogen mass share of 7% [130]. Here, thermal efficiency is reduced compared with the diesel pilot fuel, while $NO_x$ levels are also reduced. Higher smoke levels are recorded for the Jathropa oil pilot fuel. These trends for the alternative pilot fuels are due to inferior combustion resulting from their higher viscosities compared with diesel fuel, causing poorer fuel mixture formation during pilot injection.

Overall, CI engine operation with hydrogen gas requires the dual-fuel mode. There is a general increase in thermal efficiency and $NO_x$ emissions compared with normal CI engine operation. These trends are due to a faster burn rate of hydrogen dual-fuel operation compared with conventional CI engine combustion. Smoke emissions are also lowered. In addition, hydrogen gas can only provide a comparatively low fraction of total supplied fuel energy compared with the pilot fuel during dual-fuel engine operation. Specifically, the pilot fuel provides more than 50% of the fuel energy. This is due to a combination of lower volumetric efficiencies, high stoichiometric hydrogen-air ratios as well as the risk of abnormal combustion phenomenon. Charge diluents (such as EGR) can be used to reduce $NO_x$ emissions as well as "hydrogen knock" tendencies, however, further reduced volumetric efficiencies are recorded.

## 2.5 Gaseous Fuel Storage

In addition to how natural gas and hydrogen gas perform in IC engine combustion, both gaseous fuels have to match conventional fuels in terms of stored fuel energy density (when taken on board a vehicle for example). While both natural gas and hydrogen have higher combustion enthalpies (45 MJ/kg and 120 MJ/kg respectively) compared with conventional liquid fuels (typically about 40-44 MJ/kg), they have very low densities (0.79 kg/m$^3$ and 0.09 kg/m$^3$ respectively) compared with conventional liquid fuels (which are of the order of 860 kg/m$^3$) at standard state conditions. As a result, both gases must be either compressed or liquified in order to contain energy densities (either energy per unit mass or energy per unit volume) within an order of magnitude of the energy density of typical hydrocarbon fuels.

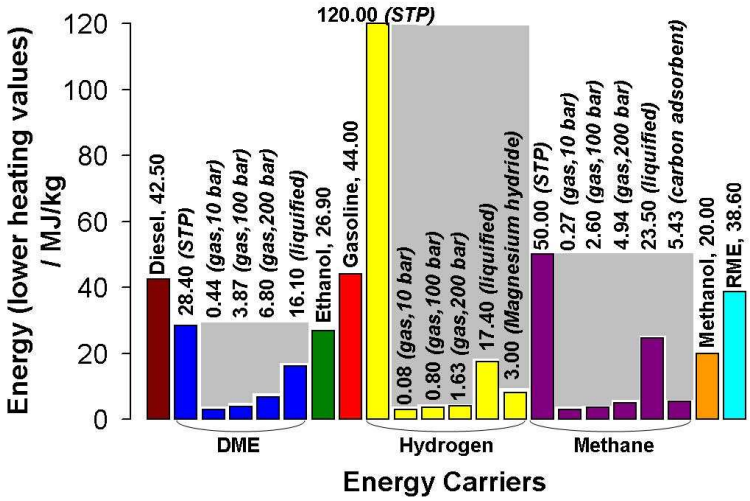


Figure 43: Energy densities per unit mass for different energy carriers [36]

Figures 43 and 44 show the effective energy densities of different automotive fuels in terms of energy per unit mass (sometimes called gravimetric energy density) and energy per unit volume (volumetric energy density). The mass and volume terms shown in the figures take into account a rough estimate of the storage medium masses and volumes required, most of which were calculated during the course of the work while some were adapted from literature (which are appropriately noted in the following sections). All compressed gas energy density values were calculated using a type-K compressed gas cylinder as a reference container. The type-K cylinder was selected as it was the gas tank used to store hydrogen in the experimental work conducted. In addition, it has a comparable storage volume to typical passenger vehicle fuel tanks (about 50 litres). The various densities at the different storage

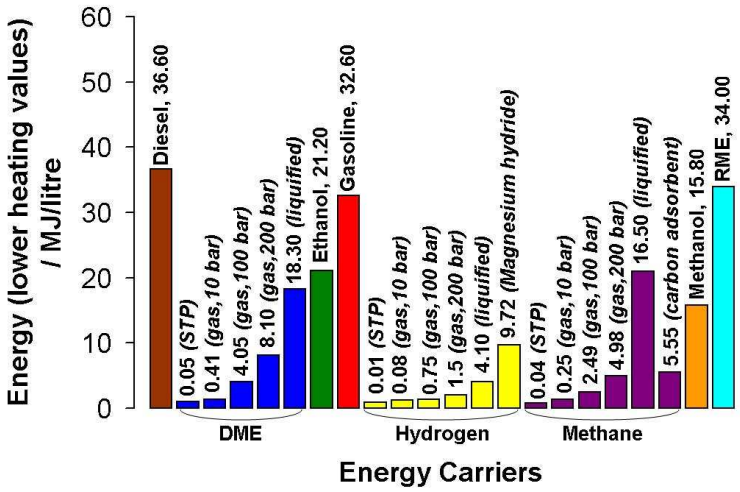


Figure 44: Energy densities per unit volume for different energy carriers [36]

pressures were calculated by treating each gas as an ideal gas.

These figures show that cryogenic liquified gaseous fuels provide the highest energy densities (compared with other gaseous fuel storage media), which remain generally lower compared with conventional liquid fuels. In addition, there are issues regarding their practicality during use as vehicular storage devices, which will be discussed in the following sections. Regardless of the gaseous fuel storage method, the current state-of-the-art cannot match the energy densities of conventional fuels, and more research into increasing gaseous fuel energy densities is needed.

### 2.5.1 Overview of Natural Gas Storage Options

As the density of natural gas is low compared with conventional liquid fuels at standard state conditions, inadequate fuel energy storage quantities are present when used as a vehicular fuel. From figures 43 and 44, liquified natural gas (LNG) contains the highest energy densities for natural gas, which are comparable to liquid fuels such as the alcohols (LNG values shown adapted from reference [131]). Also shown are carbon adsorbents, which are highly porous carbon particles that allow natural gas molecules to be adsorbed onto the carbon particle surface; much like how water vapour adsorbs onto silica gel grains. Typical storage conditions for the carbon adsorbent are of the order of 3.5 MPa and 25 degrees Celsius, which are fairly reasonable compared with either CNG or LNG (which require either significantly higher pressures or low cryogenic temperatures). However, carbon adsorbents provide comparable energy densities to CNG (at 20 MPa) and have issues with short

lifetimes [131, 132]. With regards to the last point, as the carbon adsorbent is continuously filled and drained, carbon adsorbent storage efficiency (volume of natural gas adsorbed divided by the carbon adsorbent volume) can drop by 50% over 700 cycles compared with values recorded during initial use [132]. As a result, since CNG is the most popular method to store natural gas and has no cyclic lifetime limit, only a comparison between LNG and CNG will be drawn.

Liquifying natural gas is energy intensive compared with natural gas compression, requiring a minimum percentage of about 20% of its lower heating value (considering a minimum transport distance from the gas well to the end user) [133]. At the same time, calculations made during this work found that compressing natural gas from atmospheric conditions to 20 MPa requires about 4% of its lower heating value. In addition, energy input levels for either process increase significantly with transport distance from the gas well to an end user. However, the rate of this increase is higher for CNG transport compared with LNG [133]. For example, if natural gas was to be transported over twelve thousand kilometres (roughly halfway across the globe), energy input levels for either LNG (via ship) or CNG (via pipelines) are the same [133].

LNG is also a higher quality methane carrier (i.e. contains less impurities) compared with CNG. According to reference [133], LNG has 90% less the amount of inert contaminants usually recorded in CNG as a result of the liquification process. However, due to the cryogenic temperatures required for maintaining natural gas as a liquid, significant fuel losses occur [134, 135]. Here, energy (i.e. "heat") transfer into the cryogenic tank causes the stored LNG to evaporate (otherwise known as "boil-off"), increasing the storage tank pressure. To avoid tank rupture due to over-pressurisation, this evaporated natural gas is vented causing a typical maximum fuel mass loss of the order of 10-20% per day [135]. These losses are very significant, and efforts have been taken to reduce them [135]. For instance, tripling the thickness of the insulation around the cryogenic tank can reduce losses by about 75% [135]. However, this brings issues with increased weight and volume of the storage tank. The vented natural gas can also be put to use during vehicle refuelling, possibly used to power a generator [135]. However, this requires additional extraction systems employed by the end user or during the refilling process.

Overall, LNG runs the risk of significant evaporative fuel losses during use in addition to complex cryogenic fuel systems, issues which are minimal with regards to CNG.

In addition, considering work done on high-pressure (of the order of 70 MPa storage pressure) CNG storage tanks in general [136], energy densities recorded with the current state-of-the-art can increase significantly compared with LNG storage. At the same time, comparatively low energy input requirements and losses can also be obtained. However, more work in the development of these high pressure storage tanks is required to assess these claims.

### 2.5.2 Overview of Hydrogen Storage Options

Like natural gas, the extremely low density of hydrogen gas at standard conditions presents problems in terms of adequate fuel energy storage quantities. From figures 43 and 44, solid metal hydrides as well as cryogenic liquid storage are the most promising as they have significantly higher energy densities (chemical energy per unit mass and volume) available compared with compressed gas tanks (which are the standard storage option for most uses). As a result, only these three options are discussed in this investigation.

Metal hydrides are metal lattices containing interstitial sites into which hydrogen atoms can diffuse and remain until released [137]. Hydrogen gas absorbs into the metal hydride and in doing so produce heat energy, after which the lattice can release hydrogen gas when heated. The absorption process might require a catalyst depending on the hydride used, as absorption can take place at a temperature higher than the melting point of a particular hydride [137]. The process details of releasing hydrogen gas from a metal hydride also depends on the metal hydride used, as some hydrides require higher pressures and temperatures to release hydrogen compared with others [137, 138]. For example, magnesium hydride ($MgH_2$) needs conditions of about 1 MPa and 300 degrees Celsius in order to release hydrogen gas, while up to 35 MPa and 600 degrees Celsius is needed for lithium borohydride($LiBH_4$) [137]. From figure 43, metal hydrides have lower energy densities by mass compared with liquified hydrogen, while still bettering compressed hydrogen gas (values shown for metal hydrides adapted from reference [139]). Other work [140] found similar results. This is due to the comparatively larger mass of metal hydride storage media compared with cryogenic storage (of the order of 100 kg) [139]. However, while the literature generally agrees with the energy density by mass trends, some discrepancies with volumetric energy density trends exist. An energy density per unit volume comparison can be seen in table 4. From these values, metal hydrides have lower

volumetric energy densities than cryogenic liquid hydrogen, while higher volumetric energy densities are shown in figure 44. These discrepancies can due to the different storage media (in terms of tank sizes, heat exchangers, supply pipework etc) which can vary significantly with the metal hydride in question. As some metal hydrides operate at high pressures and temperatures, heating/ cooling mechanisms are needed in order to release and absorb hydrogen. The purity of the hydrogen gas stored is also important as the lack of it can affect the life of the metal hydride significantly [139]. For example, some metal hydrides can easily react with air, reducing their hydrogen absorption capability [137] resulting in the requirement of sealed components. Purification equipment can also be required. All these factors require additional ancillary equipment and adds complexity as well as mass/ volume to the overall hydrogen fuel supply system.

Table 4: Energy density of hydrogen in different storage options [141]

| Storage Technology | Energy Density / MJ/litre |
|---|---|
| Compressed Hydrogen Gas (70 MPa) | 2.0-4.0 |
| Cryogenic Liquid Hydrogen (20 K) | $> 4.0$ |
| Metal Hydrides | 3.5 |

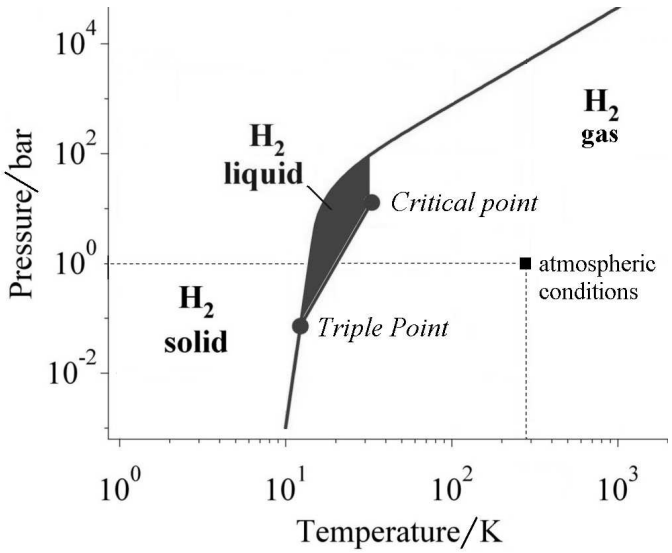


Figure 45: Hydrogen phase diagram, adapted from [142]

While metal hydrides are still a fairly recent technology, cryogenic liquid hydrogen storage has been investigated since the mid-1970s [143, 144]. Cryogenic hydrogen storage usually involves liquifying and storing hydrogen gas in a heavily insulated vessels, by reducing its temperature to roughly 20 K (-253.15 degrees Celsius), in

most cases maintaining atmospheric pressure (as seen from figure 45). Once liquified, cryogenic hydrogen has about 800 times the energy density of gaseous hydrogen at standard state conditions and double the density of high pressure (70 MPa) compressed hydrogen gas [140]. These high energy densities allow hydrogen vehicles to close the gap on the operating ranges of conventional vehicles as they are able to carry more fuel energy. This is further illustrated in figures 43 and 44 (liquid hydrogen tank size used to calculated values shown taken from reference [143]). However, there are issues associated with the extreme temperatures needed to store liquid hydrogen [136, 137, 140, 141, 145]. Similar to cryogenic LNG storage discussed earlier, liquid hydrogen evaporates within the storage tank over time, increasing its pressure. To alleviate this pressure and avoid over-pressurising the tank, this "boiled-off" hydrogen gas is released at a typical rate of 1% of the total contained liquid hydrogen volume per day [137,141,145]. In addition, the entire liquid hydrogen volume expands during storage specifically between the storage temperature of 20 K and its critical temperature of 30 K. As a result, liquid hydrogen tanks can only be filled to 85-95% of total tank capacity to accommodate this expansion, reducing the energy density [136]. Secondly, the energy required to liquify hydrogen is substantial, stated to be up to 40% of its lower heating value (about 50 MJ/kg) [136]. This is especially significant compared with other fuels such as natural gas, which requires about 4% of its lower heating value (about 2 MJ/kg) for compression to typical gaseous storage pressures of around 20 MPa (which gives comparable volumetric energy densities to liquified hydrogen, as seen in figure 44).

These drawbacks can be less severe by storing liquid hydrogen under pressure [136]. Increasing the pressure at which the liquid hydrogen is stored in a vessel increases the time taken for liquid hydrogen to vaporise and then released, otherwise known as the dormancy period. The dormancy period for liquid hydrogen stored under ambient pressure is stated to be 5 days, while for liquid hydrogen stored under high pressure (about 20 MPa) has a dormancy period of 17 days [136]. As a result, these pressurised liquid hydrogen vessels significantly reduce the evaporative losses commonly seen in normal liquid hydrogen tanks. When left to reach thermal equilibrium with the surroundings, an ambient pressure liquid hydrogen tank can retain only 1% of its initial liquid hydrogen volume as most of the hydrogen will evaporate and dissipate, while a liquid hydrogen storage vessel pressurised at about 20 MPa can retain 30% of its initial volume [136].

These high pressure liquid hydrogen vessels are also safer in the event of a tank

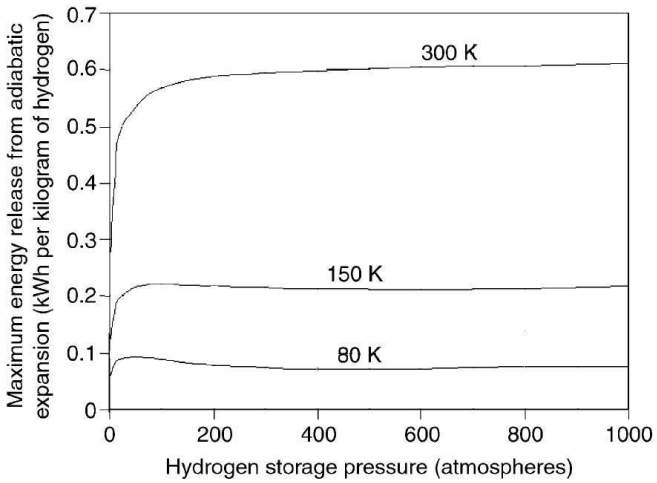


Figure 46: Mechanical energy variation with hydrogen storage pressures and temperatures (adapted from [136])

rupture. Figure 46 shows a comparison of maximum mechanical energy exerted by hydrogen gas during instantaneous adiabatic expansion for different hydrogen storage pressures and temperatures. Typical compressed hydrogen gas tanks (which usually store hydrogen at about 20 MPa and standard state temperature) possess mechanical energies of the order of 0.6 kWh/kg, while ambient pressure liquid hydrogen vessels (i.e. hydrogen at about 0.1 MPa, low temperatures about 20 K) can possess significantly lower mechanical energies (>0.1 kWh/kg). This translates to a theoretically less violent tank rupture due to rapid expansion [136]. It is also interesting to note that increasing hydrogen storage pressures to more than 20 MPa (at any temperature) does not significantly affect maximum mechanical energy when compared with the effect of temperature. Storing liquid hydrogen under pressure also allows higher hydrogen densities to be used. For example, liquid hydrogen stored at 24 MPa has a density of 86.5 kg/m$^3$ while liquid hydrogen stored under ambient pressure has a density of 70.6 kg/m$^3$ [136].

Cryogenic and metal hydride hydrogen storage will have to compete with compressed hydrogen storage, which is the most popular hydrogen storage medium. Compressed tanks are usually the default storage medium for the current hydrogen infrastructure, as storing hydrogen gas under pressure is considered the easiest and most straightforward method available. In addition to being a tried-and-tested technology, compressing hydrogen gas to pressure requires significantly lower energy input levels compared with cryogenic hydrogen liquification, where only 10% of hydrogen's lower heating value is needed for compression compared with 40% for

liquification [136, 137].

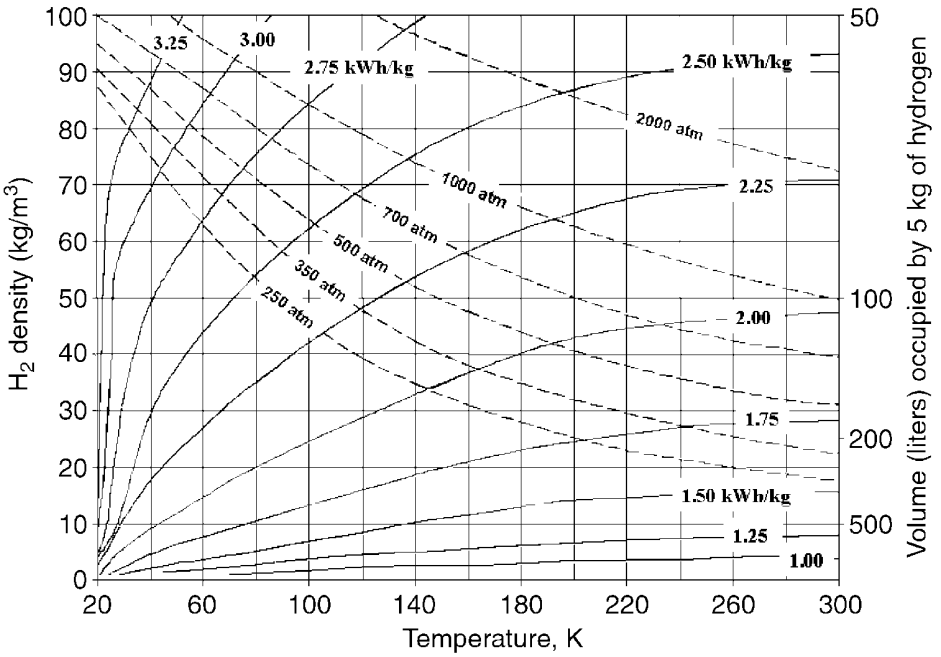


Figure 47: Energy input requirements (solid lines) as a function of hydrogen temperature and density. Also shown are pressure levels (dashed lines) corresponding to hydrogen density and temperature, in addition to the change in occupied volume of 5 kg of hydrogen [136]

Figure 47 shows the amount of energy input required per unit mass of hydrogen to achieve a certain hydrogen density at a particular pressure and temperature (with standard state conditions as the baseline, beginning at the bottom right corner of the plot). Also shown (on the right ordinate) is the change in occupying volume of 5 kg of hydrogen corresponding to temperature and pressure changes. As an example, cryogenic hydrogen has a density of about 70 kg/m$^3$. In order reach this density from standard state conditions and maintain about 300 K, around 2.25 kWh/kg of compression energy would be needed to compress gaseous hydrogen to about 200 MPa. If a density of 70 kg/m$^3$and a pressure of about 0.1 MPa (atmospheric pressure) is to be maintained, then a significantly large temperature drop (from 300 K down to about 20-30 K) that needs around 3.25 kWh/kg of energy is required (unfortunately pressures lower than 25 MPa are not shown). Therefore, compressing hydrogen gas to a similar density as liquid hydrogen requires comparatively less energy input. In addition, compressed gas tanks have no need for heating or cooling mechanisms as per metal hydrides. However, most compressed gas tanks are made of steel and store hydrogen under 20 MPa. As a result, these tanks are heavy relative to the mass of hydrogen they carry and have low energy densities relative to cryogenic liquid or metal hydride storage. There are lighter tanks made of composite

materials such as carbon-fiber that can store hydrogen gas under pressures of up to 70 MPa, which can give roughly half the volumetric density available with cryogenic storage [136]. Further research and development can result in gas tanks that store up 200 MPa, at which point the storage density would roughly equal liquid cryogenic storage [136].

Overall, liquified hydrogen is the only way to currently maintain a comparable energy density with that of typical hydrocarbon fuels. However, like LNG there are issues with overall system practicality and complexity. Metal hydrides are still in the experimental stage, and as a whole cannot compete with liquified or compressed hydrogen. Compressed gaseous hydrogen technology also needs to improve, as the current state-of-the-art provides unacceptable energy density levels compared with conventional fuels. More research and development in increasing the energy density of all the storage media discussed is required.

## 2.6 Research Methodology

From the literature review in the previous sections, it was found that hydrogen dual-fuel CI engine operation has not been investigated to the same depth as natural gas dual-fuel CI engine operation, with recent work fairly lacking in comparison. In addition, there is very limited literature on alternative pilot fuels for dual-fuel CI operation (for either natural gas or hydrogen). Furthermore, water addition to hydrogen dual-fuel CI engine combustion (in order to reduce $NO_x$ emissions) has not been assessed in the previous work. As a result, dual-fuel CI engine work with hydrogen gas ignited by various high-cetane number pilot fuel (neat and emulsified) was set as the primary investigation.

# 3 Experimental Apparatus Description and Data Analysis

## 3.1 Overview

This section details work done a single-cylinder CI engine, which was used to obtain all presented experimental data (performance and emissions) in the following section for both normal CI engine operation as well as dual-fuel CI engine operation. The fuels used during normal CI engine operation were diesel fuel, rapeseed methyl ester (RME), a 5% by volume water-in-RME emulsion and a 10% by volume water-in-RME emulsion. During dual-fuel operation, all the aforementioned liquid fuels were used as the high-cetane number pilot fuels while natural gas and hydrogen gas were used as the high-octane number gaseous fuels.

## 3.2 Single-Cylinder Engine Experimental Apparatus

The single-cylinder CI engine used was a 1.5 litre four-stroke Gardner 1L2 direct-injection engine, the specifications of which are shown in table 5. At TDC, the clearance volume consists primarily of the hemispherical piston bowl volume and a relatively small volume between the flat cylinder head (from the middle of which the injector protrudes) and the piston edges; giving a "Bowler" hat-shaped volume. Pictures of the cylinder head and piston head as well as a cut-away drawing (figure 118) can be seen in appendix B. Figure 48 illustrates the engine, hydraulic brake, fuel supply lines, various emission analysers and instrumentation.

For normal CI engine operation, diesel fuel was sourced from a header tank above the lab. Fuel from this tank flowed into a fuel measuring flask (comprising three 20 ml segments) and then into the Gardner engine fuel system. For all other liquid fuels used (neat RME, emulsions etc), an auxiliary fuel supply was used. Here the auxiliary tank was filled with the amount of fuel necessary for running the test, after which the fuel flowed into a separate fuel measuring flask (comprising three 50 ml segments) and then into the Gardner engine fuel system. There were two ball valves on the inlet of the Gardner fuel system which allowed switching between either fuel source. The RME batch used (S060616 in these tests) was provided by Shell Global Solutions. As for the emulsions, each water-in-RME emulsion was

Table 5: Gardner engine specifications

| | |
|---|---|
| Engine Model | Gardner 1L2 |
| No. of cylinders | 1 |
| Bore | 107.95 mm |
| Stroke | 152.40 mm |
| Swept volume | $1394.83 \times 10^{-6}\text{m}^3$ |
| Clearance volume | $115.15 \times 10^{-6}\text{m}^3$ |
| Compression ratio | 13.11:1 |
| Max. power | 11 kW @ 1500 r/min |
| Inlet valve opening | 10° BTDC |
| Inlet valve closing | 40° ABDC |
| Exhaust valve opening | 50° BBDC |
| Exhaust valve closing | 15° ATDC |
| Injection timing (16 MPa opening pressure) | 23-26° BTDC |
| Injection timing (23 MPa opening pressure) | 18-21° BTDC |
| Injector nozzle holes | 4 |
| Injector throat diameter | 220 $\mu$m |

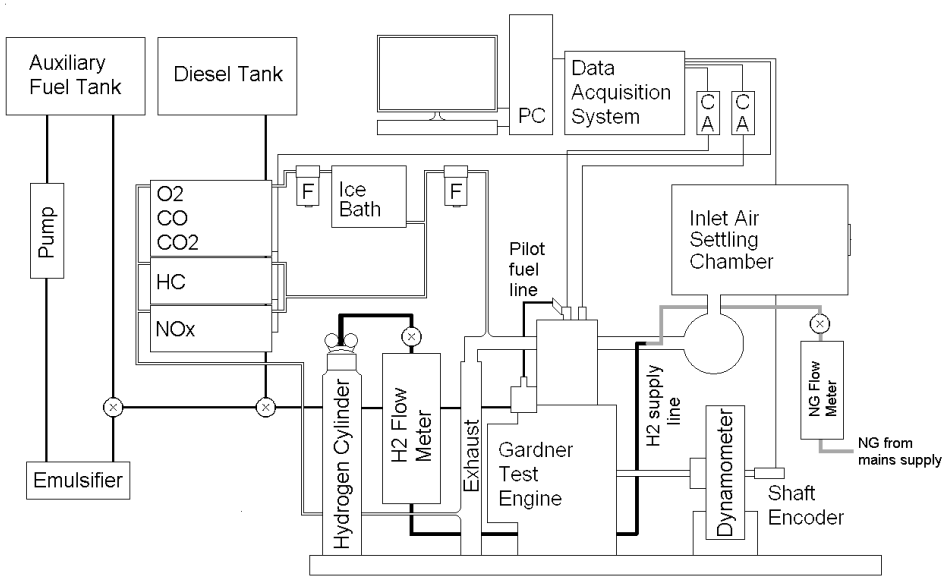


Figure 48: Layout of experimental apparatus

prepared separately in measuring tubes. For instance in the case of the 5% water-in-RME emulsion, 5% of a total fixed volume (2 litres) was distilled water and 95% was RME. The 10% water-in-RME emulsion was made using the same process, this time with 10% of the total volume being distilled water. The auxiliary fuel tank was

filled with the mixed emulsion and forced to run through a mechanical emulsifier (consisting of an electric motor driving a chopper blade inside a mixing chamber) and then back into the auxiliary tank via a closed circuit by means of a centrifugal pump for 20-30 minutes. When the emulsion was ready for injection the circuit was opened via a ball valve, supplying emulsion to the 50 ml measuring flask and the engine fuel system.

For dual-fuel CI engine operation with natural gas, natural gas was sourced directly from the building mains supply. From the mains supply, natural gas flowed through one solenoid valve, two ball valves and two diaphragm valves. Natural gas then flowed through a natural gas flow meter (0-100 litre/min scale) to be inducted into the engine inlet manifold via a stainless steel tube along with the incoming air under the engine's own suction. For dual-fuel CI engine operation with hydrogen gas, gaseous hydrogen with a purity of 99.995% was sourced from a 20 MPa compressed hydrogen gas cylinder supplied by the British Oxygen Company (BOC). A hydrogen pressure regulator with a flame arrestor fitted to the tank fed the hydrogen fuel line at 0.15 MPa (while the hydrogen feed pressure at the line outlet cannot drop more than 700 Pa below atmospheric pressure). The fuel line was connected to a hydrogen flow meter (0-44 litre/min scale). From the flow meter, hydrogen fed into the intake manifold of the engine (via a ball valve) under the engine's own suction via the same stainless steel tube as natural gas. This tube was orientated such that the outlet pointed into the incoming intake air stream (against the air flow) in order to enhance mixing between the fuel gas and the incoming air. All pilot fuels were injected directly into the cylinder through the standard engine fuel system. In an effort to reduce rough combustion during the hydrogen tests (which inherently has increased tendencies for abnormal combustion), an injector spring with a higher opening pressure than standard (23 MPa instead of 16 MPa) was used to ensure a fast open/ close operation of the injector (avoiding pilot fuel "dribbling" past the injector). Table 3 shows the chemical properties and characteristics of each neat fuel.

For all normal fuelling tests as well as the natural gas dual-fuel tests, the engine was run at 1000 r/min (intermediate engine speed) and 1500 r/min (maximum engine speed). For the hydrogen work, not enough hydrogen could be inducted at 1500 r/min (nor at 1250 r/min) to sustain engine operation across a suitably wide load range (a problem encountered to a lesser extent with natural gas dual-fuel operation). The maximum engine speed during dual-fuel tests with both gaseous

fuels was restricted by gaseous fuel starvation. This occurred because, for a fixed gaseous fuel mass flow rate, less gaseous fuel would be inducted during each cycle the higher the engine speed. While the hydrogen fuel flow rate was maximised in an attempt to compensate, the maximum rated flow rate of the flow meter was not sufficient to reach the desired engine operating point. With regards to the natural gas supply, further increases in flow rate could not be obtained as the mains supply pressure was insufficient. Adjusting the hydrogen gas cylinder supply pressure also could not compensate for this gaseous fuel starvation, as a pressure drop across the flow meter control valve drops the pressure almost instantaneously to the intake manifold pressure. As a result, the hydrogen dual-fuel tests were run at 750 r/min and 1000 r/min to provide adequate comparisons at 2 speeds.

For normal CI engine operation at each speed, the load placed on the engine started at 0.126 MPa brake mean effective pressure (BMEP) and went up to 0.63 MPa BMEP in 0.126 MPa increments. One set of readings was taken for each steady load. During natural gas dual-fuel operation at 1000 r/min, the amount of pilot fuel injected was fixed at a setting meant for 0.126 MPa BMEP during normal engine operation. The engine load was then increased further by adjusting the flow rate of natural gas inducted by the engine. As a result of gaseous fuel starvation at 1500 r/min, the maximum BMEP that could be reached (with the pilot fuel amount fixed at 0.126 MPa BMEP) was about 0.3 MPa BMEP during natural gas dual-fuel operation. During hydrogen dual-fuel operation, the amount of pilot fuel injected was fixed at a flow rate setting meant for 0.378 MPa BMEP during normal engine operation. The pilot fuel was introduced at this intermediate load (instead of 0.126 MPa BMEP as per the natural-gas tests) as the engine was unable to induct enough hydrogen gas to provide approximately full power with a lower amount of pilot fuel. The engine load was then increased further by adjusting the flow rate of hydrogen inducted by the engine. The typical maximum load of 0.63 MPa BMEP was restricted to 0.6 MPa BMEP during hydrogen dual-fuel operation to maintain engine stability. This is because the engine would not stabilise long enough to record readings at 0.63 MPa BMEP. Tables 6 and 7 show the pilot fuel enthalpy fractions for natural gas dual-fuel operation at 1000 r/min and 1500 r/min. Tables 8 and 9 show the pilot fuel enthalpy fractions for hydrogen dual-fuel operation at 750 r/min and 1000 r/min.

Exhaust gas was sampled from the Gardner exhaust manifold through steel and PTFE tubing via a heated filter (maintained at 190 degrees Celsius). A Signal

Table 6: Pilot fuel enthalpy fractions at 1000 r/min for selected loads during natural gas dual-fuel operation

| BMEP / MPa | RME | 10% emulsion | 5% emulsion |
|---|---|---|---|
| 0.126 | 1.00 | 1.00 | 1.00 |
| 0.378 | 0.44 | 0.36 | 0.36 |
| 0.630 | 0.38 | 0.33 | 0.31 |

Table 7: Pilot fuel enthalpy fractions at 1500 r/min for selected loads during natural gas dual-fuel operation

| BMEP / MPa | RME | 10% emulsion | 5% emulsion |
|---|---|---|---|
| 0.126 | 1.00 | 1.00 | 1.00 |
| 0.252 | 0.50 | 0.50 | 0.51 |
| ≈0.3 | 0.47 | 0.34 | 0.34 |

Table 8: Pilot fuel enthalpy fractions at 750 r/min for selected loads during hydrogen dual-fuel operation

| BMEP / MPa | RME | 10% emulsion | 5% emulsion |
|---|---|---|---|
| 0.378 | 1.00 | 1.00 | 1.00 |
| 0.504 | 0.76 | 0.75 | 0.75 |
| ≈0.6 | 0.67 | 0.64 | 0.63 |

Table 9: Pilot fuel enthalpy fractions at 1000 r/min for selected loads during hydrogen dual-fuel operation

| BMEP / MPa | RME | 10% emulsion | 5% emulsion |
|---|---|---|---|
| 0.378 | 1.00 | 1.00 | 1.00 |
| 0.504 | 0.77 | 0.75 | 0.74 |
| ≈0.6 | 0.64 | 0.62 | 0.65 |

4000VM chemiluminescence analyser was used to measure NO and $NO_x$ emissions, while unburnt HC emissions was measured by a Rotork Analysis model 523 flame ionisation detector (FID) (both analysers sampled wet exhaust gas via a heated line at 160 degrees Celsius). A Servomex 4210C exhaust gas analyser measured CO, $CO_2$ and oxygen ($O_2$) concentrations (all on a dry-volume basis) using non-dispersive infrared sensors and a paramagnetic sensor respectively. A water trap and silicon oxide moisture filter is used to remove moisture from the Servomex sample gas. Bosch smoke numbers were obtained via an optical Bosch smoke meter used together with Bosch smoke filter paper. The combustion chamber pressure data (detected with a Kistler type 6123 water-cooled transducer), exhaust temperatures (detected

using type-K thermocouples) and emission readings were sampled to a National Instruments data acquisition system (at 500 kS/s and 200 kS/s respectively) and fed into a computer running LabVIEW.

### 3.2.1 Experimental Data Analysis

A particularly important parameter is the rate of net energy conversion during combustion (commonly referred to as the net "heat-release" rate). When plotted against crank-angle, this parameter is useful in determining the point of ignition during CI engine combustion. This is because the ignition point is not fixed in CI engines as it depends on other factors such as air-fuel composition, chamber and charge conditions, compared with SI engines where the ignition point is practically the spark timing. These energy conversion rate plots are also used for estimating the chemical reaction or combustion rate and duration.

A single-zone model based on the principle of energy conservation for a closed system was used to calculate the net energy conversion rate from cylinder pressure data [36, 95]. The cylinder charge was treated as a single homogeneous fluid and assumed to have the same averaged properties throughout. No distinction was made in this respect between burnt zones, unburned zones or fuel zones, and charge flow into crevices such as between the piston and cylinder walls was excluded. As the initial reactants (fuel + air) were changing into combustion products during the chemical reaction, there was a change in composition as well as internal energy and temperature levels. This caused a temperature rise within the system and the combustion process was treated as a corresponding energy supply to a system of a non-changing composition. With these assumptions, the following equation was obtained:

$$Q_{\mathrm{to}} + W_{\mathrm{to}} = \Delta U \tag{6}$$

where $Q_{\mathrm{to}}$ is the "heat" transfer to the system, $W_{\mathrm{to}}$ is the work done to the system by the piston and $\Delta$U is the increase in internal energy of the system going from an initial state (prior to combustion) to a final state (after combustion). This internal energy increase can be further divided into fuel enthalpy (subscript f), internal energy of reactants (subscript r), and internal energy of products (subscript p), as shown below:

$$\Delta U = m_{\mathrm{p}} u_{\mathrm{p}} - m_{\mathrm{r}} u_{\mathrm{r}} - m_{\mathrm{f}} h_{\mathrm{f}} \tag{7}$$

A mass balance between the products and reactants gives $m_{\mathrm{p}} = m_{\mathrm{r}} + m_{\mathrm{f}}$ and is

substituted in equation 7 to give:

$$\Delta U = (m_{\mathrm{r}} + m_{\mathrm{f}})u_{\mathrm{p}} - m_{\mathrm{r}}u_{\mathrm{r}} - m_{\mathrm{f}}h_{\mathrm{f}} \tag{8}$$

which is rearranged and rewritten (from the definition of enthalpy $h = u + Pv$) to give:

$$\begin{aligned} \Delta U &= m_{\mathrm{r}}(u_{\mathrm{p}} - u_{\mathrm{r}}) + m_{\mathrm{f}}(u_{\mathrm{p}} - h_{\mathrm{f}}) \\ &= m_{\mathrm{r}}(u_{\mathrm{p}} - u_{\mathrm{r}}) + m_{\mathrm{f}}[(u_{\mathrm{p}} - u_{\mathrm{f}}) - (P_{\mathrm{f}}v_{\mathrm{f}})] \end{aligned} \tag{9}$$

The term $(u_{\mathrm{p}} - u_{\mathrm{f}})$ can be expanded to give:

$$(u_{\mathrm{p}} - u_{\mathrm{f}}) = (u_{\mathrm{p}} - u_{\mathrm{p}}^0) + (u_{\mathrm{p}}^0 - u_{\mathrm{f}}^0) + (u_{\mathrm{f}}^0 - u_{\mathrm{f}}) \tag{10}$$

where the terms with the superscript 0 are at standard-state reference conditions.

As a result, $(u_{\mathrm{p}}^0 - u_{\mathrm{f}}^0)$ is the specific internal energy of combustion of the fuel at standard state conditions. Previous work [95] has concluded that the magnitudes of $(u_{\mathrm{p}} - u_{\mathrm{p}}^0)$, $(u_{\mathrm{f}}^0 - u_{\mathrm{f}})$ and $P_{\mathrm{f}}v_{\mathrm{f}}$ are very small (only 1.15% of the specific internal energy of the fuel) and therefore negligible. The following equation is obtained when equation 10 is replaced into equation 9:

$$\Delta U = m_{\mathrm{r}}(u_{\mathrm{p}} - u_{\mathrm{r}}) + m_{\mathrm{f}}(u_{\mathrm{p}}^0 - u_{\mathrm{f}}^0) \tag{11}$$

This is substituted in equation 6 and rearranged to give:

$$-m_{\mathrm{f}}(u_{\mathrm{p}}^0 - u_{\mathrm{f}}^0) = -Q_{\mathrm{to}} - W_{\mathrm{to}} + m_{\mathrm{r}}(u_{\mathrm{p}} - u_{\mathrm{r}}) = E_{\mathrm{ch}} \tag{12}$$

where $E_{\mathrm{ch}}$ is the "gross" chemical energy resulting from the combustion process. By replacing $W_{\mathrm{to}}$ by its definition $-PdV$ (where $P$ is the instantaneous cylinder pressure and $dV$ is the change in cylinder volume) in equation 12 and rewriting the equation for small incremental changes, the following equation is obtained:

$$dE_{\mathrm{ch}} + dQ_{\mathrm{to}} = PdV + m_{\mathrm{r}}du \tag{13}$$

where $du = u_{\mathrm{p}} - u_{\mathrm{r}}$. Following this, $du$ is replaced by its definition $c_{\mathrm{v}}dT$ so that

$$dE_{\mathrm{ch}} + dQ_{\mathrm{to}} = PdV + m_{\mathrm{r}}c_{\mathrm{v}}dT \tag{14}$$

where $c_{\mathrm{v}}$ is the instantaneous isochoric specific heat capacity of the system and $dT$ is the temperature change. $dT$ can be written using the corresponding differential form of the ideal gas equation $PV = m_{\mathrm{r}}RT$ to give:

$$dE_{\mathrm{ch}} + dQ_{\mathrm{to}} = PdV + m_{\mathrm{r}}c_{\mathrm{v}}\left(\frac{VdP + PdV}{m_{\mathrm{r}}R}\right) \tag{15}$$

where $V$ is the instantaneous cylinder volume, $dP$ is the change in cylinder pressure and $R$ is the specific gas constant of the reactants. Finally, equation 15 can be rearranged to give:

$$dE_{\mathrm{n}} = dE_{\mathrm{ch}} + dQ_{\mathrm{to}} = \left(1 + \frac{c_{\mathrm{v}}}{R}\right) P(dV) + \left(\frac{c_{\mathrm{v}}}{R}\right) V(dP) \tag{16}$$

where $dE_{\mathrm{n}}$ is the net energy conversion during combustion (from reactants to products), which is the sum of $dE_{\mathrm{ch}}$ and $dQ_{\mathrm{to}}$. Dividing through by time increment $dt$ equation 16 becomes:

$$\frac{dE_{\mathrm{n}}}{dt} = \left(1 + \frac{c_{\mathrm{v}}}{R}\right) P\left(\frac{dV}{dt}\right) + \left(\frac{c_{\mathrm{v}}}{R}\right) V\left(\frac{dP}{dt}\right) \tag{17}$$

The term $dE_{\mathrm{n}}/dt$ shown in the above equation is the sum of the gross energy conversion rate during combustion and the "heat" transfer rate to the charge fluid (normally negative during the combustion period as "heat" transfer is from the charge fluid to the engine cooling water). This net energy conversion rate is dependant on the cylinder pressure change rate ($dP/dt$), cylinder volume change rate ($dV/dt$), instantaneous cylinder pressure ($P$), instantaneous cylinder volume ($V$), isochoric specific heat capacity of the cylinder charge ($c_{\mathrm{v}}$) and the specific gas constant of the cylinder charge ($R$). The latter two terms usually correspond to dry air during normal CI engine operation, while the intake manifold-inducted gaseous fuels are taken into account (via mass fractions of the total inducted charge) during dual-fuel CI engine operation.

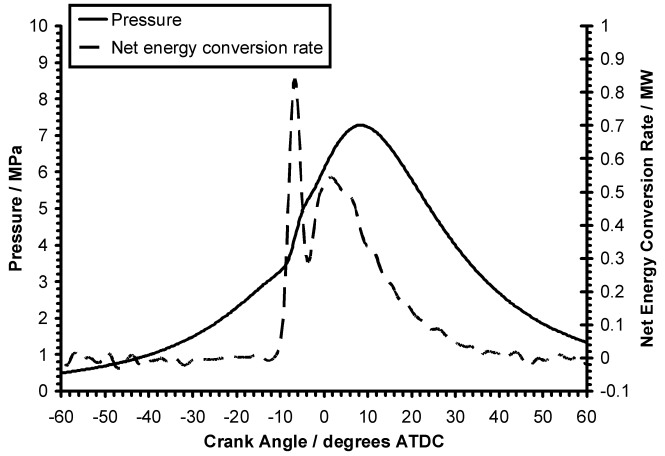


Figure 49: Cylinder pressure and net energy conversion rate during combustion ("heat-release" rate) comparison for normal engine operation with diesel fuel at 1000 r/min and 0.63 MPa BMEP

An example of the net energy conversion rate for normal CI engine operation is shown in figure 49 [57]. The ignition point is identified to be the crank angle at which the

plots in the figure suddenly rises above the datum. Ignition delay is defined as the time period between the start-of-injection and the ignition point [35]. Figure 50 shows a comparison of cylinder pressure as well as first and second cylinder pressure derivatives plotted against crank angle at the same engine condition as figure 49 [57]. An inflection in the cylinder pressure trace shows a sudden increase in the pressure-rise rate which indicates the start-of-combustion (ignition). The point where both pressure derivative curves suddenly changes and rises into a steep slope also indicates ignition. This point (in terms of crank angle) is exactly the same as the point where the energy conversion rate plot also suddenly rises above the datum. As all three plots have the same inflection points indicating ignition, most of the ignition delay values in this work were obtained via a first pressure derivative analysis.

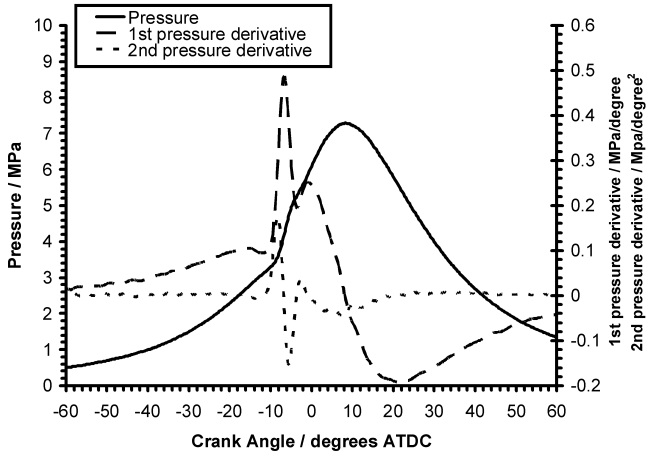


Figure 50: Cylinder pressure, first and second derivative comparison for normal engine operation with diesel fuel at 1000 r/min and 0.63 MPa BMEP

Emissions data are shown in specific terms, i.e. mass of gas species per unit energy produced by the engine. The actual mole fractions of the different gas species in the exhaust gas were worked out from the dry/ wet gas concentrations, after which the mass flow rate of each gas species was calculated, then divided by the engine power output. The details of this calculation is in appendix C. All emissions data are plotted against equivalence ratio as the amount of exhaust gas species produced during combustion are a function of equivalence ratio. Other engine parameters such as power output, efficiency etc were calculated using the standard equations detailed in appendix C (where a sample calculation is made) and are plotted against engine load (BMEP). Shown on the various performance and emission result plots are error bars, which show the widest variation in the calculated parameters that can result from the combined instrument sensitivities (details of calculations shown in appendix D). Repeatability assessments which illustrate the quality of data recorded

during the various modes are in appendix E. Equations 18 and 19 show the general chemical equations for the different test cases.

Complete natural gas combustion in excess air, ignited by an emulsified oxygenated hydrocarbon is illustrated by the following equation:

$$\begin{aligned}(C_xH_yO_z + \gamma H_2O) + \alpha CH_4 + \beta(x + 0.25y - 0.5z + 2\alpha)(O_2 + 3.76N_2) \rightarrow \\ \rightarrow (x+\alpha)CO_2 + (\gamma + 0.5y + 2\alpha)H_2O + \beta(x + 0.25y - 0.5z + 2\alpha)3.76N_2 + \\ +(x + 0.25y - 0.5z + 2\alpha)(\beta - 1)O_2 \quad (18)\end{aligned}$$

Complete hydrogen combustion in excess air, ignited by an emulsified oxygenated hydrocarbon is illustrated by the following equation:

$$\begin{aligned}(C_xH_yO_z + \gamma H_2O) + \alpha H_2 + \beta(x + 0.25y - 0.5z + 0.5\alpha)(O_2 + 3.76N_2) \rightarrow \\ \rightarrow xCO_2 + (\gamma + 0.5y + \alpha)H_2O + \beta(x + 0.25y - 0.5z + 0.5\alpha)3.76N_2 + \\ +(x + 0.25y - 0.5z + 0.5\alpha)(\beta - 1)O_2 \quad (19)\end{aligned}$$

As the amount of gaseous fuel was varied with regards to a fixed amount of pilot fuel, the $\alpha$ term was introduced. In addition, as CI engines generally run fuel-lean, the $\beta$ term was introduced in order to account for the excess air that will be present in the exhaust products. As a result, $\beta$ is generally always larger than unity. $\gamma$ is the mole fraction of water present in the emulsion. For the emulsified pilot fuel tests, only the effective fuel mass (i.e. with the water component subtracted from recorded emulsified pilot fuel mass flow rates) was taken into account when calculating pilot fuel enthalpy fractions, thermal efficiency, specific fuel consumption and fuel-air equivalence ratio. This is because water is not a fuel, and cannot be included in fuel parameters. For stoichiometric combustion of a neat fuel during normal CI engine operation, the $\alpha$ and $\gamma$ terms go to zero while $\beta$ becomes unity.

# 4 Experimental Results and Discussion

## 4.1 Conventional Engine Operation

The following section presents data for 4 different high-cetane number fuels during normal CI engine operation at 1000 r/min and 1500 r/min using the single-cylinder engine. These two speeds were selected as 1500 r/min is the maximum speed of the engine while 1000 r/min represents an appropriate intermediate speed (as idle speed is about 500 r/min). Conventional diesel fuel is tested to establish a baseline comparison for the other tested fuels, while the term "neat" indicates (throughout the document) that no water is mixed in with the fuel.

### 4.1.1 Ignition Behavior

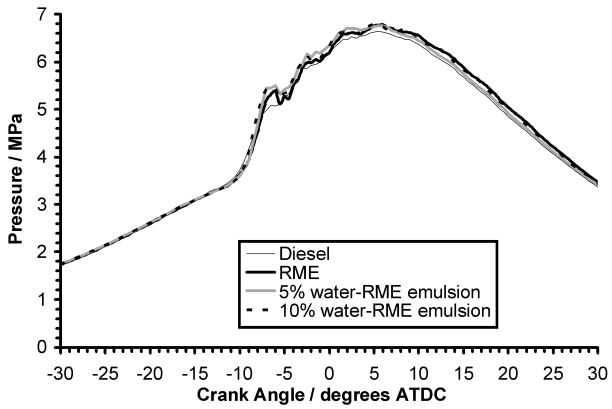


Figure 51: Cylinder pressure comparison for normal engine operation with neat diesel fuel, neat RME and two water-in-RME emulsions at 1000 r/min and 0.63 MPa BMEP

Figures 51 and 52 show combustion chamber pressure plotted against crank angle at 1000 r/min and 1500 r/min respectively. At 1000 r/min, there is minimal difference in the ignition delay between the neat fuels and both emulsions (less than 2% variation). Here all tested fuels give an overall common ignition delay (2.1 ms). It appears that neither the cooling affect of water vapourisation nor the higher fuel-air mixing rates (resulting from "microexplosions" as defined in the literature) have a significant affect on ignition delay or peak combustion pressure values during normal CI engine operation at this speed.

At 1500 r/min, it is noted that neat RME has the shortest ignition delay (1.5 ms)

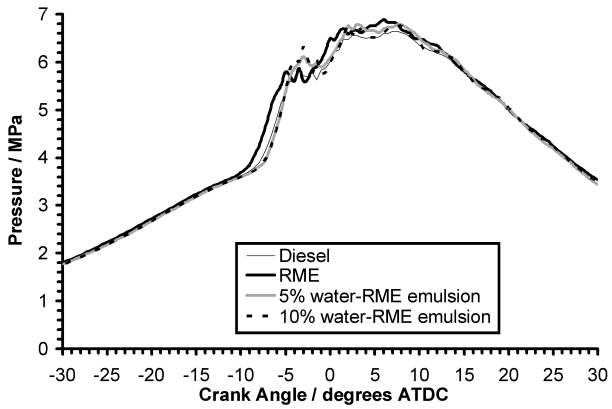


Figure 52: Cylinder pressure comparison for normal engine operation with neat diesel fuel, neat RME and two water-in-RME emulsions at 1500 r/min and 0.63 MPa BMEP

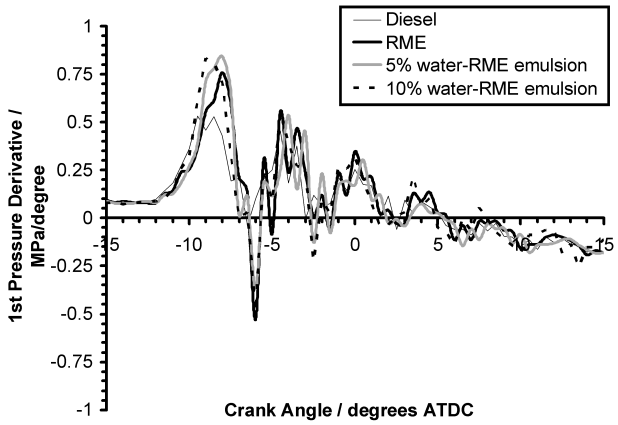


Figure 53: First pressure derivative comparison for normal engine operation with neat diesel fuel, neat RME and two water-in-RME emulsions at 1000 r/min and 0.63 MPa BMEP

compared with neat diesel fuel (1.6 ms). This is likely a result of cycle-to-cycle variations (see repeatability tests in appendix E) instead of the marginally higher cetane number of RME. Both emulsions had a common ignition delay with each other (1.7 ms), which is slightly longer compared with the neat fuels. An extension of 0.2 ms is fairly minor considering cycle-to-cycle variations constitute 50% of the extension, suggesting that any charge cooling as a result of water vapourisation is negligible. In addition, increasing the water concentration (from 5% to 10% by volume) in the emulsion does not affect ignition delay significantly, if at all. As a result, peak pressure levels are generally maintained between all tested fuels with a maximum difference of only about 0.2 MPa (which can result from cycle-to-cycle variations).

These trends are further illustrated in first pressure derivative plots (shown in fig-

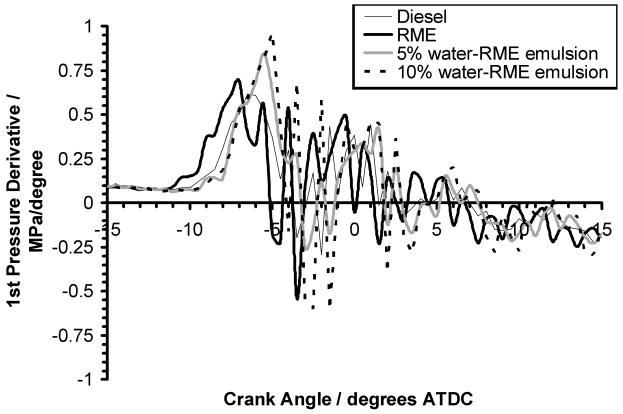


Figure 54: First pressure derivative comparison for normal engine operation with neat diesel fuel, neat RME and two water-in-RME emulsions at 1500 r/min and 0.63 MPa BMEP

ures 53 and 54). The emulsions produce marginally higher pressure-rise rates compared with the neat fuels at 1500 r/min, while common trends are observed at 1000 r/min. The higher pressure-rise rates of the emulsified fuels at this speed probably result from the extended ignition delays instead of the "microexplosion" phenomenon (which was expected to provide higher levels of fuel-air mixing).

### 4.1.2 Performance

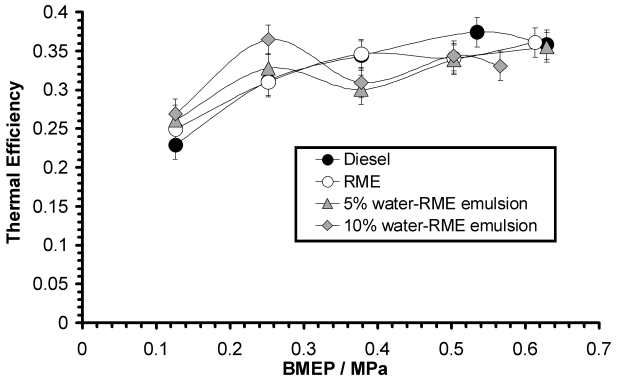


Figure 55: Thermal efficiency comparison for normal engine operation with neat diesel fuel, neat RME and two water-in-RME emulsions at 1000 r/min

Figure 55 and figure 56 show a thermal efficiency comparison with BMEP at 1000 r/min and 1500 r/min respectively. At both speeds, there is minimal difference between diesel fuel and RME. This follows from both fuels having similar physical and chemical properties, resulting in similar levels of combustion quality. Throughout this document where emulsified fuels are concerned, thermal efficiency is calculated

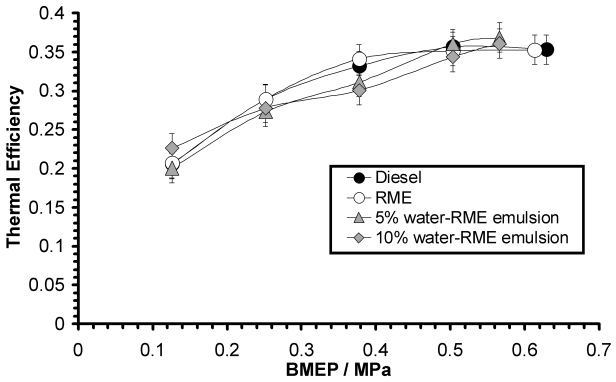


Figure 56: Thermal efficiency comparison for normal engine operation with neat diesel fuel, neat RME and two water-in-RME emulsions at 1500 r/min

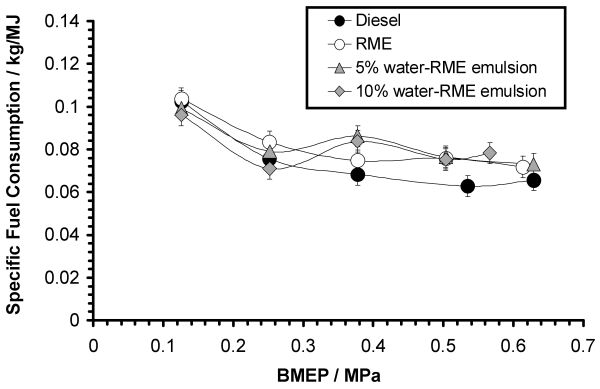


Figure 57: Specific fuel consumption comparison for normal engine operation with neat diesel fuel, neat RME and two water-in-RME emulsions at 1000 r/min

with the water component excluded. At 1000 r/min, the emulsified fuels produce slightly higher efficiencies compared with the neat fuels at lower loads (just beyond the reach of the error bars). The plotted error bars show the maximum possible variation resulting from the combined accuracies of the measuring instruments used (see appendix D). This may reflect the positive effect of "microexplosions" giving a more homogeneous fuel mixture. However, as their influence on combustion progress was not apparent in the pressure data at these conditions this effect appears to be minor. Thermal efficiency levels drop in comparison with the neat fuels at a BMEP value of about 0.378 MPa. At 1500 r/min, both emulsions generally follow the neat fuels throughout the load range, with a minor drop at 0.378 MPa BMEP.

Figure 57 shows that at 1000 r/min that neat RME has higher specific fuel consumption (SFC) when compared with diesel fuel. This is because of its comparatively

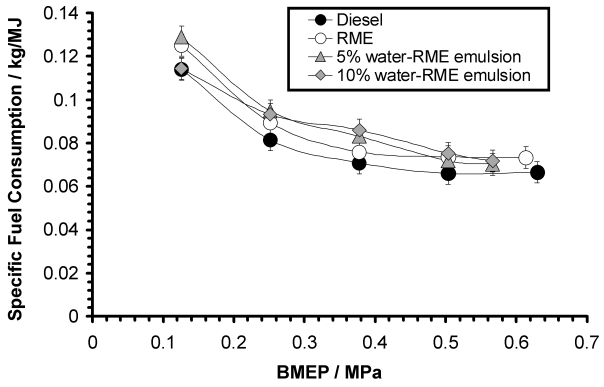


Figure 58: Specific fuel consumption comparison for normal engine operation with neat diesel fuel, neat RME and two water-in-RME emulsions at 1500 r/min

smaller lower heating value. Like thermal efficiency, SFC is calculated with the water component excluded. The emulsions, while fairly similar when compared with each other, have a slightly higher specific fuel consumption than the neat fuels at a BMEP value of 0.378 MPa. Before and after this particular load setting SFC levels are at comparable levels with the neat fuels (considering the error bars). At 1500 r/min, both emulsions have a generally similar trend as 1000 r/min (as noted in figure 58), where at 0.378 MPa BMEP where the emulsions again have a marginally higher SFC than either neat diesel fuel or neat RME. It is unclear why this increase occurs at this particular load for both emulsions. Peak pressure values and ignition delay times are comparable between all tested fuels at this particular load for 1000 r/min. As a result there are no combustion anomalies (significantly lower combustion pressures or extended ignition delays for example) which can cause this sudden SFC increase. As a result, it is likely that these particular data points are anomalous as they are only just beyond the error bar range and would be eliminated if repeat tests were conducted.

### 4.1.3 Emissions

Figures 59 and 60 show the specific emission of nitric oxide (NO) plotted against fuel/air equivalence ratio at 1000 r/min and 1500 r/min respectively. Nitrogen oxides ($NO_x$) were not measured since the analyser had been set to detect NO during calibration. As NO is the main constituent of $NO_x$ [35], the emission trends of both gas species are expected to correlate. At 1000 r/min, it would appear that RME produces higher levels of specific NO compared with diesel fuel throughout the

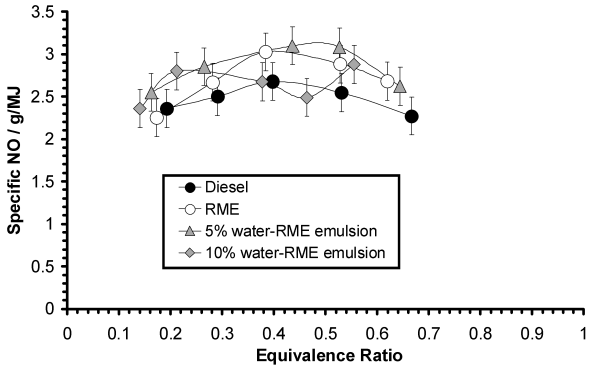


Figure 59: Specific NO comparison for normal engine operation with neat diesel fuel, neat RME and two water-in-RME emulsions at 1000 r/min

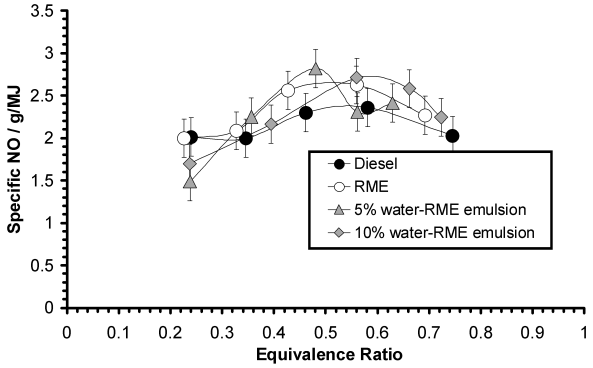


Figure 60: Specific NO comparison for normal engine operation with neat diesel fuel, neat RME and two water-in-RME emulsions at 1500 r/min

load range. Injection timing advances commonly reported as the cause of increased $NO_x$ with biodiesels is not the case here, as all tested fuels produced very similar timings. However, as the differences are within the respective error bars this increase is negligible. Generally both emulsions produce comparable specific NO levels as neat RME at 1000 r/min; with the exception of the 10% emulsion at an equivalence ratio of about 0.45. This dip was initially thought to be a result of charge cooling. However, this is unlikely as it is the only instance where NO reduction occurs. It is also unlikely that this NO reduction results from the slightly reduced thermal efficiency noted at intermediate loads, as no such reduction occurs with the 5% emulsion. At 1500 r/min (seen in figure 60), the trends of diesel fuel and neat RME noted at 1000 r/min are more or less repeated. While the emulsions do not reduce NO levels significantly compared with neat RME, there is a curious drop in NO levels with the 5% emulsion at an equivalence ratio of about 0.55. These

apparently random drops in NO levels are unlikely to be a result of analyser issues, considering zero and span calibration was carried out before each test run. It is suspected, though unconfirmed, that the emulsions are separating slightly in the fuel line (considering separation begins as soon as the emulsion leaves the emulsifying circuit); allowing slightly more water to be injected at different times. This can result in anomalous trends in charge temperature and therefore $NO_x$ formation rates. Fortunately it does not appear to affect the overall trend beyond the error bar range.

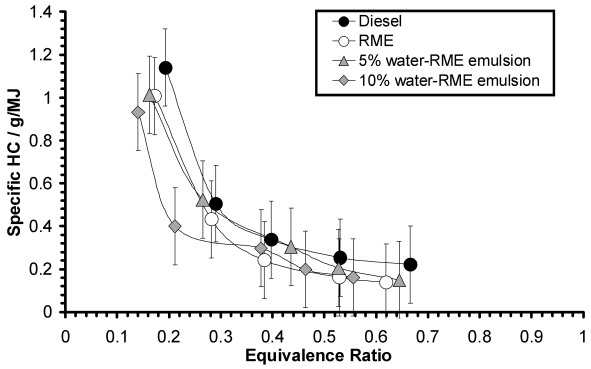


Figure 61: Specific HC comparison for normal engine operation with neat diesel fuel, neat RME and two water-in-RME emulsions at 1000 r/min

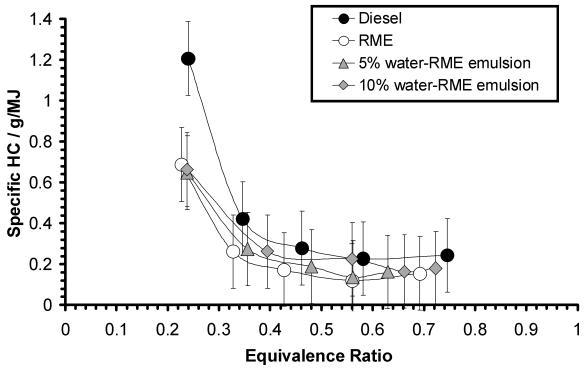


Figure 62: Specific HC comparison for normal engine operation with neat diesel fuel, neat RME and two water-in-RME emulsions at 1500 r/min

Figures 61 and 62 show specific unburnt hydrocarbons (HC) plotted against equivalence ratio at 1000 r/min and 1500 r/min. At 1000 r/min, both emulsified and neat RME fuels produce very similar levels of HC, all of which are slightly lower than diesel fuel. These trends are also present at 1500 r/min. It is noteworthy that the recorded HC emissions levels are very low (as a result of the lean operating nature of CI engines in general, hence the wide error bars) and the trends shown could be

significantly influenced by the instrument sensitivity.

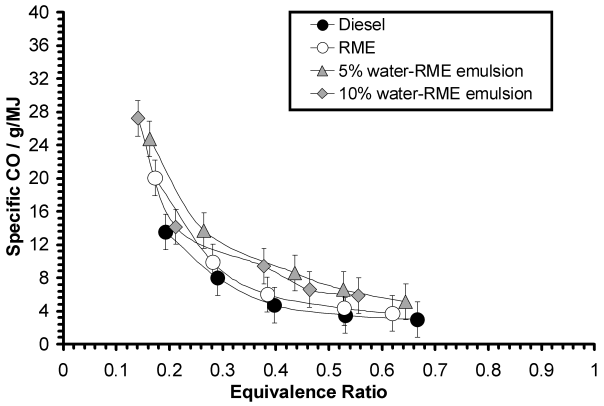


Figure 63: Specific CO comparison for normal engine operation with neat diesel fuel, neat RME and two water-in-RME emulsions at 1000 r/min

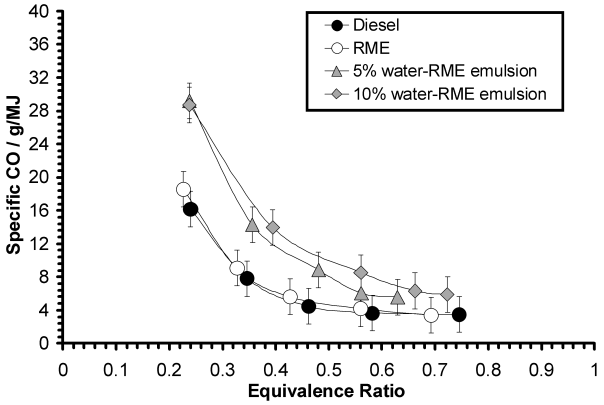


Figure 64: Specific CO comparison for normal engine operation with neat diesel fuel, neat RME and two water-in-RME emulsions at 1500 r/min

Figures 63 and 64 show specific carbon monoxide (CO) plotted against equivalence ratio at 1000 r/min and 1500 r/min. At both speeds, both neat RME and diesel fuel produce very similar trends. Both emulsions produce similar trends compared with each other, while being comparatively higher than the neat fuels throughout the load range. This increase in CO emissions has not been reported in the literature, and it is uncertain what can cause it in these cases. CO levels are inherently low in typical CI engines, as a result of their lean operation. Increased CO emissions can indicate dissociation of $CO_2$ or more importantly incomplete combustion. However, the maintained HC levels (and $CO_2$ levels, shown next) as well as thermal efficiencies do not support this. At present they are believed to be within the noise of repeatability compared with the order of magnitude higher $CO_2$ levels.

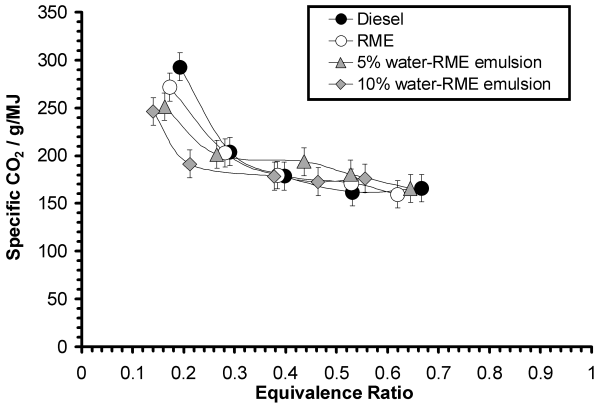


Figure 65: Specific $CO_2$ comparison for normal engine operation with neat diesel fuel, neat RME and two water-in-RME emulsions at 1000 r/min

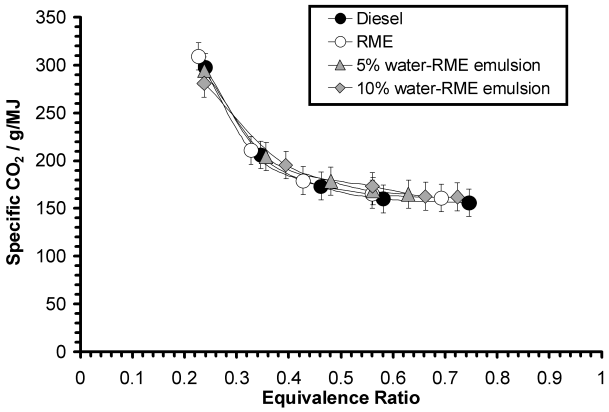


Figure 66: Specific $CO_2$ comparison for normal engine operation with neat diesel fuel, neat RME and two water-in-RME emulsions at 1500 r/min

Figures 65 and 66 show specific carbon dioxide ($CO_2$) plotted against equivalence ratio at 1000 r/min and 1500 r/min. At 1000 r/min, diesel fuel and neat RME produce very similar trends. This is due to a similar amount of carbon being injected, producing similar amounts of $CO_2$ products. While there are more carbon atoms in the neat RME molecule compared with diesel fuel, diesel fuel has a higher carbon fraction relative to total molecular mass. Combined with the higher specific fuel consumption when running on neat RME, both fuels produce similar trends. Both emulsions produce generally similar trends to the neat fuels. At 1500 r/min, similar trends between the tested fuels are seen.

Figures 67 and 68 shows a Bosch smoke number comparison at different equivalence ratios at 1000 r/min and 1500 r/min. At 1000 r/min the emulsions produce higher smoke levels compared with the neat fuels only at high loads. Initial assessments

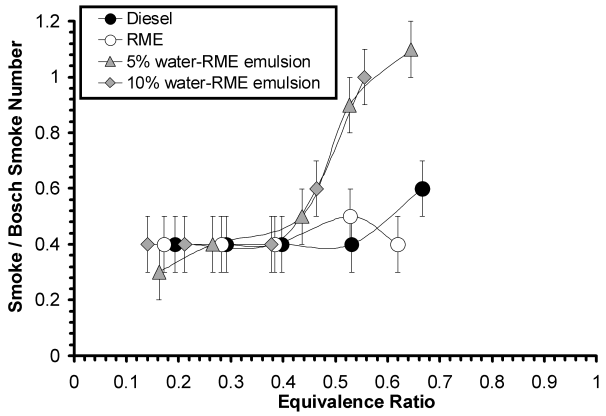


Figure 67: Bosch smoke number comparison for normal engine operation with neat diesel fuel, neat RME and two water-in-RME emulsions at 1000 r/min

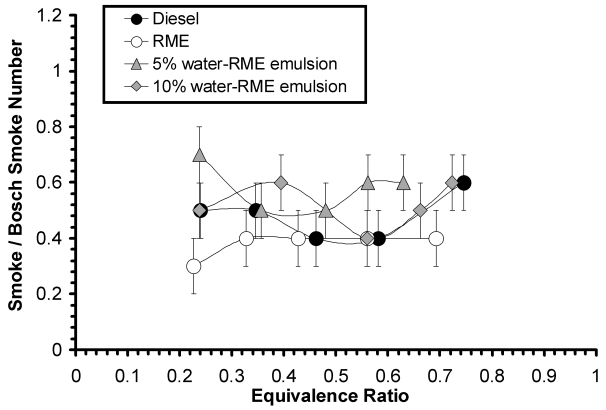


Figure 68: Bosch smoke number comparison for normal engine operation with neat diesel fuel, neat RME and two water-in-RME emulsions at 1500 r/min

suggested that this results from comparatively lower combustion temperatures (following from the cooling effect of water vapourisation) and incomplete combustion which prevents soot formed in fuel-rich regions from being fully oxidised. However, this does not occur at 1500 r/min where both emulsions consistently produce comparable smoke levels as the neat fuels. Smoke increases of this magnitude would normally coincide with changes in other emission/ performance trends (such as lower $NO_x$ emissions) but none were encountered. As a result this trend is suspect and could also be an artifact of the Bosch smoke filter technique. It would be interesting to measure the particulate emission on a mass basis since it could be that "microexplosions" produce more smaller particles but with less mass. It is notable that unlike with non-transesterified vegetable oil [96,97], where emulsification significantly reduced particulate formation, there is no such effect with emulsified RME. This possibly follows from RME's comparable viscosity to diesel fuel, which reduces

the intensity and frequency of "microexplosions".

Overall, neat RME produces generally similar results when compared with diesel fuel with the exception of slightly higher SFC levels. The higher SFC levels is a result of the comparatively smaller lower heating value of RME. Comparable $NO_x$ emissions are also obtained. Both water-in-RME emulsions affect $NO_x$ emissions only slightly, which suggests the cooling effect of water vapourisation (initially estimated to reduce $NO_x$ by a substantial margin) is negligible considering experimental repeatability. Both emulsions also increase SFC levels compared with the neat fuels at only one operating condition (0.378 MPa BMEP, for reasons that are as yet unexplained) while levels remain comparable at other conditions. This same trend applies to thermal efficiency. Smoke levels are generally comparable compared with the neat fuels. Significant smoke reductions recorded with emulsified non-transesterified vegetable oil [96, 97] does not seem to occur with fuels with comparable viscosities to typical diesel fuel.

## 4.2 Dual-Fuel Engine Operation with Natural Gas

The previous section shows normal CI engine operation with 4 fuels at 1000 r/min and 1500 r/min using the single-cylinder engine. Prior to the current work, extensive dual-fuel engine tests on the same engine with natural gas were conducted by Prof. Bob-Manuel and Dr. John Olsen, with 3 different fuels used for pilot ignition. The fuels used were neat diesel fuel, neat RME and dimethyl ether (DME, not discussed in the present work). It was established in this previous dual-fuel work in addition to the previous section that RME (as an alternative for diesel fuel) performs well in terms of performance and emissions as fuel for both normal CI engine operation as well as dual-fuel operation. As a result, neat RME is set as the baseline pilot fuel for all following dual-fuel mode discussion. The pilot fuel selection mentioned earlier is further expanded in the current work to include the two water-in-RME emulsions (5% and 10% water substitution by volume) as pilot fuels during natural gas dual-fuel operation. Emulsified pilot fuels during natural gas dual-fuel operation has not been presented in the literature at the time of writing, though there have been tests with liquified petroleum gas (LPG) [146]. Emulsified pilot fuels are investigated in the current work in an attempt to reduce $NO_x$ emissions (via charge cooling) in addition to increasing thermal efficiency at low and intermediate loads (thereby reducing high recorded levels of unburnt hydrocarbon and CO) via the effect of "microexplosions" as defined in the literature.

### 4.2.1 Ignition Behaviour

Figure 69 shows pressure crank angle data for all tested pilot fuels at 1000 r/min and 0.63 MPa BMEP. The neat RME pilot dual-fuel case has a significantly higher peak pressure value compared with normal CI engine operation with neat RME (by about 2.3 MPa). This is due to the high pressure-rise rates after pilot fuel combustion, as a result of premixed natural gas combustion (which is faster than normal CI diffusion combustion) as seen in figure 70.

Extended ignition delays compared with the neat pilot fuel were recorded with the emulsified pilot fuels. The neat RME pilot fuel case has the shortest ignition delay (1.9 ms), followed by normal CI engine operation with neat RME (2.0 ms). This is a minor difference, and could be attributed to cycle-to-cycle variations (see appendix E) rather than possible influence of natural gas on charge mixture properties.

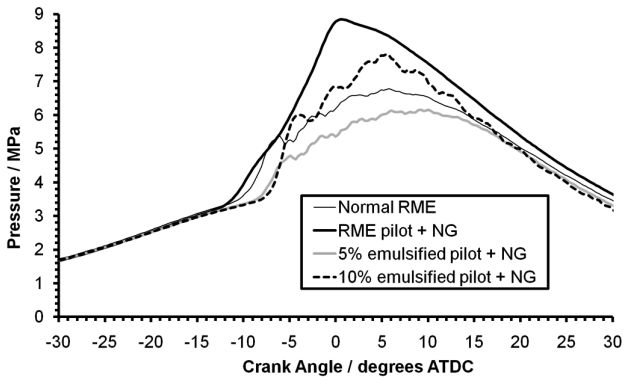


Figure 69: Pressure comparison between natural gas dual-fuelling with neat RME and emulsified RME pilots, and normal CI engine operation with neat RME at 1000 r/min and 0.63 MPa BMEP

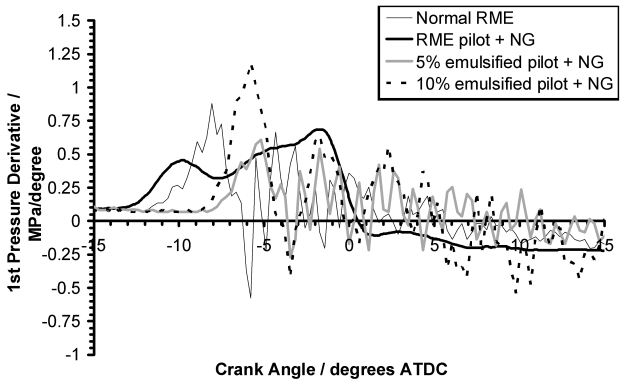


Figure 70: First pressure derivative comparison between natural gas dual-fuelling with neat RME and emulsified RME pilots, and normal CI engine operation with neat RME at 1000 r/min and 0.63 MPa BMEP

The 5% emulsified pilot fuel has an ignition delay of about 2.5 ms, while the 10% emulsified pilot fuel has an ignition delay of about 2.6 ms. The emulsification of RME lengthens pilot fuel ignition delay significantly (considering engine load levels and natural gas energy levels are comparable for all pilot fuels at this speed), which could be a result of the cooling affect of water vapourisation on charge conditions. This increase is significantly longer than that recorded during normal CI engine operation with emulsified fuels (as seen in the previous section). Significantly delayed ignition could explain the lower peak pressure levels seen with the emulsified pilot fuel cases compared with the neat pilot fuel. The higher peak pressure of the 10% emulsified pilot fuel case compared with the 5% emulsified pilot fuel case can also be caused by significantly higher pressure-rise rates during the pilot fuel combustion phase (as noted in figure 70). An extended ignition delay can result in higher

pressure-rise rates, which is the case of the emulsified pilot fuels compared with the neat pilot fuel. However, when the two emulsified fuel cases are compared the increases in peak pressure-rise rates between them are larger than what would be expected (from cycle-to-cycle variations). As the 10% emulsified pilot fuel case has an ignition delay extension of only 0.1 ms compared with the 5% emulsion (a minor extension which would not result in such an increase in pressure-rise rates), it is speculated that the high pressure-rise rates may be attributed to the "microexplosion" phenomenon occurring on a larger scale with the higher water concentration, resulting in a better distribution of fuel across the combustion chamber. This would allow more potential ignition points to form, accelerating combustion. In addition, the 5% emulsion does not have as much water suspended in the atomised droplets of emulsion, which may restrict the number and intensity of "microexplosions". As a result, the intuitive suggestion that higher water concentrations in an emulsion means a higher cooling effect does not apply in this case.

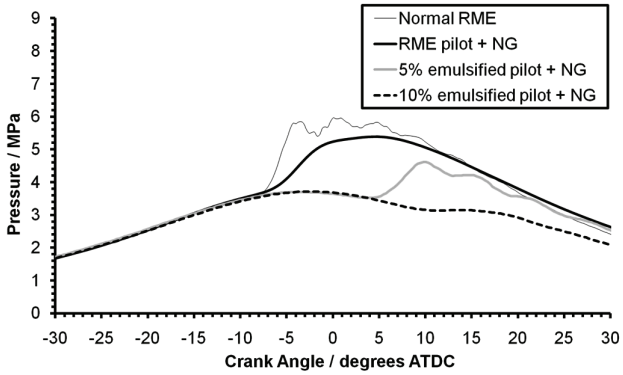


Figure 71: Pressure comparison between natural gas dual-fuelling with neat RME and emulsified RME pilots, and normal CI engine operation with neat RME at 1500 r/min and 0.3 MPa BMEP

Figure 71 shows pressure crank angle data for all pilot fuels at 1500 r/min and 0.3 MPa BMEP. Data at higher BMEP levels was not recorded as the engine was unable to induct enough natural gas at the higher speed. As natural gas is inducted by the engine directly from mains supply (and not via a mixing device or injection system), a comparatively higher gaseous fuel flow rate is needed at higher speeds to maintain the same amount of gaseous fuel inducted into the cylinder per cycle as at lower speeds. As the maximum natural gas flow rate on the test rig is limited by the mains supply pressure, not enough gaseous fuel could be supplied to the engine to reach higher BMEP levels. From figure 71, normal CI engine operation with neat RME produces the highest peak pressure, followed by the neat RME pilot dual-fuel case

(which is about 0.4 MPa lower). This reduction is attributed to the lower amount of natural gas inducted during dual-fuel operation at the higher speed. Both the 5% and 10% emulsified pilot fuel cases produce peak pressures about 0.8 MPa and 1.7 MPa lower than the neat RME pilot fuel case respectively.

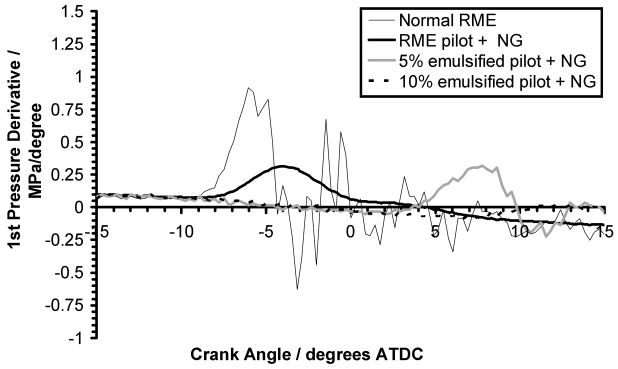


Figure 72: First pressure derivative comparison between natural gas dual-fuelling with neat RME and emulsified RME pilots, and normal CI engine operation with neat RME at 1500 r/min and 0.3 MPa BMEP

Figure 72 also reflects these trends in terms of pressure-rise rates. It is noted that combustion takes place significantly late (after TDC) for both emulsified pilot fuel cases. At this particular speed and load condition, normal CI engine operation with neat RME produces an ignition delay of about 1.7 ms, while natural gas dual-fuel operation with neat RME pilot fuel has an ignition delay of about 1.8 ms. The 5% emulsified pilot fuel case has an ignition delay of 3 ms and the 10% emulsified pilot fuel case has an ignition delay of about 3.5 ms. These significant extensions may result from the cooling effect (of water vapourisation) on the charge conditions. As the load achieved during dual-fuel operation in this case (0.252 MPa BMEP) is significantly lower than what is normally reached during normal operation (0.63 MPa BMEP), it is speculated that combustion temperatures may not have been high enough to generate "microexplosions", resulting in the larger water concentration of the 10% emulsion giving a larger cooling affect. This can cause a significant extension of ignition delay (and hence a larger drop in peak cylinder pressure) compared with the 5% emulsion, a relationship not observed at 1000 r/min. This raises the question of when do the effects of "microexplosions" (which help achieve more homogeneous mixtures resulting in higher thermal efficiencies) offset the cooling affect of water vapourisation, which extends ignition delay.

To illustrate this behavior at various load conditions during natural gas dual-fuel

combustion, the following figures are presented. Figures 73, 74 and 75 show pressure-crank angle diagrams obtained during low, intermediate and high engine loads for the neat RME pilot fuel and both emulsified pilot fuel cases at 1000 r/min.

The neat RME pilot fuel case has a clear shortening of ignition delay with increasing load, which is the expected behavior during both dual-fuel and normal CI engine operation. This trend is a result of progressively higher residual charge temperatures and pressures with increasing load. For the 5% emulsified pilot fuel case, there is a minor extension in ignition delay going from the low to intermediate load while there is a significant shortening of delay at the high load condition. For the 10% emulsified pilot case, the ignition delay is lengthened noticeably going from the low load to the intermediate load, only to shorten significantly at the high load condition. At low and intermediate loads (which are comparable for all pilot fuels at the different conditions), it is speculated that the cooling effect of water vapourisation alters the behavior noted with the neat RME pilot case by offsetting the increase in residual charge temperatures. In addition, at high load the "microexplosion" phenomenon appears to overcome this initial cooling affect. This shows that there might be a load/ mixture temperature threshold above which the "microexplosion" phenomenon would take place on a significant scale. Below this threshold, the emulsified pilot fuel does not disperse as widely as they would as a result of the violent break-up of the fuel droplet at the high load, resulting in deteriorated and slowed combustion. This temperature threshold can also explain the relatively maintained peak pressure values for the emulsified pilot fuels going from low to intermediate loads; while there is an increase in peak pressure for the neat pilot fuel case.

Considering normal fuelling operation with emulsified fuels, this temperature threshold is not apparent. The general similarity in ignition delay, peak pressure and pressure-rise rates at maximum BMEP levels for all tested fuels (noted in the previous section) is also present at intermediate and low BMEP levels. This could be a result of a ratio between total inducted fuel (gaseous fuel + pilot fuel) and water. During normal operation, increasing/ lowering the amount of injected liquid fuel increases/ lowers the engine speed and load. As a result, the proportion of water to total fuel is expected to remain the same throughout the engine operating range. This does not occur during dual-fuel operation as the injected liquid fuel (the pilot fuel) amount is fixed, while load control is obtained by controlled induction of natural gas. It is speculated that the behaviour of water droplets in the emulsion changes (compared with normal operation) when this water-to-total-fuel proportion is not

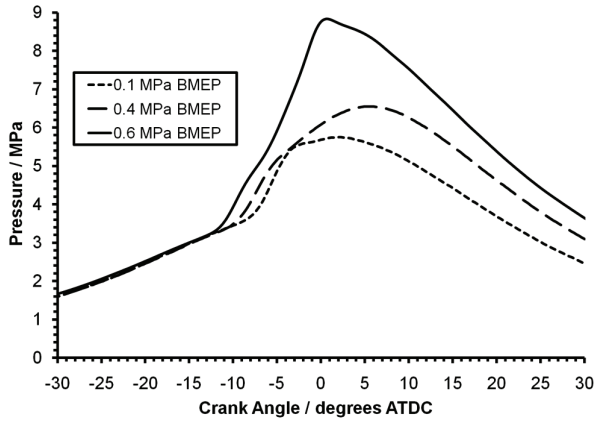


Figure 73: Pressure-crank angle diagram at 3 loads for neat RME pilot fuel at 1000 r/min during dual-fuel operation with natural gas

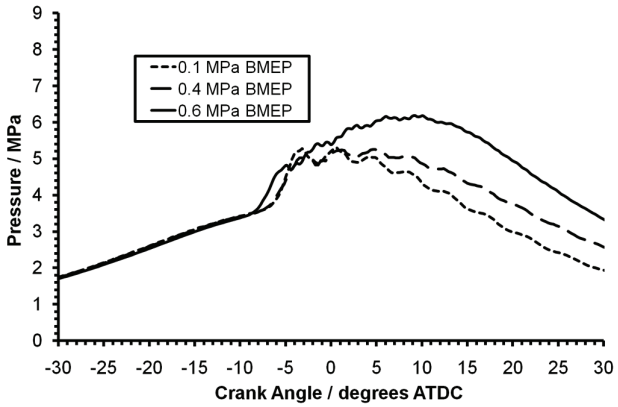


Figure 74: Pressure-crank angle diagram at 3 loads for 5% emulsified pilot fuel at 1000 r/min during dual-fuel operation with natural gas

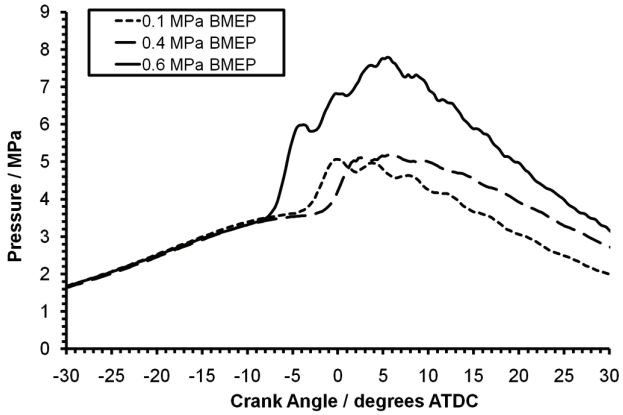


Figure 75: Pressure-crank angle diagram at 3 loads for 10% emulsified pilot fuel at 1000 r/min during dual-fuel operation with natural gas

held constant (it is reduced in the dual fuelling case by the addition of gaseous fuel).

It is not clear how this behaviour changes from the available data, however, optical assessment of dual-fuel combustion (possibly via pictures or high-speed video) with emulsified pilot fuel may shed some light on this issue.

### 4.2.2 Performance

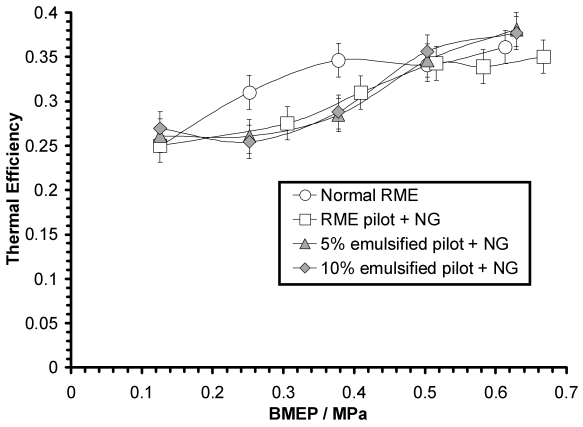


Figure 76: Thermal efficiency comparison between natural gas dual-fuelling with neat RME and emulsified pilots, and normal CI engine operation with neat RME at 1000 r/min

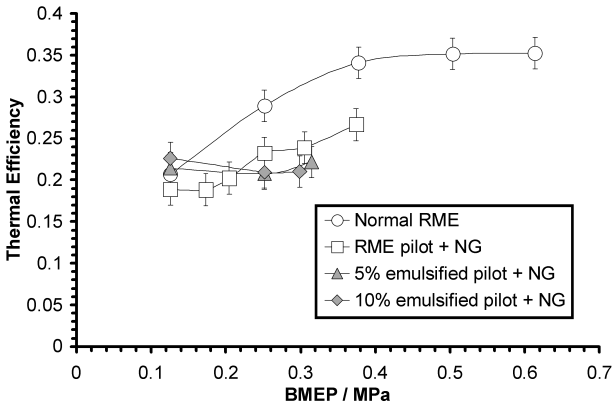


Figure 77: Thermal efficiency comparison between natural gas dual-fuelling with neat RME and emulsified pilots, and normal CI engine operation with neat RME at 1500 r/min

Figures 76 and 77 show a thermal efficiency comparison for normal CI engine operation with neat RME as well as natural gas dual-fuel operation with neat RME pilot fuel and both emulsified pilot fuels at 1000 r/min and 1500 r/min respectively. At 1000 r/min all the tested pilot fuels produce fairly similar magnitudes to each other, which are lower than normal CI engine operation at low and intermediate loads. This indicates incomplete combustion during natural gas dual-fuel operation at these conditions, possibly a result of the pilot fuel not igniting the natural gas-

air charge properly. This could follow from local regions of natural gas-air mixture being too lean to allow flame propagation throughout the charge (i.e. overleaning). At high loads however, thermal efficiency levels increase to match normal engine operation. At intermediate loads, the emulsified pilot fuels appear to produce slightly lower thermal efficiencies than the neat pilot fuel. However, this reduction is negligible considering they remain within the error bar range (see appendix D). At high loads, it was initially expected that the positive effect of "microexplosions" (which break up the fuel droplet and give a better distribution of pilot fuel across the chamber) discussed in earlier sections could offset the cooling affect resulting in comparatively higher thermal efficiencies. However, it appears that these effects are negligible (if they occur) when compared with the neat pilot fuel. At 1500 r/min, normal CI engine operation with neat RME produces significantly higher thermal efficiencies throughout the load range compared with the dual-fuel cases. This is because of incomplete combustion occurring to a larger extent than at 1000 r/min (at the same BMEP levels), which can result from gaseous fuel starvation at this speed. However, the neat RME pilot fuel case improves with engine load, indicating an improvement in dual-fuel combustion quality with increasing load. The emulsified pilot fuel cases do not improve with increasing load, though they remain with the error bar range of the neat pilot fuel.

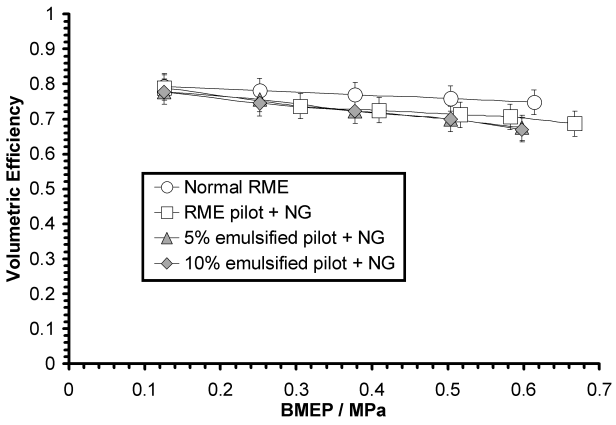


Figure 78: Volumetric efficiency comparison between natural gas dual-fuelling with neat RME and emulsified pilots, and normal CI engine operation with neat RME at 1000 r/min

Figures 78 and 79 show volumetric efficiency comparisons for the tested conditions. Natural gas dual-fuel operation reduces volumetric efficiency by at least 4% (considering the error bar range) compared with normal CI engine operation, while at 1500 r/min levels are not reduced significantly (considering the baseline point at 0.126 MPa BMEP). As the apparatus for gaseous fuel induction is a permanent fixture

in the engine's intake manifold (even during normal engine operation), it is likely that the differences between the two modes would be larger should the induction apparatus be removed during normal engine operation.

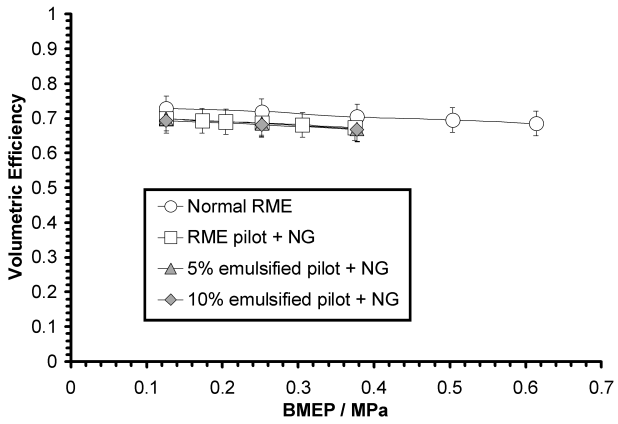


Figure 79: Volumetric efficiency comparison between natural gas dual-fuelling with neat RME and emulsified pilots, and normal CI engine operation with neat RME at 1500 r/min

### 4.2.3 Emissions

Figures 80 and 81 show specific nitrogen oxide (NO) emissions plotted against equivalence ratio for all tested conditions at 1000 r/min and 1500 r/min. As NO is the main constituent of $NO_x$ [35], the emission trends of both gas species are expected to correlate. At both speeds all the dual-fuel cases produce lower NO levels compared with normal CI engine operation. This could result from incomplete combustion occurring at these conditions as a result of local regions of natural gas-air mixture being too lean to allow flame propagation throughout the charge. This increases combustion inefficiencies, which will be evidenced by high unburnt HC and CO emissions (to be shown later). Emission levels rise towards normal engine operation levels at maximum engine load conditions at 1000 r/min. This could result from the relatively high equivalence ratio achieved with natural gas dual-fuel operation (which approaches unity). The emulsified pilot fuel cases produce similar amounts of NO to the neat RME pilot fuel case at low and intermediate equivalence ratios at 1000 r/min. It is also noted that both emulsions have similar trends when compared with each other. After an equivalence ratio of 0.55 at 1000 r/min however, NO emissions of the emulsified fuel rise significantly above that of the neat RME pilot. Considering the engine load and natural gas energy substitution levels are generally comparable for all pilot fuels, it is speculated that the "microexplosion"

phenomenon has a greater influence on combustion at these high equivalence ratios (indicated by the earlier pressure data discussion), resulting in improved distribution of fuel droplets. This could improve ignition quality as well as enhance flame propagation through the natural gas-air mixture, therefore possibly increasing $NO_x$ formation rates. This may also be the cause of the difference in NO levels between the emulsified fuels at high loads.

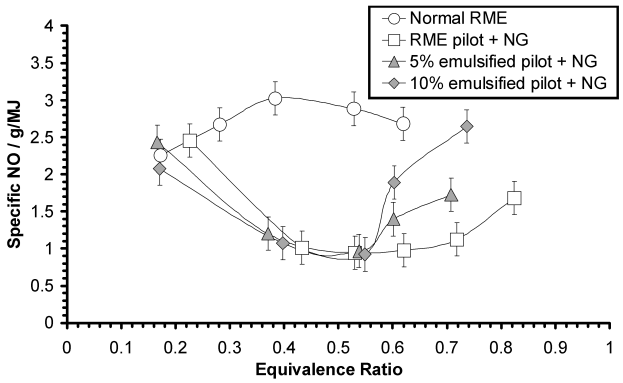


Figure 80: Specific NO comparison between natural gas dual-fuelling with neat RME and emulsified pilots, and normal CI engine operation with neat RME at 1000 r/min

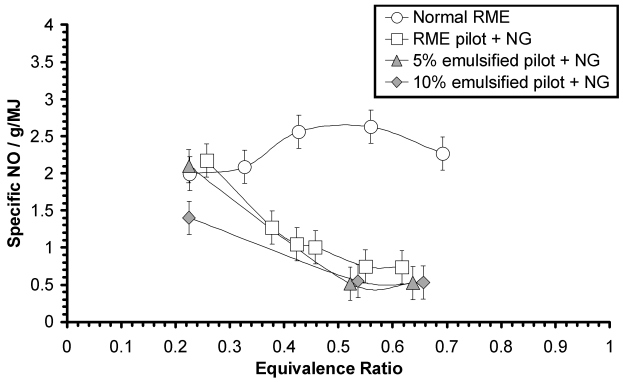


Figure 81: Specific NO comparison between natural gas dual-fuelling with neat RME and emulsified pilots, and normal CI engine operation with neat RME at 1500 r/min

This trend does not occur at 1500 r/min, where the emulsified pilot fuel cases produce lower values than the neat pilot fuel throughout the equivalence ratio range. This is because at this speed the engine could not reach maximum BMEP levels during dual-fuel operation, restricting maximum temperature levels.

Figures 82 and 83 show a specific unburnt hydrocarbon (HC) comparison for the tested conditions. It is noted that the plotted error bars are very small in comparison

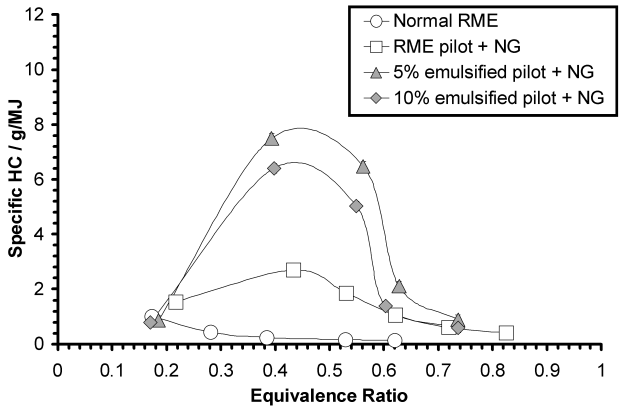


Figure 82: Specific HC comparison between natural gas dual-fuelling with neat RME and emulsified pilots, and normal CI engine operation with neat RME at 1000 r/min

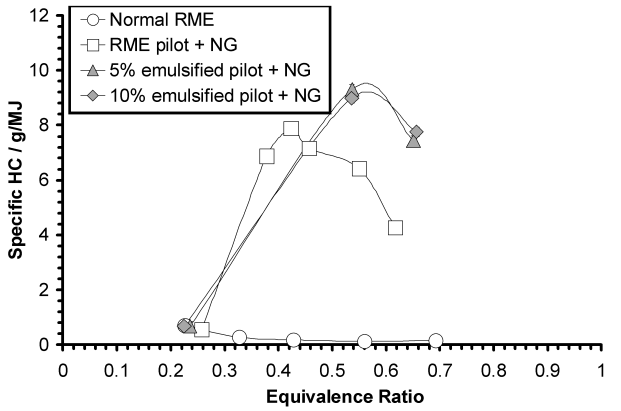


Figure 83: Specific HC comparison between natural gas dual-fuelling with neat RME and emulsified pilots, and normal CI engine operation with neat RME at 1500 r/min

with the y-axis scale (which is about 50 times as much). At both speeds unburnt HC emissions produced during natural gas dual-fuel operation are significantly higher than normal CI engine operation throughout the equivalence ratio range. Coupled with the lower thermal efficiencies and lower NO levels, the HC emission trend further indicates that incomplete combustion of the gaseous fuel is prevalent at low and intermediate loads during dual-fuel operation. These excessively high HC levels can also be a result of large amounts of gaseous fuel trapped in the crevice volumes of the combustion chamber (compared with typical levels recorded during normal CI engine operation). However, at high engine load conditions (at 1000 r/min in particular), levels are reduced closer to normal CI engine operation levels as a result of more gaseous fuel being consumed for combustion. In addition, the emulsified pilot fuel cases produce significantly higher HC emissions than the neat RME pilot fuel case at 1000 r/min, especially at equivalence ratios less than 0.6. This could be

a result of water vapourising after pilot injection, reducing combustion temperatures and hindering flame propagation at these conditions (as indicated in the pressure data discussion). Increased flame quenching at the cooler walls (compared with the neat RME pilot case) can also contribute to higher HC emissions.

At 1500 r/min, all natural gas dual-fuel cases produce consistently higher HC levels than normal CI engine operation. The emulsified pilot fuel cases continue to produce higher levels compared with the neat pilot fuel at this condition, which can be a result of the significantly extended ignition delay. Here combustion is initiated after TDC for both emulsified pilot fuel cases (while ignition took place before TDC for the neat RME pilot fuel and normal CI engine operation cases). This causes combustion to occur well into the expansion stroke, which deteriorates combustion quality and increases combustion inefficiencies.

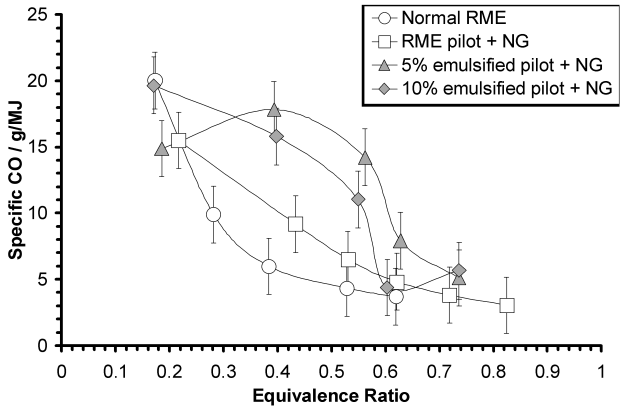


Figure 84: Specific CO comparison between natural gas dual-fuelling with neat RME and emulsified pilots, and normal CI engine operation with neat RME at 1000 r/min

Figures 84 and 85 show a specific CO comparison for the tested conditions. At both speeds, the trends noted for unburnt HC emissions are also mirrored here, where natural gas dual-fuel operation significantly increases CO levels compared with normal CI engine operation. In addition, it is suggested that the lower combustion temperatures of the emulsified pilot fuel conditions (compared with the neat RME pilot fuel case) prevent the complete oxidation of CO to $CO_2$, in addition to only partially reacting with gaseous fuel. At 1500 r/min, similar trends as 1000 r/min are repeated albeit with a much larger difference between the emulsified pilot fuel cases and the neat RME pilot case. This could be a result of the engine running a significantly richer fuel-air mixture considering the relatively low load range (compared with 1000 r/min).

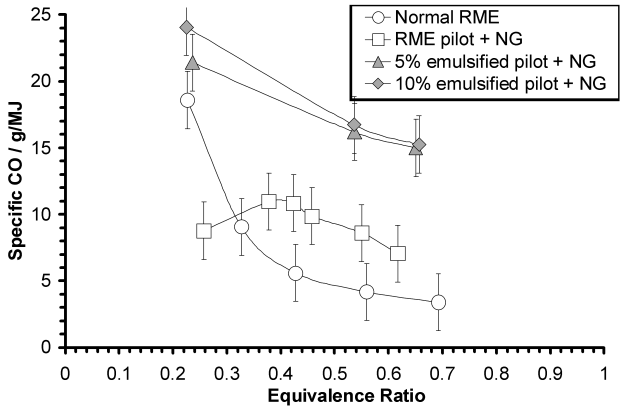


Figure 85: Specific CO comparison between natural gas dual-fuelling with neat RME and emulsified pilots, and normal CI engine operation with neat RME at 1500 r/min

These emission trends show that all pilot fuels do not seem to be initiating combustion of the natural gas-air mixture as effectively at 1500 r/min. This could be because at 1500 r/min ignition occurs as the compression stroke is nearly completed or, in the case of the emulsified pilot fuel cases, early in the expansion stroke. This is significant compared with trends at 1000 r/min, where ignition begins while the compression stroke is still progressing. As a result, the combustion pressures and temperatures seen at 1500 r/min are lower than at 1000 r/min. This expansion quenches the flames and prevents propagation across the combustion chamber, causing the lower specific NO, higher specific HC and higher specific CO values seen at 1500 r/min for all pilot fuel cases. In addition, at 1000 r/min the 5% emulsified pilot fuel generally produces slightly higher levels of CO, HC and slightly lower levels of NO at lower equivalence ratios compared with the 10% emulsion. It is speculated that this could result from the comparatively lower concentration of water limiting the number of "microexplosions" compared with the 10% emulsion. Previous work [100] suggests that after injection, smaller microdroplets of water are suspended in the atomised droplets of emulsion. During the compression stroke these water microdroplets (which are present in the outer boundary of the droplet) evaporate first, leaving behind a boundary of neat fuel surrounding the droplet. The thickness of this boundary varies with the concentration of water present, where the more water evaporating creates a thicker boundary and vice-versa. If the boundary is too thick, the "microexplosion" of the droplet may be relatively minor, or may not occur at all. If the boundary is too thin, the droplet is considered unstable and can explode violently. In the results presented in this work, the 5% emulsified pilot fuel could have droplet boundaries which are thick enough to restrict "microexplo-

sions" from occurring at 1000 r/min for the lower equivalence ratio range. However, it should be said this effect would be fairly minor considering that most of these trends are just outside the presented error bar ranges.

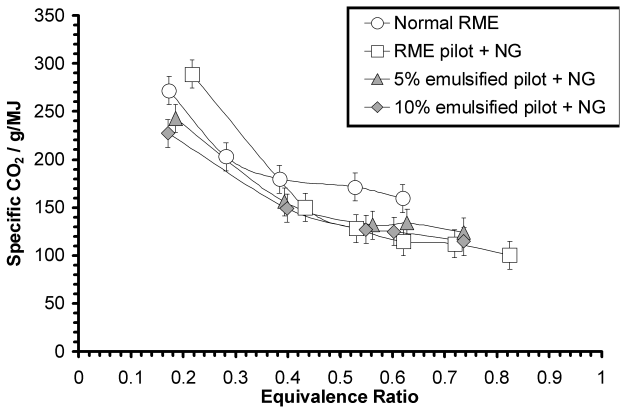


Figure 86: Specific $CO_2$ comparison between natural gas dual-fuelling with neat RME and emulsified pilots, and normal CI engine operation with neat RME at 1000 r/min

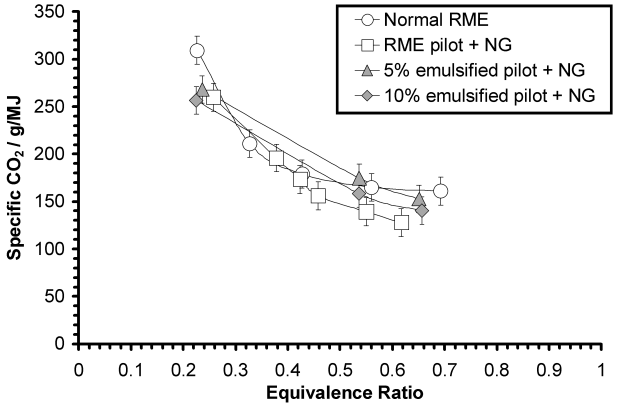


Figure 87: Specific $CO_2$ comparison between natural gas dual-fuelling with neat RME and emulsified pilots, and normal CI engine operation with neat RME at 1500 r/min

Figures 86 and 87 show a specific $CO_2$ comparison for the tested conditions. $CO_2$ levels during natural gas dual-fuel engine operation are generally lower than normal CI engine operation at intermediate and high engine loads. This is a result of natural gas (which is primarily methane) containing a higher hydrogen-carbon ratio than typical CI engine fuels. In addition, the levels of specific $CO_2$ are more or less similar between all pilot fuel cases at both speeds. Here all the values are quite close and should reflect the hydrogen-carbon ratios of the pilot fuels which are relatively close. This is assessed from a stoichiometric combustion calculation, where 1 g of natural gas produces 2.75 g of $CO_2$ and 1 g of RME produces 2.87 g of $CO_2$.

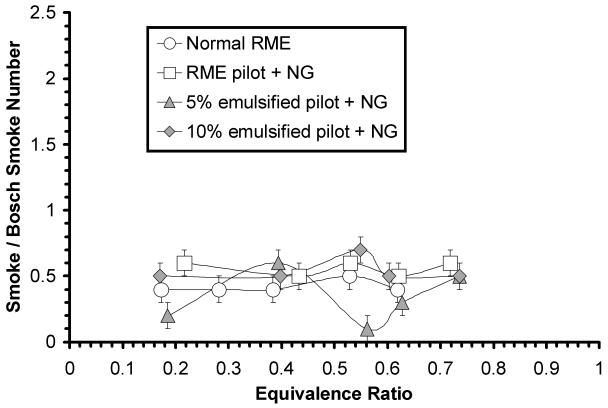


Figure 88: Bosch smoke number comparison between natural gas dual-fuelling with neat RME and emulsified pilots, and normal CI engine operation with neat RME at 1000 r/min

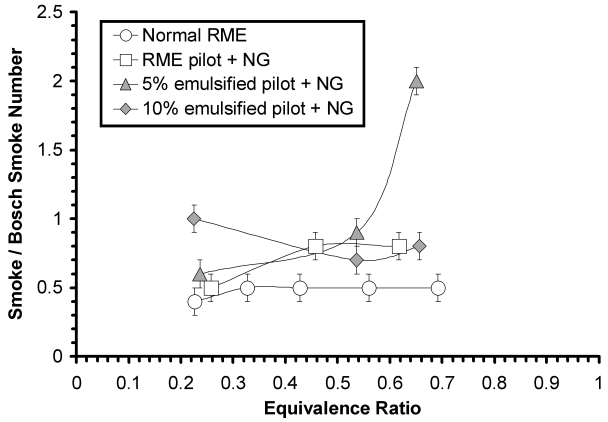


Figure 89: Bosch smoke number comparison between natural gas dual-fuelling with neat RME and emulsified pilots, and normal CI engine operation with neat RME at 1500 r/min

Figures 88 and 89 show a Bosch smoke number comparison for the tested conditions. At 1000 r/min, natural gas dual-fuel engine operation produces comparable smoke levels with normal CI engine operation (which for this engine and tuning are low). This result is contrary to the general trend of reduced smoke levels in the literature and probably follows from the inherently low smoke levels recorded during normal CI engine operation (with the engine employing a fairly early injection timing compared with other engines of a similar age and type). This reduces smoke formation while generating high $NO_x$ levels. In addition, all pilot fuels produce similar trends to each other with the exception of the 5% emulsified pilot case. At equivalence ratios of about 0.15 and 0.55, smoke emissions of the 5% emulsion is much lower than the general trend. It is likely that these reductions are anomalous as the 10% emulsion shows no such effect. At 1500 r/min there is not much variation between the liquid pilot fuels, except for the 5% emulsified pilot at the highest equivalence

ratio. The reason for this increase is unclear. An initial assessment suggests that the combustion temperatures at this speed and load is not high enough to promote "microexplosions" (which would help reduce smoke formation). However, as no such increase occurs with the 10% emulsion it is difficult to justify. It is suspected that with a repeat test these anomalous data points would return to the established trends.

Overall, natural gas dual-fuel operation reduces $NO_x$ (of which NO is the principal constituent) and $CO_2$ emissions while maintaining thermal efficiencies compared with normal CI engine operation. However, significantly higher unburnt HC and CO emissions are recorded at low and intermediate engine loads as a result of lower combustion efficiencies. This could be due to the pilot fuel failing to ignite the natural gas-air charge on a scale seen at higher loads (as a result of locally fuel-lean regions preventing adequate ignition and flame propagation). Maximum BMEP levels recorded during normal CI engine operation are limited by the amount of gaseous fuel that can be inducted (via the intake manifold) into the cylinder per cycle, where fuel starvation occurs at high speed. Volumetric efficiency is also reduced during dual-fuel operation at almost all conditions as a result of air displacement by natural gas. With regard to the water-in-RME emulsified pilot fuels, the trade-off between the cooling effect (as a result of water vapourisation) and better fuel-air mixing (as a result of "microexplosions") is seemingly more apparent during the dual-fuel mode compared with normal CI engine operation. For example, an engine-load/ cylinder charge-temperature threshold can be established; above which the "microexplosion" phenomenon could take place at a significant scale offsetting the charge cooling effect (which might be dominant at lower loads). As a result, the cooling effect can negatively influence combustion quality (in terms of higher unburnt HC/ CO levels) at low and intermediate loads; while the effect of "microexplosions" can enhance fuel-air mixing (which increases $NO_x$ production) at high loads. Smoke levels are not reduced to the extent seen in literature, which could be a result of inherently low smoke levels from this engine even during normal CI engine operation.

## 4.3 Dual-Fuel Engine Operation with Hydrogen Gas

The previous section shows natural gas dual-fuel engine operation with 3 pilot fuels at 1000 r/min and 1500 r/min using the single-cylinder engine. As hydrogen had not been used in this laboratory prior to this work, extensive preliminary dual-fuel engine tests with hydrogen gas were conducted to determine viable engine operating conditions at different speeds which would allow a minimum amount of pilot fuel to be used while achieving maximum BMEP levels. It was found that the same test conditions (i.e. pilot fuel enthalpy fractions) recorded with natural gas dual-fuel tests could not be repeated with hydrogen gas. This was primarily due to hydrogen gas having a significantly lower energy density by volume compared with that of natural gas. This resulted in a comparatively larger amount of pilot fuel being required compared with the natural gas dual-fuel tests in order to achieve the same maximum BMEP levels with hydrogen. Here the pilot fuel amount was set at 0.378 MPa BMEP (the middle of the load range), instead of 0.126 MPa BMEP used in the natural gas tests. As a result, 1500 r/min tests with hydrogen dual-fuelling were rendered irrelevant as the minimum pilot fuel amount would have to increase further (to 0.5 MPa BMEP) in order to compensate for the expected lesser amount of gaseous fuel inducted. This would have eliminated 3/4 of the data recorded in a typical full load range engine test. Therefore, tests at 750 r/min were conducted instead to allow an appropriate speed comparison to be made with speed variation (where maximum BMEP is achieved with a common pilot fuel setting). The same selection of pilot fuels as the previous section were used, and (like natural gas) water-in-fuel emulsions used as pilot fuels for hydrogen dual-fuel operation has not been presented in the literature at the time of writing.

### 4.3.1 Ignition Behaviour

Figure 90 shows that all hydrogen dual-fuel cases generates higher peak combustion pressures compared with normal CI engine operation (roughly 0.5 to 1 MPa higher) at 750 r/min. These high peak pressures can result from higher pressure-rise rates (as seen in figure 91), following from the higher flame propagation speed of premixed hydrogen-air mixtures (compared with conventional mixture-controlled CI engine combustion). Natural gas dual-fuel operation generates significantly higher peak pressure values than all other modes (about 1.5 MPa higher). This can result from comparatively higher pressure-rise rates occurring early in the expansion stroke (seen

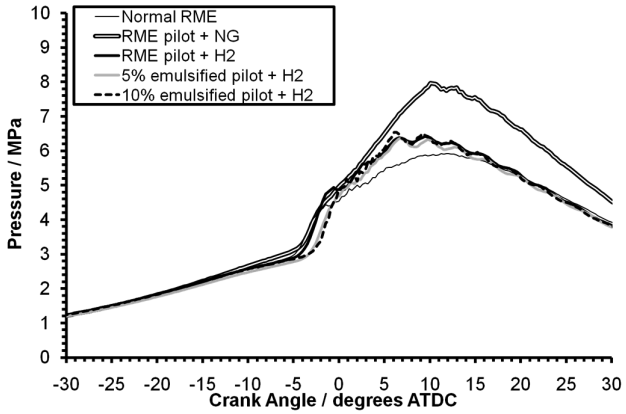


Figure 90: Pressure comparison between hydrogen gas dual-fuel operation with neat RME and emulsified RME pilots, normal CI engine operation with neat RME, and natural gas dual-fuel operation with neat RME pilot at 750 r/min and 0.63 MPa BMEP

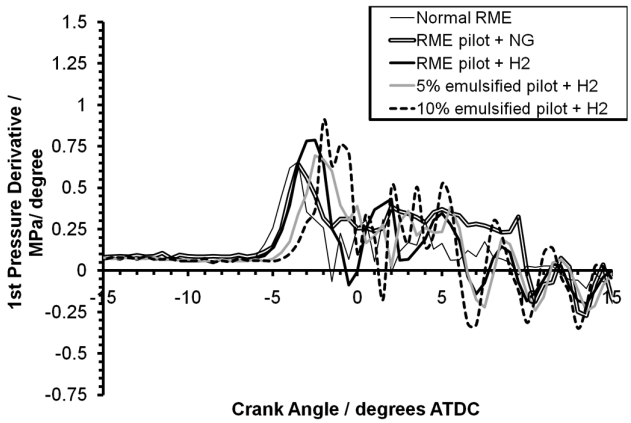


Figure 91: First pressure derivative comparison between hydrogen gas dual-fuel operation with neat RME and emulsified RME pilots, normal CI engine operation with neat RME, and natural gas dual-fuel operation with neat RME pilot at 750 r/min and 0.63 MPa BMEP

in figure 91). This in turn can result from a more extensive diffusion-combustion phase (which constitutes most of the combustion reaction) compared with the other modes. Peak pressure levels of the various tested pilot fuels for the hydrogen dual-fuel case are fairly similar to one another.

Hydrogen dual-fuel CI engine operation does not seem to affect ignition delay significantly compared with normal CI engine operation at this speed, where both operating modes with neat RME fuel produce the same ignition delay (about 2.9 ms). Natural gas dual-fuel operation presents an ignition delay of about 3.0 ms, a small variation which can follow from cycle-to-cycle variations (see appendix E). At the same condition, the 5% emulsified pilot fuel case produces an ignition delay of about 3.3 ms while the 10% case produces 3.6 ms. These increases in ignition delay

may result from the evaporating water cooling the chamber during engine operation since engine load levels and hydrogen energy levels are similar (as suggested previously in the natural gas section). Figure 91 also shows that both emulsified pilot fuel cases generate delayed pressure-rise rates (with comparable peak magnitudes) to the neat RME pilot fuel. This follows mainly from the extended ignition delay with the cooling effect possibly extending the ignition delay of the 10% case further. The "microexplosion" phenomenon could have an effect on peak pressure-rise rates (when comparing the 10% emulsion to the 5% emulsion test case), though it is marginal at best when cycle-to-cycle variations are considered.

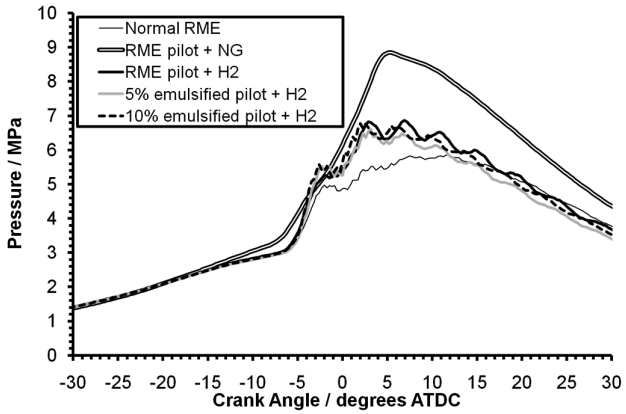


Figure 92: Pressure comparison between hydrogen gas dual-fuel operation with neat RME and emulsified RME pilots, normal CI engine operation with neat RME, and natural gas dual-fuel operation with neat RME pilot at 1000 r/min and 0.63 MPa BMEP

At 1000 r/min, the peak pressures for all tested conditions are slightly higher than those at 750 r/min (as seen in figure 92). In addition, peak pressures occur about 4 crank angle degrees earlier than at 750 r/min for all tested conditions. This could result from the shorter ignition delay in addition to higher mixture temperatures compared with 750 r/min. Similar ignition delay trends as seen at 750 r/min are obtained at 1000 r/min. Here both normal CI engine operation with RME and hydrogen dual-fuel CI engine operation ignited by the neat RME pilot fuel produce an ignition delay of about 2.3 ms, which is comparable with the natural gas dual-fuel case. The 5% emulsified pilot fuel produces an ignition delay of about 2.7 ms, while the 10% emulsified pilot fuel produces an ignition delay of about 2.6 ms.

Figure 93 shows that both emulsified pilot fuel cases generate higher pressure-rise rates than the neat pilot fuel case. This could be mainly a result of the extended ignition delay. A more homogeneous fuel-air mixture resulting from "microexplosions" may also account for the larger difference peak pressure-rise rates between

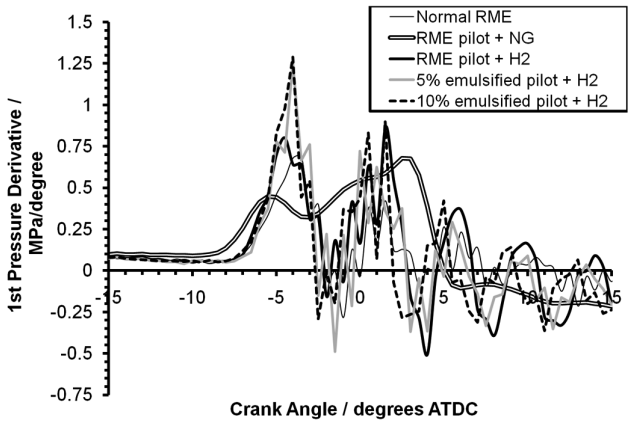


Figure 93: First pressure derivative comparison between hydrogen gas dual-fuel operation with neat RME and emulsified RME pilots, normal CI engine operation with neat RME, and natural gas dual-fuel operation with neat RME pilot at 1000 r/min and 0.63 MPa BMEP

the emulsified pilot fuels and the neat pilot fuel at this speed. At both speeds, what appears to be light "hydrogen knock" occurs during hydrogen dual-fuel operation. This can be a result of higher pressure-rise rates, which can cause a regular audible sound similar to that caused by traditional knock (i.e. autoignition of the end-gas ahead of the combustion flame) [35].

### 4.3.2 Performance

Figures 94 and 95 show a thermal efficiency comparison of hydrogen dual-fuel CI engine operation (with neat RME pilot fuel and emulsified RME pilot fuel) with normal CI engine operation with neat RME fuel as well as natural-gas dual-fuel operation with neat RME pilot fuel at 750 r/min and at 1000 r/min. During hydrogen dual-fuel CI engine operation at 750 r/min, thermal efficiency levels are slightly lowered compared with normal CI engine operation at maximum load. This is contrary to the general trend in the literature [48], and implies that there is incomplete combustion of the hydrogen-air charge at high engine loads in addition to increased heat energy losses. However, as we were unable to determine unburnt hydrogen exhaust gas concentrations nor measure heat energy loss we cannot say this with 100% certainty. This reduction in efficiency between the two operating modes is less apparent at 1000 r/min, which suggests that higher fuel-air mixing rates (as a result of higher levels of turbulence at the higher speed) are allowing more homogeneous fuel-air mixtures to form. There are minimal differences with the emulsified fuel cases compared with the neat pilot fuel, suggesting the influence

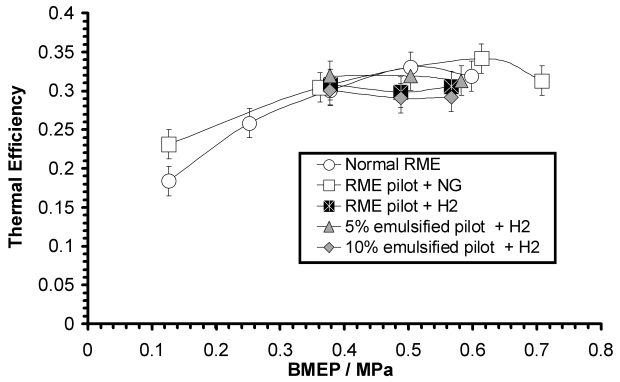


Figure 94: Thermal efficiency comparison between hydrogen gas dual-fuel operation with neat RME and emulsified RME pilots, normal CI engine operation with neat RME, and natural gas dual-fuel operation with neat RME pilot at 750 r/min

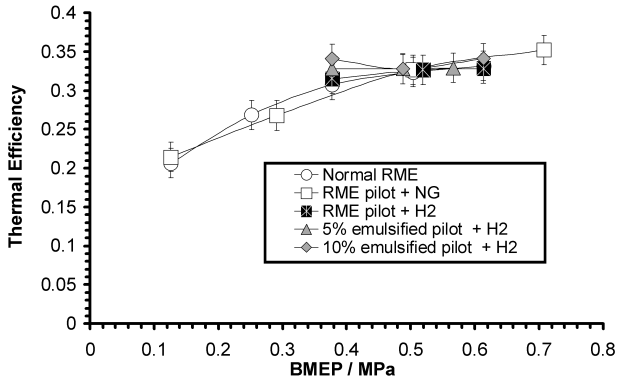


Figure 95: Thermal efficiency comparison between hydrogen gas dual-fuel operation with neat RME and emulsified RME pilots, normal CI engine operation with neat RME, and natural gas dual-fuel operation with neat RME pilot at 1000 r/min

of "microexplosions" and cooling are negligible. At 750 r/min, natural gas dual-fuel operation initially appears to have generally higher efficiencies. However, there is a 5% increase in thermal efficiency at the lowest load setting during natural gas dual-fuel operation compared with the same point during normal engine operation. As these points are essentially the same condition (where no natural gas is inducted) ideally they should be matched (as they are at 1000 r/min). As a result, the likely trend is instead a general lowering of efficiency during the intermediate loads, while efficiencies are maintained at high loads. This low efficiencies at intermediate load conditions are a result of incomplete combustion of the natural gas-air charge as a result of overleaning of natural gas-air mixture (as discussed in the previous section).

Figures 96 and 97 show volumetric efficiency comparisons for the tested conditions.

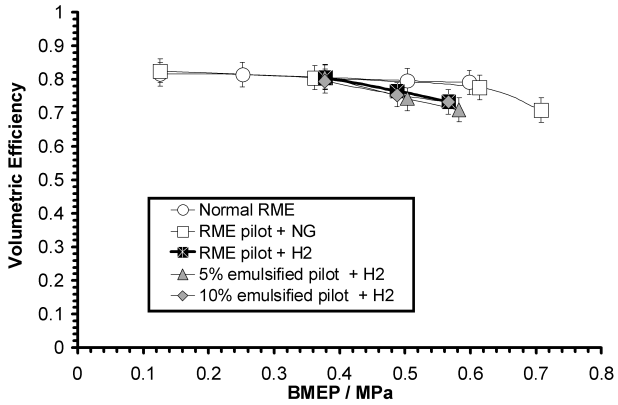


Figure 96: Volumetric efficiency comparison between hydrogen gas dual-fuel operation with neat RME and emulsified RME pilots, normal CI engine operation with neat RME, and natural gas dual-fuel operation with neat RME pilot at 750 r/min

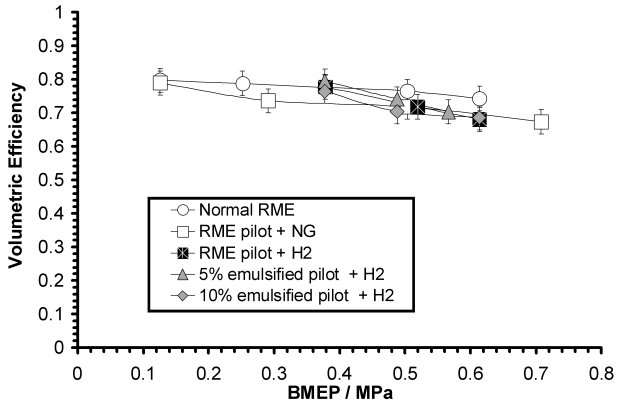


Figure 97: Volumetric efficiency comparison between hydrogen gas dual-fuel operation with neat RME and emulsified RME pilots, normal CI engine operation with neat RME, and natural gas dual-fuel operation with neat RME pilot at 1000 r/min

There is a clear reduction in volumetric efficiency during hydrogen dual-fuel operation (about 4% lower taking into account error bars, see appendix D). This can be a result of hydrogen gas displacing a volume of air in the intake manifold, reducing airflow into the engine. Hydrogen also has a significantly higher stoichiometric air-fuel ratio compared with the liquid fuels (of the order of 127%). This means a larger amount of air is needed to burn a given amount of hydrogen compared with conventional fuels. As a result, inducting enough air for combustion is an issue when running an engine on hydrogen inducted in the intake manifold. The choice of pilot fuel does not affect volumetric efficiency, and the variations present can result from varying atmospheric conditions (i.e. intake air density) of each test day. The engine is also significantly louder during hydrogen dual-fuel operation compared with normal CI engine operation. To avoid the risk of engine damage as a result of severe

"hydrogen knock" in addition to the possibility of traditional knock, the maximum engine loads normally achieved during normal CI engine operation had to be reduced slightly. As a result, the engine (when in hydrogen dual-fuel mode) could not reach BMEP levels recorded during normal CI engine operation. For example, the maximum BMEP during dual-fuel operation was about 0.61 MPa while maximum BMEP during normal CI engine operation was about 0.63 MPa. Power output is therefore reduced (to the order of 8% maximum) at some conditions with hydrogen dual-fuelling compared with normal CI engine operation. Natural gas dual-fuel operation lowers volumetric efficiency by a similar amount (as hydrogen dual-fuel operation) compared with normal engine operation. This is significant considering that natural gas supplies up to a 70% enthalpy fraction compared with a maximum of 40% for the hydrogen test cases. To provide the same maximum enthalpy fraction as the natural gas dual-fuel tests, the hydrogen flow rate into the engine would need to increase significantly, possibly further reducing volumetric efficiency.

### 4.3.3 Emissions

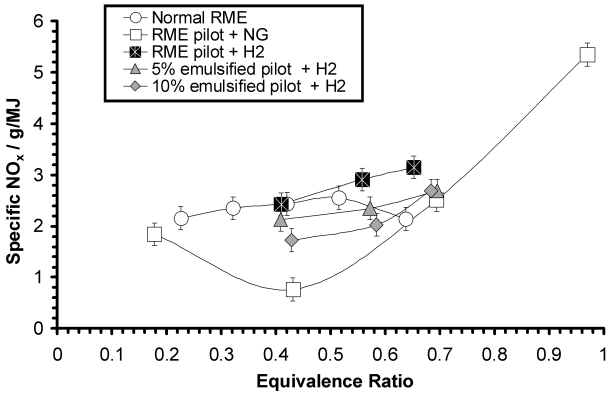


Figure 98: Specific $NO_x$ comparison between hydrogen gas dual-fuel operation with neat RME and emulsified RME pilots, normal CI engine operation with neat RME, and natural gas dual-fuel operation with neat RME pilot at 750 r/min

Figures 98 and 99 shows a specific $NO_x$ comparison for the tested conditions. Hydrogen dual-fuel operation with the neat pilot fuel increases $NO_x$ emissions (of which NO is the main constituent) compared with normal CI engine operation by about 50% at both speeds. This increase can be due to the higher combustion chamber pressures (and temperatures) recorded during dual-fuel operation. In addition, higher combustion reaction rates during the premixed combustion phase as well as the mixing controlled phase contribute to increased $NO_x$ formation. This trend does

not occur with the emulsified pilot fuel cases however. At 750 r/min, both emulsified pilot fuels reduce $NO_x$ emissions slightly when compared with the normal CI engine operation (except at maximum load) and the neat RME pilot fuel case (at all conditions). It is speculated that this could follow from the cooling effect of water vapourising in the cylinder (considering that engine load and hydrogen energy proportions are similar), reducing combustion temperatures. The 10% emulsion seems to produce lower $NO_x$ relative to the 5% emulsion, which might result from charge cooling on a larger scale. However, considering the error bar range these effects are marginal at best. At high loads, $NO_x$ levels increase above that of normal CI engine combustion, while still remaining slightly below the neat RME pilot fuel level.

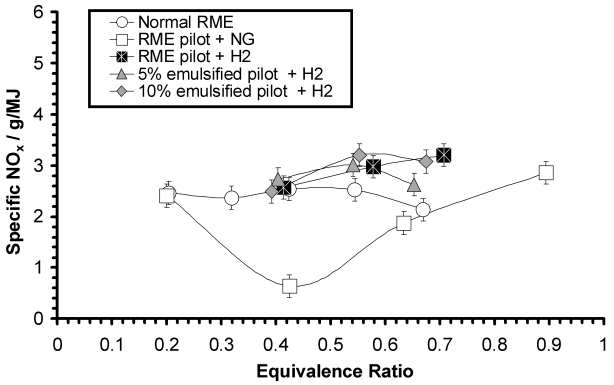


Figure 99: Specific $NO_x$ comparison between hydrogen gas dual-fuel operation with neat RME and emulsified RME pilots, normal CI engine operation with neat RME, and natural gas dual-fuel operation with neat RME pilot at 1000 r/min

At 1000 r/min, all the hydrogen dual-fuel cases generate higher $NO_x$ levels than normal engine operation throughout the load range. Both emulsified pilots have a differing trend compared with the neat RME pilot case however. $NO_x$ levels increase with equivalence ratio, only to decrease again at the maximum equivalence ratio. This is opposite to the trend at 750 r/min, and could result from several factors. While cooling appears to be significant at 750 r/min, it may not be as significant at 1000 r/min for both emulsified pilot fuels. The higher water content in the 10% emulsion might also account for a higher rate of "microexplosions" resulting in a more homogeneous fuel mixture, offsetting the cooling effect of water vapourisation. However, this effect would be minor considering the presented error bar range. Dual-fuel operation with natural gas has higher levels of specific $NO_x$ emissions compared with hydrogen dual-fuel operation at the highest loads at both speeds. This is a result of higher peak combustion chamber pressures (and higher temperatures) as well as a comparatively high equivalence ratio (which approaches

unity and encourages high $NO_x$ formation rates). At lower load conditions, levels are significantly reduced primarily as a result of the low combustion temperatures (following from the low combustion quality) apparent at these conditions.

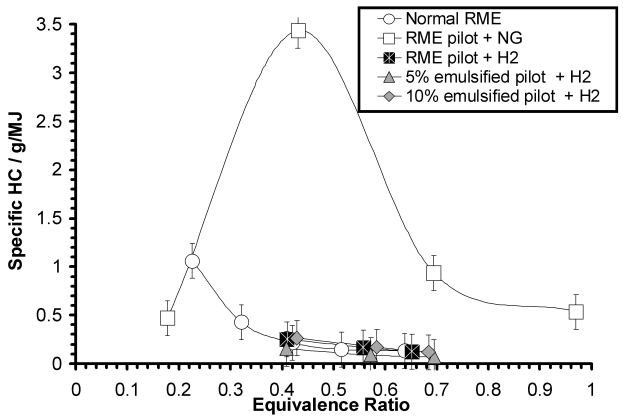


Figure 100: Specific HC comparison between hydrogen gas dual-fuel operation with neat RME and emulsified RME pilots, normal CI engine operation with neat RME, and natural gas dual-fuel operation with neat RME pilot at 750 r/min

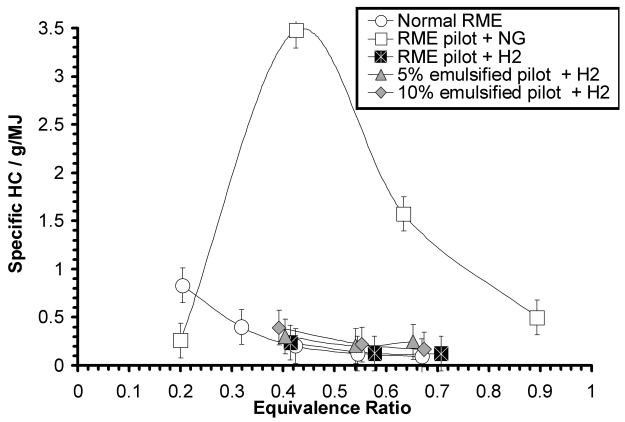


Figure 101: Specific HC comparison between hydrogen gas dual-fuel operation with neat RME and emulsified RME pilots, normal CI engine operation with neat RME, and natural gas dual-fuel operation with neat RME pilot at 1000 r/min

Figures 100 and 101 shows a specific unburnt HC comparison for the tested conditions. Dual-fuel operation with hydrogen produces very similar trends to normal CI engine operation at both speeds. All the tested pilot fuels also produce comparable results. During hydrogen dual-fuel CI engine operation, most unburnt HC that survives through the exhaust may originate from fuel that leaks from the injector nozzle sac late in the expansion stroke in addition to flame quenching at the cylinder walls. This unburnt fuel (originating from the pilot fuel injection during dual-fuelling) usually mixes slowly with the charge in the expansion stroke, where charge conditions

are unsuitable for ignition. In addition, the levels of HC produced are within the errors of the measuring instrument. This indicates HC emissions from this engine in both of these operating modes are inherently low. Dual-fuel operation with natural gas produces significantly higher specific HC levels at low and intermediate loads compared with hydrogen dual-fuel operation as a result of overleaning. This results in incomplete combustion of the natural gas-air mixture following from the stratified nature of the pilot fuel where there are substantial pockets of fuel mixture that are too lean to sustain combustion. Significant amounts of unburnt natural gas can also originate from trapped in crevice volumes.

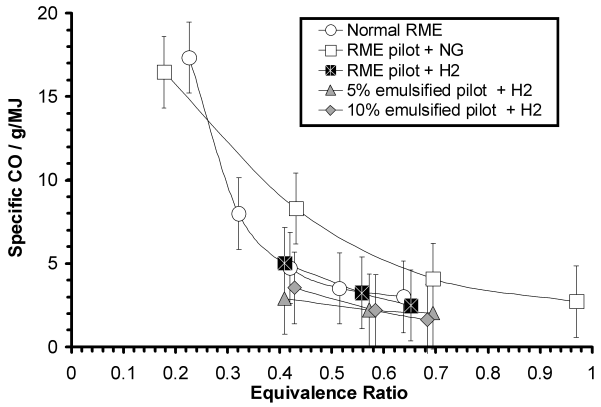


Figure 102: Specific CO comparison between hydrogen gas dual-fuel operation with neat RME and emulsified RME pilots, normal CI engine operation with neat RME, and natural gas dual-fuel operation with neat RME pilot at 750 r/min

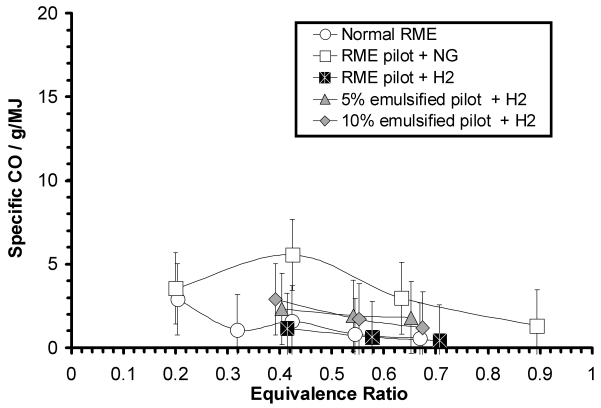


Figure 103: Specific CO comparison between hydrogen gas dual-fuel operation with neat RME and emulsified RME pilots, normal CI engine operation with neat RME, and natural gas dual-fuel operation with neat RME pilot at 1000 r/min

Figures 102 and 103 show a specific CO comparison for the tested conditions. Dual-fuel operation with hydrogen produces fairly similar trends to normal CI engine

operation at both speeds for all pilot fuels. Considering that CI engines generally produce very low amounts of CO emissions during normal operation due to generally fuel-lean combustion (of the order of 0.1% of exhaust gas composition by volume, which corresponds to the instrument error), this trend for both dual-fuel cases is as expected. Similar trends noted in unburnt HC emissions during natural gas dual-fuel operation is also recorded here for CO, which can also result from low combustion quality at intermediate load conditions.

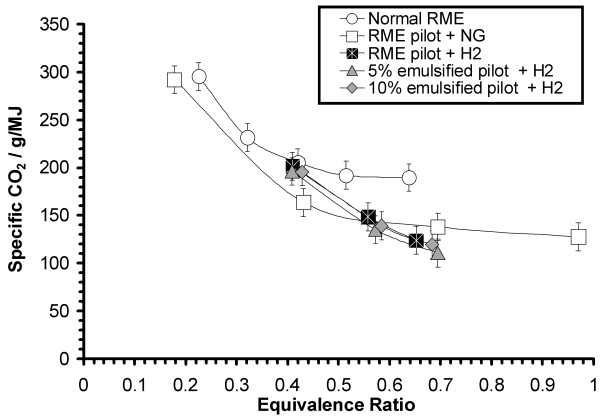


Figure 104: Specific $CO_2$ comparison between hydrogen gas dual-fuel operation with neat RME and emulsified RME pilots, normal CI engine operation with neat RME, and natural gas dual-fuel operation with neat RME pilot at 750 r/min

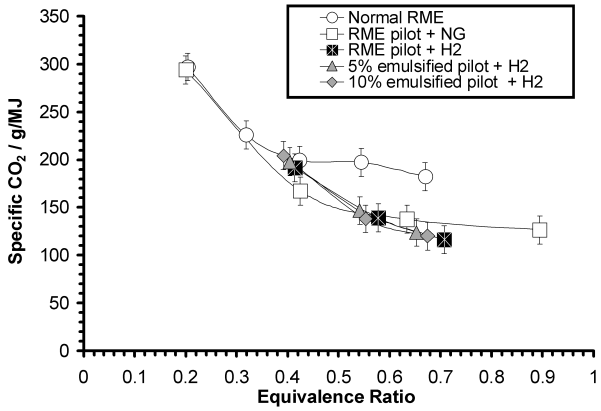


Figure 105: Specific $CO_2$ comparison between hydrogen gas dual-fuel operation with neat RME and emulsified RME pilots, normal CI engine operation with neat RME, and natural gas dual-fuel operation with neat RME pilot at 1000 r/min

Figures 104 and 105 show a specific $CO_2$ comparison for the tested conditions. There is a significant reduction in $CO_2$ emissions with increasing load during hydrogen dual-fuel operation with all the tested pilot fuels (roughly 40% compared with normal CI engine operation). As the amount of carbon inducted into the engine

depends on the amount of hydrocarbon fuel injected, this reduction is due to more hydrogen (which contains no carbon) being used to produce similar power levels as normal CI engine operation. The emulsified pilot fuels do not seem to affect the $CO_2$ emission significantly. Dual-fuel operation with natural gas also reduces $CO_2$ levels compared with normal CI engine operation (with a maximum enthalpy fraction of 70%), while being comparable to levels recorded during hydrogen dual-fuelling (with a maximum enthalpy fraction of 40%). This is because, while natural gas produces less $CO_2$ compared with RME in stoichiometric mixtures (where 1 g of natural gas produces 2.75 g of $CO_2$ while 1 g of RME produces 2.87 g of $CO_2$), it still contributes to $CO_2$ production while hydrogen gas does not.

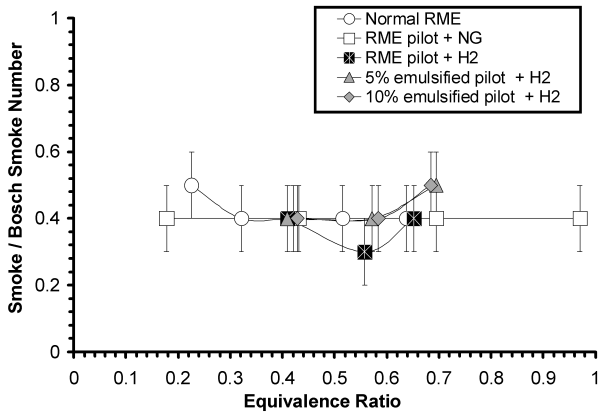


Figure 106: Bosch smoke number comparison between hydrogen gas dual-fuel operation with neat RME and emulsified RME pilots, normal CI engine operation with neat RME, and natural gas dual-fuel operation with neat RME pilot at 750 r/min

Figures 106 and 107 show a Bosch smoke number comparison for the tested conditions. At 750 r/min, there is an inconsistent reduction in smoke levels during hydrogen dual-fuel operation compared with normal CI engine operation. This reduction is fairly minimal compared with the literature [48]. There is minimal change in smoke emissions for all pilot fuels considering the inherently low measured levels. At 1000 r/min, there is no significant variation in the smoke levels with load for either engine operating mode, nor for any of the tested pilot fuels. With the pilot fuel enthalpy fraction still always more than 60% at any condition, any reduction of smoke levels below the baseline appears to be outside the sensitivity of the smoke meter used in these tests. Smoke levels obtained during natural gas dual-fuel operation were similar to hydrogen dual-fuel operation, where there is minimal reduction when compared with normal CI engine operation. This is contrary to the general trend of reduced smoke levels in the dual-fuel literature. This can be due to inherently low smoke levels recorded during normal operation in this engine.

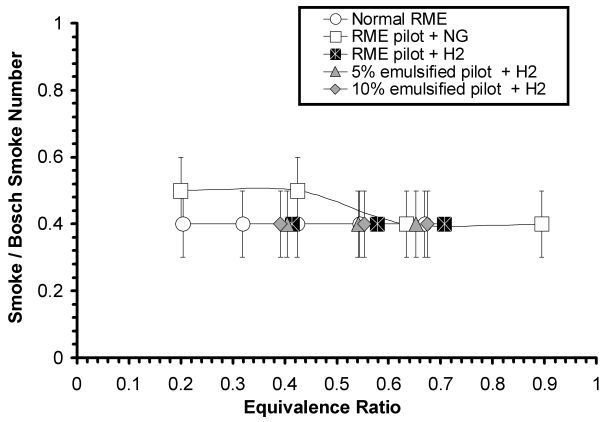


Figure 107: Bosch smoke number comparison between hydrogen gas dual-fuel operation with neat RME and emulsified RME pilots, normal CI engine operation with neat RME, and natural gas dual-fuel operation with neat RME pilot at 1000 r/min

Overall, hydrogen dual-fuel CI engine operation with all the tested pilot fuels tends to increase $NO_x$ emissions while smoke, unburnt HC and CO levels remain relatively unchanged compared with normal CI engine operation with neat RME. $CO_2$ emissions are reduced for all pilot fuels tested. Hydrogen dual-fuel operation generally maintain thermal efficiencies. This trend does not correlate with the trend in the literature, and can indicate incomplete combustion of the hydrogen gas as well as increased heat energy losses. The emulsified pilot fuels maintain thermal efficiencies compared with the neat RME pilot fuel at both speeds. $NO_x$ emissions are also generally comparable with the neat RME pilot fuel at most conditions. Smoke, unburnt HC, CO and $CO_2$ levels also remain similar to the neat RME pilot fuel. Hydrogen dual-fuel operation with all pilot fuels lowers volumetric efficiency when the gaseous fuel is inducted via the intake manifold. In addition, lower power output is also a result of maintaining engine stability and avoiding severe "hydrogen knock".

# 5 Conclusions and Recommendations

## 5.1 Conclusions

1. Neat RME and neat diesel fuel perform very closely to each other in terms of engine performance and emissions during normal CI engine operation, with the exception of higher SFC levels when using neat RME fuel. This is a result of the smaller lower heating value of RME (compared with diesel fuel) increased SFC levels.

2. The water-in-RME emulsions generally perform similarly to the neat fuels during normal CI engine operation. $NO_x$ emission reductions were minor, suggesting the cooling effect of water vapourisation was negligible overall. Similar deductions were made with regards to enhanced fuel-air mixing as a result of "microexplosions", which were not substantial enough to alter the established trends significantly.

3. Natural gas dual-fuel operation with neat pilot fuel reduces $NO_x$ and $CO_2$ emissions while maintaining thermal efficiencies compared with normal CI engine operation with neat RME. Significantly higher unburnt HC and CO emissions are recorded at low and intermediate engine loads due to overleaning of the natural gas-air mixture. This results in the pilot fuel failing to ignite the entire natural gas-air charge.

4. During natural gas operation with emulsified pilot fuel, the effect of the trade-off between the cooling effect (as a result of water vapourisation) and better fuel-air mixing (as a result of "microexplosions") seems to be more apparent compared with normal CI engine operation. An engine-load/ cylinder charge-temperature threshold can be established (about 0.5 MPa BMEP); above which the "microexplosion" phenomenon seems to take place at a significant scale.

5. Hydrogen dual-fuel operation with neat pilot fuels increases $NO_x$ emissions while smoke, unburnt HC and CO levels remain relatively unchanged compared with normal CI engine operation with neat RME. Thermal efficiency is also maintained compared with normal CI engine operation with neat RME, while $CO_2$ emissions are reduced for all pilot fuels tested.

6. Hydrogen dual-fuel operation with emulsified pilot fuels maintained thermal efficiencies compared with the neat RME pilot fuel at higher engine speeds, because

of enhanced overall mixing (resulting from higher mixture turbulence at the higher speed) offsetting the minor cooling effect which may be more significant at lower speeds. $NO_x$ emissions are generally comparable with the neat RME pilot.

## 5.2 Overall Conclusion

Two CI engine operating modes have been investigated with a variety of test fuels on the same engine with fairly mixed results. First-generation biodiesel has shown to be a suitable replacement for diesel fuel during both normal engine operation and dual-fuel operation, where engine performance and emissions of the two fuels were very similar. However, first-generation biofuels are not sustainable as they need substantial land areas to meet current fuel demand [17]. Alternative production processes (such as the biomass-to-liquid processes) are needed to produce a base fuel oil which can then be processed further (transesterified in the case of renewable diesel fuel production) to produce biofuel similar to diesel and gasoline. In addition to biodiesel, other alternative fuels (natural gas and hydrogen gas in this instance) were investigated. These fuels can be made sustainably in the long term, however, further refinement during the production process is needed to compete with typical fuel life-cycle energy and emission levels [30–32, 106]. Both gaseous fuels can be used in CI engines with the dual-fuel mode fairly successfully, however, significant optimisation is needed to improve combustion efficiency at low and intermediate engine loads. This is also noted in SI engines [36]. These issues arise as conventional engines (with which these fuels were originally tested) are designed specifically for liquid fuels. As a result, either substantial engine customisation or even complete redesign (particularly in the fuel supply system) is needed to improve the combustion quality of gaseous fuels on a scale larger than that seen in this work. On a specific note, emulsified fuels do not fundamentally affect overall engine performance and emission trends very significantly.

## 5.3 Recommendation for Future Work

Reduced volumetric efficiency is a major issue in both CI and SI engines when running on gaseous fuels, which limits engine operating ranges and power output. As the gaseous fuel was inducted into the intake manifold, this presented problems with adequate inducted fuel supply to the cylinder. In addition, preignition and engine

stability issues during hydrogen gas use were also encountered. As a result, a direct gaseous fuel system (where both the pilot fuel and gaseous fuel are electronically injected into the cylinder) would be required in order to avoid these problems. Detailed analysis of the combustion process during dual-fuel operation is also necessary to improve intermediate and low load combustion quality. In response to this, an optical combustion chamber is also being set-up as a secondary project over the course of this work (as discussed in appendix A). Completion of this chamber would allow optical assessment of dual-fuel combustion, illustrating the relationship between the pilot fuel and gaseous fuel in terms of mixing levels, ignition conditions and overall combustion progress more explicitly.

Specifically, the effect of swirling charge flow within the combustion chamber on injected pilot fuel spray can be assessed. The ignition delay can also be determined optically, and compared with recorded pressure data via a common timebase. The different colours of premixed and diffusion combustion phase flames during dual-fuel combustion can also be correlated with recorded pressure data and used to indicate possible regions of high $NO_x$ formation as well as soot formation/ oxidation. The transition of combustion flame from the pilot fuel-air mixture to the premixed gaseous fuel-air mixture can also be assessed, further indicating how dual-fuel combustion progresses. For instance, the models proposed by Karim [59] which are based on the net energy conversion rate ("heat-release" rate) can be assessed optically. With regards to emulsified fuel use, the relationship between cylinder temperature and the occurrence of "microexplosions" can be assessed more explicitly via high-speed video. Here, the "microexplosions" can be seen via the violent disintegration of the injected emulsion droplets which would increase turbulence in the chamber.

As emulsified fuels did not reduce $NO_x$ significantly, additional steps are needed to lower $NO_x$ emissions further. For example, EGR can lower $NO_x$ emissions substantially (by about 50% with a 20% EGR volume percentage) while generally maintaining combustion quality during normal engine operation with neat diesel fuel [50]. Significant reductions in volumetric efficiency will be expected (of the order of 10-20%) [50]. While this can be tolerated in normal CI engines and direct-injection dual-fuel engines, it will be problematic for dual-fuel engines with port induction in terms of adequate gaseous fuel admission. Exhaust gas after-treatments must now be considered, where previous work has shown that typical catalytic converters (i.e. 3-way catalysts) can reduce $NO_x$ emissions of engines running stoichiometric air-fuel

ratios by almost 100% [48]. 3-way catalysts on their own will not work with most hydrogen engines as they employ lean air-fuel mixtures (which cause low catalytic reaction efficiencies in the catalyst device). Therefore, alternative methods need to be found. For instance, 3-way catalysts can be used with lean-burn engines by injecting unburnt fuel into the exhaust gas stream prior to entering the catalyst device [48]. $NO_x$ emission reductions of the order of 90% can be obtained when 3% of the fuel flow into the engine is injected into the exhaust stream. Broadly speaking this arrangement is expectedly complex in terms of fuel supply design, injected quantity and timing. Selective catalytic reduction (SCR) devices (that have been used in stationary combustion applications) on the other hand do not need stoichiometric conditions to work, thereby avoiding this problem. SCR devices use reducing agents (such as ammonia or more practically urea) together with a catalyst to promote the reduction reactions. SCR devices need substantial modification and refinement for automotive applications [147]. For instance, issues relating to maintaining an acceptable level of catalyst activity under typical engine operating temperatures and automotive space restrictions are prevalent. More work in this particular area coupled to dual-fuel engines is needed.

The following recommendations are specific to improving the Gardner test rig. Multiple attempts were made near the end of this work to repeat the natural gas tests with test conditions similar to the hydrogen gas tests (i.e. the increased pilot fuel amount). Due to extensive repair/ rebuild work to the laboratory natural gas supply system this was not possible. These repeat tests would allow a more direct comparison between the two gaseous fuels during dual-fuel operation in terms of pilot fuel enthalpy fractions. The fuel emulsifying system also needs to be improved as problems with engine stability (due to non-firing cycles) during emulsified fuel tests would occur regularly. This made experiments tiresome to conduct and prevented emulsions with higher water concentrations ($> 10\%$ by volume) from being tested. The stability of the emulsions can be maintained to a much larger extent if the pilot fuel supply line to the engine (specifically the fuel pump) can be made as short as possible. Following this, the various physical properties of the water-in-fuel emulsions used in this work should be assessed in detail. For instance, bulk moduli and viscosity values of water-in-fuel emulsions could not be found over the course of this work. An exact value for a particular property would help gauge the resulting engine emission and performance trends more accurately. A hydrogen gas concentration analyser is also needed to determine levels of unburnt hydrogen gas in the exhaust gas. No measured assessment can be made of this at present.

# References


[1] Population Division United States Census Bureau International Database. World Population: 1950-2050. Available online, December 2008.

[2] British Petroleum. BP statistical review of world energy. BP annual review, June 2010.

[3] Energy Information Administration-Official Energy Statistics from the U.S. Government. Brent-Europe Crude Oil Spot Prices 1987-2010, June 2010.

[4] United States Environmental Protection Agency. Frequently Asked Questions About Global Warming and Climate Change: Back to Basics. Available online, 2010.

[5] H. Douville, F. Chauvin, S. Planton, J. F. Royer, D. Salas-Melia, and S. Tyteca. Sensitivity of the hydrological cycle to increasing amounts of greenhouse gases and aerosols. *Climate Dynamics*, 20(1):45–68, November 2002.

[6] The European Parliament and the Council of the European Union. Regulation (EC) No 715/2007 of the European parliament and of the council of 20 June 2007 on type approval of motor vehicles with respect to emissions from light passenger and commercial vehicles (Euro 5 and Euro 6) and on access to vehicle repair and maintenance information. Official Journal: OJL 171, 20 June 2007.

[7] T. Korakianitis and D. G. Wilson. Models for predicting the performance of Brayton-cycle engines. *Transactions of the ASME, Journal of Engineering for Gas Turbines and Power*, 116(2):381–388, April 1994.

[8] T. Korakianitis, J. Grantstrom, P. Wassingbo, and A. Massardo. Parametric performance of combined-cogeneration power plants with various power and efficiency enhancements. *Transactions of the ASME, Journal of Engineering for Gas Turbines and Power*, 127(1):65–72, January 2005.

[9] T. Korakianitis, L. Meyer, M. Boruta, and H. E. McCormick. Introduction and performance prediction of a nutating-disk engine. *Transactions of the ASME, Journal of Engineering for Gas Turbines and Power*, 126(2):294–299, April 2004.

[10] T. Korakianitis, M. Boruta, J. Jerovsek, and P. L. Meitner. Performance of a single nutating disk engine in the 2 to 500 kW power range. *Applied Energy*, 86(10):2213–2221, Oct 2009.

[11] T. Korakianitis. Personal Communication, 2010.

[12] M. Balat and H. Balat. A critical review of biodiesel as a vehicular fuel. *Energy Conversion and Management*, 49(10):2727–2741, October 2008.

[13] A. Murugesan, C. Umarani, R. Subramanian, and N. Nedunchezhian. Biodiesel as an alternative fuel for diesel engines-A review. *Renewable and Sustainable Energy Reviews*, 13(3):653–662, April 2009.

[14] J. M. Marchetti, V. U. Miguel, and A. F. Errazu. Possible methods for biodiesel production. *Renewable and Sustainable Energy Reviews*, 11(6):1300–1311, August 2007.

[15] A. K. Hossain and P. A. Davies. Plant oils as fuels for compression ignition engines: A technical review and life-cycle analysis. *Renewable Energy*, 35(1):1–13, January 2010.

[16] J. Sheehan, V. Camobreco, J. Duffield, M. Graboski, and H. Shapouri. An overview of biodiesel and petroleum diesel life cycles. National Renewable Energy Laboratory Report, NREL/TP-580-24772, 1998.

[17] F. Pearce. Fuels gold: Big risks of the biofuel revolution. New Scientist online, September 2006.

[18] G. W. Huber. Breaking the chemical and engineering barriers to lignocellusic biomass: Next generation hydrocarbon refineries. Workshop Report. University of Massachusetts Amherst, March 2008.

[19] R. J. Crookes and K. D. H. Bob-Manuel. RME or DME: A preferred alternative fuel option for future diesel engine operation. *Energy Conversion and Management*, 48(11):2971–2977, November 2007.

[20] A. K. Agarwal. Biofuels (alcohols and biodiesel) applications as fuels for internal combustion engines. *Progress in Energy and Combustion Science*, 33(3):233–271, June 2007.

[21] M. Lapuerta, O. Armas, and J. Rodriguez-Fernandez. Effect of biodiesel fuels on diesel engine emissions. *Progress in Energy and Combustion Science*, 34(2):198–223, April 2008.

[22] A. L. Boehman, D. Morris, J. Szybist, and E. Esen. The impact of the bulk modulus of Diesel fuels on fuel injection timing. *Energy and Fuels*, 18(6):1877–1882, November-December 2004.

[23] J. Sun, J. A. Caton, and T. J. Jacobs. Oxides of nitrogen emissions from biodiesel-fuelled diesel engines. *Progress in Energy and Combustion Science*, 36(6):677–695, December 2010.

[24] J. Huang and R. J. Crookes. Assessment of simulated biogas as a fuel for the spark ignition engine. *Fuel*, 77(15):1793–1801, December 1998.

[25] Department of Energy and Climate Change. Digest of United Kingdom Energy Statistics, 2009.

[26] International Association for Natural Gas Vehicles. Natural Gas Vehicle Statistics. In Press, December 2008.

[27] L. Dondero and J. Goldemberg. Environmental implications of converting light gas vehicles: The Brazilian experience. *Energy Policy*, 33(13):1703–1708, September 2005.

[28] E. Porpatham, A. Ramesh, and B. Nagalingam. Investigation on the effect of concentration of methane in biogas when used as a fuel for a spark ignition engine. *Fuel*, 87(8-9):1651–1659, July 2008.

[29] S. O. Bade Shrestha and G. Narayanan. Landfill gas with hydrogen addition-a fuel for SI engines. *Fuel*, 87(17-18):3616–3626, December 2008.

[30] J. M. Lopez, A. Gomez, F. Aparicio, and F. J. Sanchez. Comparison of GHG emissions from diesel, biodiesel and natural gas refuse trucks of the City of Madrid. *Applied Energy*, 86(5):610–615, May 2009.

[31] P. Dimopoulos, C. Bach, P. Soltic, and K. Boulouchos. Hydrogen-natural gas blends fuelling passenger car engines: Combustion, emissions and well-to-wheels assessment. *International Journal of Hydrogen Energy*, 33(23):7224–7236, December 2008.

[32] M. DAgosto and S. K. Ribeiro. Assessing total and renewable energy in Brazilian automotive fuels. A life cycle inventory (LCI) approach. *Renewable and Sustainable Energy Reviews*, 13(6-7):1326–1337, August-September 2009.

[33] H. M. Cho and B. He. Spark ignition natural gas engines-A review. *Energy Conversion and Management*, 48(2):608–618, February 2007.

[34] K. Zeng, Z. Huang, B. Liu, L. Liu, D. Jiang, Y. Ren, and J. Wang. Combustion characteristics of a direct-injection natural gas engine under various fuel injection timings. *Applied Thermal Engineering*, 26(8-9):806–813, June 2006.

[35] J. B. Heywood. *Internal Combustion Engine Fundamentals*. McGraw-Hill, 1988.

[36] T. Korakianitis, A. M. Namasivayam, and R. J. Crookes. Natural-gas fuelled spark-ignition (SI) and compression-ignition (CI) engine performance and emissions. *Progress in Energy and Combustion Science*, 37(1):89–112, January 2011.

[37] P. Mello, G. Pelliza, R. Catalua, and R. da Silva. Evaluation of the maximum horsepower of vehicles converted for use with natural gas fuel. *Fuel*, 85(14-15):2180–2186, October 2006.

[38] R.L. Evans and J. Blaszczyk. A comparative study of the performance and exhaust emissions of a spark ignition engine fuelled by natural gas and gasoline. *Proceedings of the Institution of Mechanical Engineers Part D-Journal of Automobile Engineering*, 211(1):39–47, 1997.

[39] C. Bach, C. Lammle, R. Bill, P. Soltic, D. Dyntar, P. Janner, K. Boulouchos, C. Onder, T. Landenfeld, L. Kercher, O. Seel, and J. D. Baronick. Clean engine vehicle. A natural gas driven EURO 4/SULEV with 30% reduced $CO_2$ emissions. SAE paper 2004-01-0645, 2004.

[40] U. Kesgin. Effect of turbocharging system on the performance of a natural gas engine. *Energy Conversion and Management*, 46(1):11–32, January 2005.

[41] N. Kahraman, B. Bilge eper, S. S. Orhan Akansu, and K. Aydin. Investigation of combustion characteristics and emissions in a spark-ignition engine fuelled with natural gas-hydrogen blends. *International Journal of Hydrogen Energy*, 34(2):1026–1034, January 2009.

[42] T. Thurnheer, P. Soltic, and P. D. Eggenschwiler. SI engine fuelled with gasoline, methane and methane/hydrogen blends: Heat release and loss analysis. *International Journal of Hydrogen Energy*, 34(5):2494–2503, March 2009.

[43] F. Ma, S. Ding, Y. Wang, Y. Wang, J. Wang, and S. Zhao. Study on combustion behaviors and cycle-by-cycle variations in a turbocharged lean burn natural gas SI engine with hydrogen enrichment. *International Journal of Hydrogen Energy*, 33(23):7245–7255, December 2008.

[44] P. Dimopoulos, C. Rechsteiner, P. Soltic, C. Laemmle, and K. Boulouchos. Increase of passenger car engine efficiency with low engine-out emissions using hydrogen-natural gas mixtures: A thermodynamic analysis. *International Journal of Hydrogen Energy*, 32(14):3073–3083, September 2007.

[45] E. Hu, Z. Huang, B. Liu, J. Zheng, and X. Gu. Experimental study on combustion characteristics of a spark-ignition engine fueled with natural gas-hydrogen blends combining with EGR. *International Journal of Hydrogen Energy*, 34(2):1035–1044, January 2009.

[46] J. Wang, H. Chen, B. Liu, and Z. Huang. Study of cycle-by-cycle variations of a spark ignition engine fueled with natural gas-hydrogen blends. *International Journal of Hydrogen Energy*, 33(18):4876–4883, September 2008.

[47] F. Ma and Y. Wang. Study on the extension of lean operation limit through hydrogen enrichment in a natural gas spark-ignition engine. *International Journal of Hydrogen Energy*, 33(4):1416–1424, February 2008.

[48] S. Verhelst and T. Wallner. Hydrogen-fueled internal combustion engines. *Progress in Energy and Combustion Science*, 35(6):490–527, December 2009.

[49] C. M. White, R. R. Steeper, and A. E. Lutz. The hydrogen-fuelled internal combustion engine: A technical review. *International Journal of Hydrogen Energy*, 31(10):1292–1305, August 2006.

[50] G. H. Abd-Alla. Using exhaust gas recirculation in internal combustion engines: A review. *Energy Conversion and Management*, 43(8):1027–1042, May 2002.

[51] E. R. Jayaratne, Z. D. Ristovski, N. Meyer, and L. Morawska. Particle and gaseous emissions from compressed natural gas and ultralow sulphur diesel-fuelled buses at four steady engine loads. *Science of The Total Environment*, 407(8):2845–2952, April 2009.

[52] L. Turrio-Baldassarri, C. L. Battistelli, L. Conti, R. Crebelli, B. De Berardis, A. L. Iamiceli, M. Gambino, and S. Iannaccone. Evaluation of emission toxicity

of urban bus engines: Compressed natural gas and comparison with liquid fuels. *Science of The Total Environment*, 355(1-3):64–77, February 2006.

[53] R. J. Crookes. Comparative bio-fuels performance in internal combustion engines. *Biomass & Bioenergy*, 30:461–468, 2006.

[54] C. Arcoumanis, H. Flora, J. W. Kim, and H. M. Xu. Injection natural gas engine for light-duty applications. International Conference on 21st Century Emissions Technology. London, England, 4-5 December, 2000.

[55] J. J. Zheng, J. H. Wang, B. Wang, and Z. H. Huang. Effect of the compression ratio on the performance and combustion of a natural-gas direct-injection engine. *Proceedings of the Institution of Mechanical Engineers Part D-Journal of Automobile Engineering*, 223(D1):85–98, January 2009.

[56] UK Department for Transport. Transport Statistics Great Britain (TSGB), 2009.

[57] A. Malynn, H. Musawi, S. Odetunde, and C. Rodrigues. Alternative automobile engine fuels for the UK market. MEng Group Thesis, Queen Mary and Westfield College, University of London, 2006.

[58] R. J. Crookes, K. D. H. Bob-Manuel, and J. Olsen. Renewable fuelling of a diesel engine in single and dual fuel operation. Technische Akademie Esslingen (TAE) 6th International Colloquium fuels, 10 - 11 January 2007.

[59] G. A. Karim. Combustion in gas fueled compression: Ignition engines of the dual fuel type. *Journal of Engineering for Gas Turbines and Power*, 125(3):827–836, July 2003.

[60] J. Kusaka, T. Okamoto, Y. Daisho, R. Kihara, and T. Saito. Combustion and exhaust gas emission characteristics of a diesel engine dual-fuelled with natural gas. *JSAE Review*, 21(4):489–496, October 2000.

[61] R. G. Papagiannakis and D. T. Hountalas. Combustion and exhaust emission characteristics of a dual fuel compression ignition engine operated with pilot diesel fuel and natural gas. *Energy Conversion and Management*, 45(18-19):2971–2987, November 2004.

[62] A. P. Carlucci, A. Ficarella, and D. Laforgia. Control of the combustion behavior in a diesel engine using early injection and gas addition. *Applied Thermal Engineering*, 26(17-18):2279–2286, December 2006.

[63] B. B. Sahoo, N. Sahoo, and U. K. Saha. Effect of engine parameters and type of gaseous fuel on the performance of dual-fuel gas diesel engines-A critical review. *Renewable and Sustainable Energy Reviews*, 13(6-7):1151–1184, August-September 2009.

[64] R. G. Papagiannakis and D. T. Hountalas. Experimental investigation concerning the effect of natural gas percentage on performance and emissions of a DI dual fuel diesel engine. *Applied Thermal Engineering*, 23(3):353–365, February 2003.

[65] M. Y. E. Selim. Pressure-time characteristics in diesel engine fueled with natural gas. *Renewable Energy*, 22(4):473–489, April 2001.

[66] G. A. Karim. A review of combustion processes in the dual fuel engine-The gas diesel engine. *Progress in Energy and Combustion Science*, 6(3):277–285, 1980.

[67] L. Shenghua, Z. Longbao, W. Ziyan, and R. Jiang. Combustion characteristics of compressed natural gas/diesel dual-fuel turbocharged compressed ignition engine. *Journal of Automobile Engineering*, 217(9):833–838, 2003.

[68] R. J. Crookes, T. Korakianitis, and A. M. Namasivayam. A systematic experimental assessment of the use of rapeseed methyl ester (RME) as a compression ignition engine fuel during conventional and dual-fuel operation. TAE 7th International Colloquium on Fuels, Stuttgart, 14-15 January, 2009.

[69] P. M. Duc and K. Wattanavichien. Study on biogas premixed charge diesel dual fuelled engine. *Energy Conversion and Management*, 48(8):2286–2308, August 2007.

[70] M. Y. E. Selim. Effect of engine parameters and gaseous fuel type on the cyclic variability of dual fuel engines. *Fuel*, 84(7-8):961–971, May 2005.

[71] A. M. Namasivayam, R. J. Crookes, T. Korakianitis, and J. Olsen. Assessment of combustion in natural gas fuelled compression ignition engines with DME and RME pilot ignition. *Proceedings of the I.Mech.E., International Journal of Engine Research*, 10(3):165–174, 2009.

[72] M. Y. E. Selim. Sensitivity of dual fuel engine combustion and knocking limits to gaseous fuel composition. *Energy Conversion and Management*, 45(3):411–425, February 2004.

[73] V. Pirouzpanah, R. Khoshbakhti Saray, A. Sohrabi, and A. Niaei. Comparison of thermal and radical effects of EGR gases on combustion process in dual fuel engines at part loads. *Energy Conversion and Management*, 48(7):1909–1918, July 2007.

[74] M. Y. E. Selim. Effect of exhaust gas recirculation on some combustion characteristics of dual fuel engine. *Energy Conversion and Management*, 44(5):707–721, March 2003.

[75] G. H. Abd-Alla, H. A. Soliman, O. A. Badr, and M. F. Abd-Rabbo. Effects of diluent admissions and intake air temperature in exhaust gas recirculation on the emissions of an indirect injection dual fuel engine. *Energy Conversion and Management*, 42(8):1033–1045, May 2001.

[76] G. P. McTaggart-Cowan, H. L. Jones, S. N. Rogak, W. K. Bushe, P. G. Hill, and S. R. Munshi. Direct-injected hydrogen-methane mixtures in a heavy duty compression ignition engine. SAE paper 2006-01-0653, 2006.

[77] K. K. Srinivasan, S. R. Krishnan, and K. C. Midkiff. Improving low load combustion, stability, and emissions in pilot-ignited natural gas engines. *Journal of Automobile Engineering*, 220(2):229–239, 2006.

[78] D. R. Tree and K. I. Svensson. Soot processes in compression ignition engines. *Progress in Energy and Combustion Science*, 33(3):272–309, June 2007.

[79] O. M. I. Nwafor. Effect of advanced injection timing on emission characteristics of diesel engine running on natural gas. *Renewable Energy*, 32(14):2361–2368, November 2007.

[80] J. Olsen, R. J. Crookes, and K. D. H. Bob-Manuel. Experiments in dual fuelling a compression ignition engine by injecting di-methyl ether as a pilot fuel to ignite varying quantities of natural gas. SAE paper 2007-01-3624, August 2007.

[81] R. G. Papagiannakis, D. T. Hountalas, and C. D. Rakopoulos. Theoretical study of the effects of pilot fuel quantity and its injection timing on the performance and emissions of a dual fuel diesel engine. *Energy Conversion and Management*, 48(11):2951–2961, November 2007.

[82] N. R. Banapurmath and P. G. Tewari. Comparative performance studies of a 4-stroke CI engine operated on dual fuel mode with producer gas and Honge

oil and its methyl ester (HOME) with and without carburetor. *Renewable Energy*, 34(4):1009–1015, April 2009.

[83] O. M. I. Nwafor. Effect of choice of pilot fuel on the performance of natural gas in diesel engines. *Renewable Energy*, 21(3-4):495–504, November 2000.

[84] N. R. Banapurmath, P. G. Tewari, and R. S. Hosmath. Experimental investigations of a four-stroke single cylinder direct injection diesel engine operated on dual fuel mode with producer gas as inducted fuel and Honge oil and its methyl ester (HOME) as injected fuels. *Renewable Energy*, 33(9):2007–2018, September 2008.

[85] M. Y. E. Selim, M. S. Radwan, and H. E. Saleh. Improving the performance of dual fuel engines running on natural gas/LPG by using pilot fuel derived from jojoba seeds. *Renewable Energy*, 33(6):1173–1185, June 2008.

[86] G. P. McTaggart-Cowan, H. L. Jones, S. N. Rogak, W. K. Bushe, P. G. Hill, and S. R. Munshi. The effects of high-pressure injection on a compression-ignition, direct injection of natural gas engine. *Journal of Engineering for Gas Turbines and Power*, 129(2):579–588, April 2007.

[87] B. E. Milton and K. Pianthong. Pulsed, supersonic fuel jets-A review of their characteristics and potential for fuel injection. *International Journal of Heat and Fluid Flow*, 26(4):656–671, August 2005.

[88] M. Mbarawa, B. E. Milton, and R. T. Casey. Experiments and modelling of natural gas combustion ignited by a pilot diesel fuel spray. *International Journal of Thermal Sciences*, 40(10):927–936, 2001.

[89] M. Mbarawa, B. E. Milton, and R. T. Casey. An investigation of the effects of diesel pilot injection parameters on natural gas combustion under diesel conditions. *Journal of the Institute of Energy*, 74(500):81–90, September 2001.

[90] F. Bedford, C. Rutland, P. Dittrich, A. Raab, and F. Wirebeleit. Effects of direct water injection on DI diesel engine combustion. SAE Paper No 2000-01-2938, 2000.

[91] A. Sarvi, P. Kilpinen, and R. Zevenhoven. Emissions from large-scale medium-speed diesel engines: 3. Influence of direct water injection and common rail. *Fuel Processing Technology*, 90(2):222–231, February 2009.

[92] H. Ozkan and M. S. Soylemez. Thermal balance of a LPG fuelled, four stroke SI engine with water addition. *Energy Conversion and Management*, 47(5):570–581, March 2006.

[93] V. Subramanian, J. M. Mallikarjuna, and A. Ramesh. Effect of water injection and spark timing on the nitric oxide emission and combustion parameters of a hydrogen-fuelled spark ignition engine. *International Journal of Hydrogen Energy*, 32(9):1159–1173, June 2007.

[94] K. S. Wain, J. M. Perez, E. Chapman, and A. L. Boehman. Alternative and low sulfur fuel options: Boundary lubrication performance and potential problems. *Tribology International*, 38(3):313–319, March 2008.

[95] F. Kiannejad. Assessment of vegetable oil and emulsions for use as fuels in diesel engines. PhD Thesis, Queen Mary and Westfield College, University of London, 1993.

[96] R. J. Crookes, M. A. A. Nazha, and F. Kiannejad. Single and multi cylinder diesel-engine tests with vegetable oil emulsions. SAE-922230, 1992.

[97] R. J. Crookes, F. Kiannejad, and M. A. A. Nazha. Seed-oil bio-fuel of low cetane number: the effect of water emulsification on diesel-engine operation and emissions. *J. Inst. Energy*, 68:142–151, 1995.

[98] J. Ghojel, D. Honnery, and K. Al-Khaleefi. Performance, emissions and heat release characteristics of direct injection diesel engine operating on diesel oil emulsion. *Applied Thermal Engineering*, 26(17-18):2132–2141, December 2006.

[99] M. Nadeem, C. Rangkuti, K. Anuar, M. R. U. Haq, I. B. Tan, and S. S. Shah. Diesel engine performance and emission evaluation using emulsified fuels stabilized by conventional and gemini surfactants. *Fuel*, 85(14-15):2111–2119, October 2006.

[100] A. Lif and K. Holmberg. Water-in-diesel emulsions and related systems. *Advances in Colloid and Interface Science*, 123-126(5):231–239, November 2006.

[101] N. Samec, B. Kegl, and R. W. Dibble. Numerical and experimental study of water/oil emulsified fuel combustion in a diesel engine. *Fuel*, 81(6):2035–2044, November 2002.

[102] C. Y. Lin and L. W. Chen. Comparison of fuel properties and emission characteristics of two and three-phase emulsions prepared by ultrasonically vibrating

and mechanically homogenizing emulsification methods. *Fuel*, 87(10-11):2154–2161, August 2008.

[103] C. Y. Lin and S. A. Lin. Effects of emulsification variables on fuel properties of two and three-phase biodiesel emulsions. *Fuel*, 86(1-2):210–217, January 2007.

[104] G. A. Karim. Hydrogen as a spark ignition engine fuel. *Journal of Engineering for Gas Turbines and Power*, 28(5):569–577, May 2003.

[105] R. Sierens, S. Verhelst, and S. Verstraeten. An overview of hydrogen fuelled internal combustion engines. Proceedings International Hydrogen Energy Congress and Exhibition (IHEC) Istanbul, Turkey, 13-15 July 2005.

[106] N. Zamel and X. Li. Life cycle analysis of vehicles powered by a fuel cell and by internal combustion engine for Canada. *Journal of Power Sources*, 155(2):1241–1253, November 2006.

[107] R. Hari Ganesh, V. Subramaniam, V. Balasubramaniam, J. M. Mallikarjuna, A. Ramesh, and R. P. Sharma. Hydrogen fuelled spark ignition engine with electronically controlled manifold injection: An experimental study. *Renewable Energy*, 33(6):1324–1333, June 2008.

[108] J. W. Heffel. $NO_x$ and performance data for a hydrogen fueled internal combustion engine at 3000 rpm using exhaust gas recirculation. *International Journal of Hydrogen Energy*, 28(11):1285–1292, November 2003.

[109] J. W. Heffel. $NO_x$ emission and performance data for a hydrogen fueled internal combustion engine at 1500 rpm using exhaust gas recirculation. *International Journal of Hydrogen Energy*, 28(8):901–908, August 2003.

[110] S. Verhelst, P. Maesschalck, N. Rombaut, and R. Sierens. Increasing the power output of hydrogen internal combustion engines by means of supercharging and exhaust gas recirculation. *International Journal of Hydrogen Energy*, 34(10):4406–4412, May 2009.

[111] S. J. Lee, H. S. Yi, and E. S. Kim. Combustion characteristics of intake port injection type hydrogen engine. *International Journal of Hydrogen Energy*, 20(4):317–322, April 1995.

[112] A. Mohammadi, M. Shioji, Y. Nakai, W. Ishikura, and E. Tabo. Performance and combustion characteristics of a direct injection SI hydrogen engine. *International Journal of Hydrogen Energy*, 32(2):296–304, February 2007.

[113] H. S. Yi, S. J. Lee, and E. S. Kim. Performance evaluation and emission characteristics of in-cylinder injection type hydrogen fueled engine. *International Journal of Hydrogen Energy*, 21(7):617–624, July 1996.

[114] D. M. Kabat and J. W. Heffel. Durability implications of neat hydrogen under sonic flow conditions on pulse-width modulated injectors. *International Journal of Hydrogen Energy*, 27(10):1093–1102, October 2002.

[115] L. M. Das. Hydrogen engine: Research and development programmes in Indian Institute of Technology (IIT), Delhi. *International Journal of Hydrogen Energy*, 27(9):953–965, September 2002.

[116] J. D. Naber and D. L. Siebers. Hydrogen combustion under diesel engine conditions. *International Journal of Hydrogen Energy*, 23(5):363–371, May 1998.

[117] S. Szwaja and K. Grab-Rogalinski. Hydrogen combustion in a compression ignition diesel engine. *International Journal of Hydrogen Energy*, 34(10):4413–4421, May 2009.

[118] G. Gopal, P. Srinivasa Rao, K. V. Gopalakrishnan, and B. S. Murthy. Use of hydrogen in dual-fuel engines. *International Journal of Hydrogen Energy*, 7(3):267–272, 1982.

[119] T. N. Patro. Combustion study of hydrogen fueled DI diesel engine: Simplified heat release analysis. *International Journal of Hydrogen Energy*, 18(3):231–241, March 1993.

[120] B. Haragopala Rao, K. N. Shrivastava, and H. N. Bhakta. Hydrogen for dual fuel engine operation. *International Journal of Hydrogen Energy*, 8(5):381–384, 1983.

[121] N. Saravanan and G. Nagarajan. Performance and emission study in manifold hydrogen injection with diesel as an ignition source for different start of injection. *Renewable Energy*, 34(1):328–334, January 2009.

[122] N. Saravanan, G. Nagarajan, K. M. Kalaiselvan, and C. Dhanasekaran. An experimental investigation on hydrogen as a dual fuel for diesel engine system

with exhaust gas recirculation technique. *Renewable Energy*, 33(3):422–427, March 2008.

[123] Z. Liu and G. A. Karim. Knock characteristics of dual-fuel engines fuelled with hydrogen fuel. *International Journal of Hydrogen Energy*, 20(11):919–924, February 1995.

[124] P. K. Bose and D. Maji. An experimental investigation on engine performance and emissions of a single cylinder diesel engine using hydrogen as inducted fuel and diesel as injected fuel with exhaust gas recirculation. *International Journal of Hydrogen Energy*, 34(11):4847–4854, June 2009.

[125] A. Tsolakis, J. J. Hernandez, A. Megaritis, and M. Crampton. Dual fuel diesel engine operation using $H_2$. Effect on particulate emissions. *Energy and Fuels*, 19(2):418–425, January 2005.

[126] M. Masood, M. M. Ishrat, and A. S. Reddy. Computational combustion and emission analysis of hydrogendiesel blends with experimental verification. *International Journal of Hydrogen Energy*, 32(13):2539–2547, September 2007.

[127] N. Saravanan, G. Nagarajan, and S. Narayanasamy. An experimental investigation on DI diesel engine with hydrogen fuel. *Renewable Energy*, 33(3):415–421, March 2008.

[128] N. Saravanan and G. Nagarajan. An experimental investigation on performance and emissions study with port injection using diesel as an ignition source for different EGR flow rates. *International Journal of Hydrogen Energy*, 33(16):4456–4462, August 2008.

[129] V. Edwin-Geo, G. Nagarajan, and B. Nagalingam. Studies on dual-fuel operation of rubber seed oil and its bio-diesel with hydrogen as the inducted fuel. *International Journal of Hydrogen Energy*, 33(21):6357–6367, November 2008.

[130] M. Senthil Kumar, A. Ramesh, and B. Nagalingam. Use of hydrogen to enhance the performance of a vegetable oil fuelled compression ignition engine. *International Journal of Hydrogen Energy*, 28(10):1143–1154, October 2003.

[131] J. Wegrzyn and M. Gurevich. Adsorbent storage of natural gas. *Applied Energy*, 55(2):71–83, October 1996.

[132] O. Pupier, V. Goetz, and R. Fiscal. Effect of cycling operations on an adsorbed natural gas storage. *Chemical Engineering and Processing*, 44(1):71–79, January 2005.

[133] European Commission Joint Research Centre (JRC). Liquefied natural gas for Europe-Some important issues for consideration. JRC Reference Report, July 2009.

[134] H. L. MacLean and L. B. Lave. Evaluating automobile fuel/propulsion system technologies. *Progress in Energy and Combustion Science*, 29(1):1–69, 2003.

[135] Q. S. Chen, J. Wegrzyn, and V. Prasad. Analysis of temperature and pressure changes in liquefied natural gas (LNG) cryogenic tanks. *Cryogenics*, 44(10):701–709, October 2004.

[136] S. M. Aceves, G. D. Berry, J. Martinez-Frias, and F. Espinosa-Loza. Vehicular storage of hydrogen in insulated pressure vessels. *International Journal of Hydrogen Energy*, 31(15):2274–2283, December 2006.

[137] D. K. Ross. Hydrogen storage: The major technological barrier to the development of hydrogen fuel cell cars. *Vacuum*, 80(10):1084–1089, August 2006.

[138] V. Ananthachar and J. J. Duffy. Efficiencies of hydrogen storage systems onboard fuel cell vehicles. *Solar Energy*, 78(5):687–694, May 2005.

[139] A. Sarkar and R. Banerjee. Net energy analysis of hydrogen storage options. *International Journal of Hydrogen Energy*, 30(8):867–877, July 2005.

[140] R. Ewald. Requirements for advanced mobile storage systems. *International Journal of Hydrogen Energy*, 23(9):803–814, September 1998.

[141] U. Eberle, G. Arnold, and R. von Helmolt. Hydrogen storage in metal-hydrogen systems and their derivatives. *Journal of Power Sources*, 154(2):456–460, March 2006.

[142] W. B. Leung, N. H. March, and H. Motz. Primitive phase diagram for hydrogen. *Physics Letters*, 56A(6):425–426, 1976.

[143] W. Peschka. Hydrogen: The future cryofuel in internal combustion engines. *International Journal of Hydrogen Energy*, 23(1):27–43, January 1998.

[144] W. Peschka. Liquid hydrogen as a vehicular fuel-a challenge for cryogenic engineering. *International Journal of Hydrogen Energy*, 9(6):515–523, 1984.

[145] F. Michel, H. Fieseler, G. Meyer, and F. Theien. On-board equipment for liquid hydrogen vehicles. *International Journal of Hydrogen Energy*, 23(3):191–199, March 1998.

[146] M. Senthil Kumar, J. Bellettre, and M. Tazerout. The use of biofuel emulsions as fuel for diesel engines: a review. *Proceedings of the Institution of Mechanical Engineers, Part A: Journal of Power and Energy*, 223(7):729–742, May 2009.

[147] M. Koebel, M. Elsener, and M. Kleemann. Urea-SCR: a promising technique to reduce NOx emissions from automotive diesel engines. *Catalysis Today*, 59(3-4):335–345, June 2000.

[148] T. Korakianitis. Thermodynamics I (DEN107) lecture notes. Queen Mary University of London, 2010.

[149] R.S. Benson. Advanced Engineering Thermodynamics. 2nd Edition, 1977.

[150] D. G. Wilson and T. Korakianitis. *The design of high-efficiency turbomachinery and gas turbines*. Prentice Hall, 2nd edition, 1998.

# 6 Appendices

## 6.1 Appendix A - Optical Chamber Experimental Apparatus

In addition to the main experimental work, a secondary project was the commissioning of an optical combustion chamber to be equipped with an electronic common-rail fuel injection system. This optical chamber ultimately would allow optical assessment (via high-speed video) of CI combustion of different fuels during normal engine operation and dual-fuel operation. Specific areas of investigation using this optical chamber (which would be a very valuable tool for combustion analysis) have been illustrated in the section on future work. A number of years prior to the author starting the current work, a four-cylinder CI engine was heavily modified by Prof. Crookes and Dr. John Olsen to include a separate combustion chamber which allows optical access.

Table 10: Ford engine specifications (with 4 operating cylinders)

| | |
|---|---|
| Engine Model | In-line OHV |
| No. of cylinders | 4 |
| Bore | 93.67 mm |
| Stroke | 90.54 mm |
| Swept volume | $6.24 \times 10^{-4}\text{m}^3$ |
| Clearance volume | $0.3466 \times 10^{-4}\text{m}^3$ |
| Compression ratio | 19:1 |
| Max. power | 50kW @ 4000 r/min |
| Inlet valve opening | 13° BTDC |
| Inlet valve closing | 39° ABDC |
| Exhaust valve opening | 51° BBDC |
| Exhaust valve closing | 13° ATDC |
| Injection timing (1500 r/min) | 5° BTDC |
| Injection timing (2500 r/min) | 9° BTDC |
| Injection timing (3500 r/min) | 12° BTDC |
| Injector nozzle holes | 4 |
| Injector throat diameter | 220 $\mu$m |
| Injector opening pressure | 24.3 MPa |

The engine used is a Ford 2.5 litre four-stroke direct-injection CI engine, the specifications of which is shown in table 10. The modifications included removing the original fuel injector on cylinder number 1 and mounting a custom-made steel optical combustion chamber (equipped with two quartz windows) in its place. In addition, the original piston in cylinder number 1 (which had a "Mexican hat"-shaped recess) was replaced with a flat-topped piston. These modifications effectively transferred most of the volume where combustion occurs from the original cylinder clearance volume to the optical chamber volume. These modifications also changed the original compression ratio of cylinder number 1 (19:1) to about 13.6:1. This would allow comparative analysis with performance and emissions data from the Gardner engine which has a similar compression ratio (13.11:1). In addition, different "swirl-rings" can be fitted inside the chamber, allowing variations in the compression ratio as well as the type of swirl generated. No current swirl ratio has been measured as yet. The other three cylinders remained as standard. At the start of the current work, the task of testing and repairing the engine test cell (specifically electrics, fuel and cooling water supplies) as well as engine diagnostics (specifically cylinder pressure data acquisition) was undertaken by the author. In addition, an independently-controlled electronic common-rail direct injection rig was also being set-up for use with the optical chamber. In the following text, the progress to-date is discussed.

Figure 108 shows a cross-section of the optical chamber, detailing its location and orientation on the engine, together with preliminary planned locations of the fuel injector and a exhaust gas sampling valve. No cooling system for this chamber was designed. Guards made of Perspex sheets were placed around the chamber to prevent accidental contact. The chamber is fitted with a piezoelectric pressure transducer and a blow-off valve while no exhaust sampling valve has been fitted as of the time of writing. However, the fuel injector has been fitted to the optical chamber just prior to final thesis submission. There is also a second piezoelectric pressure transducer located in the cylinder head of cylinder 1, which gives pressure data from the remaining clearance volume in the original cylinder. Using the pressure traces from the optical chamber, ignition delay information (based on energy conversion rates during combustion and pressure derivatives) during fired tests can be obtained in addition to the recorded high-speed video.

Figure 109 shows the log-pressure versus log-volume plot for the pressure sensor fitted in the cylinder head (which is water-cooled). Here the compression line and expansion line more or less correlate to each other as the expansion line curvature

is relatively minimal.

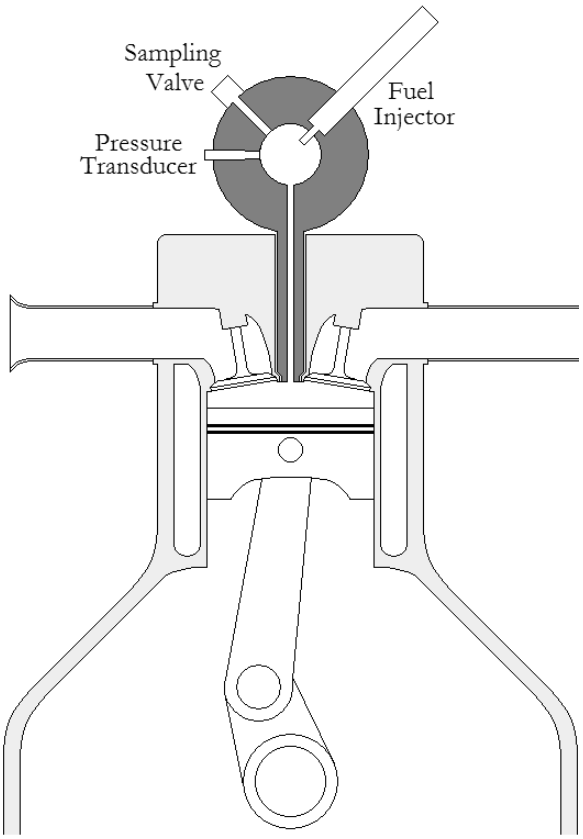


Figure 108: Position of optical chamber in cylinder, diagram courtesy of Dr. John Olsen

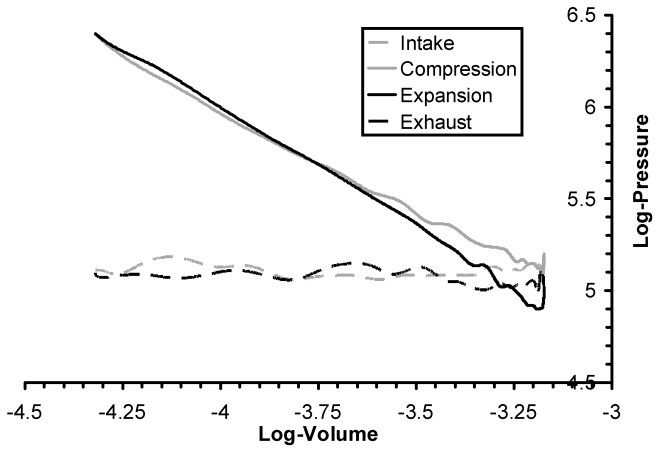


Figure 109: Log-of-cylinder pressure versus log-of-total volume (cylinder + optical chamber) during motored operation at 1000 r/min

The slopes of the compression and expansion lines in figure 109 are about 1.27 and 1.34 respectively, which are reasonable considering the polytropic relation:

$$pV^n = constant \tag{20}$$

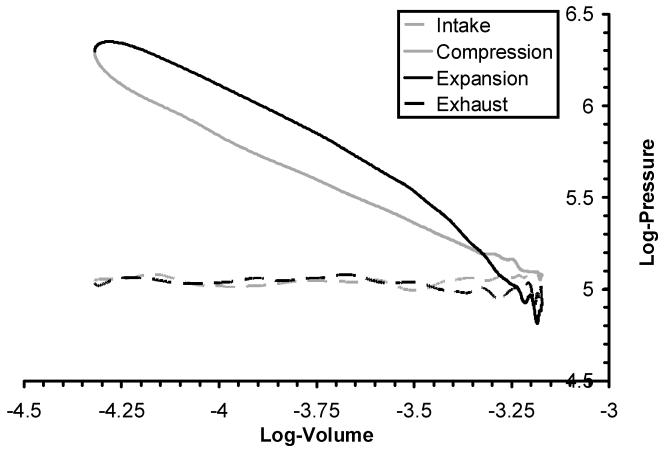


Figure 110: Log-of-optical chamber pressure versus log-of-total volume (cylinder + optical chamber) during motored operation at 1000 r/min

where $p$ is cylinder pressure, $V$ is cylinder volume and $n$ should be about 1.3 (which should match the slope values) for compression and expansion processes. However, the log-pressure versus log-volume plot of the optical chamber pressure sensor (figure 110) shows a significant curvature of the expansion line. Here the slopes of the compression and expansion lines are about 1.03 and 1.15 respectively. These values can result from substantial energy (i.e. "heat") transfer out of the optical chamber (as it is not cooled and is exposed to ambient air), in addition to charge leakage past the quartz window seals. Recent test runs where the optical chamber was motored has revealed substantial charge leakage (felt by hand) past the aluminium O-ring seals, which sit between the window and the optical chamber cap. These sealing issues could be resolved by using a softer metal material for the O-ring (possibly copper) in addition to high-temperature non-hardening gasket paste. With these improvements, it is possible that values of $n$ closer to 1.3 would be obtained.

Figure 111 shows a motored pressure trace from both sensors, plotted against crank-angle. This trace was taken with the engine motoring cylinder 1 at 1000 r/min. Here the optical chamber pressure lags behind the cylinder pressure trace (by about 9 degrees crank angle), while peak pressure values are lowered by about 0.3 MPa. The lower peak pressure can result from several factors. The first is that there is substantial charge leakage from the optical chamber (which affects the polytropic constant as discussed earlier). The pressure drop can also result from mass flow through the restriction between the larger volume in the optical chamber and the original cylinder clearance volume. The lag in the optical chamber pressure trace

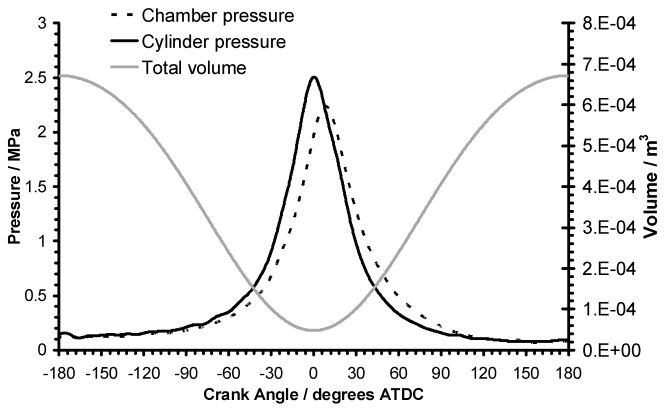


Figure 111: Cylinder pressure, optical chamber pressure and total volume (cylinder + optical chamber) during motored operation at 1000 r/min

can result from the time taken for charge mass to flow through the restriction from the cylinder clearance volume to the optical chamber volume. In addition, the pressure wave travelling through the same passage from cylinder head clearance volume to the optical chamber volume can affect this delay. With regards to the latter, order-of-magnitude calculations were made to assess if this is plausible. This was done via a rough speed-of-sound calculation, using equation 4 on page 12. To obtain the density of air under different conditions, the corresponding temperatures are required. As the optical chamber is exchanging charge with the cylinder volume, an initial assumption of constant mass (which would allow analysis via the ideal gas relationship) to obtain charge temperature would not be appropriate. Consideration was then given to open system analysis, specifically charging and discharging rigid vessels. However, a common assumption in these cases is that the vessel is exchanging working fluid with a thermodynamic reservoir at a constant pressure and temperature. This assumption is also not valid in this case as the cylinder volume is at varying pressure and temperature. The severity of charge leakage is also unknown considering figure 110, which complicates analysis further. As a result, the problem of defining the optical chamber as a thermodynamic system suitable for manageable analysis is intractable at this point in time.

As stated earlier, the optical chamber itself was made some years prior to the start of this project but no original design drawings were found. As a result, new drawings of the chamber (shown in figures 112 and 113) were made in AutoCAD 2008 in preparation for the installation of the fuel injector. The drawing shows the locations of the pressure transducer, blow-off valve, quartz windows, and the swirl ring.

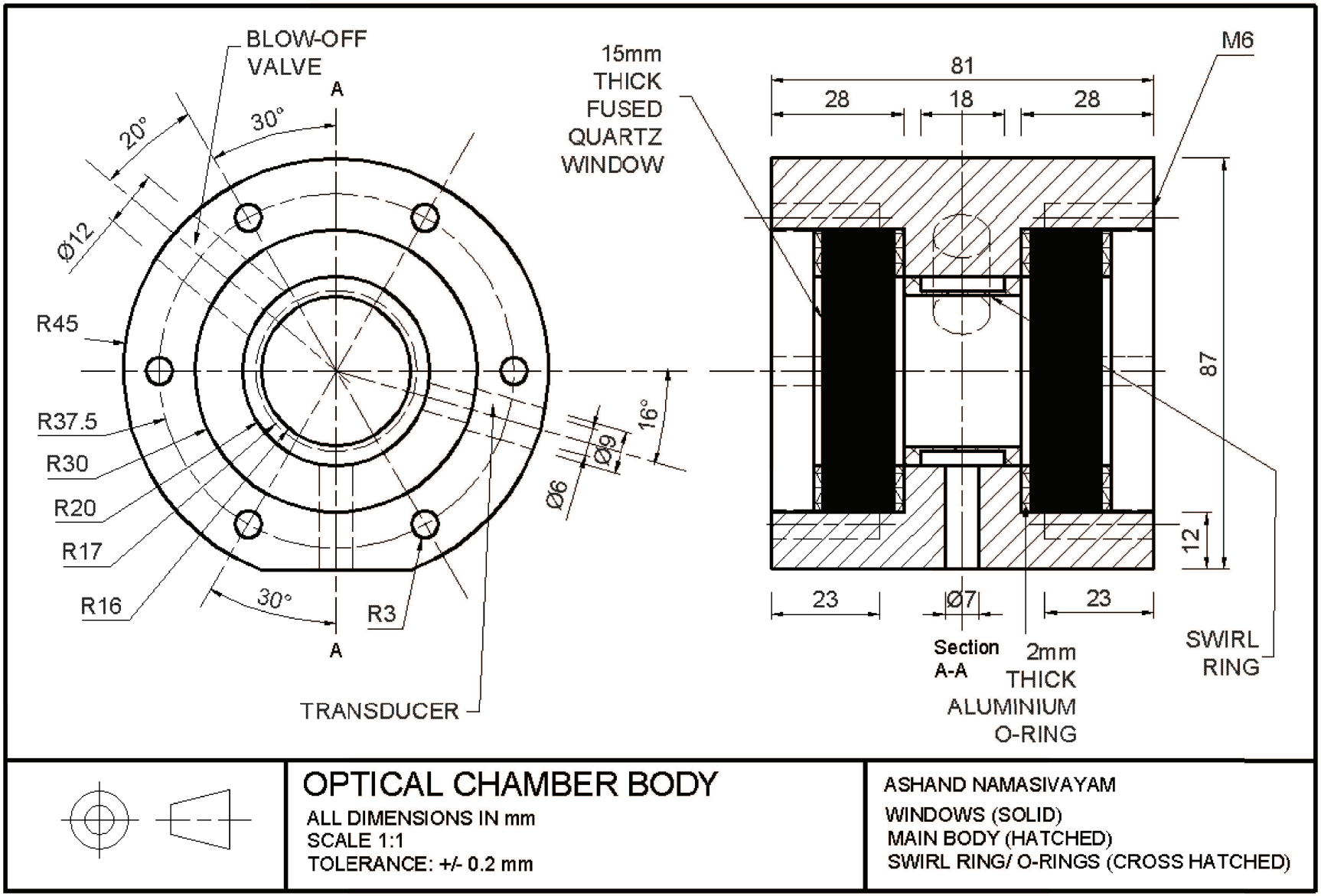


Figure 112: Optical chamber body

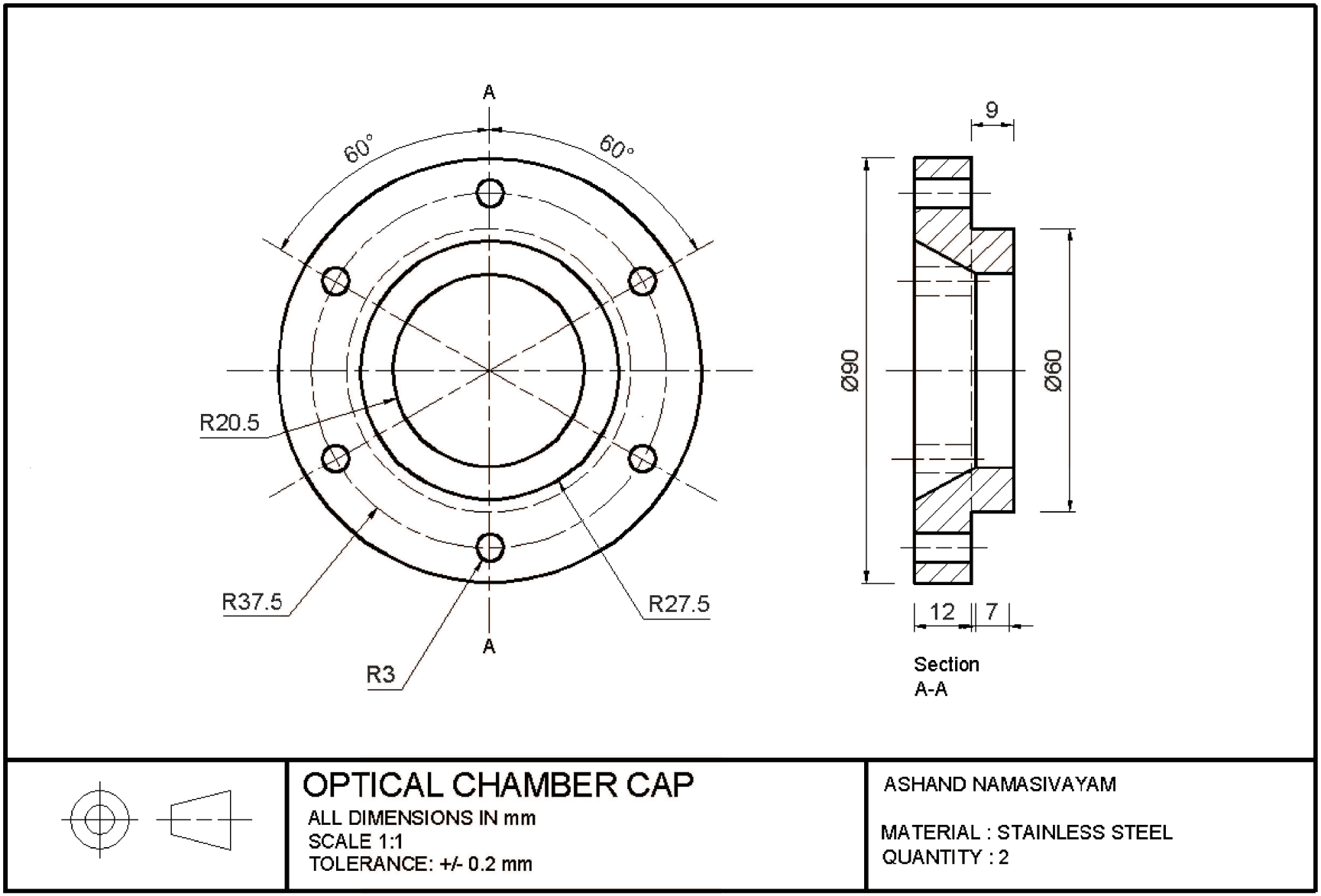


Figure 113: Optical chamber cap

Table 11: Common-rail injection system specifications

| Model | Siemens VDO PCR 2.3 Lynx |
|---|---|
| Max. operating pressure | 160 MPa |
| Pump valves supply voltage | 12 V |
| Pump valves PWM frequencies | 350 Hz (PCV)/ 200 Hz (VCV) |
| Injector supply voltage | 200 V |
| Number of injectors | 4 |
| Injector nozzle holes | 7 |
| Injector nozzle hole diameter | 110 $\mu$m |
| Injector nozzle spray angle | 152$^o$ |
| Piezo "open" delay time | 0.15 ms |
| Piezo "close" delay time | 0.15 ms |

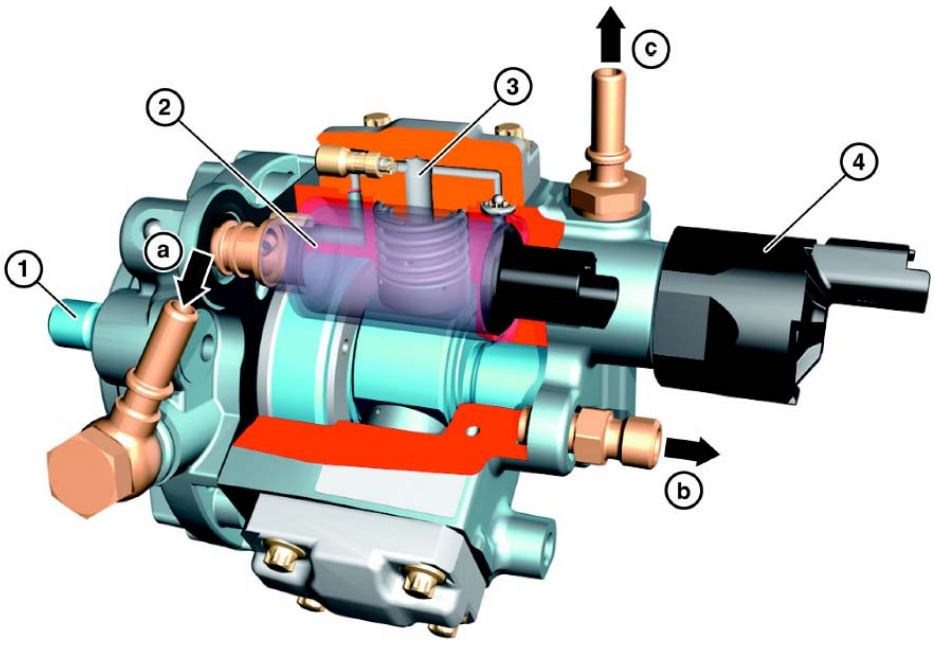


Figure 114: Siemens Lynx PCR common-rail pump, diagram from Siemens PCR Lynx service manual

The common-rail injection system used is a Siemens Piezo Common Rail (PCR) 2.3 Lynx system, where four piezoelectric injectors are used in conjunction with a fuel pump and a fuel rail. Table 11 shows the specifications of this system. A 3-phase electric motor is used to drive the common-rail pump (instead of the engine crankshaft), which feeds fuel to the fuel rail under pressure (maximum operating pressure is about 160 MPa). Figure 114 shows the common-rail pump unit itself which consists of four main components; a built-in transfer pump (1) and a high-

pressure pump (3) as well as two electronic solenoid valves, a volume control valve (VCV, 2) and a pressure control valve (PCV, 4). Also shown in the figure is the inlet port to the transfer pump (a), the outlet to the fuel-rail (b) and the fuel return outlet (c). The transfer pump draws fuel from the supply line (normally from the fuel tank) and feeds the high-pressure pump. The high-pressure pump generates the fuel pressure and feeds the common rail. The PCV connects the high pressure pump outlet to both the fuel rail outlet and the fuel return outlet (which allows excess fuel to flow from the pump back into the supply) thereby controlling the rail pressure level in the high-pressure pump. The VCV connects the transfer pump to the high-pressure pump, thereby controlling the fuel flow into the high-pressure pump. Both valves are operated via pulse-width modulated (PWM) voltage signals, which are normally fed to the valves in terms of duty cycles from an engine control unit (ECU). A duty cycle is the proportion of time a device is "on" over the regular desired interval in percentage. As an example, a device that is operated with a 50% PWM duty cycle means that the device is "on" for half a given time, while a 100% duty cycle is essentially fully on and a 0% duty cycle is essentially fully off. The VCV normally operates as part of an open loop with an ECU, and is governed by the engine's fuelling requirements (to maintain a certain speed/ load). The PCV normally operates in a closed loop with a built-in fuel rail pressure sensor and the ECU, maintaining an appropriate fuel supply pressure in the fuel rail for supplying fuel to the fuel injectors. In this case the PCV also acts as a dump-valve, reducing the fuel-rail pressure if it gets too high by releasing fuel to the fuel return line.

The common-rail pump (i.e. the transfer pump and high-pressure pump) operates when the electric motor is switched on. The pump generates about 2 MPa of pressure in the fuel rail even when both control valves remain turned off (PWM duty cycle at 0%). Using a custom-made LabVIEW program and relay circuit, full control over both the PCV and VCV (and hence the fuel-rail pressure) is allowed via user-defined PWM duty cycles. In the case of both the PCV and VCV, a duty cycle of about 20%-30% is required to produce maximum operating pressure in the fuel rail. Increasing the VCV duty cycle opens the VCV itself and allows more fuel to flow from the transfer pump to the high-pressure pump, thereby increasing the fuel supply to the fuel rail and the pressure level. Increasing the PCV duty cycle closes the PCV, restricting the fuel flow out from the high pressure pump to the fuel return line. This allows further increases in fuel-rail pressure. In addition to the original built-in fuel-rail pressure sensor, an Omega type PX41S0-30KG5V pressure sensor is fitted on one of the common-rail outlets. One common rail injector is fitted to

the fuel rail with the original high-pressure steel tubing, while the remaining two outlets are blocked off with Swagelok components.

Another custom-made LabVIEW program has already been made to operate the injector (via user-defined start-of-injection timing and injector pulse duration) based on shaft encoder and piston TDC sensor signals from the engine.

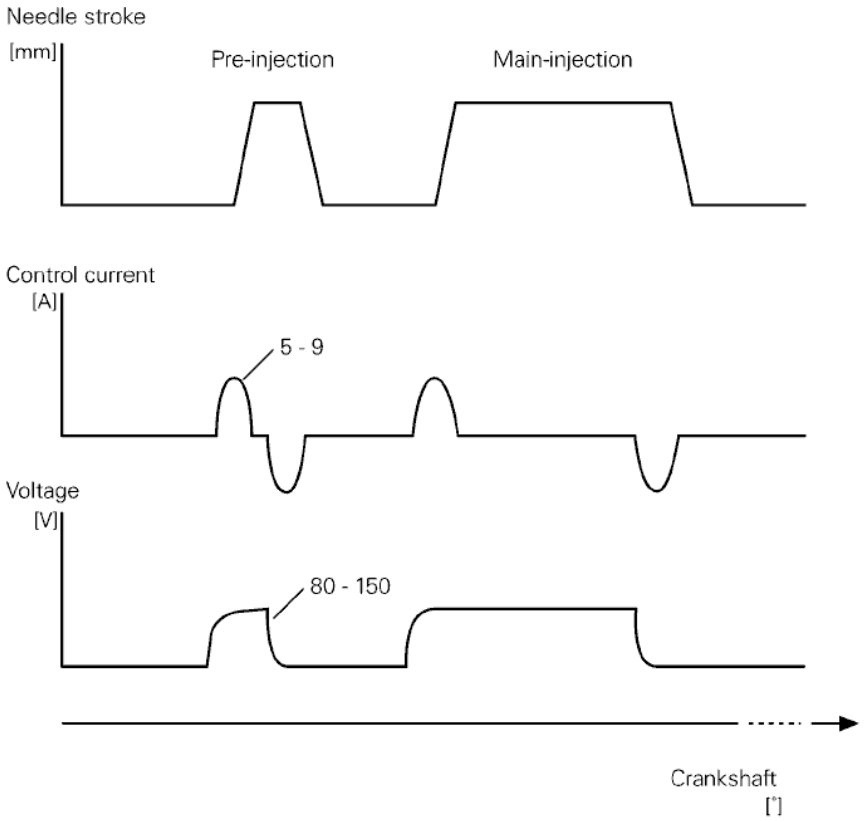


Figure 115: Typical needle lift, voltage and current profiles for piezoelectric injector operation, diagram from Siemens PCR Lynx service manual

This program employs PWM signals to generate the correct profile shapes needed to operate the injector. An example of these profiles for typical injector operation (consisting of a pilot injection and a main injection) can be seen figure 115. The hardware necessary for this is proving difficult to put together in-house using basic components, as evidenced by multiple failed injector tests with prototype circuits. Advice obtained from Ricardo UK in email correspondence suggested that building an injector driver in-house with the available resources cannot be done. As a result, an automotive injector driver has just been purchased prior to final thesis submission to operate the injector.

Following this, the optical chamber has been modified to fit the fuel injector and

Table 12: Photosonics high-speed video camera specifications

| | |
|---|---|
| Camera name | Phantom V4.3 |
| Image sensor type | SR-CMOS |
| Memory | 1024 Mb |
| Max. resolution | 800 × 600 pixels |
| Speed at max. resolution | 1000 pps |
| Speed at min. resolution | 90000 pps |
| Lens mount type | C mount |
| Lens | Nikon 60mm F2.8 Macro |

preliminary firing tests are currently being conducted. Two Photosonics high-speed video cameras (one monochrome and one colour) are used to record combustion in this combustion chamber. Table 12 shows the camera specifications. Operating instructions for the camera are shown in the camera operating manual and briefly described in appendix B. Prior to the purchase of the injector driver, preliminary video recordings using the monochrome camera of the engine running on diesel fuel (effectively motoring the optical chamber) at about 1000 r/min were obtained to establish camera and lighting positions around the engine. Here the camera frame rate was set at 3000 pictures per second (pps), with a video resolution of 320x240 pixels. At these settings, about 4.35 seconds of video was taken, showing about 40 complete non-firing cycles. A light-emitting diode (LED, shown as a white dot in the stills) was used to indicate piston TDC positions, occurring during at the end of the compression stroke (otherwise known as "combustion" TDC) and the end of the exhaust strokes (exhaust TDC). Piston crank-angle positions relative to "combustion" TDC was determined from the video time-base in conjunction with the TDC indicator LED.

Figure 116 shows selected stills from this video, displaying the interior of the optical chamber as well as the TDC LED indicator. Frame A shows the optical chamber at "combustion" TDC conditions (i.e. maximum piston compression with both intake and exhaust valves shut). Peak motored pressures and temperatures occur during this period. During combustion, the peak cylinder pressure is expected to be of the order of 6-7 MPa and peak combustion temperatures can be of the order of 2000 K (similar to levels in typical engines with similar compression ratios and fuelling requirements). Frame B shows an initial condensation of water vapour contained in the inducted air (indicated by small white wisps at the bottom of the chamber) occurring at about 56 crank angle degrees ATDC. This is a result of rapid cooling

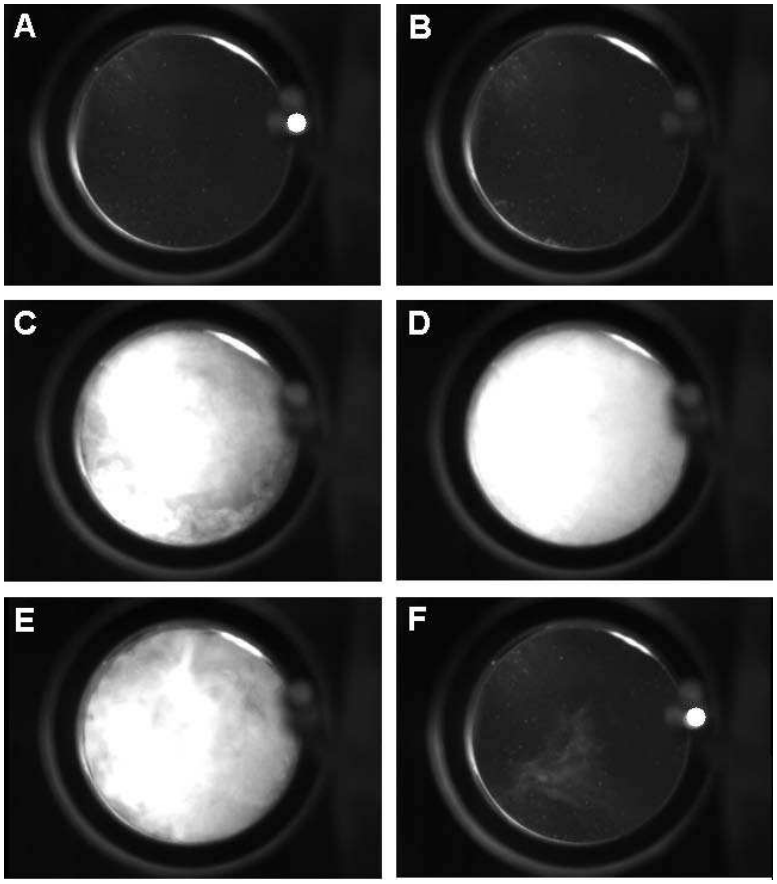


Figure 116: Selected stills from motored optical chamber video; showing conditions at "combustion" TDC (frame A) , initial condensate formation at 56 degrees ATDC (frame B), condensate formation at 90 degrees ATDC (frame C), apparent maximum condensate formation at 120 degrees ATDC (frame D), condensate dissipation at 180 degrees ATDC (frame E) and conditions at exhaust TDC (frame F)

during the expansion stroke. Frame C shows water vapour condensation building up significantly at about 90 degrees ATDC. Video recordings of injected fuel spray and resulting combustion is expected to be unaffected by this cloud formation, as combustion is expected to end by this time. Increased charge temperatures resulting from combustion might prevent condensation from occurring on a significant scale. Frame D shows an apparent maximum in water vapour condensation (indicated by a maximum perceived cloud density) occurring at about 120 degrees ATDC. Frame E shows the condensed water vapour cloud dissipating at 180 degrees ATDC (the start of the exhaust stroke). Frame F shows exhaust TDC (occurring 360 degrees ATDC, where the piston reaches TDC again), where the remnants of the condensed water vapour cloud can be seen. As the exhaust valve has been open for some time prior to this, most of the charge has been evacuated from the optical chamber. The video also shows a tolerable amount of engine vibration at this speed, which fortunately

does not distort the video significantly.

Also prior to the injector driver purchase, the common-rail injector LabVIEW program (which generates the start-of-injection and pulse duration injector signals) was tested by feeding the output signals a LED, which would visually simulate the injection event (where a lighted LED indicates a firing injector). Since the LED would be turning on/off very quickly, the monochrome camera was used to record the simulated injection events. As the common-rail injector would not be firing every cycle (to prevent damage to the windows and also to avoid overheating the chamber), the camera would need a trigger signal to begin recording just prior to the injection event. The test videos described previously in figure 116 had the camera triggered by hand, which would not be practical in this instance due to the high frequency of injection. The LabVIEW injector program has a user-defined camera trigger timing, which sends a signal to the camera to begin recording. The LabVIEW program tested successfully for a variety of injector and camera timings at a constant simulated engine speed (simulated shaft encoder readings corresponding to 1000 r/min was fed to the program as a speed input). The following is an example of how these tests were assessed. Injection (simulated by the lighted LED) was set to start at 5 degrees BTDC and the injection period was set at 10 crank angle degrees. At 1000 r/min this would give an injection duration of about 1.67 ms. The camera was then set to begin recording 7 degrees BTDC, slightly earlier in order to catch the first injection. The intended injection duration was checked against the time-base of the recorded video, and at a camera frame-rate of 1200 pps both values matched. At higher camera frame-rates however, (1900 pps in this instance), there was a discrepancy in the recorded injection duration. At 1000 r/min the intended injection duration is again fixed at 1.67 ms while the camera time-base gave a value of 1.58 ms. This can be due to the camera recording at a very high frame rate, and the frames at which the LED is only just beginning to turn on/off (an event only seen at high camera frame-rates) were mistakenly used as injection start/end references. If these particular frames are ignored and the frames at which the LED fully lights (the immediate frame after in the injection-start case, the immediate frame prior in the injection-end case) are taken as the start/end injection points instead, the recorded injection duration matches the intended value.

Videos of the original fuel injector (connected to the original fuel system running on diesel fuel) firing outside the engine into a custom-made Perspex box were also recorded with the monochrome camera. The TDC signals from the engine was fed

to an LED, which in turn was mounted in view of the camera to show combustion and exhaust piston TDC positions over the course of the video. The camera was set at 6000 pps with a video resolution of 320x240 pixels for these tests, while the engine was running at about 1600 r/min. The video obtained is about 2.3 seconds long, and shows 32 injection events. Figure 117 shows a selected sequence from the video, which includes the TDC LED indicator at the top-left corner of each frame and the injector tip (which fires 3 jets).

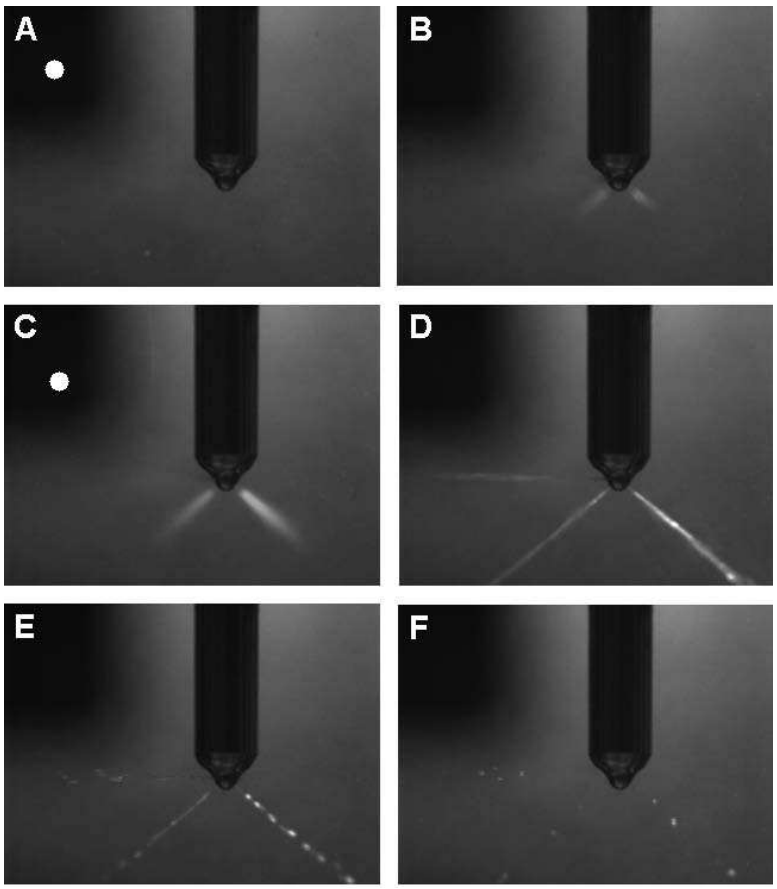


Figure 117: Selected stills from firing injector video; showing conditions at exhaust TDC (frame A) , start-of-injection at 2 degrees BTDC (frame B), conditions at "combustion" TDC (frame C), injection continuing at 90 degrees ATDC (frame D), end-of-injection at 130 degrees ATDC (frame E) and conditions at 180 degrees ATDC (frame F)

As with the previous video in figure 116, the piston crank-angle position relative to "combustion" TDC was determined from the video time-base in conjunction with the TDC indicator LED. Frame A shows the injector at 360 crank angle degrees BTDC (otherwise known as exhaust TDC) and frame B shows injection starting at 2 degrees BTDC. Frame C shows injection continuing at "combustion" TDC while frame D shows the injection ending at 130 degrees ATDC. Frame E shows the injector completely shut at 180 degrees ATDC, with the last droplets of fuel

still in view. Initial tests show that the Perspex box fills with fuel vapour after a few injections, clouding the video. This is because the original fuel injector is firing once every cycle and there is inadequate venting of the box. It is likely that the common-rail system will not have this problem, as it will fire at a much lower frequency.

Since the injector driver has been obtained just prior to final thesis submission, the common-rail injector has been test fired in the Perspex box to test injection timings in a similar manner to the original injector test video. The injector has test-fired appropriately (i.e. at the intended start time and duration), and the optical chamber has also been modified to accommodate the injector. The injector's position in the chamber depends on the spray cone angle as well as the number of nozzle holes (both shown in table 11), as fuel wetting of the windows can obscure the video. Third year undergraduate project work has provided a design for a Nimonic alloy cap that fits over the common-rail injector nozzle, blocking all holes bar one. If the expected window wetting problem cannot be solved by adjusting the injector position (i.e. how deep the injector penetrates into the chamber), this cap will be made, fitted and tested. As the injector driver purchase and optical chamber modifications were recent developments, a detailed experimental test layout was not prepared for inclusion here. The completed rig will then be used to optically assess combustion, the details of which are discussed in chapter 5.

## 6.2 Appendix B - Detailed Experimental Procedure

Tests on any engine should be conducted with two people present for safety. While lone working is possible, a technician must be notified of any activity. Steel-toe boots must always be worn regardless of the type of lab work conducted. When refilling the auxiliary fuel tanks, or when dealing with fuel in general, safety goggles, labcoats and nitrile gloves are recommended personal protective equipment. Prior to running a laboratory test on any engine, a technician must be asked beforehand to prepare the exhaust gas analysers. He or she will ensure that the analysers are calibrated and warmed-up before the test begins. If a technician is unable to prepare the analysers, there is a procedure for doing so in this appendix. Also prior to beginning a test, the cooling water supply pump switch and the main exhaust gas extraction fan must be turned on. In addition, the dynamometer mounted on the engine of interest must be placing no load on the engine prior to engine starting.

- Checklist prior to starting an engine
  - Cooling water supply is turned on and running (red light illuminated, supply pressure should be about 40 psi).
  - Main exhaust fan is turned on and running.
  - Both auxiliary extraction fans are turned on.
  - There is diesel fuel in the 20 ml measuring flask.
  - Gas analysers, vacuum pump and heated lines are turned on and running.
  - Desktop computer, both charge amplifiers and data acquisition box are turned on and running.
  - If emulsified fuel is used, ensure the emulsion was circulating through the auxiliary fuel tank and the emulsifier for at least 30 minutes prior to starting test.

### 6.2.1 Gardner 1L2 engine operation

1. The engine will always be started on diesel fuel, regardless of test. Ensure diesel fuel supply in the 20 ml measuring flask is topped up to an appropriate level to avoid fuel starvation.
2. Ensure the injector fuel line is filled with fuel by manually pumping the primer

handle on the fuel pump. Pump the handle until it becomes stiff (about 3-5 pumps is needed).

3. Turn the intake valve switch on the top right hand side of the engine upwards. This keeps the intake valve open, preventing compression and allowing the crankshaft to be turned without resistance. Attempting to turn the crankshaft without doing so can result in kickback of the handle.

4. Remove the cap on hand-crank stub and slot in the crankshaft handle until the cutout on the handle fits the protrusion on the stub.

5. With one hand on the handle (thumb held outside) and the other hand ready to turn the intake valve switch back down, begin turning the crank clockwise with increasing speed. When appropriate, turn the valve switch down swiftly. This allows compression (and therefore ignition) to occur. Continue turning the crankshaft for two or three more turns then swiftly remove the handle from the crank stub. Take care when doing this action as the handle can slip from grasp. The engine should begin firing. If not, allow the engine to settle and try again. In cold temperatures, spray a small amount of ether (commonly known as Easy-Start) into the air box above the engine while turning the crankshaft. Note: ether is highly flammable and only 3-4 sprays is required.

6. Once running, raise the engine speed above idling (about 500 r/min) by turning the fuel pump control wheel (found on the right hand side of the engine) clockwise. To lower speed, turn the wheel anti-clockwise.

7. When other liquid fuel is to be tested (biodiesel, emulsions etc), the auxiliary fuel supply needs to be used. Ensure the blue fuel tank above the Gardner engine contains the fuel to be tested, and the 3-way valve below the tank is connecting the fuel lines between the tank and the 50 ml measuring flask. Also ensure the ball valve just under the 50 ml flask is closed. Just before the Gardner fuel filter assembly on the engine, there are two ball valves. One ball valves opens/ shuts the diesel fuel supply to the fuel system, while the other opens/ shuts the auxiliary fuel supply to the fuel system. To allow fuel from the auxiliary supply to flow into the engine, open the auxiliary fuel supply valve first and then turn off the diesel fuel supply valve. If a fuel mixture is needed, the emulsifying circuit is to be used. Here the fuel tank should be filled with the appropriate amounts of the fuel mixture. The 3-way valve should be connecting the fuel tank and the inlet of the emulsifying circuit and the ball valve just under the measuring flask should be open. All the ball valves on the emulsifier should also be open. Turn on the emulsifier and the circulating pump to operate the circuit. When needed, open the ball valve on the 50 ml measuring flask

inlet to fill the flask with the fuel mixture.

8. For dual-fuel operation with natural gas, the main natural gas solenoid switch (near the lab entrance, requires a key) needs to be switched on. In addition, there are two natural gas supply valve solenoid switches that must be also turned on prior to using the gas supply. The first switch is located close to the Ricardo spark ignition engine switchboard and the second is on the far end of the Gardner engine (underneath the wet/dry mercury thermometers). On the gas supply line to the Gardner, open the two yellow ball valves first. The red button on the solenoid valve along the line must then be pushed down and the silver pull-switch on the blue diaphragm valve has to be pulled once. The natural gas supply can then be controlled by the knob underneath the natural gas flowmeter.

9. For dual-fuel operation with hydrogen gas, the ball valve on the intake manifold gas induction assembly must be opened. The hydrogen tank must then be opened via the slot key. Adjust the desired outlet pressure on the regulator (typically 0.15 MPa). The hydrogen gas supply can then be controlled by the knob underneath the hydrogen flow meter.

10. To operate the water-brake dynamometer, the spring-lock on the gate wheel must be lifted out and turned outwards. To increase load, turn the gate wheel clockwise until the desired load is shown on the load gauge. While changing the load, the load gauge must be checked to see if it is calibrated. To do so, check if the needle point underneath the load gauge is level with the needle point located directly next to it. If not, turn the wheel on top of the load gauge (clockwise to raise the needle point underneath the load gauge, anti-clockwise to lower it) appropriately. The load gauge will not show the correct load level until both needle points are at the same level.

11. Once test is finished, reduce the dynamometer load to zero then replace the lock.

12. Using the knob underneath the natural gas flowmeter, turn off the natural gas supply to the engine if the engine was running in dual-fuel mode with natural gas. When running on hydrogen gas, turn off the hydrogen supply via the knob underneath the hydrogen flow meter. Following this, close the main valve on the hydrogen tank. Then open the knob underneath the hydrogen flow meter to empty the hydrogen gas line. Then close the ball valve on the intake manifold assembly. Leaving the hydrogen gas line filled with hydrogen is unsafe and is a hazard.

13. If the engine was running on liquid fuels from the auxiliary fuel supply, switch the fuel supply over to diesel fuel. The engine should always be stopped when run-

ning on diesel fuel. Allow the engine to run on diesel fuel at a low load to purge the fuel system.

14. Reduce the engine speed to idle via the control wheel and swing the fuel pump lever next to the wheel outward away from the engine. This will shut off the fuel supply to the engine. Once the engine has settled and completely stopped rotating, return the fuel switch to its original position.

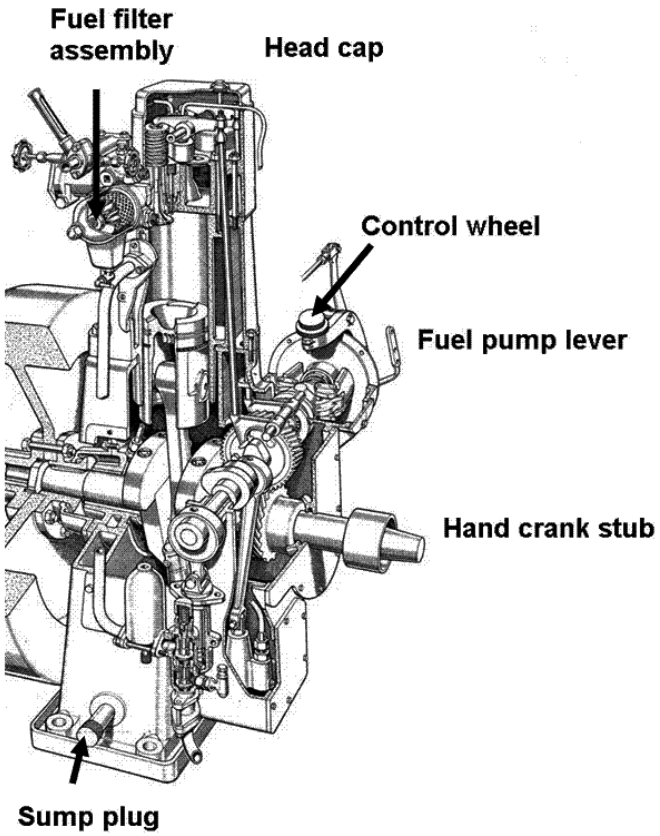


Figure 118: Cut-away drawing of Gardner engine, diagram from Gardner service manual

### 6.2.2 Gardner 1L2 engine basic maintenance

1. The engine oil grade that the Gardner requires is SAE30. This grade is equivalent to the Redwood no. 1 viscosity grade. The oil should be changed regardless of how often the engine is used at least once every 6 months. Sump oil can be drained by unscrewing the cap off the sump plug below the oil dipstick. Fresh oil has to be poured in from the top of the engine (with the head cap removed) down the rocker arm channels. Waste oil must be placed in an empty oil bottle, and disposed of via contractors such as Safety Kleen.

2. The fuel injector should be removed and the injector nozzle cleaned about the

same time and frequency as the oil change. The detailed procedure for doing so can be found in the Gardner engine manual.

3. Vibrations from the engine can loosen screws around the air box. This can cause an air leak into the inlet tract, which results in inaccurate air box pressure drop readings. Ensure these screws are always tight and giving a good seal.

4. During dual-fuel operation with either natural gas or hydrogen, if and when what sounds like knock occurs immediately reduce the gaseous fuelling rate as knocking can seriously damage the piston. At speeds below 1500 r/min, the natural gas flow rate into the engine should not go above 30 litre/ min regardless of pilot fuel setting. When running on hydrogen gas, the flow rate cannot go more than 40 litre/min at speeds below 1000 r/min if the pilot fuel setting is more than 12 kg. During engine operation with hydrogen gas, preignition can occur in the intake manifold, making a loud hollow metallic banging sound. While this preignition is not immediately hazardous, damage to the intake manifold can occur.

5. If the fuel supply to the fuel measuring flasks on any engine appears to have stopped/ run out, more fuel needs to be pumped in from the header tanks. These header tanks are the only diesel fuel source in the lab, and hand pumps are accessed via hatches on the far wall behind the gas turbine rig. Turning these hand pumps back and forth pumps fuel from the header tank to the diesel fuel line in the lab. If this does not restore the fuel supply pressure, then an auxiliary fuel system has to be used.

6. The steel and PTFE exhaust analyser sample lines need regular cleaning as the lines become blocked with soot. To do this, the lines have to be disconnected from the analysers on one end and the engine exhaust sampling assembly on the other. The PTFE lines to the Signal $NO_x$ and Rotork unburnt HC units can be pulled out from the heated lines (leaving the heater coils where they are), avoiding the need to remove the entire assemblies. Acetone can be used to clean the sample lines. Here, a sample line is filled with a sufficient amount of acetone and left to sit for 2-3 hours with the open ends sealed. The line can be shaken lightly to ensure the acetone coats the entire line. After this time, the remaining acetone can be blown out with compressed air. The process can be repeated as necessary until the line is completely clear.

7. It would be good practice to clean the combustion chamber at least once every two years or so. The cylinder head can be removed, exposing the piston. Use acetone or methylated spirit to clean the metal surfaces in addition to the inside of the inlet/ exhaust valves. Remember that new gaskets and seals would be required

when putting the engine back together.

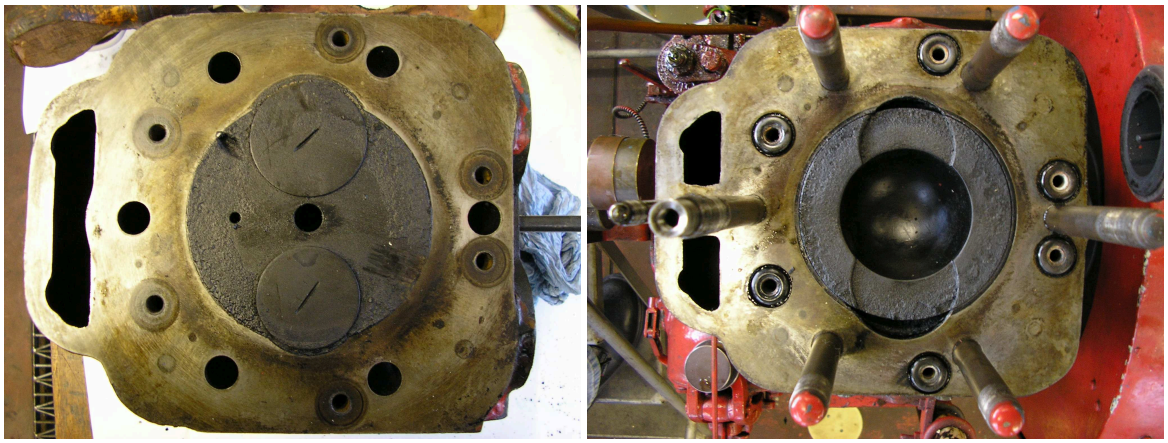

Figure 119: Gardner 1L2 cylinder head (left picture) and piston head (mounted within engine block) prior to cleaning (right picture)


Figure 120: Gardner 1L2 cylinder head (left picture); and piston (removed from engine block) after cleaning (right picture)

### 6.2.3 Ford four-cylinder engine operation

1. There is a water pump on the Ford engine which circulates cooling water through the engine block and the heat exchanger. This pump must be turned on prior to starting the engine via the switch on the extension cord above the engine. The mains power supply for extension cord can be found on the main laboratory desk (same power supply as the charge amplifier for the Gardner fuel line pressure transducer).
2. The engine will always be started on diesel fuel and fuel should be available to the engine prior to starting.
3. Ensure that the optical chamber (with either steel or quartz windows in place) is secured tightly in its seat. Also make sure that the blow off valve is adjusted appropriately and all Perspex guards are in place.
4. The engine requires a standard 12-volt car battery to start. The red alligator clip (which supplies power to the fuel pump) has to be connected to the positive terminal of the battery. On the side of the battery box, there are two switches. The switch furthest away from the user turns on the fuel pump, while the other switch turns the starter motor.
5. As any test on this engine did not require dynamometer loading for this work, there was no need to adjust the dynamometer.
6. The engine speed can be controlled via the wooden lever next to the fuel measuring flask. Loosen the wooden handle and lift it up to increase speed, pull down to decrease speed.
7. Be aware that the optical chamber will get very hot to touch and, as the engine is noisy due to operation on 3 cylinders, ear protectors are recommended.
8. To shut the engine down, simply turn off the fuel pump switch on the side of the battery box.
9. Once engine is shut down, turn off the engine's water pump and the mains switch on the main desk.

### 6.2.4 Ford four-cylinder engine basic maintenance

1. The engine oil grade that the engine requires is 10W/40. Like the Gardner, the oil should be changed regardless of engine use at least every 6 months. The sump plug is located at the bottom of the engine and fresh oil has to be poured into the cam cover (with the head cap removed). Waste oil must be disposed of via contractors such as Safety Kleen.

2. If the engine does not start, or if the engine turns over too slowly, the batteries might be discharged. The batteries can be recharged overnight with the battery charger found in the lab.
3. When removing the pressure transducer in the engine block, cooling water (that flows around the transducer housing for cooling) will flow into the transducer seat and then into the combustion chamber. To remove most of the water, use a hand pump to pump water out of the chamber via the injector hole. To ensure all the water is removed, run the engine without the chamber in place for no more than a few seconds. This will expel any water remaining in the chamber. Be aware that when the engine runs without the chamber in place, the engine will be very loud and ear protectors must be worn.
4. The quartz windows must be removed and cleaned with a microfibre cloth whenever residue builds up. In addition, they must always be stored in a secure padded box when not in use. Always ensure that the screws on the chamber caps are screwed in via a star pattern, not in a sequential clockwise direction.

### 6.2.5 Photosonics high-speed camera operation

1. Connect the lens adapter to the Nikon lens and then screw the adapter into the camera. Keep the lens cover on until the camera is ready for recording.
2. Remove the top platform of the adjustable camera mounting via the silver catch from the main body of the mount. Using the flathead screw that is supplied, screw the platform to the bottom of the camera. Make sure that the "LENS ↑" mark is pointing towards the lens side of the camera.
3. Screw the main body of the camera mount onto the tripod. Adjust the leg length as needed and place the tripod where the camera would be sitting during recording.
4. Slot the camera into the camera mount until the silver catch pops out. Make sure the camera is sitting secure in the mount and the tripod is sitting properly. Remove the lens cover.
5. Connect the power supply, Ethernet and external trigger cables. Make sure that all connections lock properly in place.
6. Plug in the power supply to the mains and the Ethernet connector to the PC. Turn on the power supply to the camera. The LEDs behind the camera should be lighting up. Change the IP address of the PC to that of the camera. The procedure for this can be found in the installation CD package of the Photosonics software.
7. Double-click the icon labelled "Phantom 640" to run the software which controls

the camera. Go to the “Acquisition” menu, and then click “Setup and Recording”.
8. Adjust the different parameters (frame rate, resolution etc) as needed.
9. Click “Capture” to begin recording of the event, and then “Trigger” to end the recording. The software will then change to playback mode. If the recording is satisfactory, ensure that the file is saved. The full instruction on how to use the software can be found in the accompanying Photosonics manual.
10. When recording is finished, remove all the camera equipment and store them in the appropriate shock-proof case.

### 6.2.6 Gas analyser startup/ calibration/ shutdown procedure

1. Switch on all analysers. Ensure that the main exhaust fan is on and the valve on the sample line manifold behind the analyser rack is closed before switching on the analysers. Leave the analysers on for one hour.
2. Behind the analyser rack is a black plastic ice bath bucket. Any water needs to be drained out via a yellow ball valve underneath the rack, on the right hand side. The water will drain through a long clear plastic tube.
3. After one hour the HC analyser can be lighted up. Open all the connected gas bottles by turning the keys (on the tanks with pressure regulators, all other tanks must be opened via the top valves) anti-clockwise and turn on the heated filter (on the switch on the far end of the Gardner test bed) as well as the HC analyser heated line (control box on the right hand side of the analyser rack). 4. The analyser will be ready to be lighted up if the two red lights are blinking on and off. Ensure the “PUMP”, “IGNITION” and “ZERO” buttons are off. To ignite the analyser, the screw on the fuel control must be completely screwed in, while the sample pressure should be maintained at 2 psi. Press the “PUMP”, “IGNITION” and “ZERO” buttons to begin lighting up. The “PUMP” button turns on the analyser’s sampling pump, “IGNITION” starts the ignition process and “ZERO” opens the nitrogen gas inlet to the analyser (which is the zero HC calibration gas). The analyser will try to light up a few times, and once it has the fuel pressure should be set via the fuel control screw to 11 psi. Leave the HC analyser on for a further 45 minutes. The air pressure should already be set to about 15 psi. 5. Behind the rack is a U-tube moisture filter which contains silicon oxide and cotton wool. The silicon oxide and cotton wool need to be removed and replaced with a dry batch prior to tests. The water trap also needs to be drained during this process. Remember to close the water trap once drained.

6. By this time the Servomex analyser and the Signal analyser will indicate when they are at operating temperatures via their displays. After this the analysers can be calibrated.
7. Set the zero reading on HC analyser with the suppression knob by pressing the "ZERO" button, where the sample pressure should be exactly 2 psi.
8. Span the HC analyser by pushing the "SPAN" button. Once again the sample pressure should be exactly 2. Set the analyser to 918 ppm (concentration of the calibrated span gas) with the calibration knob on the 0-10000 ppm scale.
9. Set the HC analyser back on zero by pushing the "ZERO" button.
10. Zero the Signal analyser by pushing the "ZERO" button and then automatically calibrate the analyser with the zero gas by pushing the "CAL" button.
11. Span the Signal analyser by pushing the "SPAN" button and then automatically calibrate the analyser with the span gas by pushing the "CAL" button.
12. Switch the Signal analyser back to zero by pushing the "ZERO" button.
13. Open the "$N_2$ zero gas" valve to the Servomex analyser. This allows nitrogen gas to flow into the analyser.
14. Set the analyser to read zero on all the gas readings via the interactive menu. A password (4000) is required to make the change.
15. Close the "$N_2$ zero gas" valve and open the "$CO_2$/ CO span gas" valve. This allows the span gas for $CO_2$/ CO detection to flow into the analyser.
16. Span the analyser with the gas concentration value that is being used (4% CO, 9% $CO_2$).
17. Close the "$CO_2$/ CO span gas" valve and open the "$O_2$ span gas" valve. This allows the span gas for $CO_2$/ CO detection to flow into the analyser. Here the span gas on compressed air, which should give 21%.
18. Close the "$O_2$ span gas" valve and open the "$N_2$ zero gas" valve again. All readings should return to zero. If not, repeat the calibration steps for the analyser.
19. Switch on Servomex sample pump plug and the Signal heated line by plugging in the plugs behind the rack, and turning on the control box next to the power sockets.
20. Ensure drain tap for the ice bath bucket is closed and fill the ice bath with ice.
21. Open sample manifold valve and ensure all other gas supply valves are shut.
22. Enable $NO_x$ and HC analyser sampling by pushing the "SAMPLE" button on each. Ensure sample pressure of the HC analyser is exactly 2.
23. Once test is finished, close the sample manifold valve. Open the "$N_2$ zero gas" valve. For the Signal and HC analysers, press the "ZERO" button. This will allows

the analysers to purge themselves of sample gas. Once the readings on both drops to values close to zero, press "STOP" on both analysers.
24. Turn off all analysers when the countdown on the Signal analyser is over.
25. All gas supply tanks must be turned off. This can be done by turning the keys (on the tanks with pressure regulators, all other tanks must be shut via the top valves) clockwise until shut. However, leave the compressed-air gas cylinder open for 30 minutes after the end of the test. Close all tanks after 30 minutes of ending the test.
26. Unplug the Servomex sample pump plug and the Signal heated line plug from the sockets behind the analyser rack. The temperature control for the HC heated line must also be turned to "O" to be switched off.
27. The intake air temperature display as well as the heated filter control on the opposite end of the Gardner engine must be turned off.

- Checklist before leaving laboratory
  - All engines are shut down.
  - All exhaust fans are turned off.
  - Cooling water supply is turned off.
  - Natural gas solenoid valve switches and valves are turned off.
  - Hydrogen tank is closed, and the hydrogen gas line has been purged.
  - All analysers are turned off.
  - All gas tanks are shut off.
  - Plugs for sample pump and heated line are unplugged.
  - Heated filter must be switched off.
  - Desktop computer, both charge amplifiers and data acquisition box are turned off.
  - Lock the door to the laboratory.

## 6.3 Appendix C - Calculation of Experimental Parameters

This section shows a complete list of all experimental parameters and how they were calculated. One set of parameters is calculated for each experimental condition. Excel sheets that have these formulas programmed in have been created and they are available for use as references.

### 6.3.1 Standard experimental parameters and sample calculations

The following section shows the various parameters recorded for data analysis. Sample recorded experimental data, in addition to the resulting calculated parameters are shown for the Gardner engine during normal CI engine operation with diesel fuel at 1000 r/min at maximum load. All sample calculations throughout this appendix are shown using this operating condition.

-Brake power ($\dot{W}_{\mathrm{b}}$) / W:

$$\dot{W}_{\mathrm{b}} = \frac{LN}{0.447} = 7315.436 \tag{21}$$

where $L$ is the dynamometer load (196.2 N), $N$ is engine speed (16.667 r/s), and 0.447 $\mathrm{m}^{-1}$ is equal to $1/2\pi x$, where $x$ is the length of the Gardner dynamometer torque arm (0.356 m).

-Brake mean effective pressure (BMEP) / MPa:

$$BMEP = \frac{\dot{W}_{\mathrm{b}} n'}{V_{\mathrm{s}} N \sigma} = 0.63 \tag{22}$$

where $n'$ is the number of revolutions per cycle (2), $V_{\mathrm{s}}$ is the swept volume of the cylinder (0.00139 $\mathrm{m}^3$) and $\sigma$ is the number of cylinders (1).

-Mass flow rate of fuel ($\dot{m}_{\mathrm{f}}$) / kg/s:

$$\dot{m}_{\mathrm{f}} = \frac{m_{\mathrm{f}}}{t} = 0.000509 \tag{23}$$

where $m_{\mathrm{f}}$ is a calibrated mass of fuel in kg (obtained from a calibrated volume in a fuel measuring flask), and $t$ is the time taken for the engine to consume this calibrated mass of fuel in seconds. For diesel fuel tests, the calibrated fuel volume is 20 ml (at the stated operating condition $t$ = 33 s), while all other liquid fuels used a different fuel measuring flask which had a calibrated volume of 50 ml.

During dual-fuel operation, the $\dot{m}_{\mathrm{f}}$ term in the following equations becomes the sum of the pilot fuel mass flow rate ($\dot{m}_{\mathrm{pf}}$) and the gaseous fuel mass flow rate ($\dot{m}_{\mathrm{gf}}$) components. The gaseous fuel mass flow rates were converted from volume flow rates read from their respective volume flow meters.

-Mass flow rate of intake air ($\dot{m}_{\mathrm{a}}$) / kg/s:

$$\dot{m}_{\mathrm{a}} = C_d A \sqrt{2\rho_a \Delta P} = 0.0105 \tag{24}$$

The above equation gives the mass flow of air through a sharp-edged orifice, which is attached on the inlet of the Gardner air box. Here $C_d$ is the discharge coefficient of the orifice (0.6), $A$ is the area of the orifice (0.000642 $\mathrm{m}^2$), $\rho_{\mathrm{a}}$ is the density of air (1.209 $\mathrm{kg/m}^3$), and $\Delta P$ is the pressure difference across the orifice (309.015 Pa).

-Volumetric efficiency ($\eta_{\mathrm{v}}$):

$$\eta_{\mathrm{v}} = \frac{\dot{m}_{\mathrm{a}} n}{V_{\mathrm{s}} \rho_{\mathrm{a}} N} = 0.75 \tag{25}$$

-Specific fuel consumption (SFC) / kg/MJ:

$$SFC = \frac{\dot{m}_{\mathrm{f}}}{\dot{W}_{\mathrm{b}}} = 0.0696 \tag{26}$$

During dual-fuel operation SFC was not calculated as it was deemed irrelevant due to the possibility of the pilot and main fuel having different values of energy content.

-Thermal efficiency ($\eta_{\mathrm{th}}$):

$$\eta_{\mathrm{th}} = \frac{\dot{W}_{\mathrm{b}}}{\dot{m}_{\mathrm{f}} LHV_{\mathrm{f}}} = 0.338 \tag{27}$$

where $LHV_{\mathrm{f}}$ is the lower heating value of the fuel used (42.5 MJ/kg).

-Equivalence ratio ($\phi$):

$$\phi = \frac{F/A}{F/A_{\mathrm{st}}} = 0.699 \tag{28}$$

where $F/A$ is the actual fuel-air ratio ($\dot{m}_{\mathrm{f}}/\dot{m}_{\mathrm{a}}$), and $F/A_{\mathrm{st}}$ is the stoichiometric fuel-air ratio (0.0691), which is calculated from the stoichiometric combustion equations of diesel fuel and air.

-Pilot fuel enthalpy fraction (PEF):

$$PEF = \frac{\dot{m}_{\mathrm{pf}} LHV_{\mathrm{pf}}}{\dot{m}_{\mathrm{pf}} LHV_{\mathrm{pf}} + \dot{m}_{\mathrm{gf}} LHV_{\mathrm{gf}}} = 1 \tag{29}$$

where the subscripts "pf" and "gf" represent the pilot fuel and gaseous fuel components respectively (at this operation condition, no gaseous fuel was inducted).

The enthalpy fraction of the gaseous fuel can be found by subtracting the pilot fuel fraction from unity.

-Specific emissions / g/MJ:

Specific emission readings show the mass of a particular exhaust gas species that is emitted during the production of 1 MJ of brake engine energy. The mass flow rate of each individual measured exhaust gas species is found using combustion chemical equations as well as a mass balance drawn between the total mass flow of reactants into the engine and the mass flow rate of combustion products in the exhaust gas. The process is lengthy and custom made Excel sheets showing these calculations in detail are available for reference. Here, a sample calculation detailing how to obtain specific oxygen levels from the Gardner engine during normal CI engine operation at 1000 r/min and 0.63 MPa BMEP is shown.

First, the $\beta$ term in the relevant combustion equation for normal diesel combustion is found by dividing the measured air molar flow rate ($\dot{n}_{\mathrm{a}}^{*}$, obtained from the measured air mass flow rate) by a computed air molar flow rate ($\dot{n}_{\mathrm{a}}$, obtained from the chemical combustion equations), as seen in the relationship below:

$$\beta = \frac{\dot{n}_{\mathrm{a}}^{*}}{\dot{n}_{\mathrm{a}}} = 1.43 \tag{30}$$

Using this value to complete the combustion equation, the computed mole fraction of water in the exhaust gas products ($MF_{\mathrm{H_2O}}$) can then be found by dividing the number of moles of water in the exhaust products by the total moles of exhaust products (for diesel combustion in dry air during normal CI engine operation):

$$MF_{\mathrm{H_2O}} = \frac{0.5y}{x + 0.5y + 3.76\beta(x + 0.25y - 0.5z) + (x + 0.25y - 0.5z)(\beta - 1)} = 0.0883 \tag{31}$$

The computed mole fraction of the remaining exhaust gas species in combustion equations are also found in the same manner. Shown below is the relationship for obtaining the computed mole fraction of oxygen in the exhaust ($MF_{\mathrm{O_2}}$):

$$MF_{\mathrm{O_2}} = \frac{(x + 0.25y - 0.5z)(\beta - 1)}{x + 0.5y + 3.76\beta(x + 0.25y - 0.5z) + (x + 0.25y - 0.5z)(\beta - 1)} = 0.0604 \tag{32}$$

The total computed mole fraction of non-water products in the exhaust gas ($MF_{\mathrm{non-H_2O}}$) is found by subtracting $MF_{\mathrm{H_2O}}$ from unity.

$$MF_{\mathrm{non-H_2O}} = 1 - MF_{\mathrm{H_2O}} = 0.912 \tag{33}$$

At the same time, the computed molecular weight of a certain amount of gas species in the exhaust products is obtained by multiplying the computed mole fraction of the gas species by its respective molecular weight. For example, obtaining the computed molecular weight of oxygen contained in the exhaust gas ($MW_{O_2}$) is shown below:

$$MW_{O_2} = (MF_{O_2})(32) = 1.933 \tag{34}$$

The computed molecular weight of the other exhaust product gas species is then found in a similar manner and the sum ($MW_{\text{total}}$) obtained:

$$MW_{\text{total}} = MW_{O_2} + MW_{N_2} + MW_{H_2O} + MW_{CO_2} = 28.908 \tag{35}$$

To obtain a computed molar flow rate of all the exhaust gas products defined in the combustion equations, the total mass flow rate of inducted reactants ($\dot{m}_{\text{total}}$) is needed. This is derived from the understanding that there is a mass balance between the reactants and exhaust products:

$$\dot{m}_{\text{total}} = \dot{m}_{\text{f}} + \dot{m}_{\text{a}} = 0.0111 \ \text{kg/s} \tag{36}$$

The molar flow rate of all the exhaust products ($\dot{n}_{\text{total}}$) is then calculated by dividing $\dot{m}_{\text{total}}$ by $MW_{\text{total}}$:

$$\dot{n}_{\text{total}} = \frac{\dot{m}_{\text{total}}}{MW_{\text{total}}} = 0.000382 \ \text{kmol/s} \tag{37}$$

The computed molar flow rate of water in the exhaust gas ($\dot{n}_{H_2O}$) is then obtained by multiplying $\dot{n}_{\text{total}}$ with $MF_{H_2O}$:

$$\dot{n}_{H_2O} = (\dot{n}_{\text{total}})(MF_{H_2O}) = 0.0000337 \ \text{kmol/s} \tag{38}$$

The corresponding mass flow rate of water in the exhaust gas ($\dot{m}_{H_2O}$) is then found by multiplying $\dot{n}_{H_2O}$ by the molecular weight of water:

$$\dot{m}_{H_2O} = (\dot{n}_{H_2O})(18) = 0.000607 \ \text{kg/s} \tag{39}$$

$\dot{m}_{H_2O}$ is then subtracted from $\dot{m}_{\text{total}}$ to give the mass flow rate of non-water exhaust gas ($\dot{m}_{\text{non}-H_2O}$):

$$\dot{m}_{\text{non}-H_2O} = \dot{m}_{\text{total}} - \dot{m}_{H_2O} = 0.0104 \ \text{kg/s} \tag{40}$$

This mass flow rate of non-water products in the exhaust gas will now be used to obtain a molar flow rate of the dry measured exhaust gas species. Here, the dry measured gases are $O_2$, $CO_2$, CO; while $NO_x$ and unburnt HC are measured wet.

In order to obtain the molar flow rate of the dry measured exhaust gas, the average molecular weight of the measured dry exhaust gas needs to be found. First, the measured volumetric concentrations of each exhaust gas species must be converted to mole fractions. This is done by converting the original volumetric measurement (either % or ppm) to fractions then multiplying by $MF_{\mathrm{non-H_2O}}$. For $NO_x$ and HC calculations, the sum of $MF_{\mathrm{H_2O}}$ and $MF_{\mathrm{non-H_2O}}$ (i.e. unity) is used as these gases are measured wet. At this engine operating condition, an oxygen concentration of 7.445% (in dry exhaust gas) was measured. Here, the measured mole fraction of oxygen ($MF^*_{\mathrm{O_2}}$) is obtained by the following relationship:

$$MF^*_{\mathrm{O_2}} = \left(\frac{7.445}{100}\right)(MF_{\mathrm{non-H_2O}}) = 0.0679 \tag{41}$$

The measured mole fractions of each individual exhaust gas species are then obtained and added together to give the total measured mole fraction ($MF^*_{\mathrm{total}}$).

$$MF^*_{\mathrm{total}} = MF^*_{\mathrm{O_2}} + MF^*_{\mathrm{CO}} + MF^*_{\mathrm{CO_2}} + MF^*_{\mathrm{NO_x}} + MF^*_{\mathrm{HC}} = 0.157 \tag{42}$$

However, to obtain the total molecular weight of the measured products the measured mole fraction of nitrogen gas in the exhaust ($MF^*_{\mathrm{N_2}}$) is required. To obtain this value, the sum of all the mole fractions of the individual gas species is subtracted from unity:

$$MF^*_{\mathrm{N_2}} = 1 - MF^*_{\mathrm{total}} = 0.843 \tag{43}$$

This is based on the assumption that nitrogen is the only remaining exhaust gas species. Following this, the molecular weight of each gas species in the measured exhaust gas is obtained by multiplying its measured mole fraction with its respective molecular weight. Below is the relationship for obtaining this value of oxygen:

$$MW^*_{\mathrm{O_2}} = (MF^*_{\mathrm{O_2}})(32) = 2.172 \tag{44}$$

The total molecular weight of the measured exhaust gas ($MW^*_{\mathrm{total}}$) is the sum of each measured molecular weight of the measured exhaust gas species ($N_2$, $NO_x$ approximated to NO, HC, $CO_2$, CO, $O_2$):

$$MW^*_{\mathrm{total}} = MW^*_{\mathrm{O_2}} + MW^*_{\mathrm{CO}} + MW^*_{\mathrm{CO_2}} + MW^*_{\mathrm{NO_x}} + MW^*_{\mathrm{HC}} + MW^*_{\mathrm{N_2}} = 29.676 \tag{45}$$

The molar flow rate of non-water products in the measured exhaust gas ($\dot{n}_{\mathrm{non-H_2O}}$) is now found by dividing $\dot{m}_{\mathrm{non-H_2O}}$ by the $MW^*_{\mathrm{total}}$:

$$\dot{n}_{\mathrm{non-H_2O}} = \frac{\dot{m}_{\mathrm{non-H_2O}}}{MW^*_{\mathrm{total}}} = 0.000352 \ \ \mathrm{kmol/s} \tag{46}$$

Now the molar flow rate of each individual measured exhaust gas species can be found. For $NO_x$ and HC calculations, the total exhaust product molar flow rate is used. For the measured molar flow rate of oxygen ($\dot{n}^*_{O_2}$), this is shown by the following relationship:

$$\dot{n}^*_{O_2} = (\dot{n}_{non-H_2O})(MF^*_{O_2}) = 0.0000239 \ \text{kmol/s} \tag{47}$$

The mass flow rate of each measured gas species can then be found using their respective molecular weight. The measured mass flow rate of oxygen ($\dot{m}^*_{O_2}$) is shown by the relationship below:

$$\dot{m}^*_{O_2} = (\dot{n}^*_{O_2})(32) = 0.000764 \ \text{kg/s} \tag{48}$$

Finally, $\dot{m}^*_{O_2}$ is then divided by $\dot{W}_b$ to give the specific emission of that particular exhaust gas species, as shown in the following equation:

$$Specific\ O_2 = \frac{\dot{m}^*_{O_2}}{\dot{W}_b} = 104.455 \ \text{g/MJ} \tag{49}$$

Special thanks to Dr. John Olsen and Prof. Roy Crookes for providing the base Excel sheets containing these equations at the start of the project.

## 6.4 Appendix D - Quantification of Measuring Equipment Errors

Table 13: Accuracies of measuring instruments used in percentage of full scale deflection (FSD) unless otherwise stated*

| Instrument | Measurement range | Accuracy |
|---|---|---|
| Digital stopwatch* | - | +/- 0.10 s (human error) |
| Inclined manometer | 0-100 mm $H_2O$ | +/- 0.50% |
| $NO/NO_x$ analyser | 0-4000 ppm | +/- 1.00% |
| HC analyser | 0-10000 ppm | +/- 1.00% |
| $O_2$ analyser | 0-100% | +/- 1.00% |
| CO, $CO_2$ analysers | 0-10% | +/- 1.00% |
| Water-brake | 0-25 kg | +/- 0.40% |
| Tachometer | 0-2500 r/min | +/- <1.00% |
| Natural gas flowmeter | 0-100 litre/min | +/- 1.25% |
| Hydrogen gas flowmeter | 0-44 litre/min | +/- 1.25% |
| Piezoelectric transducer | 0-20 MPa | +/- 1.00% |
| Charge amplifier | - | +/- 1.00% |
| Type K thermocouples* | -40 to 1200°C | +/- 2.50°C |

Table 13 shows the stated accuracies of all measuring instruments used. Tables 14 and 15 quantifies the effect of each instrument accuracy on the various calculated experimental parameters (such as thermal efficiency and equivalence ratio) at a typical engine running condition (i.e. normal engine operation with diesel fuel at 1000 r/min and maximum load). A dual-fuel example was not considered as the gaseous fuel flow meters (both glass variable area types) introduce less than 1% of error into the calculated parameters and as a result their influence on the combined error is negligible (compared with errors introduced by the other instruments). With regards to quantifying total errors of the presented data (thermal efficiency, specific emissions etc), a similar approach to error analysis by previous work on this test rig was adopted [95]. Here the total error of a particular parameter is taken to be the sum of the various instrument accuracies. The respective y-axis error bars shown in figures throughout this work are based on these values.

The following example calculates the effect of combined instrument errors on thermal efficiency. The variation in thermal efficiency resulting from the stopwatch accuracy (+/- 0.002), manometer accuracy (+/- 0.000), dynamometer accuracy (+/- 0.004)

and tachometer accuracy (+/- 0.014) was calculated individually, and then added together to give a total variation (+/- 0.02 or +/- 2%). This value was then used to plot y-axis error bars on the relevant graphs of experimental results. Gas analyser accuracies are omitted in this instance as they have no effect on thermal efficiency. This method is fairly simple compared with typical statistical error analysis (such as maximum standard deviations, calculated and shown in the repeatability sections). However, as experimental data from single test runs are presented (in addition to the wide range of fuels and engine operating modes used) the consideration of maximum data variability is warranted.

Table 14: Errors present in specific emissions (in g/MJ) resulting from instrument accuracies

| - | Specific $NO_x$ | Specific HC | Specific CO | Specific $CO_2$ |
|---|---|---|---|---|
| Stopwatch | +/- 0.001 | +/- 0.000 | +/- 0.001 | +/- 0.141 |
| Manometer | +/- 0.015 | +/- 0.001 | +/- 0.007 | +/- 1.606 |
| $NO_x$ analyser | +/- 0.124 | +/- 0.000 | +/- 0.000 | +/- 0.000 |
| HC analyser | +/- 0.000 | +/- 0.169 | +/- 0.000 | +/- 0.000 |
| CO analyser | +/- 0.000 | +/- 0.000 | +/- 2.086 | +/- 0.000 |
| $CO_2$ analyser | +/- 0.000 | +/- 0.000 | +/- 0.000 | +/- 3.621 |
| Water-brake | +/- 0.002 | +/- 0.001 | +/- 0.009 | +/- 1.844 |
| Tachometer | +/- 0.082 | +/- 0.007 | +/- 0.034 | +/- 7.381 |
| Total error | +/- 0.224 | +/- 0.178 | +/- 2.137 | +/- 14.593 |

Table 15: Errors present in calculated parameters resulting from instrument accuracies

| - | $\eta_{th}$ | $\eta_v$ | SFC / kg/MJ | $\phi$ | BMEP / MPa |
|---|---|---|---|---|---|
| Stopwatch | +/- 0.002 | +/- 0.000 | +/- 0.001 | +/- 0.006 | +/- 0.000 |
| Manometer | +/- 0.000 | +/- 0.006 | +/- 0.000 | +/- 0.006 | +/- 0.000 |
| Water-brake | +/- 0.004 | +/- 0.000 | +/- 0.001 | +/- 0.000 | +/- 0.006 |
| Tachometer | +/- 0.014 | +/- 0.030 | +/- 0.003 | +/- 0.000 | +/- 0.000 |
| Total error | +/- 0.020 | +/- 0.036 | +/- 0.005 | +/- 0.012 | +/- 0.006 |

## 6.5 Appendix E - Repeatability Assessment

The following sections present repeatability tests of the tested modes at a particular engine condition. Standard mean deviations of each parameter were calculated, and these deviations were used to judge repeatability of the experimental data presented in the main experimental result sections. A full set of natural gas repeatability data was unobtainable at the time of writing as the building supply system was under repair.

### 6.5.1 Normal CI engine operation

This section presents sets of experimental parameters taken for one engine operating condition (normal engine operation at 1000 r/min) with one fuel (neat diesel fuel). These results were picked from data sets taken over the span of 2 months.

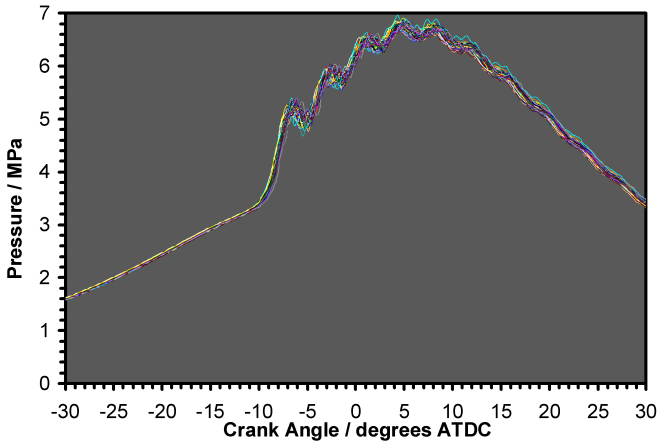


Figure 121: 50 consecutive combustion chamber pressure traces taken during normal engine operation with neat diesel fuel at 1000 r/min and 0.63 MPa BMEP

Figure 121 shows combustion chamber pressure traces of 50 consecutive cycles, taken at the aforementioned test condition at 0.63 MPa BMEP. The pressure traces themselves appear very similar to each other, while peak pressure values have a maximum standard deviation of 0.22 MPa. There are differences in the inflection point from cycle-to-cycle, which suggests variations in ignition delay. Figure 122 shows first pressure derivatives (with respect to crank angle) of the same 50 consecutive cycles as figure 121. From these plots, the maximum standard deviation in ignition delay is of the order of 0.1 ms. Figure 123 shows fuel line injection pressures recorded during the same 50 consecutive cycles as the previous figures. Here, the maximum standard

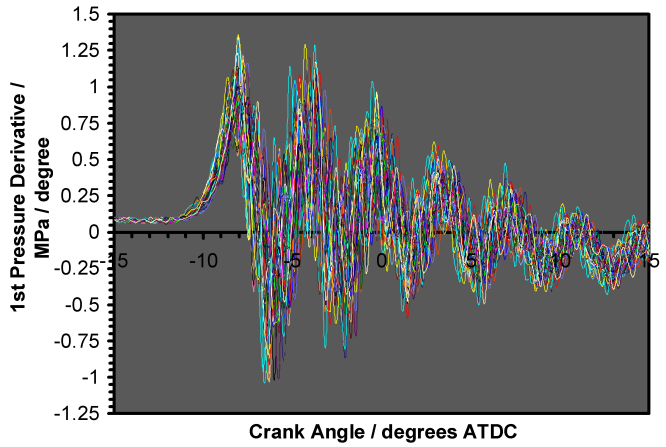


Figure 122: 50 consecutive first pressure derivative traces taken during normal engine operation with neat diesel fuel at 1000 r/min and 0.63 MPa BMEP

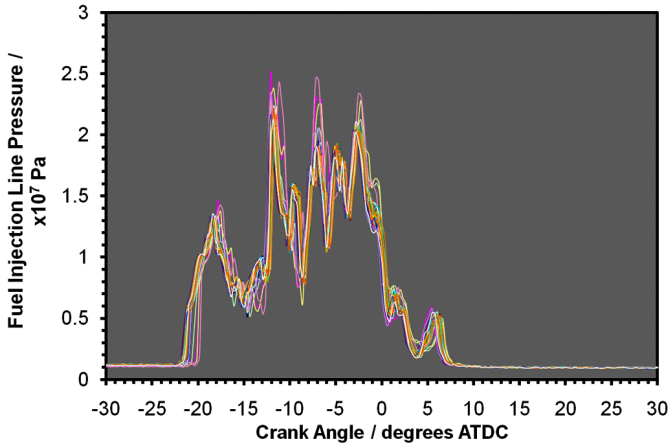


Figure 123: 50 consecutive fuel injection line pressure traces taken during normal engine operation with neat diesel fuel at 1000 r/min and 0.63 MPa BMEP

deviation in injection timing is of the order of 0.6 crank angle degrees. The same difference applies for the end of injection. As a result, test variables (such as ignition delay and peak pressure) with other test conditions are only considered significantly altered if the variations are greater than the maximum differences established here.

Figure 124 shows a thermal efficiency comparison for four separate test cases, all at a common test condition (normal engine operation at 1000 r/min) with neat diesel fuel. While thermal efficiency values remain generally similar across the load range for test cases 1,2 and 4; test 3 has some anomalous readings at higher engine loads. Normally this does not occur, and can be a result of fuel supply problems (air bubbles in the fuel line, low fuel pressure) that happen occasionally. Considering the trend at lower loads and the other test cases, it is likely that these points will

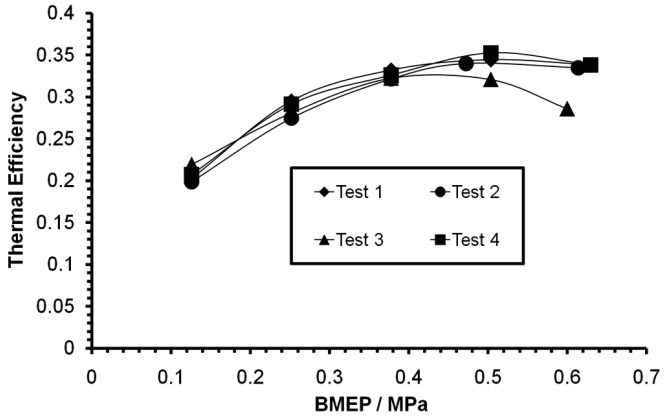


Figure 124: Thermal efficiency trends taken over 4 separate test runs during normal engine operation with neat diesel fuel at 1000 r/min

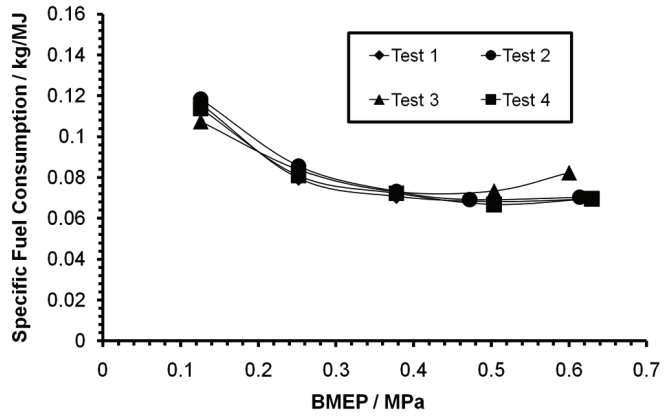


Figure 125: Specific fuel consumption trends taken over 4 separate test runs during normal engine operation with neat diesel fuel at 1000 r/min

fall in line with the other cases should test 3 be repeated. Ignoring these points, a maximum difference (difference between data points at the extremes of the data range) of thermal efficiency of all the test cases is about 2%.

Figure 125 shows a specific fuel consumption (SFC) comparison for the same test cases at the same test condition. SFC values remain very similar for each test case, with a maximum difference of 0.01 g/MJ occurring at the lowest load. As in the thermal efficiency plot, test 3 appears to have some anomalous readings at higher engine loads. Normally this does not occur, and can be a result of fuel supply problems in this particular instance (air bubbles in the fuel line, low fuel pressure). It is likely that should this test case be repeated, it will fall in line with the other cases.

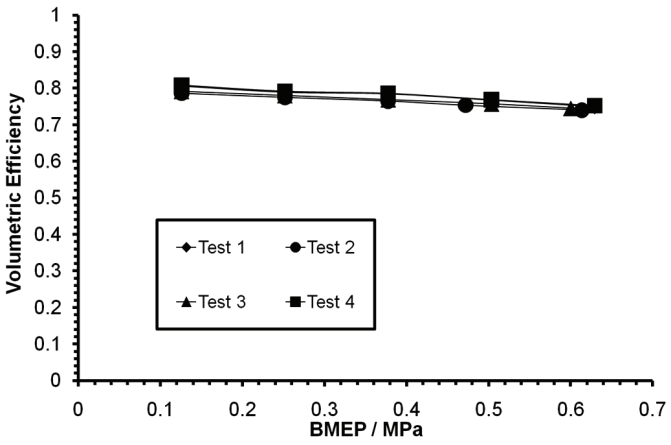


Figure 126: Volumetric efficiency trends taken over 4 separate test runs during normal engine operation with neat diesel fuel at 1000 r/min

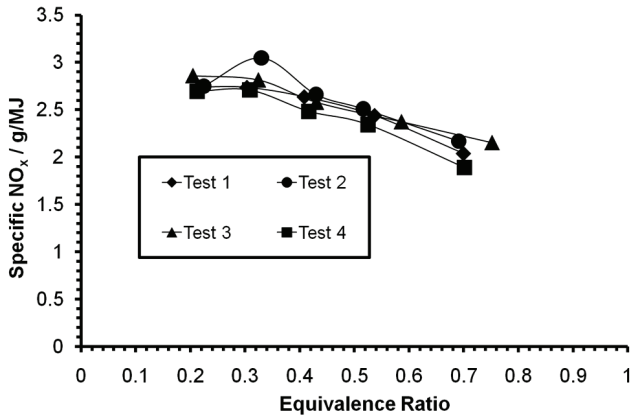


Figure 127: Specific $NO_x$ trends taken over 4 separate test runs during normal engine operation with neat diesel fuel at 1000 r/min

Figure 126 shows a volumetric efficiency comparison for the same test cases at the same test condition above plot. Volumetric efficiency values remain very similar for each test case, with a maximum difference of 2% between the maximum and minimum recorded points.

Figure 127 shows a specific $NO_x$ comparison for the same test cases at the same test condition. $NO_x$ emissions are fairly comparable between the test cases, with an anomalous point at an equivalence ratio about 0.33 during test 2. Across the entire equivalence ratio range, the maximum difference is about 0.3 g/MJ.

Figure 128 shows a specific unburnt hydrocarbon (HC) comparison for the same test cases at the same test condition. Unburnt HC emissions are fairly comparable

between all the test cases, with a comparatively large variation at low loads. Here the maximum difference is also about 0.3 g/MJ.

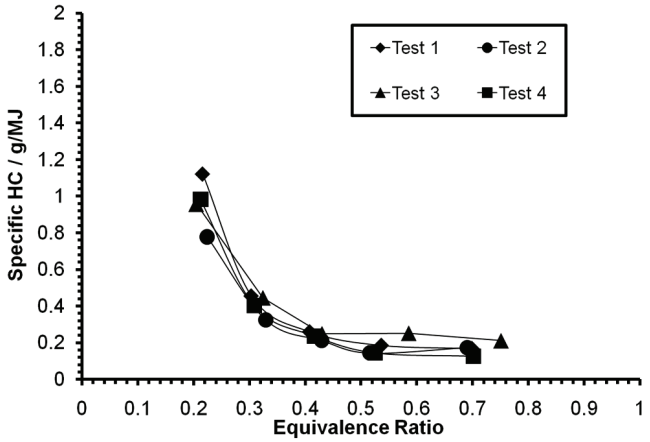


Figure 128: Specific unburnt HC trends taken over 4 separate test runs during normal engine operation with neat diesel fuel at 1000 r/min

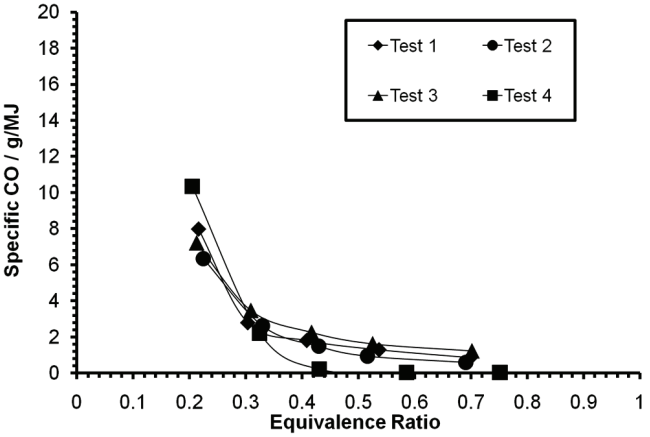


Figure 129: Specific CO trends taken over 4 separate test runs during normal engine operation with neat diesel fuel at 1000 r/min

Figure 129 shows a specific CO comparison for the same test cases at the same test condition. CO emissions are fairly comparable between all the test cases, with a comparatively large variation at low loads. With regards to test 4, almost zero levels of CO were recorded. However, the maximum difference occurs at low loads and is about 4 g/MJ.

Figure 130 shows a specific $CO_2$ comparison for the same test cases at the same test condition. $CO_2$ emissions are fairly comparable between all the test cases, with the exception of an anomalous reading at the maximum load for test 4. Considering the trend during low and intermediate equivalence ratios, it is likely this point will fall

in line with the other test cases if repeated. With this point ignored, the maximum difference is about 18 g/MJ.

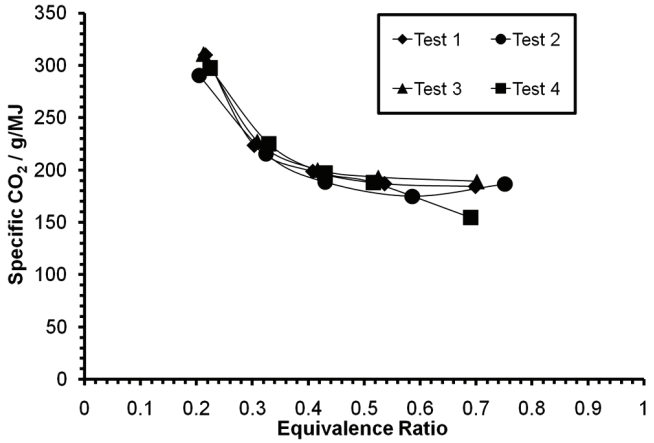


Figure 130: Specific $CO_2$ trends taken over 4 separate test runs during normal engine operation with neat diesel fuel at 1000 r/min

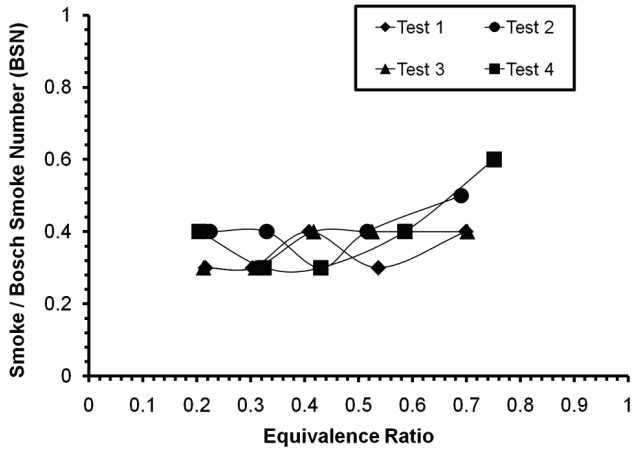


Figure 131: Bosch smoke number trends taken over 4 separate test runs during normal engine operation with neat diesel fuel at 1000 r/min

Figure 131 shows a Bosch smoke number comparison for the same test cases at the same test condition. Smoke emissions are fairly comparable between all the test cases, with the exception of an anomalous reading at the maximum load for test 4. Considering the trend during low and intermediate equivalence ratios, it is likely this point will fall in line with the other test cases if repeated. With this point ignored, the maximum difference is 0.2 BSN.

As the largest differences taken between the maximum and minimum extreme points pointed out previously do not occur throughout the load/ equivalence ratio range, standard deviations for the above parameters were also calculated to establish a

general repeatability trend. Table 16 shows the maximum standard deviations for the above calculated parameters in all four test cases. Overall, results taken from single test runs are fairly repeatable while the odd anomalous reading (which differs from the expected trend) can be easily identified.

Table 16: Maximum standard deviations for typical calculated test parameters during normal engine operation with neat diesel fuel

| | |
|---|---|
| Ignition delay | 0.10 ms |
| Peak pressure | 0.22 MPa |
| Injection timing | 0.6° CA |
| Thermal efficiency | 2.2% |
| Specific fuel consumption | 0.0054 kg/MJ |
| Volumetric efficiency | 0.94% |
| Specific $NO_x$ | 0.13 g/MJ |
| Specific HC | 0.12 g/MJ |
| Specific CO | 1.6 g/MJ |
| Specific $CO_2$ | 14.3 g/MJ |
| Bosch smoke number | 0.1 BSN |

### 6.5.2 Hydrogen gas dual-fuel CI engine operation

This section presents sets of experimental parameters taken for one engine operating condition (dual-fuel operation with hydrogen gas at 1000 r/min) with one pilot fuel (neat diesel fuel). These results were picked from data sets taken over a day.

Figure 132 shows combustion chamber pressure traces of 50 consecutive cycles, taken at the aforementioned test condition at 0.63 MPa BMEP. The pressure traces themselves appear very similar to each other, while peak pressure values have a maximum standard deviation of 0.3 MPa. There are differences in the inflection point from cycle-to-cycle, which suggests variations in ignition delay. Figure 133 shows first pressure derivatives (with respect to crank angle) of the same 50 consecutive cycles as figure 132. From these plots, the maximum standard deviation in ignition delay is of the order of 0.12 ms.

Figure 134 shows fuel line injection pressures recorded during the same 50 consecutive cycles as the previous figures. Here, the maximum standard deviation in

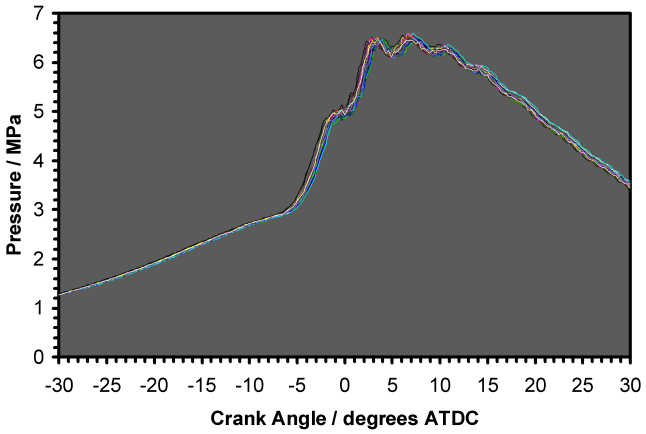


Figure 132: 50 consecutive combustion chamber pressure traces taken during dual-fuel operation with hydrogen gas with neat diesel pilot fuel at 1000 r/min and 0.63 MPa BMEP

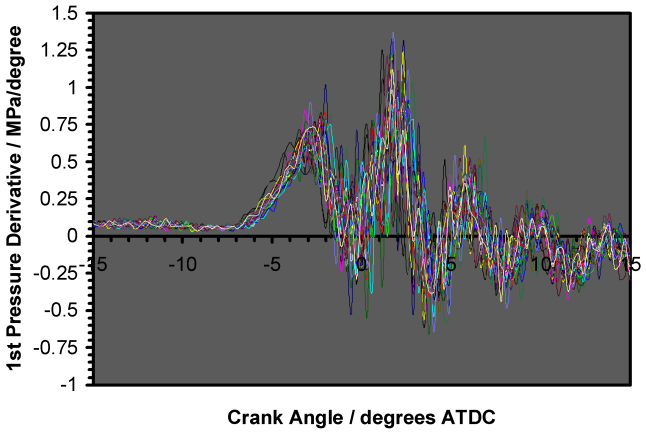


Figure 133: 50 consecutive first pressure derivative traces taken during dual-fuel operation with hydrogen gas with neat diesel pilot fuel at 1000 r/min and 0.63 MPa BMEP

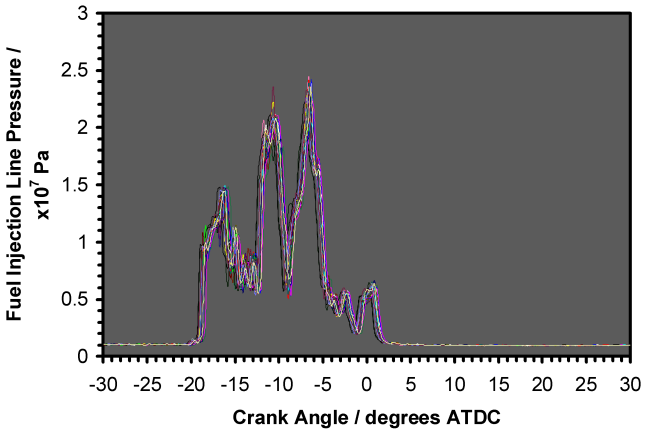


Figure 134: 50 consecutive fuel injection line pressure traces taken during dual-fuel operation with hydrogen gas with neat diesel pilot fuel at 1000 r/min and 0.63 MPa BMEP

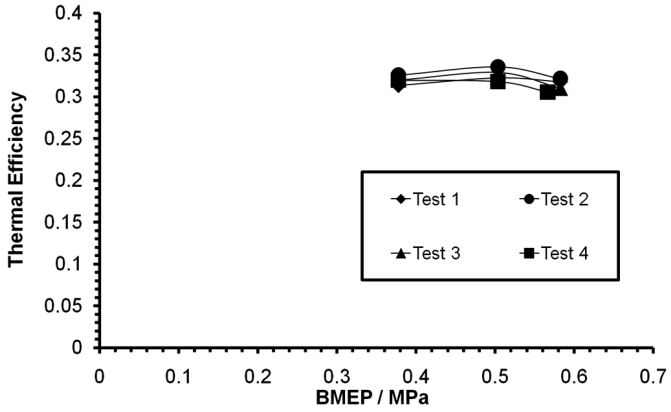


Figure 135: Thermal efficiency trends taken over 4 separate test runs during dual-fuel operation with hydrogen gas with neat diesel pilot fuel at 1000 r/min

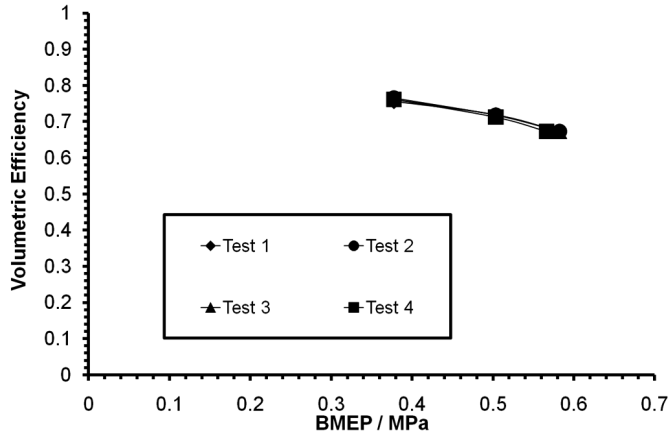


Figure 136: Volumetric efficiency trends taken over 4 separate test runs during dual-fuel operation with hydrogen gas with neat diesel pilot fuel at 1000 r/min

injection timing is of the order of 0.4 crank angle degrees. The same variation applies for the end of injection. As a result, test variables (such as ignition delay and peak pressure) with other test conditions are only considered significantly altered if the variations are greater than the maximum standard deviations established here.

Figure 135 shows a thermal efficiency comparison for four separate test cases, all at a common test condition (dual-fuel operation with hydrogen gas) with neat diesel pilot fuel. While thermal efficiency values remain generally similar across the load range for all test cases, test case 3 and 4 have thermal efficiencies (at the highest load) about 1.5% lower than test case 1 and 2. Considering all the plotted points, a maximum difference (difference between data points at the extremes of the data range) of thermal efficiency of all the test cases is about 2%.

Figure 136 shows a volumetric efficiency comparison for the same test cases at the same test condition above plot. Volumetric efficiency values remain the same for each test case.

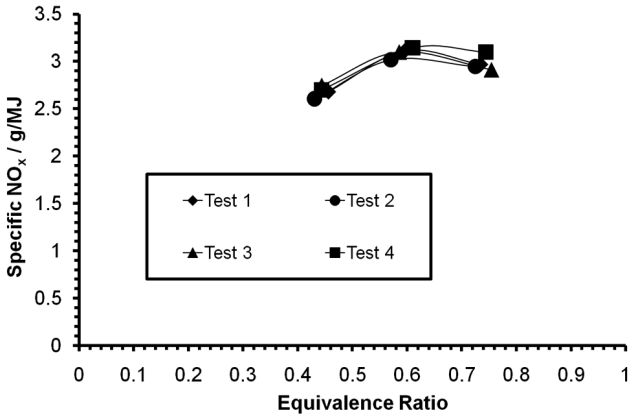


Figure 137: Specific $NO_x$ trends taken over 4 separate test runs during dual-fuel operation with hydrogen gas with neat diesel pilot fuel at 1000 r/min

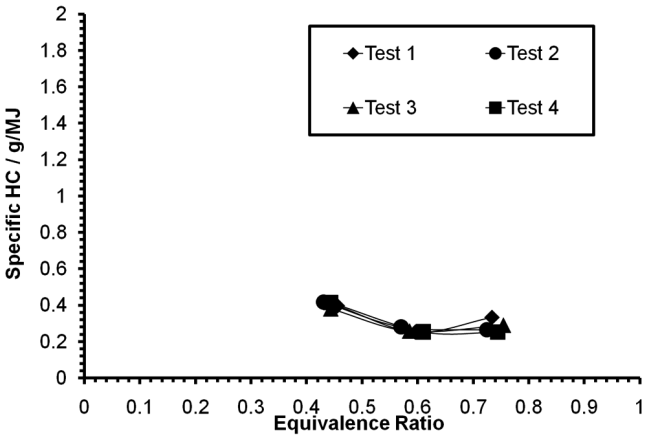


Figure 138: Specific unburnt HC trends taken over 4 separate test runs during dual-fuel operation with hydrogen gas with neat diesel pilot fuel at 1000 r/min

Figure 137 shows a specific $NO_x$ comparison for the same test cases at the same test condition. $NO_x$ emissions are fairly comparable between the test cases. Across the entire equivalence ratio range, the maximum difference is about 0.2 g/MJ.

Figure 138 shows a specific unburnt hydrocarbon (HC) comparison for the same test cases at the same test condition. Unburnt HC emissions are fairly comparable between all the test cases. Here the maximum difference is about 0.08 g/MJ.

Figure 139 shows a specific CO comparison for the same test cases at the same test

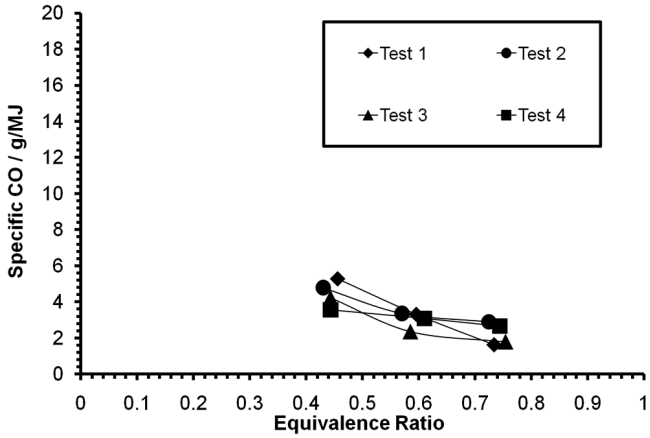


Figure 139: Specific CO trends taken over 4 separate test runs during dual-fuel operation with hydrogen gas with neat diesel pilot fuel at 1000 r/min

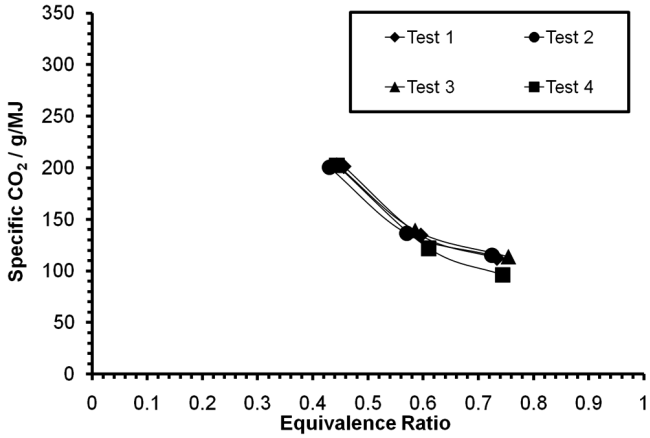


Figure 140: Specific $CO_2$ trends taken over 4 separate test runs during dual-fuel operation with hydrogen gas with neat diesel pilot fuel at 1000 r/min

condition. CO emissions are fairly comparable between all the test cases, with a larger variation at all loads compared with the other specific emissions plots. This can be due to the instrument measuring CO concentrations of similar magnitude to its sensitivity. Here, the maximum difference occurs at low loads and is about 1.7 g/MJ.

Figure 140 shows a specific $CO_2$ comparison for the same test cases at the same test condition. $CO_2$ emissions are fairly comparable between all the test cases. Here, the maximum difference is about 18 g/MJ.

Figure 141 shows a Bosch smoke number comparison for the same test cases at the same test condition. Here, the maximum difference is 0.1 BSN.

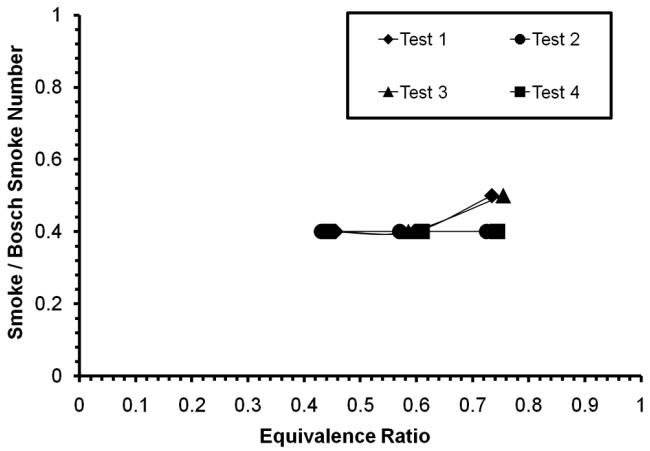


Figure 141: Bosch smoke number trends taken over 4 separate test runs during dual-fuel operation with hydrogen gas with neat diesel pilot fuel at 1000 r/min

As the largest differences taken between the maximum and minimum extreme points pointed out previously do not occur throughout the load/ equivalence ratio range, standard deviations for the above parameters were also calculated to establish a general repeatability trend. Table 17 shows the maximum standard deviations for the above calculated parameters in all four test cases. Overall, results taken from single test runs are fairly repeatable while the odd anomalous reading (which differs from the expected trend) can be easily identified.

Table 17: Maximum standard deviations for typical calculated test parameters during hydrogen dual-fuel operation with neat diesel pilot fuel

| | |
|---|---|
| Ignition delay | 0.12 ms |
| Peak pressure | 0.3 MPa |
| Injection timing | 0.4° CA |
| Thermal efficiency | 0.68% |
| Volumetric efficiency | 0.34% |
| Specific $NO_x$ | 0.07 g/MJ |
| Specific HC | 0.031 g/MJ |
| Specific CO | 0.65 g/MJ |
| Specific $CO_2$ | 7.7 g/MJ |
| Bosch smoke number | 0.1 BSN |

## 6.6 Appendix F - Carnot Efficiency Calculations

The following illustrates an attempt to estimate the Carnot coefficient of the test engine used in this work. The discussion mainly involves the charge temperature-versus-charge entropy diagram, while the cylinder pressure-versus-cylinder volume diagram is provided for comparison.

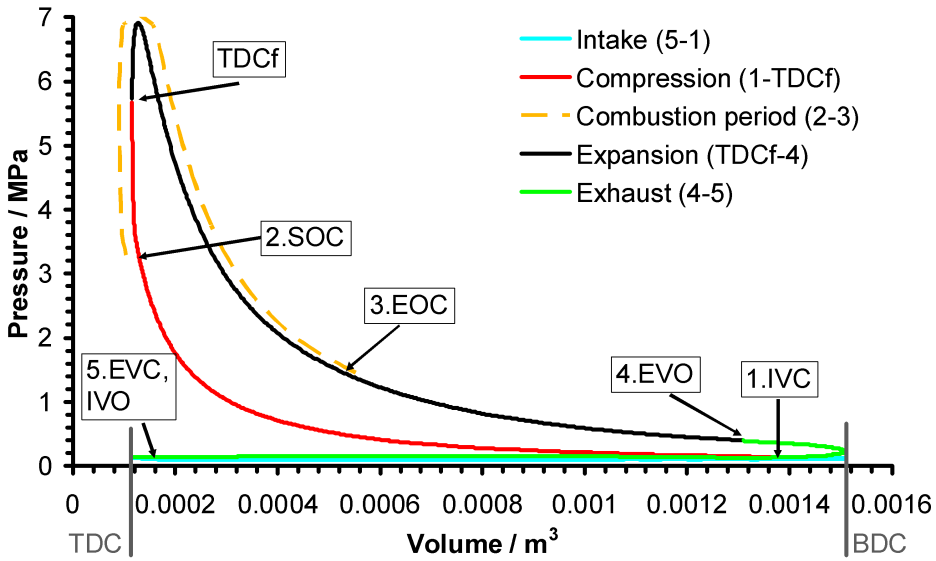


Figure 142: Cylinder pressure-cylinder volume diagram from the Gardner engine during normal operation at 1500 r/min, 0.63 MPa BMEP

Figures 142 and 143 show a pressure-volume diagram and a temperature-specific entropy diagram obtained using experimental data (normal-fuelling mode) from the test engine used in this work running at maximum speed and load. In this discussion, the intake period is defined as the crank angle period between inlet valve open (IVO) and inlet valve close (IVC) timings. The compression period is defined as the crank angle period between IVC timing and firing TDC (TDCf). The expansion period is defined as the crank angle period between TDCf and exhaust valve open (EVO) timing. The exhaust period is defined as the crank angle period between EVO and exhaust valve close (EVC) timings. The gas-exchange process from one cycle to the next is defined as the period between EVO and IVC timings. Charge pressure inside the cylinder is measured throughout the cycle (via a piezoelectric transducer) while charge volume in the cylinder is calculated from crank angle and the engine specifications. For the period between the IVC and EVO timings, the instantaneous charge temperature values inside the cylinder are calculated using

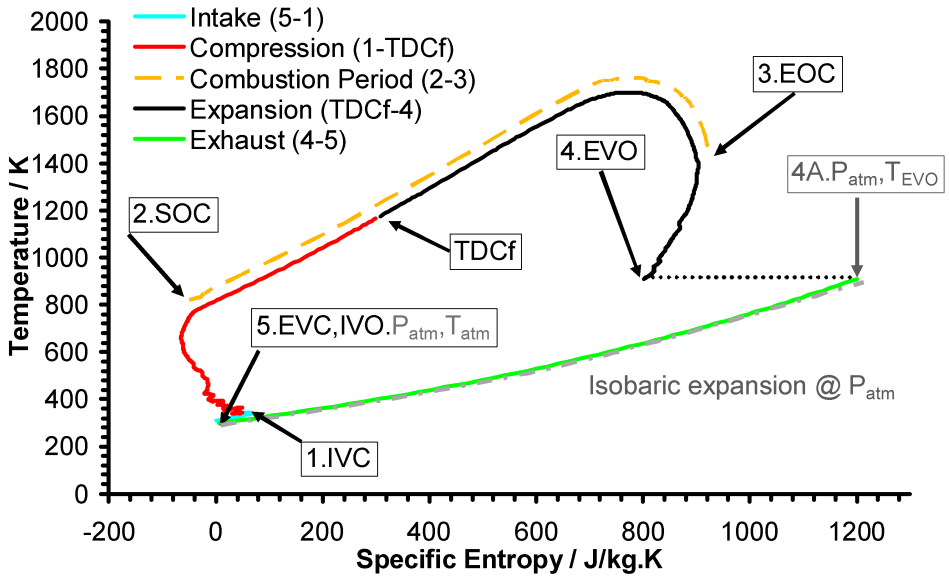


Figure 143: Charge temperature-charge specific entropy diagram from the Gardner engine during normal operation at 1500 r/min, 0.63 MPa BMEP

the ideal gas relationship between two states. The initial charge state (with a corresponding known initial cylinder pressure and volume) is set at IVC timing. The initial charge temperature is approximated equal to the engine cooling water temperature once warmed up (343.15 K maximum, established by previous work [95]). The temperature at any final state after IVC timing and before EVO timing is then found with the corresponding known final cylinder pressure and volume. The trapped air mass in the cylinder during this period is obtained via inlet air mass flow rates measured with an inclined manometer (taking into account the measured volumetric efficiency). The instantaneous specific entropy values of the charge are calculated using one of the equations for the entropy change of a perfect gas [148] (seen below). All terms with subscript "0" indicate values at reference conditions (atmospheric conditions in this case).

$$s - s_0 = c'_{\mathrm{p}} ln \frac{T}{T_0} - R ln \frac{P}{P_0} \tag{50}$$

where $s$ is specific entropy, $T$ is charge temperature, $P$ is charge pressure and $R$ is the specific gas constant. $T$ is used to calculate the corresponding isochoric specific heat capacity ($c_{\mathrm{v}}$, via correlations in reference [149]), which in turn is used to calculate the isobaric specific heat capacity ($c_{\mathrm{p}}$) via $R$. $c'_{\mathrm{p}}$ is the average of the calculated $c_{\mathrm{p}}$ values at $T$ and $T_0$ respectively. The charge is assumed to be air only, as the injected fuel mass is very small compared with the air mass [95]. There are

similar mathematical models evaluating $c_p$ as functions of temperature and fuel-air ratio for fuel-air mixtures as well as products of combustion, for instance used in [7, 150]. However, the effect of accounting for fuel-air ratio and mixtures of fuel-air or products of combustion is minimal in relation to the estimates made in this appendix.

The following describes each process in the cycle (as noted in figures 142 and 143) in sequence. At point 5 on both plots, the charge is assumed to be at atmospheric temperature and pressure ($T_{atm}$ and $P_{atm}$). After EVC timing the intake process is from point 5 to point 1. In figure 143, the apparent slight increase in charge temperature and entropy from atmospheric levels during the intake process is the result of energy-transfer (i.e. "heat"-transfer) from the cylinder walls to the charge. Dynamic pressure changes (i.e. the "ram" effect) as the piston begins to move up from BDC (just before IVC) can also contribute. The charge temperature increases further as a result of compression after IVC timing (i.e. point 1). Charge entropy levels are reduced during compression (from point 1 to point 2). This is attributed to "heat"-transfer from the charge to the comparatively cooler cylinder walls (as a result of rising charge temperature). At the start-of-combustion (SOC, point 2), both charge temperature and entropy levels rise significantly as a result of energy and entropy addition from the combustion process. Charge temperatures continue to rise until a maximum is reached (about 1700 K). Past this point, charge temperatures begin to fall (while entropy continues to increase slightly) until the end-of-combustion (EOC) at point 3. The energy addition process at temperature $T'_H$ occurs between SOC and EOC. The period at which these points occur can be approximated by net energy conversion rate plots (i.e. "heat-release" plots). The SOC definition is explained in earlier sections of the thesis, while the EOC is defined here as the crank angle at which the net energy conversion rates reduce to zero (illustrated by figure 144). A rough estimation of EOC from the net energy conversion rate plots maintains simplicity and introduces a variation of +/- 1 degree crank angle (compared with fuel mass burn rate calculations). As a result, the error in the EOC period would not affect the Carnot temperature calculations significantly. If the determination of the EOC via 90% of cumulative net energy conversion (comparable with burned fuel mass fractions calculations in SI engines) were used, a slightly higher value of $T'_H$ would be obtained (about 20 K higher). This increase in $T'_H$ would result in a negligible increase in the Carnot coefficient value. The temperature $T'_H$ at which the energy addition occurs during the combustion process is then estimated to be about 1302 K (as explained on page 5).

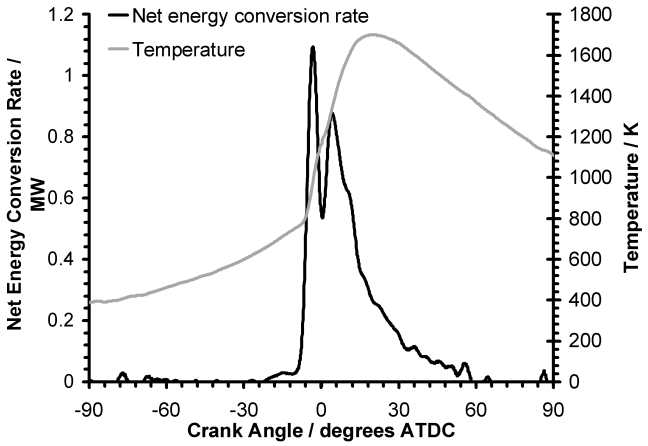


Figure 144: Net energy conversion rate ("heat-release" rate) and cylinder temperature at 1500 r/min, 0.63 MPa BMEP

Once combustion ends, "heat"-transfer continues to occur from the charge to the cooler cylinder walls and takes entropy from the charge along with it. This reduces entropy levels from point 3 until EVO timing (point 4). At EVO timing a throttling process occurs across the exhaust valve, which drops the cylinder pressure at EVO timing from about 0.4 MPa to $P_{atm}$ at point 4A. Applying the steady flow energy equation [148] between point 4 and point 4A shows that stagnation enthalpy is conserved during the throttling process (this is a very fast process in which no work is exchanged and throttling is considered adiabatic). This results in no change in stagnation charge temperature from EVO timing to point 4A (about 910 K, $T_{EVO}$). From point 4A to point 5, significant decreases in entropy and temperature result from the cylinder contents being evacuated isobarically at $P_{atm}$ until the cylinder charge is at $T_{atm}$. This isobaric closing of the thermodynamic cycle is accomplished by the atmosphere, acting as a thermodynamic reservoir. It is during this process that energy rejection occurs at an average temperature $T'_C$ (found to be about 556.7 K as explained on page 5). Together with the value of $T'_H$, this gives a Carnot coefficient value of about 57% for the tested engine. Increasing BMEP for the engine increases $T'_H$ but also increases $T'_C$. Overall higher-BMEP engines will have higher values of Carnot coefficients, with modern slow-speed marine diesel engines having Carnot coefficients between 62 and 67%, depending on the exact assumptions made in the calculation, similar to this appendix [11]. Special thanks to Prof. Alexander for his time helping the author understand the theory behind these calculations.

## 6.7 Appendix G - List of Papers Published/ Presented

Conference papers

A.M. Namasivayam, R.J. Crookes, and T. Korakianitis. Combustion characteristics of a sustainable dual-fuel compression ignition engine. 9th Conference on Energy for a Clean Environment, Portugal, 2-5 July 2007.

A.M. Namasivayam, R.J. Crookes, T. Korakianitis, and J. Olsen. Combustion in natural gas fuelled compression ignition engines with DME and RME pilot ignition. 32nd International Symposium on Combustion-The Combustion Institute, Montreal, 3-8 August 2008.

R.J. Crookes, T. Korakianitis, and A.M. Namasivayam. A systematic experimental assessment of the use of rapeseed methyl ester (RME) as a compression ignition engine fuel during conventional and dual-fuel operation. TAE 7th International Colloquium on Fuels, Stuttgart, 14-15 January 2009.

A.M. Namasivayam, R.J. Crookes, T. Korakianitis and K.D.H. Bob-Manuel. Combustion characteristics of dual-fuel diesel engine using emulsified bio-fuel for pilot ignition. SAE paper 2009-01-0490, SAE World Congress, Detroit, 20-23 April 2009.

R.J. Crookes, A.M. Namasivayam, A.Diez and T. Korakianitis. Combustion, performance and emissions characteristics of compression-ignition engines fuelled by sustainable fuels. TAE 8th International Colloquium on Fuels, Stuttgart, 19-20 January 2011.

Journal papers

A.M. Namasivayam, R.J. Crookes, T. Korakianitis, and J. Olsen. Assessment of combustion in natural gas fuelled compression ignition engines with DME and RME pilot ignition. *Proceedings of the I.Mech.E., International Journal of Engine Research*, 10(3):165-174, 2009.

A.M. Namasivayam, T. Korakianitis, R.J. Crookes, K.D.H. Bob-Manuel and J. Olsen. Biodiesel, emulsified biodiesel and dimethyl ether as pilot fuels for natural gas fuelled engines. *Applied Energy*, 87(3):769-778, 2010.

T. Korakianitis, A.M. Namasivayam, and R.J. Crookes. Natural-gas fuelled spark-ignition (SI) and compression-ignition (CI) engine performance and emissions. *Progress*

*in Energy and Combustion Science*, 37(1): 89-112, 2011.

T. Korakianitis, A.M. Namasivayam, and R.J. Crookes. Diesel and Rapeseed Methyl Ester (RME) pilot fuels for hydrogen dual-fuel combustion in compression-ignition engines. *Fuel*, Article under review, 2010.

T. Korakianitis, A.M. Namasivayam, and R.J. Crookes. Hydrogen dual-fuelling of compression ignition engines with emulsified biodiesel as pilot fuel. *International Journal of Hydrogen Energy*, 35(24): 13329-13344, 2010.